Universitat de València

Facultat de Química
Instituto de Ciencia Molecular (ICMol)

# Diseño y síntesis de nuevos materiales conmutables basados en el fenómeno de transición de espín

**Programa de Doctorado:**
Programa de Doctorado en Nanociencia y Nanotecnología (RD99/2011)

**Doctorando:**
Rubén Turo Cortés

**Directores de la tesis:**
Prof. Dr. José Antonio Real Cabezos y Dr. Carlos Bartual Murgui

Abril, 2023

El Prof. Dr **José Antonio Real Cabezos**, Catedrático del Departamento de Química Inorgánica de la Universitat de València y el Dr. **Carlos Bartual Murgui**, investigador doctor sénior en la Universitat de València, ambos adscritos al Instituto de Ciencia Molecular (ICMol).

**CERTIFICAN**:

Que la presente tesis doctoral, titulada: **Diseño y síntesis de nuevos materiales conmutables basados en el fenómeno de transición de espín**, se ha realizado bajo su dirección en el Instituto de Ciencia Molecular (ICMol) de la Universitat de València por el Graduado en Química Rubén Turo Cortés y autorizan su presentación para optar al grado de Doctor en Nanociencia y Nanotecnología por la Universitat de València.

En Paterna, a 28 de Abril de 2023.

Prof. Dr. José Antonio Real Cabezos
Tutor y Director de la tesis Doctoral

Dr. Carlos Bartual Murgui
Director de la tesis Doctoral

# AGRADECIMIENTOS

Aquí *c'est fini* la etapa predoctoral. Estoy agradecido porque no solo me ha permitido aprender sobre el fenómeno *Spin Crossover* sino que también, gracias al entorno altamente multidisciplinar presente en el Instituto de Ciencia Molecular, he podido aprender (en menor medida quizá, pero útil de igual modo) sobre otros campos de la química, física y ciencia de materiales. Me considero extremadamente afortunado por haber podido realizar el doctorado en este entorno. He podido colaborar con gente magnífica que me ha hecho crecer como investigador y, lo que considero más importante, me ha aportado métodos para seguir creciendo en el futuro. En un sentido más personal, el doctorado me ha permitido conocer a gente muy diversa de diferentes culturas y que me han ayudado en diferentes aspectos del camino.

Para empezar, es necesario apuntar que esta tesis no habría existido sin el primero de mis directores de tesis, José Antonio Real Cabezos. Me permitiste unirme a tu grupo de investigación para realizar el Trabajo de Fin de Grado y a partir de ahí, has sido una de las figuras clave que me ha guiado en el camino del investigador. He de agradecerte la dedicación total que haces a la investigación y a la enseñanza, ya sea sobre *Spin Crossover* y sus distintas aplicaciones y sinergias con otros materiales u otros temas científicos del momento. Gracias también por los diálogos informales sobre viajes a lugares como Nepal o sobre conocimientos culturales en general que han amenizado más de una sesión de preparar tubos cristalográficos y que han conseguido que obtuviese conocimientos que difícilmente habría conseguido por otras vías. No puedo tampoco dejar de valorar la influencia de mi segundo director de tesis, Carlos Bartual Murgui, he de agradecerte profundamente el esfuerzo que haces en el tutelaje *día a día* y el apoyo que has dado cuando surgía cualquier imprevisto en el laboratorio. Has tenido la paciencia suficiente para poder soportar mi curiosidad científica y has sido un apoyo ejemplar tanto en el desarrollo de la tesis doctoral como fuera de ella. Recordaré nuestras conversaciones sobre cualquier tema de la actualidad y como has conseguido que sea un poco más crítico con lo que ocurre a mi alrededor.

El segundo pilar del grupo de investigación, pero no por ello menos importante, es Mª Carmen Muñoz Roca. Puedo afirmar sin duda alguna que tu labor científica y práctica es esencial (sin ti nada de esto funcionaría). Has sido la encargada de poner orden en la sala y

una de las personas que ha limitado mi tendencia natural a dejar todos los trámites para el último momento. Agradezco muchísimo tu gran preocupación por el bienestar de todos los integrantes del grupo, presentes y pasados, pues hacen que en realidad más que un pequeño grupo de investigación esto sea una gran familia. También aprovecho para agradecer a Sacramento Ferrer Llusar su disposición colaborativa desinteresada dentro del grupo de investigación durante todos estos años y por aceptar formar parte de mi tribunal de tesis doctoral.

A los miembros del tribunal y evaluadores les agradezco el esfuerzo que realizan al acceder a valorar la presente tesis Doctoral.

A la red de excelencia María de Maeztu promovida por el Ministerio de Ciencia e Innovación (dentro de la cual se incluye al Instituto de Ciencia Molecular de la Universitat de València) por la ayuda predoctoral FPI (PRE2018-084918) que me ha permitido realizar el doctorado.

En general, me gustaría dar las gracias a todos los miembros del grupo *Switchable Molecular Materials* (*SMolMat*) de la Universitat de València, con los que he compartido los años de tesis y previos. Habéis hecho que el tiempo que he invertido aquí haya parecido corto. En primer lugar, a Ana Belén Gaspar te agradezco que durante el poco tiempo en el que hemos interactuado, haya estado siempre disponible para cualquier duda que me pudiese surgir. Muchas gracias a Maksym Seredyuk por ser siempre la definición del investigador por excelencia, has sido una de las personas a las que he acudido cuando alguna síntesis no funcionaba y siempre me has ayudado a buscar una solución adecuada. He de agradecerte también la posibilidad que me diste de poder visitar Ucrania, espero que esta guerra innecesaria acabe pronto y que en un futuro no muy lejano puedas volver a España para hacernos una visita. A Javi Valverde Muñoz, te agradezco que cuando llegué al grupo y no sabía casi nada de la investigación me enseñaras todas las bases de lo que necesitaba saber (aspectos prácticos del SQUID, síntesis y caracterización), y que estuvieses dispuesto a contestar a mis incesantes preguntas (tienes la paciencia de un santo). Tuve la gran suerte de coincidir durante unos meses cuando entré en el grupo de investigación con Lucía Piñeiro López, aunque fuese muy poco tiempo me demostraste ser una de las personas más trabajadoras y metódicas que conozco, cualidades que combinas con una amabilidad asombrosa. La mayor parte de los años en el doctorado los he compartido junto a Manuel

Meneses Sánchez, te agradezco tu actitud tranquila y el siempre estar dispuesto a echar una mano con cualquier cosa. La última incorporación al laboratorio ha sido Alejandro Orellana Silla, en tu caso has sido mi amigo desde que empezamos el grado en Química en un año que aquí no mencionaré porque me hace sentirme viejo, durante el tiempo que hemos compartido en el doctorado hemos tenido algunas etapas “explosivas” y otras más tranquilas, en tu caso he tenido la oportunidad compartir algunos de los conocimientos que me han otorgado las personas de más arriba.

Esta tesis Doctoral sería de peor calidad si en el ICMol no contásemos en el equipo técnico con Gloria Agustí y José María Martínez (Chema), los cuales me han ayudado en la caracterización de los compuestos que están descritos en la presente tesis. Os agradezco enormemente el apoyo profesional con las medidas de DSC y TGA, y el apoyo 24/7 con cualquier problema que diera el SQUID, en lo personal os agradezco las charlas cuando hemos coincidido en la jaula de pájaros (SQUID) o estaba midiendo en difracción de rayos X de polvo o simplemente nos cruzábamos a la hora de comer. Por supuesto, realizar la tesis doctoral en el ICMol me ha permitido conocer a personas magníficas como Nico, Rafa, Renato, Marta, Delia, Alejandro, Ignacio, Rita, Paula, Cristina y Juan. Tampoco puedo olvidar aquellos compañeros que ya conocía del grado y máster y que han permanecido realizando la tesis doctoral Irene, Isaac, Adrián, Manolo, Antonio, Mireia y Carmen. En cuanto al grado agradezco especialmente al “pequeño grupo” formado por Lorenzo, Rafa, Ferran y Álex, que me habéis prestado vuestra amistad desde el inicio y estáis ahí para cualquier quedada o sesión de juegos o discusión filosófica para desconectar.

Agradezco también a los colaboradores que han participado en los trabajos recogidos en esta tesis, Javi Castells-Gil y Carlos Martí-Gastaldo de la unidad de investigación FuniMat del Instituto de Ciencia Molecular de la Universitat de València y a Teresa Delgado del centro de investigación química Chimie ParisTech.

Muchísimas gracias a Azzedine Bousseksou por permitirme realizar la estancia predoctoral en su grupo de investigación *Matériaux Moléculaires Commutables* donde he tenido la oportunidad de vivir la investigación en el campo SCO desde la otra cara de la moneda, allá donde en València trabajamos predominantemente en la obtención de nuevos materiales SCO, en Toulouse el objetivo principal es la aplicación práctica de estos. La estancia me ha permitido valorar cuan necesarias son ambas perspectivas. También por

supuesto gracias a Gabor Molnár, Lionel Salmon, William Nicolazzi, Saioa Cobo y Karl Ridier por ayudar para que la estancia fuese altamente productiva en términos científicos. Y por supuesto al “ejército” de investigadores pre y postdoctorales con el que compartí esos tres meses, Ehsan, Maryam, Shiteng, Alejandro, Livia, Oleksander, Onkar, Fayan, Mario, Ion, Lijun, Xinyu, Yuteng, Yonjian. Os agradezco que me hicieseis sentir casi como en casa.

En el plano completamente personal no puedo olvidar a mis padres Carmen y Vicent, ambos sois el motivo principal por el cual he llegado a donde estoy, gracias a recordarme (continuamente en el primer caso, pues puedo decir que soy bastante entrópico) que me centrase en lo que me tenía que centrar. Me habéis apoyado continuamente para llegar hasta aquí y no tengo dudas de que eso jamás cambiará. Aunque el nuestro no haya sido un camino de rosas, estoy seguro de que el futuro será mejor que el pasado. Mamá, te quiero más de lo que se puede expresar en un texto. Papá sé que estarás allí conmigo el día que defienda la tesis. Aunque el resto de la familia no haya estado tan presente a lo largo del camino, en algunos casos por la gran distancia que nos separa, os agradezco también el apoyo que me habéis dado cuando hemos podido coincidir.

# Indice

## RESUMEN

Esta Tesis Doctoral actúa como compendio de síntesis y caracterización de nuevos materiales, generalmente porosos, que presentan el fenómeno de transición de espín (en inglés *Spin Crossover*, SCO). El principal objetivo de la Tesis Doctoral ha consistido en el diseño de estos nuevos polímeros de coordinación que combinan de forma sincrónica el fenómeno SCO asociado a los centros metálicos de $Fe^{II}$ con otras propiedades de interés, siendo la motivación última su futura aplicación en dispositivos espintrónicos. Más concretamente, los esfuerzos sintéticos se han dedicado a la obtención de polímeros de coordinación de tipo Hofmann 2D que presentan: propiedades anfitrión-huésped selectivas, fluorescencia y la posibilidad de ser depositadas fácilmente en forma de monocapas manteniendo sus propiedades SCO características.

El capítulo uno introduce los conceptos más importantes del fenómeno SCO. Esta propiedad implica la conmutación reversible entre el estado de espín alto y el estado de espín bajo que muestran algunos complejos pseudoctaédricos de los metales de transición con configuraciones electrónicas $3d^4$ a $3d^7$. El estímulo que promueve este cambio de estado de espín puede ser una variación de temperatura y/o presión, irradiación con luz o interacción con un analito adecuado. El cambio de estado de espín va acompañado de cambios en un número importante de las propiedades físicas del material SCO, entre las cuales se encuentran el color, la respuesta magnética o el volumen.

Al final de este capítulo introductorio se encuentran los objetivos planteados en la presente tesis doctoral, así como la metodología experimental establecida para la síntesis y caracterización de los polímeros de coordinación obtenidos.

El capítulo dos contiene la síntesis y caracterización de una nueva serie de polímeros de coordinación bidimensionales (2D) de tipo Hofmann basados en la coordinación del ion $Fe^{II}$, por los ligandos 5-aminopirimidina (5-$NH_2$Pym) y tetracianometalato ($[M(CN)_4]^{2-}$, M = Pt, Pd). Esta combinación da lugar a materiales con fórmula general $\{Fe(5\text{-}NH_2pym)_2[M(CN)_4]\}\cdot G$ (**$1^{M}\cdot G$**, donde M = Pt, Pd; G = ninguno, $H_2O$, MeOH, o EtOH). La funcionalización del ligando axial con el grupo amino dota a los sistemas 2D SCO resultantes de una química anfitrión-huésped versátil, así como flexibilidad estructural debido a la generación de una extensa red de enlaces de hidrógeno. El material desolvatado adsorbe reversiblemente moléculas pequeñas dotadas de grupos hidroxílicos tales como el agua,

metanol o etanol. La interconversión entre los diferentes solvatos y la fase desolvatada ocurre de forma “Monocristal a Monocristal”, por lo que es posible seguir las propiedades SCO de todos los materiales mediante la técnica Difracción de Rayos X de Monocristal (SCXRD, del inglés *Single Crystal X-Ray Diffraction*). Las propiedades SCO varían en función de la molécula invitada, el compuesto desolvatado presenta una transición cooperativa en una etapa mientras que los solvatos con $H_2O$ y MeOH/EtOH presentan transiciones en dos y media etapa, en este segundo caso la fracción de alto espín queda bloqueada a $n_{HS} = 0.5$ a bajas temperaturas. Los resultados obtenidos demuestran que las reorganizaciones estructurales reversibles asociadas a estos procesos de adsorción-desorción (**$1^{M}$** ↔ **$1^{M}$·G**) siguen un mecanismo “gate-opening” cuya cinética depende no solo de la naturaleza de la molécula invitada y de la estructura anfitrión (**$1^{Pt}$** o **$1^{Pd}$**) sino también en sus interacciones recíprocas. Además, se ha observado una modulación predecible y reversible del SCO mediante la interacción con los diferentes huéspedes y se ha relacionado precisamente con las transformaciones cristalográficas determinadas mediante difracción de rayos X.

El capítulo tres presenta la síntesis de los ligandos 4-metildisulfanilpiridina ($pyS_2Me$) y 4-etildisulfanilpiridina ($pyS_2Et$) y su uso como unidades de construcción para la formación de nuevos polímeros de coordinación SCO de tipo Hofmann formulados $\{Fe(pyS_2R)[\{M^{II}(CN)_4\}]\}$ (**MpyS₂R**; R = Me, Et; $M^{II}$ = Pt, Pd. El principal motivo de la elección de estos ligandos periféricos fue la expectación de que los grupos disulfanilo favorecerán el anclado y crecimiento de monocapas sobre sustratos de oro además de favorecer un transporte de electrones óptimo en dispositivos espintrónicos basados en las propiedades SCO. La exposición de este tipo de ligandos ricos en azufre a superficies de oro resulta en la fragmentación del enlace S-S (PyS-SR) que asegura que los grupos -SR quedan anclados actuando de espaciadores en la superficie entre los ligandos -SPy, dando lugar a una base adecuada para la construcción de la capa SCO. Todos los compuestos presentan SCO de primer orden, para **PtpyS₂Me**, **PtpyS₂Et** y **PdpyS₂Et** las transiciones son completas y cooperativas con ciclos de histéresis mientras que el compuesto **PdpyS₂Me** exhibe una transición en varias etapas. El comportamiento de este último material probablemente se debe al desorden del grupo Me-S-S-, el cual induce frustración elástica en la red cristalina del material. La Calorimetría Diferencial de Barrido (DSC, del inglés *Differential Scanning Calorimetry*) confirma los valores de $\Delta T$ y $T_c$ observados a partir de las medidas magnéticas. Los compuestos **PdpyS₂Me**, **PtpyS₂Et** y **PdpyS₂Et** exhiben efecto LIESST (del Inglés *Light Induced Spin State Trapping*) caracterizados por fracciones de espín alto tales que $n_{HS} = 0.64$,

0.96 y 0.96 respectivamente con $T_{LIESST}$ = 50, 68 y 70 K. El objetivo último de este trabajo es la futura aplicación de monocapas de estos compuestos en dispositivos espintrónicos.

El capítulo cuatro describe la síntesis de una nueva serie de materiales formulados $\{Fe(AnPy)_2[M(CN)_2]_2\}\cdot XBz$ [AnPy = 4-(antracen)piridina; M = Ag (**AnPyAg·XBz**), Au (**AnPyAu·XBz**); XBz = benceno sustituido]. La utilización del ligando 4-(antracen)piridina se basa en la posibilidad de que la presencia del fragmento Antraceno introduzca propiedades luminiscentes en los materiales resultantes. Efectivamente, los compuestos obtenidos combinan las propiedades SCO del $Fe^{II}$ junto a la luminiscencia derivada del Antraceno. La dependencia térmica de las propiedades magnéticas y calorimétricas, así como los estudios de espectroscopia de absorción UV-Vis sobre monocristales y los estudios estructurales reflejan la naturaleza en varias etapas del SCO. Las temperaturas de transición de cada derivado están marcadas significativamente por el invitado XBz (X = Cl, Br, I, $CH_3$ y $NO_2$), que está incluido en poros definidos por el empaquetamiento de las láminas bimetálicas contiguas. Dependiendo de la interacción del huésped con la red anfitrión se han caracterizado dos fases cristalográficas, una ortorrómbica y otra triclínica que aparece únicamente en disolución y al exponerse al aire se transforma a la forma ortorrómbica estable, probablemente debido a una pérdida parcial de moléculas de invitado. Todos los compuestos presentan una fuerte fluorescencia azul que desaparece gradualmente al aumentar la temperatura. Además, para algunos derivados (X = I [Ag, Au] y Cl [Au]), aparece una señal excímero/exciplex en la región del verde y esta aumenta en intensidad en paralelo con la población del estado HS del $Fe^{II}$. Estos últimos compuestos representan nuevos ejemplos de sinergia entre el SCO y la luminiscencia.

El capítulo cinco contiene las conclusiones generales de la tesis doctoral.

Finalmente, el apéndice recoge los artículos científicos que han dado lugar a esta tesis doctoral.

## SUMMARY

This doctoral thesis is devoted to the synthesis and characterization of new materials, mostly porous, that display the spin crossover phenomena (hereafter SCO). The main objective of this thesis has been to design new $Fe^{II}$ coordination polymers that present SCO behaviour coupled with other interesting physicochemical properties in view of their potential application in spintronic devices. More precisely, the synthetic efforts have been focussed on the preparation of 2D coordination polymers of the Hofmann type displaying tuneable host-guest interactions, fluorescence, and the possibility of being easily grafted as thin films while keeping the SCO properties.

Chapter one introduces the most important concepts of SCO phenomena. The SCO behaviour concerns the reversible switching between the High-Spin state and Low-Spin state that experience some pseudo-octahedral complexes of mainly first row transition metal ions with $3d^4$ to $3d^7$ electronic configurations. This switching is commonly induced by variations in temperature and/or pressure, light irradiation or interaction with a suitable analyte. The spin-state switch is accompanied by a change in an important number of physical properties of the material, such as colour, magnetism, dielectric constant, structure, etc.

The main objectives have been included at the end of this introductory chapter, as well as the experimental methodology for the synthesis and characterization of the obtained coordination polymers.

Chapter two contains the synthesis and characterization of a new series of Hofmann-type 2D coordination polymers based on the coordination of the 5-aminopyrimidine (5-$NH_2$Pym) and tetracyanomelate ($[M(CN)_4]^{2-}$ M = Pt, Pd) ligands towards the $Fe^{II}$ centre. This combination gives rise to materials with general formula $\{Fe(5\text{-}NH_2Pym)_2[M(CN)_4]\}\cdot G$ (**$1^{M}\cdot G$** M = Pt, Pd; G = none, $H_2O$, MeOH or EtOH). The functionalization of the axial ligand with an amine group confers versatile host-guest chemistry and structural flexibility to the 2D SCO framework primarily driven by the generation of extensive H-bond interactions. Solvent free **$1^{M}$** species reversibly adsorb small protic molecules such as water, methanol or ethanol. The interconversion between the different solvates and the desolvated phase occurs in a Single-Crystal-to-Single-Crystal fashion, being possible to follow the SCO properties of all compounds via SCXRD (Single Crystal X-Ray Diffraction). The SCO properties vary as a function of the guest molecule, the desolvated compound undergoes a cooperative one-step

transition while for the $H_2O$ and MeOH/EtOH solvates the transition occurs in two complete cooperative steps and half step with the high spin state locked to $n_{HS}$ = 0.5 at low temperatures, respectively. These results demonstrate that the reversible structural rearrangements accompanying these adsorption/desorption processes (**$1^{M}$** ↔ **$1^{M}$·G**) follow a gate-opening mechanism whose kinetics depend not only on the nature of the guest molecule and that of the host framework (**$1^{Pt}$** or **$1^{Pd}$**) but also on their reciprocal interactions. In addition, a predictable and reversible guest-induced SCO modulation has been observed and accurately correlated with the associated crystallographic transformations monitored in detail by single crystal X-ray diffraction.

Chapter three explores the use of 4-methyldisulfanylpyridine ($pyS_2Me$) and 4-ethyldisulfanylpyridine ($pyS_2Et$) as axial ligands for the formation of new Hofmann-type SCO coordination polymers formulated {Fe($pyS_2R$)[{$M^{II}(CN)_4$]} (**M$pyS_2R$**; R = Me, Et; $M^{II}$ = Pt, Pd). The primary motivation of the choice of these peripheral ligands was the expectation that the disulphanyl groups will favour anchoring and growing of monolayers on gold substrates as well as optimal electron transport in spintronic devices based on SCO properties. The exposition of this kind of sulphur-rich ligands to a gold surface results in the fragmentation of the S-S bond (PyS-SR) ensuring that the -S-R groups stay anchored acting as spacers in the surface between the -S-Py ligands, giving rise to a suitable base to further build the SCO layer. All compounds undergo first order SCO, for **Ptpy$S_2$Me**, **Ptpy$S_2$Et** and **Pdpy$S_2$Et** all the transitions are complete and cooperative with hysteresis loops whilst the **Pdpy$S_2$Me** compound shows a gradual multi-stepped spin transition. This behaviour seems to be associated with the disorder found in the Me-S-S- group which, supposedly, induces an elastic frustration between adjacent interdigitated 2D layers during the SCO. The Differential Scanning Calorimetry (DSC) studies confirm the values of $T_c$ and $\Delta$T observed from the magnetic measurements. Compounds **Pdpy$S_2$Me**, **Ptpy$S_2$Et** and **Pdpy$S_2$Me** exhibit LIESST effect (*Light Induced Excited Spin State Trapping*) characterized by High-Spin fractions $n_{HS}$ = 0.64, 0.96 and 0.96 and $T_{LIESST}$ = 50, 68 and 70 K, respectively. The ultimate objective of this work is the future application of monolayers of these compounds in spintronic devices.

Chapter four describes the synthesis of the new series of 2D coordination polymers of the Hofmann-type formulated {Fe$(AnPy)_2$[$M(CN)_2]_2$}·XBz [AnPy = 4-(anthracene)pyridine; M = Ag (**AnPyAg·XBz**), Au (**AnPyAu·XBz**); XBz = substituted benzene]. The choice of the 4-(anthracene)pyridine ligand was motivated by the presence of the Anthracene moiety and its

capability to impart luminescent properties to the resulting SCO materials. The thermal dependence of the magnetic and calorimetric properties as well as Single Crystal UV-Vis absorption spectroscopy and structural studies reflect the occurrence of a multi-stepped SCO behaviour. The transition temperatures of each derivative are markedly modulated by the XBz guest (XBz = Cl, Br, I, $CH_3$ and $NO_2$), which is included in the pores defined by the packing of consecutive bimetallic layers. Depending on the guest interaction with the host 2D framework, two different crystallographic phases have been characterized, one triclinic phase which is only stable while the crystals stay in the mother liquor. The other phase, orthorhombic, appears when the triclinic phase is exposed to ait, most likely due to partial release of guest molecules. All compounds exhibit strong blue fluorescence that gradually vanishes upon temperature increase. Furthermore, in some of the derivatives (X = I [Ag, Au] and Cl [Au]), an excimer/exciplex signal appears in the green region and increases in intensity as the population of the High-Spin state of the $Fe^{II}$ increases. These latter compounds afford new examples of synergy between SCO and luminescence.

Chapter five collects the general conclusions of the doctoral thesis.

Finally, the appendix gathers all peer reviewed scientific articles that have led to this doctoral thesis

CAPÍTULO 1

# Introducción

# CAPÍTULO 1

# Introducción

## 1.1- Consideraciones generales e históricas del fenómeno de transición de espín (SCO)

El fenómeno conocido como transición de espín (en adelante SCO, del inglés *Spin Crossover*) se enmarca dentro del campo de la magnetoquímica. Desde su descubrimiento en complejos de coordinación de $Fe^{III}$ en el año 1931[1] ha estado vinculado intrínsecamente al desarrollo de la química de coordinación.[2] Los centros SCO muestran configuraciones electrónicas lábiles intercambiables entre el estado de espín alto (HS, del inglés *High Spin*) y el de espín bajo (LS, del inglés *Low Spin*). La transición entre estos dos estados da lugar a cambios característicos en el magnetismo, el color y la estructura del material, que pueden ser inducidos por variaciones de temperatura, presión, la irradiación con luz, presencia de moléculas invitadas, entre otros posibles estímulos[3]. Cuando los cambios estructurales asociados a la transición de espín se transmiten de forma cooperativa a través del cristal se pueden producir transiciones de espín cooperativas acompañadas de histéresis (efecto “memoria”), confiriendo así carácter biestable (o multiestable) al material.

La posibilidad de que una molécula o conjunto de ellas puedan ser utilizadas como dispositivos electrónicos ha estimulado la creatividad de los científicos desde hace mucho tiempo.[4-10] Una de las estrategias más simples para tal fin se basa en el concepto de biestabilidad molecular que se fundamenta en el cambio entre dos estados moleculares, tal y como sucede en el interruptor binario.[11]

Una posible definición de biestabilidad molecular es “la propiedad de un sistema molecular para cambiar entre dos estados estables de manera reversible y detectable en respuesta a una perturbación externa”.[12] Basándonos en esta definición, la transición de espín representa un ejemplo singular de biestabilidad molecular la cual puede presentarse tanto en disolución como en estado sólido. En el primero de los casos el proceso es

esencialmente molecular, debido a las interacciones intermoleculares débiles propiciadas por el medio. En estado sólido, el fenómeno puede verse acompañado de efectos cooperativos dependiendo de la naturaleza de las interacciones moleculares implicadas y de la naturaleza del complejo metálico. La cooperatividad es una de las propiedades más interesantes de las transiciones de espín, pues suele verse acompañada de discontinuidad en las propiedades ópticas, magnéticas, dieléctricas y estructurales. En los casos más favorables, esta discontinuidad está acompañada de histéresis térmica en dichas propiedades. Este hecho les confiere a estos sistemas la capacidad potencial para almacenar información a nivel molecular.

Desde el punto de vista sintético, el control de las propiedades cooperativas representa un reto de gran dificultad que implica el control de las interacciones intermoleculares entre las unidades individuales que constituyen el sólido. Esta actividad corresponde al ámbito de la “ingeniería cristalina”, uno de los campos más activos de lo que hoy en día se conoce como química supramolecular.[13,14] No obstante, a pesar del progreso realizado en las últimas décadas, no es todavía posible predecir teóricamente si una disposición molecular resultará más o menos efectiva que otra desde el punto de vista de la cooperatividad, o incluso si se va a favorecer o impedir el intercambio de espín. En este sentido, actualmente el químico carece de una guía conceptual que permita la síntesis dirigida de sólidos con unas propiedades magnéticas determinadas.

Conceptualmente, el estudio del fenómeno de transición de espín implica la incursión en un dominio de conocimiento caracterizado por una vasta riqueza conceptual interdisciplinar que abarca desde la química sintética pasando por la química de coordinación y la ciencia de materiales hasta la física del estado sólido. Esta amplia interdisciplinaridad queda patente por las distintas aplicaciones posibles descritas en la literatura actual[15]. El siguiente apartado introduce los principales conceptos teóricos relacionados con el fenómeno de la transición de espín.

### 1.1.1- Teoría del campo de ligandos y diagramas de energía potencial, fundamentos teóricos

En una simetría octaédrica los complejos de metales de transición con configuraciones electrónicas [Ar]$3d^4$-$3d^7$ pueden presentar dos estados electrónicos fundamentales distintos, según el desdoblamiento de los orbitales d en los subconjuntos $e_g$ y $t_{2g}$. Cuando la separación energética entre estos dos subconjuntos (la fuerza del campo de ligandos), $\Delta$, es mayor que la energía de repulsión interelectrónica, P, los electrones tienden a ocupar los orbitales de más baja energía, es decir, el subconjunto $t_{2g}$ y el complejo metálico adopta el estado LS. Si $\Delta$ es menor que P los electrones d cumplen la regla de máxima multiplicidad de Hund y el complejo adopta el estado HS. Si bien los complejos de Cr(II), Mn(II), Mn(III), Fe(II), Fe(III), Co(II) y Co(III) pueden presentar estas dos posibilidades electrónicas, la familia de compuestos de Fe(II) es, con amplia mayoría, la más estudiada y numerosa en la literatura basándonos en el estudio de la propiedad SCO, debido a la gran diferencia entre los dos estados HS (S = 2) y LS (S = 0).

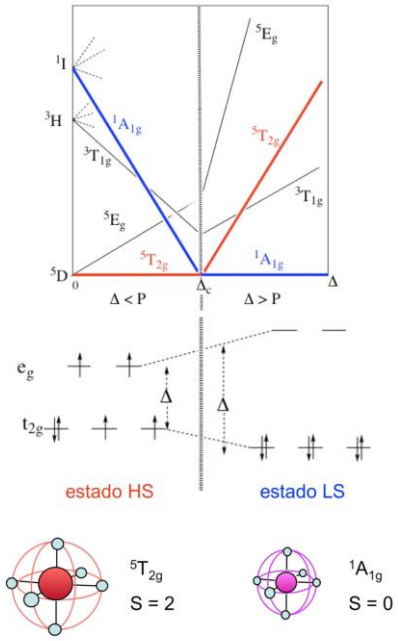


**Fig. 1.-** Diagrama Tanabe-Sugano simplificado ilustrando la dependencia relativa de los estados HS y LS y las configuraciones electrónicas correspondientes.

Tal y como se aprecia en el diagrama de Tanabe-Sugano mostrado en la Figura 1, en los alrededores del punto de cruce, $\Delta_c$, donde Δ y P presentan valores similares, la diferencia de energía entre los estados HS y LS es del orden de magnitud de la energía térmica ($k_BT$). En esta región singular se sitúa la familia de compuestos denominados de transición de espín (SCO), que pueden adoptar ambos estados de espín e interconvertirse de manera controlada, detectable y reversible bajo el efecto de la temperatura, presión e irradiación de luz, entre otros estímulos.

En el caso de los complejos de Fe(II) los ligandos de campo débil, como el $H_2O$, favorecen la estabilización del estado HS (cuyo estado fundamental es el $^5T_{2g}$) mientras que al aumentar la fuerza del campo de los ligandos, por ejemplo mediante el uso de ligandos de campo fuerte, como el SCN (tiocianato) se favorece la estabilización del estado LS (cuyo estado fundamental es el $^1A_{1g}$).

El fenómeno de las transiciones de espín puede considerarse como una transferencia electrónica intra-iónica, donde los electrones se mueven entre los orbitales $e_g$ y $t_{2g}$. Dado el carácter antienlazante del subconjunto $e_g$, su población/despoblación tiene lugar junto a un aumento/disminución de las distancias de enlace metal-ligando. El cambio opuesto se da en la población del subconjunto $t_{2g}$ que afecta a la retro-donación entre el ión metálico y los orbitales π* vacantes de los ligandos. Ambos factores σ y π contribuyen al cambio de las distancias de enlace metal-ligando. Este $\Delta R$ es de aproximadamente 0.20, 0.15 y 0.10 Å para el Fe(II), Fe(III) y Co(III), respectivamente. Así pues, un cambio considerable de tamaño tiene lugar durante el SCO, no solo en las distancias de enlace sino también en los ángulos implicados. Consecuentemente, las moléculas experimentan un cambio drástico de $\Delta$ con la transición, que se estima de $\Delta_{LS}/\Delta_{HS} \approx (\Delta r_{HS}/\Delta r_{LS})^n$ con n = 5 – 6. Por ejemplo, $\Delta_{LS} \approx 1.75\Delta_{HS}$ para el Fe(II). Esta estimación abandona la dependencia angular de Δ y considera que $\Delta r$ es el parámetro de cambio estructural más importante.[16]

La fuerza del campo de ligandos depende no sólo del ligando coordinado al centro metálico, sino también de la distancia de enlace metal-ligando. Al pasar al estado de LS las distancias Fe-N disminuyen, esto implica un cambio en el orden de enlace y por tanto un aumento de la energía de vibración (observable mediante espectroscopía IR y Raman), como consecuencia del aumento de la constante de fuerza del enlace, f.

Así pues, cada estado de espín se puede asociar en primera aproximación a una parábola caracterizada por una energía potencial tal que:

$$Ep_i = \tfrac{1}{2}(f_i R_i^2) \qquad i = HS, LS \qquad (1)$$

$R_i$ = distancia media Fe-N

Esta energía potencial representa esencialmente la energía electrónica de los estados HS y LS. Ambas parábolas están separadas en sus mínimos por las distancias R características para iones Fe(II) $R_{LS} \approx 2.0$ Å y $R_{HS} \approx 2.2$ Å (siendo $\Delta R_{HL} \approx 0.20$ Å). Estas curvas contienen información acerca de la energía vibracional. Así pues, dichas parábolas representan también el modo de vibración totalmente simétrico del octaedro ($A_{1g}$). En la Figura 2 se puede consultar la representación de las energías $Ep_i$ de las parábolas asociadas a los estados HS y LS frente a R. El desplazamiento horizontal de ambas parábolas corresponde a $\Delta R_{HL} \approx 0.20$ Å, mientras que el desplazamiento vertical indica que para una molécula aislada el estado LS se encuentra estabilizado con respecto al estado HS por una energía $\Delta E_{HL}$.

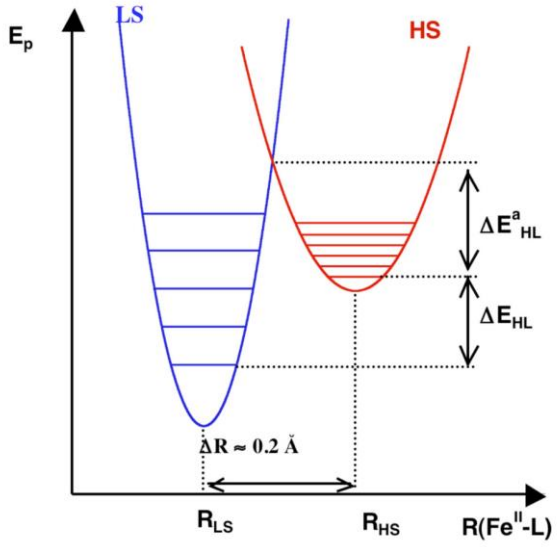


**Figura 2.** Curvas de energía potencial de los estados HS y LS mostrando la diferencia entálpica $\Delta E_{HL}$, la energía de activación $\Delta E^a_{HL}$ y los estados vibracionales correspondientes.

La energía vibracional de los diferentes niveles será:

$$E^{vibr}_i\,(n) = (n + 1/2)\,h\nu_i \qquad \nu_i = 1/2\pi\,(f_i/m)^{1/2}\ (\text{m es la masa reducida}) \qquad (2)$$

En esta representación, los diferentes niveles vibracionales están representados como líneas horizontales igualmente espaciadas dentro de las correspondientes parábolas (Figura 2). Dado que $f_{LS} > f_{HS}$ el número de niveles vibracionales por unidad de energía es mayor para el estado HS que para el LS, es decir, la separación entre los niveles vibracionales es menor en el estado HS. Igualmente, la multiplicidad de espín del estado HS es mayor que la del estado LS.

A muy bajas temperaturas, la molécula se encuentra en el nivel vibracional fundamental (n = 0) del estado LS. A medida que aumenta la temperatura, la molécula va transformando la energía térmica aportada en energía vibracional ocupando niveles vibracionales excitados hasta alcanzar el punto de cruce de ambas parábolas donde se produce el cambio de estado de espín, en el que la geometría del estado precursor, LS, y el sucesor, HS, es la misma. De acuerdo con el principio de Franck-Condon es en este punto donde tiene lugar la transformación HS ↔ LS. Este punto de cruce, $\Delta_c$, representa una región inestable donde las especies transitorias pueden cambiar su estado de espín.

El coste energético para salvar la diferencia entálpica, $\Delta E_{HL}$, entre ambos estados está compensado por la diferencia de entropía de estos, que favorece la población del estado HS a altas temperaturas. Visto de otra forma, la molécula absorbe energía para compensar la diferencia entálpica $\Delta E_{HL}$ que desfavorece el estado HS. Dicha energía es de origen entrópico y tiene dos componentes diferentes. Por un lado, hay una componente electrónica relacionada con el cambio de multiplicidad de espín (2S + 1) [HS (S = 2) y LS (S = 0) para el ion Fe(II)]:

$$AS_{el.} = R \ln [(2S + 1)_{HS}/[(2S + 1)_{LS}] = R \ln (5/1) = 13.45\ J\ K^{-1}\ mol^{-1} \qquad (3)$$

Por otro lado, hay una componente vibracional que deriva del mayor número de niveles vibracionales por unidad de energía ($g_i$) asociado al estado HS, dada la menor magnitud de la constante de fuerza de enlace $f_{HS}$:

$$AS_{vibr.intr.} = R \ln (g_{HS}/g_{LS}) \qquad (4)$$

El acceso experimental a la relación $g_{HS}/g_{LS}$ conlleva serias dificultades, pero es posible estimarla a partir de la entropía total obtenida de las medidas de calorimetría y del análisis de los espectros IR y/o Raman correspondientes a los estados HS y LS.[17] Por consiguiente el comportamiento SCO térmicamente inducido es un proceso controlado por la entropía.

La influencia de la presión en la transición de espín también puede entenderse a partir de la representación de los pozos de potencial. Sin tener en cuenta cual sea la fuente de la presión (química o mecánica) el efecto principal es la desestabilización del estado HS, ya que el volumen de éste es mayor que el del estado LS. Así pues, la presión disminuye $\Delta R_{HL}$ y aumenta $\Delta E_{HL}$, desplazando la parábola verticalmente.[18] Como consecuencia, la presión disminuye la energía de activación, $E^a_{HL}$, correspondiente a la diferencia en energía entre el nivel vibracional n = 0 del estado HS y el punto de cruce definido por los dos pozos de potencial.

Generalmente, a temperaturas mayores de 100 K la energía térmica, $k_BT$, es mayor que la energía de activación, $E^a_{HL}$, y esto determina la cinética de la conversión HS ↔ LS, incluso a presión atmosférica. Por ello la cinética del proceso se caracteriza por una constante de velocidad, $k_{HL} \approx 10^6 - 10^8\ s^{-1}$, que garantiza el equilibrio termodinámico de las magnitudes físicas observadas.

Cuando la energía térmica es del orden o menor que la energía de activación, $k_BT \leq E^a_{HL}$, esta afirmación ya no es válida y la constante $k_{HL}$ disminuye hasta valores del orden de $10^{-1} - 10^{-7}\ s^{-1}$, con lo que es posible "bloquear" el estado HS a temperaturas donde no es estable, ya que la molécula no dispone de la energía suficiente para superar la barrera de paso $E^a_{HL}$ desde el estado HS al LS.

A temperaturas del orden de 50 - 90 K es fácil estudiar las cinéticas de relajación, que en principio son de primer orden, pudiéndose correlacionar la variación térmica de $k_{HL}$ en términos de la representación de Arrhenius.

A temperaturas muy bajas, en los compuestos típicos SCO de Fe(II), se observa que el proceso de relajación ya no sigue una ley de Arrhenius pura, sino que se desvía, más

cuanto menor es la temperatura, hasta observar una independencia térmica de $\ln(k_{HL})$, hecho que suele tener lugar por debajo de 40 K. De hecho por debajo de 30 K, $k_{HL}$ es muy pequeña, $[k_{HL}(T \rightarrow 0)] \approx 10^{-7}\ s^{-1}$, e independiente de la temperatura, y el proceso de relajación tiene lugar esencialmente vía efecto túnel. La velocidad de relajación en la región túnel puede relacionarse con los desplazamientos "vertical" y "horizontal" de las curvas de energía potencial de los estados HS y LS a través del marco conceptual de los procesos de relajación no adiabáticos multifonónicos.[19]

Sin embargo, este no es el caso para compuestos de Fe(III) y Co(II), que normalmente presentan relajaciones muy rápidas incluso a temperaturas por debajo de 10 K. Para estos sistemas el cambio de energía configuracional es menor que para los compuestos de Fe(II), ya que el cambio en las distancias de enlace es también mucho menor. La relajación HS ↔ LS en compuestos SCO es un proceso modelo que participa del comportamiento clásico y el mecano-cuántico, y ha sido estudiado en profundidad por Hauser y colaboradores entre otros.[20]

### 1.1.2- Fotoconversión en compuestos de transición de espín, efecto LIESST

La luz es una herramienta muy eficaz para interaccionar con un sistema molecular, especialmente cuando se trata de encontrar posibles aplicaciones tecnológicas. La foto-inducción en compuestos SCO fue observada por primera vez por primera vez por McGarvey y Lawthers en disolución a temperaturas relativamente altas,[21] sin embargo, el tiempo de vida media de los estados inducidos era muy corto. Más adelante, en 1994, Decurtins y colaboradores observaron por primera vez el proceso de foto-inducción en materiales SCO en estado sólido a bajas temperaturas para el complejo $[Fe(1\text{-propiltetrazol})_6](BF_4)_2$.[22] Al irradiar la muestra en el estado LS con luz verde (λ = 514.5 nm) a temperaturas por debajo de 50 K el color de la muestra pasa del violáceo intrínseco del estado LS al blanco, propio del HS. El fenómeno descubierto fue acuñado como "light induced excited spin state trapping" (LIESST).

En la mayoría de los compuestos SCO, a temperaturas suficientemente bajas el estado LS puede estar totalmente poblado, de forma que el espectro visible del sistema $d^6$ en simetría octaédrica se caracteriza por dos bandas relativamente intensas

correspondientes a las transiciones $v_1$ ($^1A_{1g} \rightarrow {}^1T_{1g}$) (≈ 12000 – 20000 $cm^{-1}$) y $v_2$ ($^1A_{1g} \rightarrow {}^1T_{2g}$) (≈ 20000 – 25000 $cm^{-1}$) que a menudo están enmascaradas por las bandas de transferencia de carga metal ligando TCML ($d_M \rightarrow \pi^*_L$).

La irradiación con luz verde estimula la transición $^1A_{1g} \rightarrow {}^1T_{1g}$. El tiempo de vida media del estado excitado $^1T_{1g}$ es de tan sólo nanosegundos, por lo que el sistema se relaja rápidamente. Dicha relajación normalmente tiene lugar al estado inicial $^1A_{1g}$. Sin embargo, mediante mecanismos de cruce de sistemas (en inglés "intersystem crossing", ISC), existe una pequeña probabilidad de relajación a través de los estados de espín intermedio $^3T_{1g}$ y $^3T_{2g}$ permitidos por acoplamiento espín-órbita de segundo orden. De nuevo, la relajación desde los estados de espín intermedio puede ocurrir por medio de dos procesos ISC, uno implica la relajación al estado fundamental $^1A_{1g}$ y otro al metastable $^5T_{2g}$, donde las moléculas permanecerán atrapadas siempre que $k_BT$ sea suficientemente menor que $E^a_{HL}$. A bajas temperaturas el estado metaestable $^5T_{2g}$ tiene un tiempo de vida media muy largo,[23] debido a que la relajación $^5T_{2g} \rightarrow {}^1A_{1g}$ está prohibida.

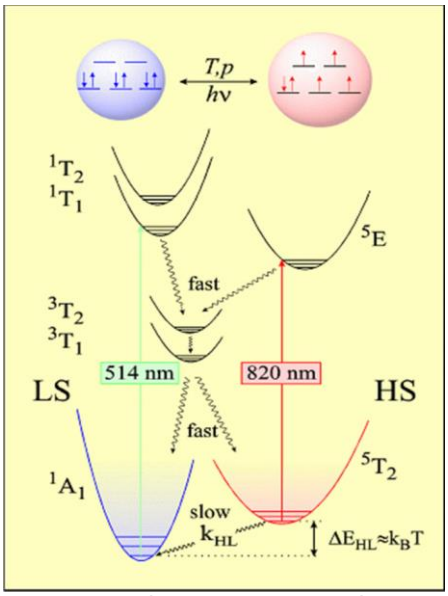


**Figura 3.** Esquema representativo del fenómeno de foto-inducción de una transición de espín, efecto LIESST.

La foto-excitación durante un período de tiempo suficiente, implica la población total del estado metaestable HS, $^5T_{2}g$, a costa del despoblamiento del LS, con lo que se invierte

la población de los estados. El estado metaestable HS puede volver al estado LS de partida irradiando con luz roja (λ = 820 nm), siguiendo el mecanismo del llamado efecto LIESST inverso ($^5T_{2g} \rightarrow {}^3T_{1g} \rightarrow {}^1A_{1g}$), o simplemente aumentado la temperatura.

El descubrimiento del efecto LIESST representó un avance importante sobre el estudio de la dinámica del comportamiento SCO en estado sólido, dado que el rango de temperaturas en las cuales el equilibrio termodinámico podía ser foto-perturbado se extendió considerablemente. Desde entonces, el número de compuestos en los que se ha observado y estudiado el efecto LIESST ha aumentado considerablemente.

### 1.1.3- Interacción entre los centros con transición de espín, cooperatividad

Si bien el origen del fenómeno de transición de espín es puramente molecular, la manifestación macroscópica del sólido es el resultado de la interacción cooperativa entre las moléculas que constituyen el material. La naturaleza cooperativa de la conversión de espín ha estimulado mucho interés dado que las transiciones de fase de primer orden que se producen pueden estar acompañadas de histéresis térmica, hecho que confiere a estos materiales un cierto grado de memoria. Esta propiedad es muy interesante pues abre las puertas para ser potencialmente aprovechada en futuras aplicaciones. El origen de la cooperatividad en estos sistemas viene esencialmente dado por la diferencia de tamaño que presenta el entorno del centro SCO en cada uno de los estados de espín. Así pues, tiene carácter elástico que da lugar a interacciones de largo alcance. Estas interacciones podrían ilustrarse como una presión interna, que crece con el aumento de las especies LS/HS e interactúa con todos los centros SCO del cristal con la misma intensidad, independientemente de las distancias.[24]

En sistemas simples es posible explicar el carácter continuo, discontinuo, histéresis o incluso la temperatura crítica $T_C$ (temperatura para la cual la fracción molar de especies HS y LS es 0.5) en términos de la termodinámica de transiciones de fase descrita por Slichter y Drickamer.[25]

Si se considera un número N de moléculas que pueden dar lugar al fenómeno SCO, cada molécula podrá existir en el estado HS o en el estado LS, de manera que podemos

definir la fracción molar de las moléculas HS como $\gamma_{HS}$, y la fracción molar de moléculas LS (1 - $\gamma_{HS}$). En ausencia de interacciones intermoleculares podemos introducir en la expresión de la energía libre de Gibbs, G, un término para la entropía de mezcla, $S_{mix}$. Este término representa las diferentes posibilidades de distribuión de las poblaciones HS ($\gamma_{HS}$) y LS (1 - $\gamma_{HS}$), para el total de moléculas N. La entropía de mezcla $S_{mix}$ se expresa como:

$$S_{mix} = k\,[N \ln N - \gamma_{HS} N \ln \gamma_{HS} N - (1 - \gamma_{HS}) N \ln (1 - \gamma_{HS}) N] \quad (5)$$

que puede rescribirse como:

$$S_{mix} = -R[\gamma_{HS} \ln \gamma_{HS} - (1 - \gamma_{HS})\ln(1 - \gamma_{HS})] \quad (6)$$

donde R es la constante de gases. $S_{mix}$ es máxima para $\gamma_{HS} = 0.5$ y desaparece para $\gamma_{HS} = 0$ o 1. Al tener en cuenta el término $S_{mix}$, la expresión de la energía libre de Gibbs queda:

$$G = \gamma_{HS} G_{HS} + (1 - \gamma_{HS})G_{LS} - T S_{mix} \quad (7)$$

donde $G_{HS}$ y $G_{LS}$ corresponden a las energías libres de Gibss para los estados electrónicos HS y LS, respectivamente. La derivada parcial de G con respecto a $\gamma_{HS}$ es

$$\left(\frac{\partial G}{\partial \gamma_{HS}}\right) = \Delta G + RT \ln\left(\frac{\gamma_{HS}}{1-\gamma_{HS}}\right) \quad (8)$$

La condición de equilibrio térmodinámico para el fenómeno SCO a cualquier temperatura y presión es:

$$\left(\frac{\partial G}{\partial \gamma_{HS}}\right)_{T,\,P} = 0 \quad (9)$$

por lo que

$$\ln\left(\frac{1-\gamma_{HS}}{\gamma_{HS}}\right) = \frac{\Delta G}{RT} = \frac{\Delta H}{RT} - \frac{\Delta S}{R} \quad (10)$$

Teniendo en cuenta que $\Delta G = 0$ cuando $\gamma_{HS} = \gamma_{LS} = 0.5$ y que por tanto $T_C = \Delta H/\Delta S$, se obtiene

$$\gamma_{HS} = \frac{1}{1+\exp\left[\frac{\Delta H}{R}\left(\frac{1}{T}-\frac{1}{T_{1/2}}\right)\right]} \qquad (11)$$

Las interacciones moleculares vienen reflejadas en el modelo de Slichter y Drickamer por un parámetro de interacción, $G_{int}$.

$$G_{int} = \Gamma\, \gamma_{HS}\,(1 - \gamma_{HS}) \qquad (12)$$

donde $\Gamma$ es el parámetro de la cooperatividad.

Tomando $G_{LS}$ como el origen de energías, podemos escribir,

$$G = \gamma_{HS}\Delta H + \Gamma\gamma_{HS}(1 - \gamma_{HS}) + T[R\gamma_{HS}\ln\gamma_{HS} + R(1 - \gamma_{HS})\ln(1 - \gamma_{HS}) - \gamma_{HS}\Delta S] \qquad (13)$$

Esta ecuación permite representar curvas de energía libre, G, frente a la fracción molar de HS, $\gamma_{HS}$, para diferentes valores de $\Delta H$, $\Delta S$, $\Gamma$ y T. Teniendo en cuenta de nuevo la condición de equilibrio se llega a

$$\ln\left(\frac{1-\gamma_{HS}}{\gamma_{HS}}\right) = \frac{\Delta H + \Gamma(1-2\gamma_{HS})}{RT} - \frac{\Delta S}{R} \qquad (14)$$

Si $\Delta G < 0$ el estado electrónico de las moléculas es HS y cuando $\Delta G > 0$ el estado de las moléculas es el LS. En condiciones de equilibrio termodinámico, $\Delta G = 0$ y $\gamma_{HS} = \gamma_{LS}$. Si además se tiene en cuenta la influencia de la presión en la TS, se introduce un nuevo término en la ecuación, quedando:

$$\ln\left(\frac{1-\gamma_{HS}}{\gamma_{HS}}\right) = \frac{\Delta H + P\Delta V + \Gamma(1-2\gamma_{HS})}{RT} - \frac{\Delta S}{R} \qquad (15)$$

Resumiendo, la ecuación de estado puede describirse de la forma siguiente:

$$\ln[(1-\gamma_{HS})/\gamma_{HS}] = [\Delta H + P\Delta V + \Gamma\,(1 - 2\,\gamma_{HS}) - T\,\Delta S] / RT \qquad (16)$$

siendo $\gamma_{HS}$ la fracción molar de HS. ΔH y ΔS son las variaciones de entalpía y entropía por mol involucradas en el cambio de estado de espín y se pueden obtener directamente a partir de las medidas de calorimetría ($C_p$ vs. T), y ΔV es el cambio de volumen molar asociado a SCO que se suele obtener directamente de las medidas de difracción de rayos X a bajas temperaturas (este término es despreciable a presión atmosférica). Es importante resaltar que la relación ΔH/ΔS corresponde a la temperatura característica de la transición, cuya nomenclatura en la bibliografía suele ser $T_c$ o $T_{1/2}$ , a la cual $\gamma_{HS} = \gamma_{LS} = 0.5$, y se obtiene directamente de la curva SCO. Por otro lado, se considera que el término PΔV es puramente entálpico y aumenta principalmente la diferencia de energía libre entre las fases HS y LS.

El parámetro de la cooperatividad, Γ, representa la tendencia de una molécula o centro activo, en un estado de espín determinado, a rodearse de moléculas o centros activos con el mismo estado de espín. Por tanto, Γ refleja la eficacia con que se transmiten a lo largo del cristal los cambios estructurales asociados a la transición de espín por vía de interacciones intermoleculares y, en última instancia, es responsable de la manifestación cooperativa de las propiedades físicas del sistema.

La ecuación de estado posibilita simular los comportamientos más representativos de las curvas SCO, que van desde la transición gradual (Γ = 0, donde no existen interacciones entre los centros SCO) a una transición de primer orden y con histéresis ($\Gamma > 2RT_c$) (Figura 4 izquierda y centro, respectivamente). Modificando la ecuación pueden simularse también transiciones incompletas con fracciones residuales de HS y/o LS a altas y bajas temperaturas respectivamente, o incluso transiciones en dos etapas (Figura 4 derecha).

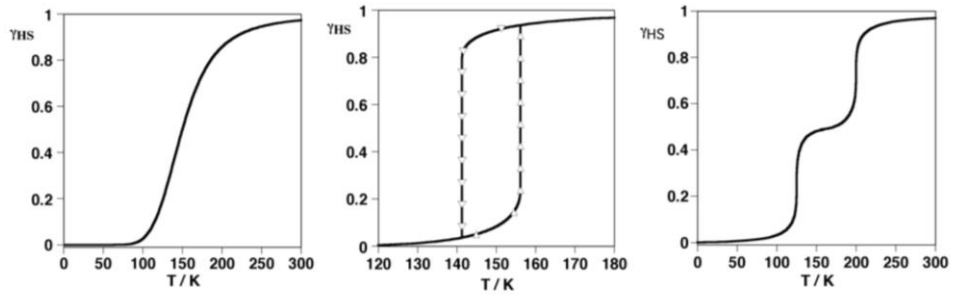


**Figura 4.-** Tipos principales de curvas SCO representadas en la forma de $\gamma_{HS}$ frente a T: gradual (izquierda), abrupta y con histéresis (centro) y en dos etapas (derecha).

En la mayor parte de las publicaciones el parámetro $\gamma_{HS}$ normalmente se suele obtener a partir de medidas magnéticas, aun así, en los casos en los que sea necesario es posible cuantificarlo mediante espectroscopía Mössbauer (en el caso de compuestos con hierro), espectroscopia electrónica (en el rango de la luz visible, o en el caso de que los compuestos sean activos, en la región UV) y vibracional (IR y/o Raman) e incluso a partir de medidas de difracción de rayos X (sobre polvo o monocristal).

Este modelo, al igual que otros equivalentes, explica los aspectos principales de la transición de fase. Es, por lo tanto, insensible con respecto a pequeñas modificaciones estructurales y electrónicas que en muchos de los casos publicados afectan drásticamente a la cooperatividad y al campo de ligandos del centro metálico. Estas modificaciones son generalmente provocadas por grupos voluminosos, o ligandos con capacidad de dar lugar a apilamiento $\pi$ o a interacción mediante enlaces de hidrógeno, pero también en muchos de los casos por la presencia de moléculas de disolvente y aniones o cationes en la red cristalina.

La aparición de polimorfismo, que tiene su origen en pequeñas diferencias en la cristalización, a través de parámetros tales como la temperatura, el método de síntesis, mezclas de disolventes, etc. En general la racionalización de estos factores es considerablemente difícil, dado que no son siempre coherentes de un sistema a otro y suelen ser impredecibles.

### 1.1.4- Caracterización de compuestos con transición de espín

Las técnicas experimentales que se emplean en la caracterización de los materiales con transición de espín pueden agruparse según el tipo de información que proporcionen.

En primer lugar, la obtención de los materiales SCO requiere ligandos orgánicos no necesariamente comerciales, por ello, en esos casos es necesario realizar previamente su síntesis y caracterización mediante técnicas tales como la resonancia magnética nuclear (RMN, en inglés NMR), la espectrometría de masas con ionización por electroespray (en inglés, ESI-MS) o el análisis elemental.

En segundo lugar, la pureza de las fases es esencial para la correcta interpretación de los resultados obtenidos. Las técnicas más comúnmente utilizadas son la espectrometría de masas (ESI-MS), el análisis elemental, el análisis termogravimétrico (en inglés, TGA) y la difracción de rayos X de polvo (en inglés, PXRD).

En tercer lugar, por un lado, se emplean técnicas para conocer las configuraciones electrónicas de los centros SCO entre las que se encuentran la espectroscopia UV-Visible, la espectroscopia IR, la espectroscopia Mössbauer y las medidas de susceptibilidad magnética. Por otro, encontramos técnicas que permiten obtener los parámetros termodinámicos asociados al fenómeno SCO, entre las que se encuentran las medidas de calorimetría (DSC). Por último, los métodos de resolución estructural permiten estudiar los cambios estructurales que tienen lugar en la esfera de coordinación de los centros SCO, así como cambios en la red cristalina. Entre los distintos métodos encontramos la difracción de rayos X (para polvo y monocristal), estudios de radiación sincrotrón (XAS o “X-ray Absorption Spectroscopy”, EXAFS o “Extended X-ray Absorption Fine Structure”, XANES o “X-ray absorption near edge structure”, NFS o “Nuclear Forward Scattering”).[15a,26]

Además de las técnicas arriba mencionadas, el desarrollo y el avance en el estudio de las transiciones de espín ha comenzado a hacer uso de técnicas no tan convencionales que permiten obtener información y realizar un seguimiento de la conversión, como por ejemplo la resonancia magnética nuclear (NMR), la resonancia paramagnética electrónica (EPR, sólo para compuestos de $Fe^{III}$ y $Co^{II}$), la elipsometría, la espectroscopía de aniquilación de positrones (PAS) o la rotación del espín muónico (MuSR).[15a,26]

## 1.2- Estado de la ciencia en el ámbito tratado en la presente tesis doctoral

En el apartado anterior se ha presentado los fundamentos teóricos generales de la transición de espín. A continuación, se realiza una revisión en la que se incluyen algunos artículos/revisiones relevantes recientemente publicados algunos de los cuales han servido de inspiración y guía de la presente tesis doctoral, particularmente en lo referente al estudio de la transición de espín en el contexto de la química anfitrión-huésped, la deposición de capas finas sobre superficies y las propiedades fluorescentes.

### 1.2-1. Materiales SCO: Propiedades anfitrión-huésped

Las propiedades anfitrión-huésped han tenido especial interés en los materiales SCO desde hace bastante tiempo. Los primeros sistemas descritos en la bibliografía en los que se estudió la influencia del huésped son materiales bidimensionales que tienen la fórmula general $[FeL_2(SCN)_2]\cdot Solv$ [L = 1,2-di(4-piridil)-etileno (tvp)[27] y trans-4-4'-azopiridina (azpy)[28]]. Actualmente, la síntesis de polímeros de coordinación de tipo Hofmann (en inglés, HCPs) formulados $\{Fe(L)_y[M(CN)_x]\}$ [y = 1 (ligandos bismonodentados) o 2 (ligandos monodentados); x = 2 (M = Ag, Au) y 4 (M = Ni, Pd, Pt] ha generado mucho interés debido a la alta modularidad y estabilidad que presentan este tipo de materiales. Además, la porosidad intrínseca que caracteriza a estos compuestos ha motivado un número elevado de investigaciones cuyo objetivo último es la modulación de las propiedades SCO mediante el control de la interacción anfitrión-huésped[29]. Dicha modulación puede explicarse mediante dos vías:

-Efectos estéricos, que inducidos por el huésped, modifican las interacciones elásticas anfitrión-huésped perturbando la contracción-expansión natural de la red anfitrión y por lo tanto su transformación HS-LS.[30]

-Efectos electrónicos, que reflejan la influencia que ejercen las moléculas huésped mediante interacciones supramoleculares (π- π, enlace de hidrógeno, etc) sobre el campo de los ligandos del $Fe^{II}$ de la red anfitrión.[31]

En particular, una de las estrategias más utilizadas recientemente para favorecer la inclusión de invitados es el uso de ligandos axiales con grupos funcionales que favorecen la formación de interacciones dador-aceptor en las cavidades interlaminares donde residen las moléculas invitadas. Este método se ha utilizado especialmente en la síntesis de una

serie de ligandos derivados del anillo triazol químicamente sustituido con una amplia gama de grupos funcionales dando lugar a ejemplos muy interesantes de comportamientos SCO multiestables.[32] Estudios similares se han desarrollado con ligandos basados en el anillo piridina.[33]

### 1.2-2. Materiales SCO: Síntesis de capas delgadas de sistemas SCO

La deposición de capas delgadas de materiales SCO sobre distintos tipos de sustratos ha suscitado un gran interés asociado a la aplicación potencial de estos materiales en dispositivos electrónicos y espintrónicos. Dependiendo del diseño químico del sistema seleccionado, existen distintas metodologías experimentales para la preparación de dichas capas delgadas.[34] A continuación se describen brevemente las tres más utilizadas.

Históricamente, la primera preparación de capas delgadas con propiedades SCO se realizó a partir del complejo amfifílico $[Fe(OP_3)(NCS)_2$ ($OP_3$ = 1,10-fenantrolina sustituida con tres cadenas $C_{18}$) utilizando el método de Langmuir-Blodgett (LB) en el año 1988[35]. Esta metodología fue también fue aplicada con éxito en la fabricación de capas delgadas de complejos relacionados, formulados genéricamente $\{Fe(L)_2(NCS)_2\}$(L = bipiridina sustituida),[36] culminando en complejos basados en el ligando L = N-alcoxisalicilidenil-N'-etil-N-etilendiamina.[37]

Una de las metodologías más extendidas para la síntesis de capas delgadas SCO es el crecimiento secuencial, particularmente bien adaptada a los polímeros de coordinación conocidos como clatratos de Hofmann.[38] Entre estos últimos y en el área SCO, el primer ejemplo de crecimiento epitaxial lo representa el polímero 3D $\{Fe(pz)[Pt(CN)_4]$, reportado en 2006.[39] Esta metodología se ha extendido con éxito a otros sistemas 3D en los que el ligando puente axial piracina (pz) se ha sustituido por los ligandos 4,4'-azopyridina[40] y bis-(4-piridil)acetileno.[41] Más recientemente, se han descrito algunos sistemas 2D análogos $\{Fe(L)_2[Pt(CN)_4]\}$ con ligandos axiales monodentados tales como piridina (L = Py),[42] pirimidina e isoquinolina (L = Pym, Isoq).[43]

En lo que respecta a compuestos mononucleares neutros con estructura y estabilidad adecuadas es posible utilizar técnicas de sublimación de alto vacío para la elaboración de capas delgadas. El primer precedente basado en esta metodología data de 2006 y corresponde al complejo arquetípico $\{Fe(phen)_2(NCS)_2\}$.[44] Recientemente, esta técnica se ha aplicado a otros compuestos sublimables de interés entre los que cabe

destacar los derivados de ligandos aniónicos bis(pirazolil)borato,[45] hidrotris-(3,5-dimetil-pirazolil)borato[46] e hidrotris-(triazolil)borato[47]

### 1.2-3. Materiales SCO: Propiedades fluorescentes

La integración de la fluorescencia en los compuestos SCO es deseable para el desarrollo de nuevos materiales multifuncionales.[48] A pesar de que ciertos metales de transición (por ejemplo, $Fe^{II}$, $Co^{II}$, $Ni^{II}$) son considerados como bloqueantes de la luminiscencia existen algunos ejemplos publicados de compuestos SCO que presentan este tipo de sinergia. En el caso de los compuestos basados en el $Fe^{II}$ la interacción entre la fluorescencia y el SCO se basa en la superposición de la emisión fluorescente del luminóforo y la banda de absorción del $Fe^{II}$ en el estado LS, que desaparece en el estado HS. El primer ejemplo de coexistencia de las propiedades SCO y fluorescencia se observó en los complejos mononucleares [Fe(bzp-H)] y [Fe(bzp-$H_2$)[·$(ClO_4)_2$ (bzp = 2,6-bis(benzimidazol-2'-yl)piridina) en 2002[49]. La coexistencia entre ambos fenómenos también se ha observado en algunos polímeros de coordinación 1D y sistemas polinucleares discretos[50] y, en algunos casos, se ha procedido a la elaboración de los materiales en forma de nanopartículas/capas delgadas[51], sin embargo, no ha sido hasta recientemente que se han reportado los primeros polímeros de coordinación SCO fluorescentes.[52]

En particular, analizando la bibliografía presente correspondiente a los polímeros de coordinación de tipo Hofmann, la sinergia SCO/fluorescencia puede obtenerse mediante dos estrategias: i) de tipo intrínseco, basada en el uso de fluoróforos como ligandos[52a] ejemplificada con los sistemas formulados{Fe(bpan)$[M(CN)_2]_2$} (M = Ag, Au; Bpan = 4-bis(pyridyl)antraceno); ii) de tipo extrínseco, basada en la inclusión de invitados fluorescentes en las cavidades generadas[53] dando lugar a los sistemas {Fe(bpb)$[M(CN)_2]_2$}·Pyr y {Fe(bpben)$[M(CN)_2]_2$}·Pyr (bpb = bis(4-piridil)butadiino; bpben = 1,4-bis(4-piridil)benceno) donde el pireno huésped actúa como luminóforo. Además de estos ejemplos 3D, hasta el momento solo ha sido reportado un único caso de polímero de coordinación de tipo Hofmann 2D fluorescente[54] {[Fe(ppma)$_2$[$Pt(CN)_4$]}, mediante el uso del ligando ppma [(E)-N-fenil-1-(piridin-4-il)metanimina].

## 1.3- Objetivos de la tesis doctoral

Siguiendo la rica trayectoria de las tesis presentadas en la unidad de investigación sobre la síntesis y caracterización de materiales SCO con propiedades adheridas al mismo, la presente tesis doctoral se ha centrado en la obtención de materiales basados en la estructura general de los clatratos de Hofmann que combinan la amplia diversidad química de este tipo de sistemas (porosidad, estabilidad, …) con la propiedad del SCO. El objetivo final ha sido, por tanto, obtener materiales de $Fe^{II}$ que presentan entornos de coordinación aptos para presentar SCO (en este caso $[Fe^{II}N_6]$) junto con ligandos del tipo diciano o tetracianometalatos, que actúan como soporte estructural y método principal para aportar cooperatividad a los sistemas y ligandos axiales que dotan a los materiales obtenidos de las propiedades deseadas.

La tesis contiene tres trabajos de investigación claramente diferenciados que se basan en sistemas del tipo Hofmann bidimensionales (2D):

El primer trabajo, que se corresponde con el capítulo 2, contiene materiales basados en el uso del ligando axial 5-Aminopirimidina. Este ligando aporta a los sistemas bidimensionales obtenidos la habilidad de formar enlaces de hidrógeno estables con moléculas invitadas próticas R-OH (R = H, Me, Et) de modo que las propiedades SCO varían significativamente en función del huésped. Además, las transformaciones del material activado (completamente desolvatado) hacia los sistemas que contienen invitados ocurren mediante mecanismos monocristal a monocristal, otorgando gran estabilidad al sistema y permitiendo que los intercambios tengan lugar sin que ello implique la pérdida de las propiedades SCO.

El segundo trabajo, que se corresponde con el capítulo 3, contiene materiales basados en el uso de los ligandos axiales 4-alquildisulfanilpiridina (El grupo alquil siendo metil y etil). La elección de este tipo de ligandos reside en la presencia del grupo disulfanil -S-S-, este tipo de enlace se fragmenta que ante su exposición a superficies metálicas (por ejemplo, Ag o Au) dando lugar a uniones fuertes entre la molécula y la superficie. La aparición de estas interacciones se utilizará como herramienta para la construcción de

capas delgadas de estos materiales SCO y su futuro uso como interfaces espintrónicas en dispositivos moleculares.

El tercer trabajo, que se corresponde con el capítulo 4, contiene materiales basados en el uso del ligando axial 4-(antracen-9-il)piridina. El uso de este ligando se basa en la posible aportación de luminiscencia a los materiales resultantes, además, los canales generados en la estructura permiten la presencia de moléculas orgánicas invitadas derivadas del benceno (XBz con X = Cl, Br, I, $CH_3$ y $NO_2$). Los diferentes invitados en la red provocan ligeros cambios estructurales y electrónicos en el entorno de los centros de $Fe^{II}$ que se traducen en propiedades SCO claramente diferenciadas.

## 1.4- Metodología

**Preparación de ligandos.** Los ligandos no comerciales py$S_2$Me, py$S_2$Et y AnPy se sintetizaron siguiendo procedimientos experimentales previamente publicados. Posteriormente, fueron caracterizados mediante resonancia magnética nuclear (RMN).

**Síntesis de los compuestos SCO.** Los polímeros de coordinación de tipo Hofmann se sintetizaron en forma de monocristales siguiendo procedimientos de difusión lenta de las disoluciones madre, dependiendo del caso en tubos en H, tubos en H de tres patas o tubos de ensayo.

**Caracterización físico-química.** En términos generales los materiales sintetizados se caracterizaron en primera instancia mediante análisis elemental, análisis termogravimétrico y difracción de rayos X de polvo. Una vez conocida la pureza de los compuestos se caracterizaron las propiedades magnéticas en un magnetómetro SQUID en el rango de temperaturas 2-400K y, en los casos en los que fue posible, se estimaron los parámetros termodinámicos ($\Delta$H y $\Delta$S) asociados a las transiciones a través de calorimetría diferencial de barrido en el rango de 130K a 300K. Por último, para los materiales que presentaban una calidad cristalina suficiente, se realizaron medidas mediante difracción de rayos X de monocristal con el objetivo de determinar la estructura de los compuestos en función de la temperatura. Además de estas técnicas de caracterización básicas, se realizaron isotermas de adsorción/desorción de diferentes invitados en el capítulo 2 y se

monitorizó el comportamiento SCO a través de espectroscopia UV-Vis y de fluorescencia para los compuestos presentados en el capítulo 4.

## 1.5- Bibliografia


[1] L. Cambi and A. Cagnasso, *Atti Accad. Naz. Lincei, Cl. Sci. Fis. Mat. Nat., Rend*, 1931, **13**, 809.

[2] O. Kahn, *Molecular magnetism*, VCH, New York, 1993.

[3] (a) J.A. Real, A. B. Gaspar and M. C. Muñoz, *Dalton Trans.*, 2005, 2062-2079; (b) P. Gütlich, V. Ksenofontov and A.B. Gaspar, *Coord. Chem. Rev*., 2005, **249**, 1811-1829; (c) C. Lefter, R. Tan, J. Dugay, S. Tricard, G. Molnár, L. Salmon, J. Carrey, W. Nicolazzi, A. Rotaru and A. Bousseksou, *Chem. Phys. Lett.*, 2016, **644**, 138-141; (d) Z.-L. Liu, Md. N. Hoque, W. Liu, J.-Y. Li, Y.-C. Chen and M.-L. Tong, *Coord. Chem. Rev.*, 2017, **335**, 28-43 (e) E. Resines-Urien, E. Fernandez-Bartolome, A. Martinez-Martinez, A. Gamonal, L. Piñeiro-López and J. Sanchez Costa, *Chem. Soc. Rev.* 2023, Advanced Article (DOI: 10.1039/d2cs00790h).

[4] R. Feynman, *Miniaturization, Ed. A. Gilbert*, (Reinhold, New York), 1961, 282.

[5] W. A. Little, *Phys. Rev.*, 1964, **A 134**, 1416-1424.

[6] W. A. Little, *J. Polym. Sci., Polym. Lett. Ed.,* 1970, 29

[7] F. L. Cater (Ed.), *Molecular Electronic Devices* (M. Dekker, New York), 1982

[8] F. L. Cater (Ed.), *Molecular Electronic Devices II* (M. Dekker, New York), 1982

[9] (a) J. S. Miller, *Adv. Mater.*, 1990, **2**, 378-379; (b) J. S. Miller, *Adv. Mater.*, 1990, **2** 495-497; (c) J. S. Miller, *Adv. Mater.*, 1990, **2**, 601-603.

[10] D. Goldhaber-Gordon, M. S. Montemerlo, J. C. Love, G. J. Opiteck, J. C. Ellenbogen, Proceeding of the IEEE, 1997, **85**, 521-540.

[11] R. C. Haddon, A. A. Lamola, *Proc. Natl. Acad. Sci. USA*, 1985, **82**, 1874-1878.

[12] O. Kahn, J. P. Launay, *Chemtronics*, 1988, **3**, 140-151.

[13] J. M. Lehn, *Supramolecular Chemistry. Concepts and perspectives,* VCH, Weinheim, 1995.

[14] J. P. Sauvage, *Acc. Chem. Res.,* 1990, **23**, 319-327.

[15] (a) M. A. Halcrow (Ed.), *Spin-Crossover Materials: Properties and Applications*., Wiley, New York, 2013; (b) O. I. Kucheriv, V. V. Oliynyk, V. V. Zagorodnii, V. L. Launets. I. O. Fritsky and I. A. Gural'skiy, *Modern Magnetic and Spintronic*

*Materials* (A. Kaidatzis, S. Sidorenko, I. Vladymyrskyi, D. Niarchos (Eds.)), 2020, 119-143; (c) T. K. Ekanayaka, G. Hao, A. Mosey, A. S. Dale, X. Jiang, A. J. Yost, K. R. Sapkota, G. T. Wang, J. Zhang, A. T. N'Diaye, A. Marshall, R. Cheng, A. Naeemi, X. Xu and P. A. Dowben, *Magnetochemistry*, 2021, **7**, 37-56; (d) J. Seo, J. D. Braun, V. M. Dev and J. A. Mason, *J. Am. Chem. Soc.*, 2020, **144**, 6493-6503.

[16] A. Hauser, *J. Chem. Phys.*, 1991, **94**, 2741-2748.

[17] (a) A. Bousseksou, J. J. McGarvey, F. Varret, J. A. Real, J. P. Tuchagues, A. C. Dennis and M. L. Boillot, *Chem. Phys. Lett.*, 2000, **318**, 409-416; (b) N. Moliner, L. Salmon, L. Capes, M. C. Muñoz, J. F. Létard, A. Bousseksou, J. P. Tuchagues, J. J. McGarvey, A. C. Dennis, M. Castro, R. Burriel and J. A. Real, *J. Phys. Chem. B.,* 2002, **106**, 4276-4283; (c) G. Molnár, V. Niel, A. B. Gaspar, J. A. Real, A. Zwick, A. Bousseksou and J. J. McGarvey, *J. Phys. Chem. B.*, 2002, **106**, 9701-9707; (d) M. Sorai and S. Seki, *J. Phys. Chem. Solids,* 1974, **35**, 555-570.

[18] (a) T. Granier, B. Gallois, J. Gaultier, J. A. Real and J. Zarembowitch, *Inorg. Chem*., 1993, **32***,* 5305-5312; (b) P. Gütlich, V. Ksenofontov and A. B. Gaspar, *Coord. Chem. Rev.*, 2005, **249**, 1811-1829.

[19] (a) E. Buhks, M. Bixon and J. Jortner, *J. Am. Chem. Soc.*, 1980, **102**, 2918-2923; (b) C. L. Xie and D. N. Hendrickson, *J. Am. Chem. Soc*., 1987, **109**, 6981-6988.

[20] A. Hauser, *Comments Inorg. Chem.*, 1995, **17**, 17-40.

[21] J. J. McGarvey and I. Lawthers, *J. Chem. Soc., Chem. Commun.,* 1982, 906-907.

[22] (a) S. Decurtins, P. Gütlich, C. P. Köhler, H. Spiering and A. Hauser, *Chem. Phys. Lett.*, 1984, **139**, 1-4; (b) S. Decurtins, P. Gütlich, K. M. Hasselbach, H. Spiering and A. Hauser, *Inorg. Chem.,* 1985, **24**, 2174-2178.

[23] (a) C. Brady, J. J. McGarvey, J. K. McCusker, H. Toftlund and D. N. Hendrickson, *Spin Crossover in Transition Metal Compounds III, Top. Curr. Chem.,* 2004, **235**, 1-22. (b) J.-F. Létard, G. Chastanet, P. Guionneau and C. Desplanches, (M. A. Halcrow (Ed.)) *Spin-Crossover Materials: Properties and Applications*, 475-506, Wiley, New York, 2013. (c) G. Chastanet, C. Desplanches, C. Baldé, P. Rosa, M. Marchivie and P. Guionneau, *Chem. Sq.* 2018, **2**, 2-18

[24] (a) H. Spiering, T. Kohlhaas, H. Romstedt, A. Hauser, C. Bruns-Yilmaz, J. Kusz and P. Gütlich, *Coord. Chem. Rev*., 1999, **190-192**, 629-647; (b) M. Paez-Espejo, M. Sy and K. Boukheddaden, *J. Am. Chem. Soc.*, 2016, **138**, 3202-3210.

[25] (a) C. P. Slichter, H G. Drickamer, *J. Chem. Phys*., 1972, **56**, 2142-2160; (b) J. M. Honig, *J. Chem. Ed*., 1999, **76**, 848-853.

[26] (a) P. Gütlich, H. Goodwin (Eds., *Top. Curr. Chem*., 2004, **233-235.**

[27] J. A. Real, E. Andrés, M. C. Muñoz, M. Julve, T. Granier, A. Bousseksou and F. Varret, *Science*, 1995, **268**, 365-267.

[28] G. J. Halder, C. J. Kepert, B. Moubaraki, K. S. Murray and J. D. Cashion, *Science*, 2002, **298**, 1762-1765.

[29] (a) K. A. Hofmann, F. Küspert, *Z. Anorg. Chem.* 1987, **15**, 204-207; (b) Z.-P. Ni, J.-L Liu, Md. N. Hoque, W. Liu, J.-Y Li, Y.-C. Chen and M.-L. Tong, *Coord. Chem. Rev.*, 2017, **335**, 28-43; (c) R. Ohtani and S. Hayami, *Chem.-Eur J.*, 2017, **23**, 2236-2248; (d) M. C. Muñoz and J. A. Real, *Coord. Chem. Rev.* 2011, **255**, 2068-2093.

[30] M. Ohba, K. Yoneda, G. Agustí, M. C. Muñoz, A. B. Gaspar, J. A. Real, M. Yamasaki, H. Ando, Y. Nakao, S. Sakaki and S. Kitagawa, *Angew. Chem. Int. Ed.*, 2009, **48**, 4767-4771.

[31] C. Bartual-Murgui, A. Akou, H. J. Shepherd, G. Molnár, J. A. Real, L. Salmon and A. Bousseksou, *Chem.-Eur. J.*, 2013, **19**, 15036-15043.

[32] (a) K. A. Zenere, S. G. Duyker, E. Trzop, E. Collet, B. Chan, P. W. Doheny, C. J. Kepert and S. M. Neville, *Chem. Sci*., 2018, **9**, 5623; (b) M. M. Ndiaye, S. Pillet, E.-E. Bendeif, M. Marchivie, G. Chastanet, K. Boukheddaden and S. Triki, *Eur. J. Inorg. Chem.*, 2018, 305-313; (c) N. F. Sciortino, F. Ragon, Y. M. Klein, C. E. Housecroft, C. G. Davies, G. N. L. Jameson, G. Chastanet and S. M. Neville, *Inorg. Chem.*, 2018, **57**, 11068-11076; (d) N. F. Sciortino, K. A. Zenere, M. E. Corrigan. G. J. Halder, G. Chastanet, J.-F. Létard, C. J. Kepert and S. M. Neville, *Chem. Sci.*, 2017, **8**, 701; (e) M. J. Murphy. K. A. Zenere, F. Ragon, P. D. Southon, C. J. Kepert and S. M. Neville, *J. Am. Chem. Soc.*, 2017, **139**, 1330-1335; (f) E. Milin, V. Patinec, S. Triki, E.E. Bendeif, S. Pillet, M. Marchivie, G. Chastanet and K. Boukheddaden, *Inorg. Chem.*, 2016, **55**, 11652-11661; (g) N. F. Sciortino, F. Ragon, K. A. Zenere, P.D. Southon, G. J. Halder, K. W. Chapman, L. Piñeiro-Lopez, J. A. Real, C. J. Kepert and S. M. Neville, *Inorg. Chem.*, 2016, **55**, 10490-10498; (h) Y. M. Klein, N. F. Sciortino, F. Ragon, C. E. Housecroft, C. J. Kepert and S. M. Neville, *Chem. Commun.*, 2014, **50**, 3838-3840.

[33] (a) F.-L. Liu and J. Tao, *Chem.-Eur. J.*, 2017, **23**, 18252-18257; (b) W. Liu, Y.-Y. Peng, S.-G. Wu, Y.-C. Chen, Md. N. Hoque, Z.-P. Ni, X.-M. Chen and M.-L. Tong, *Angew. Chem., Int. Ed.*, 2017, **56**, 14982-14986; (c) J. E. Clements, J. R. Price, S. M. Neville and C. J. Kepert, *Angew. Chem., Int. Ed.*, 2016, **55**, 15105-15109; (d) N. F. Sciortino, K. R. Scherl-Gruenwald, G. Chastanet, G. J. Halder, K. W. Chapman, J.-F. Létard and C. J. Kepert, *Angew. Chem., Int. Ed.*, 2012, **124**, 10301-10305; (e) G. J. Halder, K. W. Chapman, S. M. Neville, B. Moubaraki, K. S. Murray, J.-F. Létard and C. J. Kepert, *J. Am. Chem. Soc.*, 2008, **130(51)**, 17552-17562.

[34] (a) T. Mallah and M. Cavallini, *C. R. Chimie*, 2018, **21**, 1270-1286; (b) M. Cavallini, *Phys. Chem. Chem. Phys.* 2012, **14**, 11867-11876.

[35] A. Raudel-Teixier, A. Barraud, P. Coronel and O. Kahn, *Thin Solid Films,* 1988, **160**, 107-115.

[36] H. Soyer, C. Mingotaud, M. L. Boillot and P. Delhaes, *Langmuir*, 1998, **14**, 5890–5895.

[37] J. A. Kitchen, N. G. White, C. Gandolfi, M. Albrecht, G. N. L. Jameson, J. L. Tallon and S. Brooker, *Chem. Commun*., 2010, **46**, 6464–6466.

[38] C. M. Bell, M. F. Arendt, L. Gomez, R. H. Schmehl and T. E. Mallouk, *J. Am. Chem. Soc*, 1994, **116**, 8374-8375.

[39] S. Cobo, G. Molnár, J. A. Real and A. Bousseksou, *Angew. Chem. Int. Ed.*, 2006, **45**, 5786-5789.

[40] G. Agustí, S. Cobo, A. B. Gaspar, G. Molnár, C. Thibault, J. A. Real and A. Bousseksou, *Chem. Mater.* 2008, **20**, 6721-6732.

[41] C. Bartual-Murgui, A. Akou, L. Salmon, G. Molnar, C. Thibault, J. A. Real and A. Bousseksou, *Small*, 2011, **7**, 3385-3391.

[42] V. Rubio-Giménez, C. Bartual-Murgui, M. Galbiati, A. Nuñez-López, J. Castells-Gil, B. Quinard, P. Seneor, E. Otero, P. Ohresser, A. Cantarero, E. Coronado, J. A. Real, R. Mattana, S. Tatay and C. Martí-Gastaldo, *Chemical Science*, 2019, **10**, 4038-4047.

[43] V. Rubio-Giménez, G. Escorcia-Ariza, C. Bartual-Murgui, C. Sternemann, M. Galbiati, J. Castells-Gil, J. A. Real, S. Tatay and C. Martí-Gastaldo, *Chem. Mater.*, 2019, **31**, 7277-7287.

[44] S. Shi, G. Schmerber, J. Arabski, J.-B. Beaufrand, D. J. Kim, S. Boukari, M. Bowen, N. T. Kemp, N. Viart, G. Rogez, E. Beaurepaire, H. Aubriet, J. Petersen, C. Becker and D. Ruch, *Appl. Phys. Lett.*, 2009, **95**, 043303.

[45] C. Lefter, S. Rat, J. S. Costa, M. D. Manrique-Juarez, C. M. Quintero, L. Salmon, I. Seguy, T. Leichle, L. Nicu, P. Demont, A. Rotaru, G. Molnár and A. Bousseksou, *Adv. Mater.*, 2016, **28**, 7508-7514.

[46] M. Gavara-Edo, R. Córdoba, F. J. Valverde-Muñoz, J. Herrero-Martín, J. A. Real and Eugenio Coronado, *Adv. Mater.*, 2022, 2202551.

[47] (a) V. Shalabaeva, S. Rat, M. D. Manrique-Juarez, A.-C. Bas, L. Vendier, L. Salmon, G. Molnár and A. Bousseksou, *J. Mat. Chem. C*, 2017, **5**, 4419-4425; (b) K. Ridier, A.-C. Bas, Y. Zhang, L. Routaboul, L. Salmon, G. Molnár, C. Bergaud and A. Bousseksou, *Nat. Commun.*, 2020, **11**, 3611

[48] (a) M. K. Javed, A. Sulaiman, M. Yamashita and Z.-Y. Li, *Coord. Chem. Rev.*, 2022, **467**, 214625; (b) K. Sun, J.-P. Xue. Z.-S. Yao and J. Tao, *Dalton Trans.* 2022, 51, 16044-16054.

[49] M. Hasegawa, F. Renz, T. Hará, Y. Kikuchi, Y. Fukuda, J. Okubo, T. Hoshi and W. Linert, *Chem. Phys*., 2002, **277**, 21-30.

[50] (a) Y. García, F. Robert, A. D. Naik, G. Zhou, B. Tinant, K. Robeyns, S. Michotte and L. Piraux, *J. Am. Chem. Soc.*, 2011, **133**, 15850-15853; (b) C.-F. Wang, R.-F. Li, X.-Y. Chen, R.-J. Wei, L.-S. Zheng and J. Tao, *Angew. Chem. Int. Ed.*, 2015, **54**, 1574-1577.

[51] (a) H. Matsukizono, K. Kuroiwa and N. Kimizuka, *Chem. Lett.*, 2008, **37**, 446-447; (b) S. Titos-Padilla, J. M. Herrera, X.-W. Chen, J. J. Delgado, E. Colacio, *Angew. Chem. Int. Ed.*, 2011, **50**, 3290-3293.

[52] (a) C. Lochenie, K. Schötz, F. Panzer, H. Kurz, B. Maier, F. Puchtler, S. Agarwal, A. Köhler and B. Weber, *J. Am. Chem. Soc*. 2018, **140**, 700-709. (b) Y.-R. Qiu, L. Cui, J.-Y Ge, M. Kurmoo, G. Ma and J. Su, *Front. Chem.*, 2021, **9**, 692939

[53] (a) M. Meneses-Sánchez, L. Piñeiro-López, T. Delgado, C. Bartual-Murgui, M. C. Muñoz, P. Chakraborty and J. A. Real, *J. Mater. Chem. C*, 2020, **8**, 1623-1633; (b) T. Delgado, M. Meneses-Sánchez, L. Piñeiro-López, C. Bartual-Murgui, M. C. Muñoz and J. A. Real, *Chem. Sci.*, 2018, **9**, 8446-8452.

[54] C. F. Wang, J. C. Wu, and Q. Li, *Inorg. Chem. Front.*, 2022, 3251-3258.

CAPÍTULO 2

# Reversible guest-induced gate-opening with multiplex spin-crossover responses in two-dimensional Hofmann clathrates

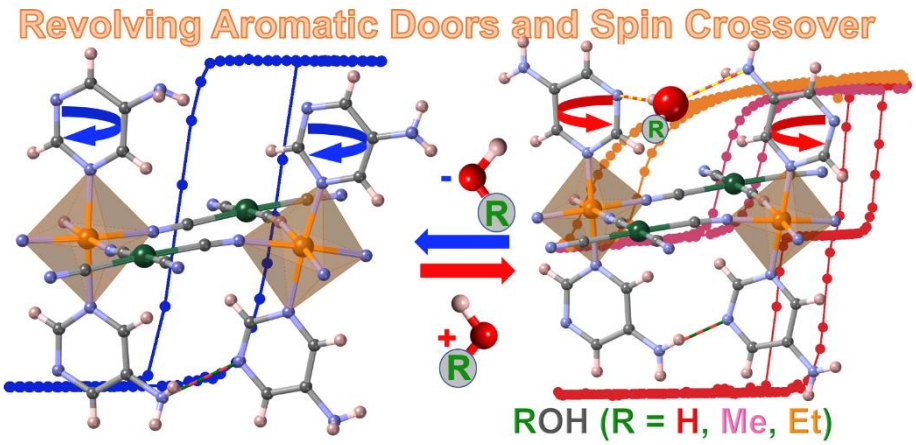


REVISTA: Chemical Science

ÍNDICE DE IMPACTO: 9.969

# CAPÍTULO 2

## Reversible guest-induced gate-opening with multiplex spin crossover responses in two-dimensional Hofmann clathrates

### 2.1.- Abstract

Spin crossover (SCO) compounds are very attractive types of switchable materials due to their potential applications in memory devices, actuators or chemical sensors. Rational chemical tailoring of these switchable compounds is key for achieving new functionalities in synergy with the spin state change. However, the lack of precise structural information required to understand the chemical principles that control the SCO response with external stimuli may eventually hinder further development of spin switching-based applications. In this work, the functionalization with an amine group in the two-dimensional (2D) SCO compound $\{Fe(5\text{-}NH_2Pym)_2[M^{II}(CN)_4]\}$ (**1$^{M}$**, 5-$NH_2$Pym = 5-aminopyrimidine, $M^{II}$ = Pt (**1$^{Pt}$**), Pd (**1$^{Pd}$**)) confers versatile host-guest chemistry and structural flexibility to the framework primarily driven by the generation of extensive H-bond interactions. Solvent free **1$^{M}$** species reversibly adsorb small protic molecules such as water, methanol or ethanol yielding the **1$^{M}$·$H_2O$**, **1$^{M}$·0.5 MeOH** or **1$^{M}$·xEtOH** (x = 0.25-0.40) solvated derivatives. Our results demonstrate that the reversible structural rearrangements accompanying these adsorption/desorption precesses (**1$^{M}$** ↔ **1$^{M}$·guest**) follow a gate opening mechanism whose kinetics depend not only on the nature of the guest molecule and that of the host framework (**1$^{Pt}$** or **1$^{Pd}$**) but also on their reciprocal interactions. In addition, a predictable and reversible guest-induced SCO modulation has been observed and accurately correlated with the associated crystallographic transformations monitored by single cristal X-ray diffraction.

### 2.2.- Introduction

Hexa-coordinated iron(II) spin crossover complexes are a singular class of materials featuring a labile and reversible electronic configuration change between the diamagnetic low-spin state [$t_{2g}^6e_g^0$ S = 0] (LS) and the paramagnetic high spin state [$t_{2g}^4e_g^2$ S = 2] (HS).[1] LS↔HS switching is an entropy-driven phenomenon which can be induced by a panoply of stimuli, *i. e.* a gradient of temperature[2] and/or pressure,[3] light irradiation,[4] application of an

electric field[5] or even through interaction with analytes,[6] thereby effecting changes in the magnetic, electric, optical, mechanical and structural properties of the material. In the solid state, the profile of the spin-state switch depends on the elastic coupling (cooperativity) between active SCO $Fe^{II}$ centres. Gradual SCO spreading over a wide range of temperatures occurs when the elastic coupling is weak. On the contrary, strong elastic coupling favours sharp abrupt first orded spin transitions which, in special cases, are accompanied by hysteretic behaviour conferring to the material bistability (memory effect). Materials exhibiting bistable SCO behaviour have attracted much interest because of their potential applications in memory devices, actuators or chemical sensors.[7]

In recent years, many studies have been devoted to the chemical design of SCO compounds in order to incorporate new functionalities acting in synergy with the purely thermal driven spin-state switching. These added properties include fluorescence,[8] electrical conductivity[9] or porosity,[10] among others. Indeed, combination of SCO and porosity has been one of the most exploited routes for achieving multifunctionality in part due to its high potential in molecular sensor applications. The first examples showing coexistence of both properties were the doubly-interpenetrated compounds with general formula $[FeL_2(SCN)_2]\cdot$Solv [L = 1,2-di(4-pyridyl)-ethylene (tvp)[11] or *trans*-4-4'azopyridine (azpy)[12]]. These compounds display SCO properties which depend on the included solvent molecules. Later, Hofmann-type coordination polymers (HCPs) formulated $\{Fe(L)_y[M(CN)_x]\}$ {including non-interpenetrated [x = 4; L = monodentate (y = 2, 2D) or bis-monodentate (y = 1, 3D) ligand; M = Pd, Pt, Ni] or interpenentrated [x = 2, L = monodentate (y = 2, 2D) or bis-monodentate (y = 1, 3D) ligand; M = Ag, Au] compounds}[6a,13] gained increasing interest due to their demonstrated structural versatility and the possibility of being processed as thin-films or nano-objects.[14] The intrinsic structural porosity offered by this family of compounds has resulted in numerous reports studying synergies between SCO and host-guest chemistry.[15] Overall, modulation of the SCO through gust adsorption can be explained by steric and/or electronic effects. The first factor involves stabilization of the HS state by the guest due to the hindering of the framework contraction associate with the HS-to-LS process.[16] The second factor entails changes in the ligand flied strength around the $Fe^{II}$ centre *via* host-guest interactions with the coordinated ligands.[17]

A suitable synthetic strategy for inducing guest inclusion synergies is the use of asymmetric ligands with hydrophilic functional groups. This type of ligands promotes intermolecular interactions leading to the lattice asymmetries which originate inter-sheet

cavities where the guest molecules are located. This structural model was exploited by using a series of asymmetric triazole-type ligands substituted with various chemical groups leading, in all cases, to multi-stable SCO compounds.[18] Similar results were also obtained for pyridine donor asymmetric ligands.[19] Overall, the shape of the SCO curves in these systems depends not only on ther selected pillaring ligand but also on the amount and nature of the adsorbed guest moleules. For example, the SCO of compound $\{Fe(bztrz)_2[Pd^{II}(CN)_4]\}\cdot G$ exhibits one, two or three steps when G = ($H_2O$,EtOH), $3H_2O$ or ~$2H_2O$, respectively, demonstrating that the elastic frustration which gives raise to multi-stability can be modulated by guest exchange.[18e] Unfortunately, with very rare exceptions,[18g] crystallinity of these 2D systems is partially or completely lost after total desorption of guest molecules preventing the evaluation of the involved structural modifications and their implication on the associated SCO changes. Moreover, the vanishing of crystallinity may also limit the accuracy of the structural characterization in a subsequent guest-dependent SCO study. The establishment of a dense network of host-host and host-guest intermolecular interactions (H-bonds, π-π stacking…) may be critical to overcome this limitation. Recently, the analogous 2D compounds $\{Fe(3\text{-}NH_2Py)_2[M(CN)_4]\}$ and $\{Fe(Pym)_2[M(CN)_4]\}\cdot xH_2O$ [3-$NH_2$Py = 3-aminopyridine;[20] Pym = pyrimidine[21] (Scheme 1); M = Pt, Pd, Ni] were reported. The former displays host-host CH···N(amino) H-bonding interactions and hysteretic SCO for all the investigated derivatives, although no host-guest properties were described. In contrast, the latter exhibits guest-dependent cooperative spin transitions attributed to the H-bonds established between the non-coordinated nitrogen of the pyrimidine and the guest water molecules. However, lack of detailed structural data after dehydration prevented the investigation of further precise magneto-structural corelations. In this work, the use of 5-aminopyrimidine (5-$NH_2$Pym, Scheme 1) ligand has led to 2D HCPs compounds $\{Fe(5\text{-}NH_2Pym)_2[M^{II}(CN)_4]\}\cdot H_2O$ [$M^{II}$ = Pt (**1$^{Pt}$·$H_2O$**) or Pd (**1$^{Pd}$·$H_2O$**)]. The combination of a donor amino group and an acceptor non-coordinated nitrogen in the 5-$NH_2$Pym axial ligand enables the coupling of contiguous [$FeN_6$] octahedrons, belonging to the same layer, through a robust network of H-bond interactions which is additionally reinforced by the inclusion of protic guest molecules. Indeed, this stiff H-bond network seems to be key for the persistence of crystallinity upon the loss of water molecules that gives rise to te unsolvated derivatives **1$^{Pt}$** or **1$^{Pd}$**. These guest-free compounds are prone to re-adsorb water or other small molecules as methanol or ethanol also following reversible single-crystal-to-single-crystal (SCSC) transformations. This has enabled us to establish precise correlations between the wide variety of SCO behaviours presented by this family of compounds and the structural transformations upon guest exchange (**1$^{M}$** ↔

**$1^{M}$·guest**). Interestingly, in agreement with the adsorption/desorption isotherm measurements, these crystallographic transformations follow a gate-opening mechanism which represents an unprecedented structural feature in combination with switchable 2D HCPs.

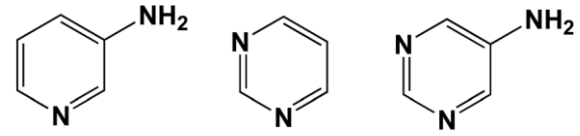


**Scheme 1.** Related axial ligands used for the synthesis of new 2D Hofmann-type SCO coordination polymers (see text)

## 2.3.- Results

### 2.3.1.- Synthesis, structure and SCO properties of $1^{Pt}$·$H_2O$ and $1^{Pd}$·$H_2O$

Single crystals of **$1^{Pt}$·$H_2O$** and **$1^{Pd}$·$H_2O$** were prepared by slow liquid-to-liquid diffusion methods from $Fe(BF_4)_2{\cdot}6H_2O$, $K_2[M^{II}(CN)_4]$ ($M^{II}$ = $Pt^{II}$ or $Pd^{II}$) and 5-aminopyrimidine (5-$NH_2$Pym) aqueous solutions separated by a water interphase in a double-H shaped tube (see experimental section in the supporting information). Yellow thin plate-shaped single crystals were obtained in good yields (*ca.* 60-70%) after 4 weeks.

Compounds **$1^{Pt}$·$H_2O$** and **$1^{Pd}$·$H_2O$** are isomorphous and crystallize in the monoclinic *C2/m* space group. The asymmetric unit is constituted by two non-equivalent $[Fe^{II}1N_6]$ and $[Fe^{II}2N_6]$ pseudo-octahedral centres connected through their equatorial coordination sites by two equivalent $[M^{II}(CN)_4]^{2-}$ units ($M^{II}$ = Pt or Pd) (Fig. 1a), thereby defining cyano-bridged bimetallic $Fe^{II}$-$M^{II}$ layers (Fig. 1b). The axial positions of each $Fe^{II}$ ion are coordinated by two equivalent terminal 5-$NH_2$Pym ligands through one of its two heterocyclic N atoms. At 260K, the average $[Fe^{II}1N_6]$/ $[Fe^{II}2N_6]$ bond lengths, 2.159 Å/ 2.164 Å for **$1^{Pt}$·$H_2O$** and 2.168 Å/ 2.171 Å for **$1^{Pd}$·$H_2O$**, are consistent with a fully populated HS state. Within a given $Fe^{II}$ centre, the apical 5-$NH_2$Pym ligands [hereafter labelled as 5-$NH_2$Pym(1) (coordinated to $Fe^{II}1$) and 5-$NH_2$Pym(2) (coordinated to $Fe^{II}2$)] are disposed in such a way that they adopt a trans conformation with respect to the orientation of the amino substituent. This enables the formation of two types of H-bonds within each layer. One, a single H-bond between the N3 atom of the amino group of 5-$NH_2$Pym(1) and the uncoordinated N7 heteroatom of the 5-$NH_2$Pym(2) ligand. The other, a double H-bond involving the adjacent N2 and N8 atoms

belonging to the heteroatom of 5-$NH_2$Pym(1) and the amino group of 5-$NH_2$Pym(2'), respectively, mediated by the interaction with the guest water molecule (Fig. 1a and b). The trapped water molecules are located within two discrete equivalent positions modelled with an occupancy of 0.5 (0.4 in the case of Pt), hence the structure contains 1 (0.8 for Pt) molecule of water per $Fe^{II}$ ion in good agreement with the TGA studies (Fig. S1a and b). The intralayer H-bon interactions define an array of parallel linear chains running along the [001] direction. As a result, the bimetallic layers are slightly corrugated (Fig. 1b) being the angles defined by the equatorial planes of the coordination Fe1-Fe2/Fe1-Pt(Pd)/Fe2-Pt(Pd) centres in the interval 14.8-15.0º/1.3-4.0º/16.2-18.8º, respectively. The layers are pillared in such a way that the apical 5-$NH_2$Pym ligands are interdigitated defining weak π-π interactions (Fig. S2a) and the $M^{II}$ centres of one layer are on top the centre of the [$Fe_2M^{II}_2$] windows of the adjacent layers (Fig. S2b). The packing of the layers generates 1D channels where the water molecules are located (Fig. 1c). The interlayer distance based on the average plane defined by the Fe1-Fe2-Pt/Pd atoms is 8.17 and 8.14 Å for **$1^{Pt}\cdot H_2O$** and **$1^{Pd}\cdot H_2O$**, respectively. Host-host and host-guest H-bond interactions found for **$1^{Pt}\cdot H_2O$** and **$1^{Pd}\cdot H_2O$** and for the rest of studied solvates are gathered in Table 1.

**Table 1.** Selected H-bond interactions (in Å) found for **$1^{M}$**, **$1^{M}\cdot H_2O$**, **$1^{M}\cdot 0.5MeOH$** and **$1^{Pt}\cdot 0.4EtOH$**

| Interaction | $1^{Pt}$ | $1^{Pd}$ | $1^{Pt}\cdot H_2O$ | $1^{Pd}\cdot H_2O$ | $1^{Pt}\cdot 0.5MeOH$ | $1^{Pd}\cdot 0.5MeOH$ | $1^{Pt}\cdot 0.4EtOH$ |
|---|---|---|---|---|---|---|---|
| **Host-Host** | | | | | | | |
| N6(amino)···N7(het.) | 3.023 | 2.973 | --- | --- | --- | --- | --- |
| N3(amino)···N7(het.) | --- | --- | 3.106 | 3.075 | --- | --- | 3.053 |
| N7(amino)···N3(het.) | --- | --- | --- | --- | 2.979 | 3.039 | --- |
| N11(amino)···N13(het.) | --- | --- | --- | --- | 3.015 | 3.042 | --- |
| **Host-guest** | | | | | | | |
| O1(guest)···N2(het.) | --- | --- | 2.885 | 2.842 | --- | --- | 2.795 |
| O1(guest)···N8(amino) | --- | --- | 3.053 | 3.035 | --- | --- | 2.963 |
| O1(MeOH)···N2(het.) | --- | --- | --- | --- | 2.724 | 2.771 | --- |
| O2(MeOH)···N10(het.) | --- | --- | --- | --- | 2.805 | 2.781 | --- |
| O1(MeOH)···N8(amino) | --- | --- | --- | --- | 2.900 | 2.914 | --- |
| O2(MeOH)···N14(amino) | --- | --- | --- | --- | 2.979 | 2.908 | --- |

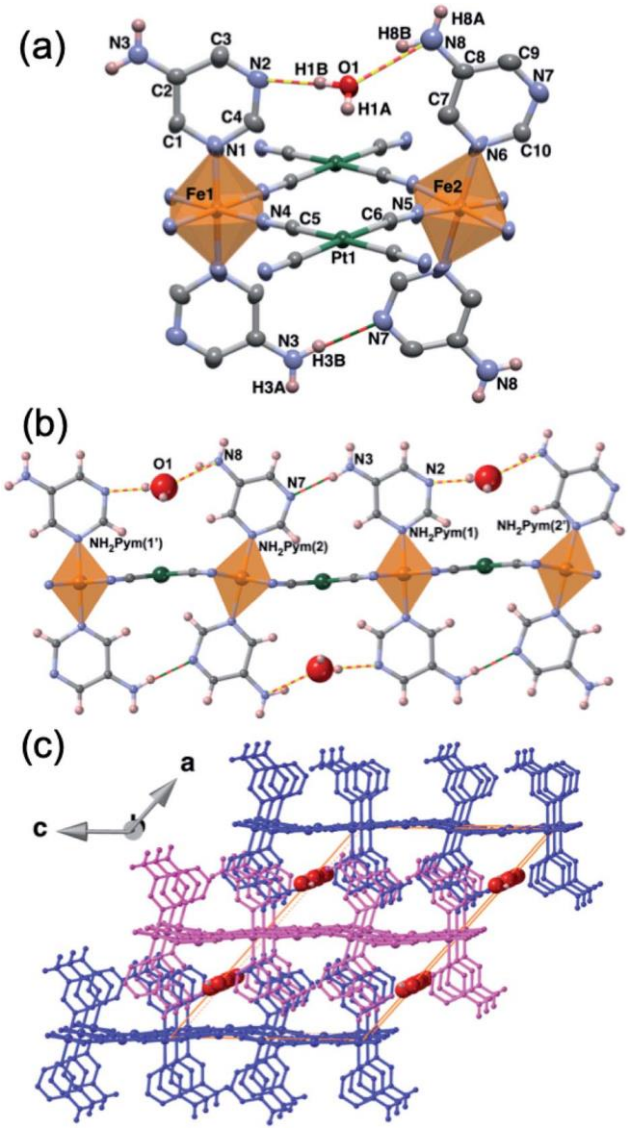


**Fig. 1.** (a) ORTEP view of the asymmetric unit of $\mathbf{1^{Pt}\cdot H_2O}$ at 260K (isostructural to $\mathbf{1^{Pd}\cdot H_2O}$) showing 50% probability displacement ellipsoids (aromatic hydrogen atoms are omitted for clarity) and (b) view along the [010] direction of a $\mathbf{1^{M}\cdot H_2O}$ (M = Pt, Pd) layer (discontinuous yellow-red and red-green lines represent host-guest and host-host H bonds, respectively). (c) 3D supramolecular fragment of $\mathbf{1^{M}\cdot H_2O}$ (M = Pt, Pd) displaying three successive pillared lyers (distinguished in pink and blue). Red spheres represent the trapped water molecules within the 1D channels.

Upon cooling to 187 K (180 K for **$1^{Pd}\cdot H_2O$**), the crystals become orange suggesting the occurrence of a HS-to-LS state change. The system retains the *C*2/*m* space group and the overall structure does not change significantly with respect to that at 260 K. However, whereas the average [Fe1$N_6$] bond length decreases by 0.194 Å for **$1^{Pt}\cdot H_2O$** and **$1^{Pd}\cdot H_2O$**, that of [Fe2$N_6$] remains barely unaltered for both **$1^{Pt}\cdot H_2O$** (2.165 Å *vs.* 2.139 Å) and **$1^{Pd}\cdot H_2O$** (2.171 Å *vs.* 2.156 Å). These values reveal that whereas Fe1 centres undergo a complete HS-to-LS transition, those of Fe2 remain in the HS configuration. This defines a ···HS-LS··· ordered state within the linear H-bond chains mentiones above (Fig. 2a) that in turn results in an infinite ordered succession of HS and LS planes running along [001] (Fig. 2b). Further cooling to 120K induces a complete spin transition as indicated by the Fe1-N/Fe2-N average distances of 1.948/1.955 and 1.961/1.963 Å for **$1^{Pt}\cdot H_2O$** and **$1^{Pd}\cdot H_2O$**, respectively. These structural data are in perfect agreement with the magnetic measurements (*vide infra*). The HS → LS process is accompanied by a contraction of the interlayer distance by 0.3 Å and 0.2 Å for **$1^{Pt}\cdot H_2O$** and **$1^{Pd}\cdot H_2O$**, respectively. Furthermore, the angles defined by the equatorial planes of Fe1-Fe2/Fe1-Pt(Pd)/Fe2-Pt(Pd) decrease by 0.7º/1.2º/2.0º when moving from the HS to the LS state for **$1^{Pt}\cdot H_2O$** and **$1^{Pd}\cdot H_2O$**, consequently the undulation of the $\{Fe[M(CN)_4]\}_n$ planes is slightly less pronounced. The main crystallographic parameters of **$1^{Pt}\cdot H_2O$** and **$1^{Pd}\cdot H_2O$** are gathered in Tables S1 and S2, respectively.

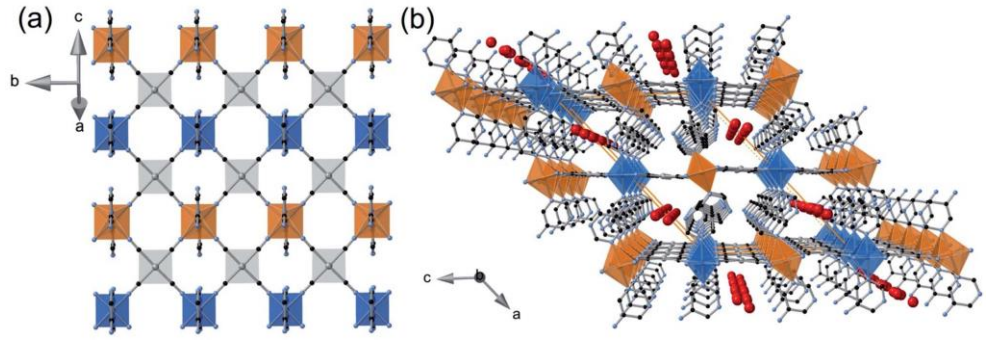


**Fig. 2.** Perspective views of **$1^{Pt}\cdot H_2O$** at 187 K (structurally equivalent to **$1^{Pd}\cdot H_2O$** at 180 K) displaying (a) a bimetallic layer in the ···HS-LS··· ordered intermediate state representic in blue the LS Fe1 sites and in orange the HS Fe2 sites and (b) three stacked layers showing the planes containing the HS or LS (hydrogen atoms are omitted for clarity).

Fig. 3 shows the magnetic properties in form of $\chi_M T$ *vs T* plots ($\chi_M$ is the molar magnetic susceptibility and *T* is the temperature) for **$1^{Pt}\cdot H_2O$** and **$1^{Pd}\cdot H_2O$** and, consequently, those of

their corresponding derivatives (*vide infra*) were constituted exclusively of single crystals which, according to the elemental analysis and powder X-ray diffraction studies (see the experimental section and Fig. S3 in the supplementary information), corresponded to a single phase. At 290K, the $\chi_M T$ value of the as-synthesized crystals of **1$^{Pt}$·H$_2$O** and **1$^{Pd}$·H$_2$O** was found to be about 3.5 cm$^3$ K mol$^{-1}$, which is consistent with the Fe$^{II}$ ion in the HS state. When cooling at 2 K min$^{-1}$, this value remains constant until it drops abruptly just below *ca.* 205 K in two marked steps, involving each one 50% of a complete HS-to-LS transformation. The average critical temperatures $T_c$ (calculated as $T_c = T_{ci}^{\uparrow} + T_{ci}^{\downarrow}/2$ where $T_{ci}^{\uparrow}$ and $T_{ci}^{\downarrow}$ ($i$ = 1, 2) are the transition temperatures in the respective heating and cooling modes) are $T_{c1}$ = 205.5 (204) K and $T_{c2}$ = 187.5 (173.5) K for **1$^{Pt}$·H$_2$O** (**1$^{Pd}$·H$_2$O**) within the first and second step, respectively, and define hysteresis loops ($\Delta T_c = T_{ci}^{\uparrow} - T_{ci}^{\downarrow}$) of $\Delta T_{c1}$ = 9 (8) K and $\Delta T_{c2}$ = 15 (9) K for **1$^{Pt}$·H$_2$O** (**1$^{Pd}$·H$_2$O**). Hence, the SCO curves of **1$^{Pt}$·H$_2$O** and **1$^{Pd}$·H$_2$O** define a plateau in the temperature range 184-205 K and 175-205 K, respectively, where, accordingly to the structural data, a HS-LS mixed state is present.

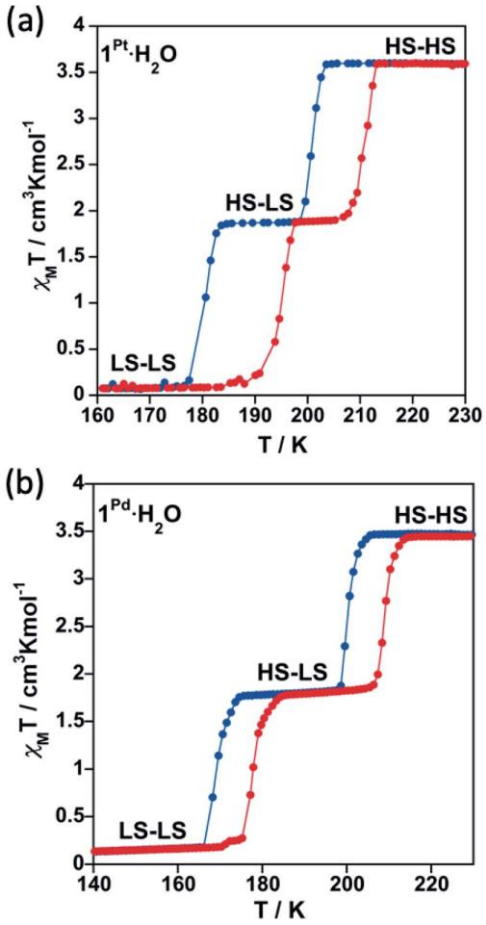


**Fig. 3.** SCO behaviour expressed as $\chi_M T$ *vs. T* plots recorded at 2 K $min^{-1}$ for (a) **$1^{Pt}$·$H_2O$** and (b) **$1^{Pd}$·$H_2O$**. Cooling and heating modes are highlighted in blue and red, respectively.

### 2.3.2.- Guest exchange properties ($1^M$·$H_2O$↔$1^M$↔$1^M$·guest)

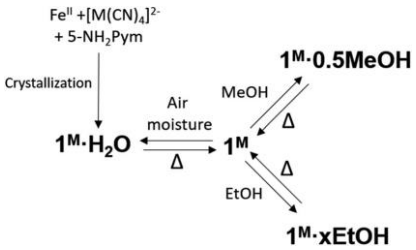


**Scheme 2.** Scheme of the main chemical transformations reported in this work.

Based on the thermogravimetric analysis (TGA) (Fig. S1a and b), **1$^{Pt}$** and **1$^{Pd}$** solvent-free single crystals were prepared by removing the included water molecule from the corresponding **1$^{Pt}$·H$_2$O** and **1$^{Pd}$·H$_2$O** counterparts through thermal treatment at 400 K for 30 minutes. The anhydrous derivatives spontaneously uptake water from atmospheric moisture yielding the primitive hydrated **1$^{Pt}$·H$_2$O** and **1$^{Pd}$·H$_2$O** derivatives (See Scheme 2) To in depth analyse this behaviour, water adsorption isotherms were performed for **1$^{Pt}$** and **1$^{Pd}$**. These compounds do not show significant water adsorption below a vale of relative pressure, $P/P_0$, equal to 0.02 for **1$^{Pt}$** and 0.08 for **1$^{Pd}$** (see Fig. 4a and c and the corresponding enlarged plots in Fig. 4b and d). Above this threshold value, a sigmoidal adsorption profile takes place first rapidly reaching a covering value of 0.83 and 0.90 mol $H_2O$/mol Fe for **1$^{Pt}$** and **1$^{Pd}$**, respectively, and then more gradually to reach a value of *ca.* 1 mol $H_2O$/mol Fe at $P/P_0$ = 0.6. This result suggests a gate-opening mechanism in which the adsorption process is accompanied by a drastic cooperative crystallographic transformation. Indeed, the resulting curve corresponds to a Type F-IV adsorption profile typical for flexible compounds exhibiting non-porous to porous structural transitions.[22]

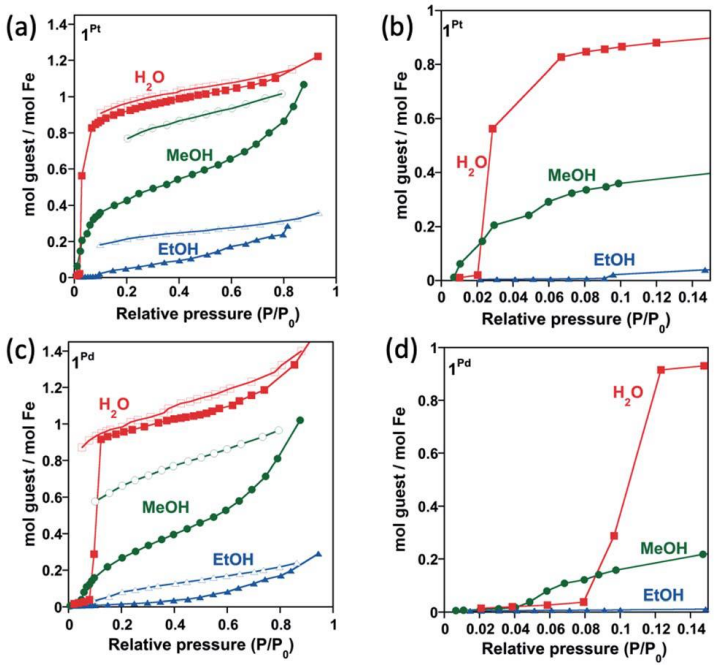


**Fig. 4.** Water, methanol and etanol isothermal adsorption (full points) and desportion (open points) curves for **1$^{Pt}$** and **1$^{Pd}$** in (a and c) full scale and (b and d) the corresponding enlarged plots at low pressures range (desorption curves are omitted in the low pressures centred curves).

In subsequent SCSC transformations, desorbed **1$^{Pt}$** and **1$^{Pd}$** crystals soaked in MeOH or EtOH for a period of 3 h afforded crystals of **1$^{M}$·0.5MeOH** and **1$^{Pd}$·*x*EtOH** (M = Pt, Pd, x = 0.25-0.4) (see Scheme 2). According to the corresponding TGA, a maximum of 0.5 molecules of MeOH per $Fe^{II}$ are trapped within the structure of **1$^{M}$** whereas *ca.* 0.4 molecules of ethanol was included in **1$^{Pt}$** (**1$^{Pt}$·0.4EtOH**). However, only 0.25 molecules of ethanol were foun in **1$^{Pd}$** (**1$^{Pd}$·0.25EtOH**) (Fig. S1c-f). Given the non-porous nature of **1$^{Pt}$** and **1$^{Pd}$**, and due to the larger molecular volume of MeOH, and especially of EtOH, their adsorption isotherms reflect much higher steric hindrance for these guests than for $H_2O$, thereby requiring higher $P/P_0$ values to include amounts close to the ones found for soaked crystals. Interestingly, the MeOH adsorption isotherm for **1$^{Pd}$** also displays a clear sigmoidal shape with a threshold relative pressure of 0.04 $P/P_0$ (see Fig. 4d) reflecting a Type F-III adsorption profile ascribed to a gradual non-porous to porous structural switching.[22] Indeed, this threshold value is even lower than that of $H_2O$ and the same trend is observed for the Pt derivative (0.01 $P/P_0$ for MeOH *vs.* 0.02 for water) (Fig. 4b). In addition, the desorption isotherm profiles for the MeOH and EtOH derivatives are significantly different to the adsorption ones defining a marked hysteretic behaviour. This fact contrasts with the water uptake whose adsorption/desorption profiles are very close to each other. All these observations suggest that the host clathrates exhibit higher chemical affinity for MeOH than for $H_2O$ at very low guest pressures and, although relatively stron interactions seem to be stablished with EtOH, its higher molecular volume may prevent an efficient adsorption. Similar results describing lower adsorption pressures for MeOH and EtOH than for $H_2O$ in non-SCO 2D framework have been reported an ascribed to the presence of hydrophobic interactions.[23]

Time-dependent thermogravimetric studies of **1$^{M}$** under water, methanol or ethanol vapors are consistent with the results described above. With the aim of extracting the kinetic parameters associated with the adsorption processes, the quantity of adsorbed guest as a function of time was fitted to the Avrami equation[24] ($\alpha = A(1 - \exp\{-K_{av}t^{n}\})$) (see Fig. S4 and Table S3). As expected regarding the adsorption isotherms, the Pt derivative presents higher amounts of adsorbed guest (A) and higher adsorption kinetic constants ($K_{av}$) than the Pd one. In addition, for a given derivative (**1$^{Pt}$** or **1$^{Pd}$**), the adsorption kinetic constants are higher for MeOH and EtOH than for water, suggesting a stronger affinity by the host framework for the formers. However, the *n* parameter, which accounts for the cooperativity of the process, indicates that the adsorption event is more cooperative for water than for the alcohol

molecules. Furthermore, for a given guest molecule, *n* is higher for the Pd derivative than for the Pt derivative).

### 2.3.3.- Guest exchange-induced structural modifications

Single crystal X-ray diffraction measurements were performed in order to assess the structural modifications involved upon subsequent guest exchanges (**$1^{M}\cdot H_2O \leftrightarrow 1^{M} \leftrightarrow 1^{M}\cdot$guest**). Furthermore, each compound was measured at temperaturs in which the different spin states (HS, LS and/or mixed ⋯HS-LS⋯) manifest according to the magnetic properties (*vide infra*) Crystals of **$1^{Pt}\cdot H_2O$** and **$1^{Pd}\cdot H_2O$** were *in situ* heated in the diffractometer at 400 K in order to remove the guest water molecule, thereby yielding the corresponding **$1^{Pt}$** and **$1^{Pd}$** dehydrated phases. The water-free structures of **$1^{Pt}$** and **$1^{Pd}$** were then successfully determined at 260 K (HS) and 120 K (LS). In a subsequent step, **$1^{Pt}$** and **$1^{Pd}$** were loaded with MeOH to give **$1^{Pt}\cdot$0.5MeOH** and **$1^{Pd}\cdot$0.5MeOH** and the crystallographic data of freshly prepared crystals collected at 260 K (HS-HS) and 100 K (HS-LS). The ethanol derivatives were prepared in a similar way. In particular, **1Pt·0.4EtOH** was analysed at 260 K (HS-HS) and 100 K (HS-LS). However, the low quantity of ethanol adsorbed by **$1^{Pd}$** led to mixed crystallographic phases that prevented the proper resolution of the structure of **$1^{Pd}\cdot$0.25EtOH**. The main crystallographic parameters of the discussed structures are displayed in Tables S1, S2, S4 and S5.

### 2.3.4.- Structure of $1^{Pt}$ and $1^{Pd}$

Removal of the included water molecule from $1^{M}\cdot H_2O$ (**$1^{M}\cdot H_2O \rightarrow 1^{M}$**) involves a crystallographic phase transformation from the monoclinic *C2/m* to the orthorhombic *Pnma* space group. Although the layered structure of **$1^{M}$** is comparable to that of the hydrated monoclinic phase, the loss of water is accompanied by noticeable structural modifications (Fig. 5): (i) Only one type of $Fe^{II}$ ion, axially coordinated by two crystallographically distinct 5-$NH_2$Pym ligands, is now observed; (ii) one of the two axial 5-$NH_2$Pym is rotated 180º in such a manner that they adopt a *cis* conformation with respect to the orientation of the amine groups; (iii) the void space generated upon desorption of water molecules is minimized by subtle reccomodaton of the bimetallic layers whose undulated corrugation is more noticeable and regular. Indeed, the equatorial plane around Fe1 defines an anglewith the $[M(CN)_4]^{2-}$

plane of 12.14º (M = Pt) and 14.95º (M = Pd) in the LS state but increases considerably up to 24.67º (M = Pt) and 29.59º (M = Pd) in the HS; (iv) the absence of included water molecules prevents the formation of the H-bonding chains observed for **$1^{Pt}\cdot H_2O$** and **$1^{Pd}\cdot H_2O$**. Instead, only one intralayer H-bond interaction (N6···N7) is established between adjacent 5-$NH_2$Pym ligands (Fig. 5 and Table 1).

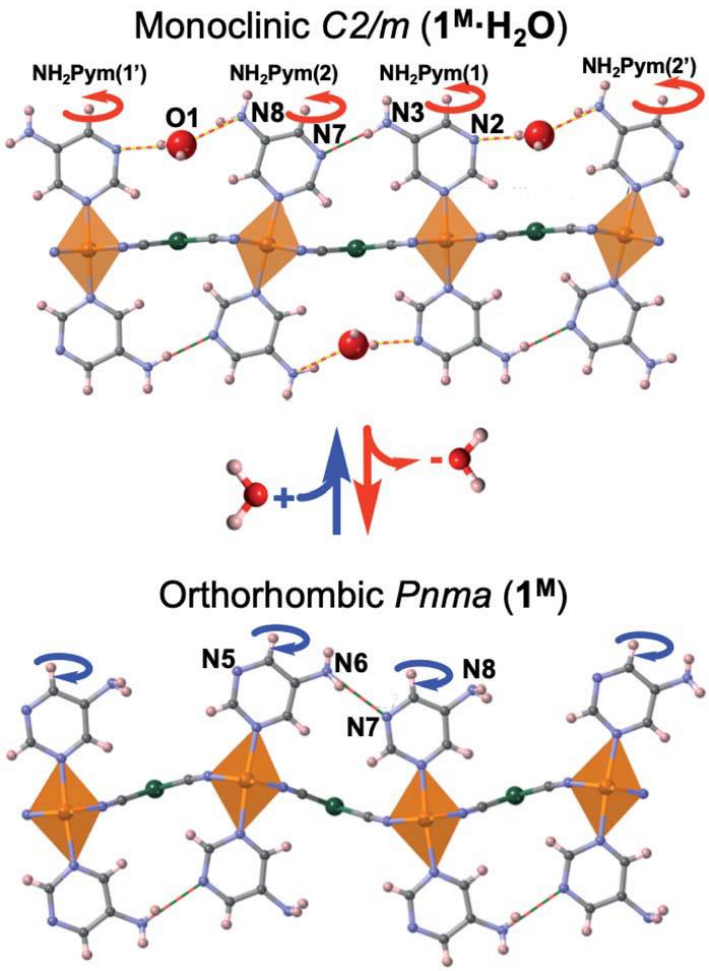


**Fig. 5.** Views along the [010] direction of a bimetallic layer of **$1^{M}\cdot H_2O$** (up) and **$1^{M}$** (down) at 260 K (M = Pt, Pd). Red/blue curved arrows indicate the 180º rotation of the 5-$NH_2$Pym ligands occurring along with the dehydration/hydration processes (discontinuous yellow-red and red-green lines represent host-guest and host-host H-bonds).

At 260 K, the [$FeN_6$] average bond length [2.161 and 2.158 Å for **$1^{Pt}$** and **$1^{Pd}$**, respectively] is consistent with 100% of the $Fe^{II}$ ions in the HS state. When cooling to 120 K, the structures remain in the *Pnma* space group but the [$FeN_6$] average bond length decreases to 1.950 Å for **$1^{Pt}$** and 1.960 Å for **$1^{Pd}$**, consistentluy with a complete HS-to-LS transition, also reflected by the observed yellow to red colour change. It is important to note that, according to the powder X-ray diffraction (Fig. S5), the spontaneous redsorption of water from air moisture (**$1^{M} \rightarrow 1^{M}\cdot H_2O$**) shows complete structural reversibility recovering the original **$1^{M}\cdot H_2O$** frameworks.

### 2.3.5.- Structure of $1^{Pt}\cdot$0.5MeOH and $1^{Pd}\cdot$0.5MeOH

The **$1^{M} \rightarrow 1^{M}\cdot$0.5MeOH** adsorption process involves a crystallographic phase change from the orthorhombic *Pnma* to the orthorhombic *Pbcm* space group. Overall, **$1^{Pt}\cdot$0.5MeOH** and **$1^{Pd}\cdot$0.5MeOH** present the ame general structure as their water counterparts (**$1^{Pt}\cdot H_2O$** and **$1^{Pd}\cdot H_2O$**) but the asymmetric unit is constituted, in addition to two different [$Fe^{II}N_6$] centres, of two inequivalent 5-$NH_2$Pym per $Fe^{II}$ and two distinct $[M^{II}(CN)_4]^{2-}$ bridging units (Fig. S6). As in **$1^{Pt}\cdot H_2O$** and **$1^{Pd}\cdot H_2O$**, the two 5-$NH_2$Pym apical ligands coordinated to a given $Fe^{II}$ centre display a *trans* conformation with respect to the amine group orientation revealing that 50% of the axial ligands undergoes a 180º rotation upon MeOH adsorption. Similarly to **$1^{M}\cdot H_2O$**, the bimeallic layers ase slightly corrugated as shown by the angles defined between consecutive equatorial planes of the metallic centres [Fe1-M1/Fe2-M1/Fe1-M2/Fe2-M2] being equal to [1.96º (2.27º)/13.24º (17.59º)/1.01º (0.25º)/16.22º (15.07º)] for **$1^{Pt}\cdot$0.5MeOH** and [1.43º (1.28º)/ 15.70º (14.15º)/1.25º (2.12º)/14.02º (17.56º)] **$1^{Pd}\cdot$0.5MeOH** in the LS and (HS) states, respectively. This irregular corrugation seems also to be guided by the formation of host-host and host-guest H-bonds. The bimetallic layers are now stacked along the (010) direction generating an array of two inequivalent 1D interlayer channels, running along the (001) direction and delimited by the $M^{II}(1)$ or $M^{II}(2)$ centres, respectively. These channels host an average of *ca*. 0.5 molecules of MeOH per $Fe^{II}$ (Fig. S7) in good agreement with the thermogravimetric analysis (Fig. S1c and d). The corresponding oxygen atom interacts *via* H-bonding with both the non-coordinated nitrogen heteroatom and the amino group of the apical 5-$NH_2$Pym ligands (Table 1). The much narrower channels created between the bimeallic layers are blocked by the (Pym)$NH_2\cdots$N(Pym)$NH_2$ hydrogen bonds.

At 260 K, the average Fe1-N/Fe2-N bond lengths (2.174 Å/2.166 Å and 2.175 Å /2.173 Å for **$1^{Pt}$·0.5MeOH** and **$1^{Pd}$·0.5MeOH** (respectively) are consistent with a fully populated HS state. When cooling down to 100 K, the crystal retains the orthorhombic *Pbcm* space group and undergoes a yellow-to-dark orange color change indicating the occurrence of a HS-to-LS change. Indeed, although the Fe1 site remains in the HS state (Fe1-N average distance = 2.174 Å (260 K) *vs.* 2.164 Å (100 K)/ 2.175 Å (260 K) *vs.* 2.154 Å (100 K) for **$1^{Pt}$·0.5MeOH** and **$1^{Pd}$·0.5MeOH**), Fe2 undergoes a complete switch to the LS state (Fe2-N average distance = 2.166 Å (260 K) *vs.* 1.984 Å (100 K)/2.173 Å (260 K) *vs*. 1.985 Å (100 K) for **$1^{Pt}$·0.5MeOH** and **$1^{Pd}$·0.5MeOH**) giving rise to an ordered ···HS-LS··· state. The packing of the layers becomes slightly denser during the SCO event as it is reflected by the decrease of between the average planes, defined by the undulated cyano-bridged bimetallic layers, from 8.197 Å/8.097 Å to 7.997 Å/7.987 Å for **$1^{Pt}$·0.5MeOH** and from 8.185 Å/8.138 Å to 8.070 Å/8.013 Å for **$1^{Pd}$·0.5MeOH**. Powder X-ray diffraction measurements have confirmed the structural reversibility of the methanol adsorption since the resulting pattern of the solid upon heating (**$1^{M}$·0.5MeOH→$1^{M}$**) coincides with that initially registered for the dehydrated compound (**$1^{M}$·$H_2O$→$1^{M}$**) (Fig. S8).

### 2.3.6.- Structure of $1^{Pt}$·0.4EtOH

The adsorption of ethanol in **$1^{Pt}$** provokes a crystallographic phase transition from the orthorhombic *Pnma* to the monoclinic *I2/m* space group. The structure of **$1^{Pt}$·0.4EtOH** is homologous to that of **$1^{M}$·$H_2O$** the main difference residing in the distinct nature of the included guests. Hence, in excellent accord with the TGA (Fig. S1e), 0.4 molecules of ethanol are located within the 1D channels in such a way that they form hydrogen bonds with both the amino and the heterocyclic N atom of adjacent 5-$NH_2$Pym ligands (Table 1).

At 260 K, the Fe1-N/Fe2-N average distances are 2.164/2.168 Å, thereby reflecting a fully populated HS state. When cooling to 100K, these distances change to 2.112/1.987 Å revealing that whereas the *ca.* 70% of the Fe1 centes remain in the HS state, the Fe2 centres undergo a complete transition to the LS state. Table 2 gathers the Fe-N average distances and the octahedral distortion parameters at each temperature for all the studied structures.

**Table 2.** Octahedral distortion parameters (Θ and ∑) at different temperatures and the associated Fe-N average distances for $1^{Pt}\cdot H_2O$ and $1^{Pd}\cdot H_2O$. (Θ is defined as $\sum_{i=1}^{i=24}(60-\theta_i)$ being $\theta_i$ the angle generated by superposition of two opposite faces of the octahedron there are four pairs of such superposition with six $\theta_i$ values each one). ∑ represents octahedron distortion defined as the sum of deviations from 90º of the 12 *cis* N-Fe-N angles in the coordination sphere $\sum_{i=1}^{i=12}(\varphi_i-90)$

| Sample | $1^{Pt}$ | | $1^{Pt}\cdot H_2O$ | | | | | |
|---|---|---|---|---|---|---|---|---|
| *T (K)* | 260 | 120 | 260 | | 187 | | 100 | |
| Spin state | HS | LS | Fe1(HS) | Fe2(HS) | Fe1(LS) | Fe2(HS) | Fe1(LS) | Fe2(LS) |
| Fe-N (Å) | 2.161 | 1.950 | 2.159 | 2.164 | 1.965 | 2.140 | 1.948 | 1.955 |
| Θ/∑ | 39/17.9 | 20.1/8.4 | 22/11.6 | 39/22.8 | 21/12.0 | 43/29.6 | 17/14.0 | 30/20.4 |
| Sample | $1^{Pd}$ | | $1^{Pd}\cdot H_2O$ | | | | | |
| *T (K)* | 260 | 120 | 260 | | 180 | | 100 | |
| Spin state | HS | LS | Fe1(HS) | Fe2(HS) | Fe1(LS) | Fe2(HS) | Fe1(LS) | Fe2(LS) |
| Fe-N (Å) | 2.158 | 1.960 | 2.168 | 2.174 | 1.987 | 2.156 | 1.961 | 1.963 |
| Θ/∑ | 52/23 | 18.7/9.2 | 16/4.8 | 28/14.8 | 19/9.2 | 33/25.2 | 14/5.6 | 29/13.2 |
| Sample | $1^{Pt}\cdot 0.5MeOH$ | | | | $1^{Pd}\cdot 0.5MeOH$ | | | |
| *T (K)* | 260 | | 100 | | 260 | | 100 | |
| | Fe1(HS) | Fe2(HS) | Fe1(HS) | Fe2(LS) | Fe1(HS) | Fe2(HS) | Fe1(HS) | Fe2(LS) |
| Fe-N (Å) | 2.174 | 2.166 | 2.164 | 1.984 | 2.174 | 2.173 | 2.155 | 1.986 |
| Θ/∑ | 29/4.7 | 28/19.7 | 37/17.6 | 26/9.7 | 32/8.4 | 28/22.4 | 32/18.0 | 25/11.9 |
| Sample | $1^{Pt}\cdot 0.5MeOH$ | | | | | | | |
| *T (K)* | 260 | | 100 | | | | | |
| | Fe1(HS) | Fe2(HS) | Fe1(HS) | Fe2(LS) | | | | |
| Fe-N (Å) | 2.164 | 2.166 | 2.112 | 1.986 | | | | |
| Θ/∑ | 17/7.2 | 36/22.8 | 34/16.4 | 22/15.6 | | | | |

### 2.3.7.- Guest-dependent SCO properties of $1^{M}$

Compounds **$1^{Pt}$·$H_2O$** and **$1^{Pd}$·$H_2O$** were dehydrated *in situ* in the SQUID chamber at 400K for one hour to afford **$1^{Pt}$** and **$1^{Pd}$** and their $\chi_M T$ *vs. T* curves subsequently recorded (see Fig. 6a and b, respectively). The resulting spin transitions remain abrupt and complete although they occur in a single step. In the case of the Pt derivative the critical temperature increases ($T_c$ = 218 K, $\Delta T_c$ = 10 K) with respect to those of the hydrated counterpart. In contrast, for **$1^{Pd}$**, the critical temperature ($T_c$ =196.5 K, $\Delta T_c$ = 9 K) lies roughly in between the two hysteresis loops displayed by **$1^{Pd}$·$H_2O$**. Importantly, as mentioned above, **$1^{M}$** recover the water molecule when exposed to air moisture yielding the initial **$1^{M}$·$H_2O$** compounds and showing full reversibility of the SCO properties (Fig. S9).

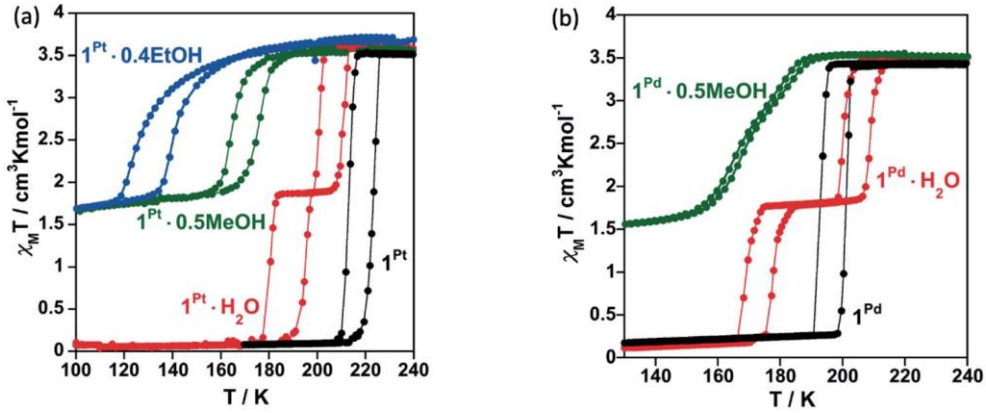


**Fig. 6.** SCO behaviour for (a) **$1^{Pt}$**, **$1^{Pt}$·0.5MeOH** and **$1^{Pt}$·0.4EtOH** and (b) **$1^{Pd}$** and **$1^{Pd}$·0.5MeOH** (scan rate: 2 K min$^{-1}$). Spin transition curves of hydrated compounds (**$1^{Pt}$·$H_2O$** and **$1^{Pd}$·$H_2O$**) are also displayed for comparison.

The SCO properties of **$1^{Pt}$·0.5MeOH**/**$1^{Pt}$·0.4EtOH** and **$1^{Pd}$·0.5MeOH** are displayed in Fig. 6a and b, respectively. The adsorption of MeOH induces a significant decrease of the SCO temperatures and whereas the transition remains cooperative displaying a one-step hysteretic curve ($\Delta T_c$ = 10 K) with $T_c$ = 170 K for **$1^{Pt}$·0.5MeOH**, it exhibits a very subtle two-step behaviour centres at similar temperatures ($T_c$ = 170.5 K) with a narrow hysteresis ($\Delta T_c$ = 3 K) for **$1^{Pd}$·0.5MeOH**. The inclusion of ethanol in **$1^{Pt}$** (compound **$1^{Pt}$·0.4EtOH**) induces an even further decrease of the spin crossover temperatures than the methanol does ($T_c$ = 131.5 K) while conserving a 13 K hysteresis wide. The $\chi_M T$ values recorded at 100 K (1.70/1.43/1.63 cm$^3$ K mol$^{-1}$ for **$1^{Pt}$·0.5MeOH**/**$1^{Pd}$·0.5MeOH**/**$1^{Pt}$·0.4EtOH**) indicate, in good agreement with structural data, that the presence of MeOH or EtOH blocks *ca.* 49/41/46% of the $Fe^{II}$ ions in

the HS state. Despite durther cooling to 50 K no additional spin transition events were observed for these compounds (Fig. S10). In contrast, the $\chi_M T$ *vs. T* curve of **$1^{Pd}$·0.25EtOH** displays a more complete two-step SCO behaviour (Fig S11a). The first step is characterized by a cooperative transition with $T_{c1}$ = 191 K ($\Delta T_{c1}$ = 10K) whereas the second one shows a gradual transition with $T_{c2}$ = 146.5 K and ($\Delta T_{c2}$ = 9 K). Among the *ca.* 79% of the $Fe^{II}$ centres that are SCO-active in **$1^{Pd}$·0.25EtOH**, *ca.* 47 % undergo the spin transition in the first step and *ca.* 32% in the second step. As shown by TGA (Fig. S1e, f and S11b), the differences in the SCO properties between **$1^{Pt}$·0.4EtOH** and **$1^{Pd}$·0.25EtOH** are likelyassignable to the lower effective quantity of ethanol present in the latter (0.4 *vs* 0.25, respectively).

The SCO properties of **$1^{Pt}$**, **$1^{Pd}$**, **$1^{Pt}$·$H_2O$**, **$1^{Pd}$·$H_2O$**, **$1^{Pt}$·0.5MeOH** and **$1^{Pd}$·0.5MeOH** were also monitored through differential scanning calorimetry (DSC) at 10 K $min^{-1}$. **$1^{Pt}$·0.4EtOH** and **$1^{Pd}$·0.25EtOH** were not analysed by this technique since their corresponding spin transitions are out of the temperature window of our calorimeter. As depicted in Fig. S12, DSC measurements reproduce very well the SCO behaviour observed for the different samples in the magnetic studies. For example, calorimetric curves of the dehydrated (**$1^{M}$**) and hydrated (**$1^{M}$·$H_2O$**) compounds show one and two singularities during both the heating and cooling modes confirming single and double stepped SCO behaviours, respectively. In addition, the $\Delta H/\Delta S$ (kJ $mol^{-1}$/J $K^{-1}$ $mol^{-1}$) parameters are 14.63/74.86, 18.06/82.32, 17.49/88.14 and 16.49/86.52 for **$1^{Pt}$**, **$1^{Pd}$**, **$1^{Pd}$·$H_2O$** and **$1^{Pd}$·$H_2O$**, respectively, in good agreement with the values typically displayed by Hofmann-like $Fe^{II}$ compounds featuring cooperative a complete SCO behaviours.[4a] In contrast, **$1^{Pt}$·0.5MeOH** and **$1^{Pd}$·0.5MeOH** present $\Delta H/\Delta S$ (kJ $mol^{-1}$/J $K^{-1}$ $mol^{-1}$) values of 7.64/40.09 and 7.10/41.40 consistent with *ca.* 50% blocking of the spin transition as detected in the corresponding magnetic measurements.

## 2.4.- Discusion

The adsorption isotherms indicate different sorption capabilities for **$1^{Pt}$** and **$1^{Pd}$** derivatives. Indeed, under the same conditions, **$1^{Pt}$** adsorbs a higher amount of guest and with faster kinetics than **$1^{Pd}$** (see Fig. 4, S4 and Table S3). It is worth mentioning that **$1^{Pt}$** and **$1^{Pd}$** desolvated forms do not present intrinsic porosity and, therefore, the uptake process occurs concomitantly to noticeable structural modifications which enable the entry of guests giving place to a gate opening adsorption mechanism. Although related phenomena have been reported for 0D[25] and 1D[26] Co(II) SCO systems, the lack of precise structural data

associated to the uptake processes prevented direct information about its origin. Kitagawa *et al.* showed a gate-opening effect on 2D nanometric thin films of {Fe(Pyridine)$_2$[Pt(CN)$_4$]} revealing that, upon adsorption, the guest molecules are hosted by inducing separation between the stacked 2D layers.[27] In contrast to the latter related example, our results here described disclose that the mechanism of structural reaccommodation upon guest sorption/desorption involves a 180º rotation of 50% of the 5-NH$_2$Pym axial ligands which seems to facilitate diffusion of the guest throughout the channels. Similar "revolving door" effect has been observed in discrete[28] and 1D[29] SCO systems. Another relevant structural change accompanying the guest uptake involves breaking the N6···N7 H-bond operating between the amino group and the non-coordinated nitrogen of adjacent 5-NH$_2$Pym ligands (Fig. 5). Once the energy barrier of this rupture process is overcome the adsorption occurs in a cooperative one-step fashion revealing the gate-opening nature. Thus, the rupture of this interaction may determine the adsorption profile for each derivative. As a consequence, the slower adsorption regime of **1$^{Pd}$** with respect to **1$^{Pt}$** may be attributed to the stronger N6···N7 H-bond interaction of the former (Table 1). Furthermore, the accessible pore volumes calculated with PLATON for the corresponding **1$^{M}$·guest** structures (Table S6) are slightly higher for Pt than for Pd derivatives, which probably facilitates the uptake and dissemination of guest molecules within the former.

The insertion of hydroxylic guest molecules in **1$^{M}$** promotes different degrees of local distortion in the 2D framework, which are responsible for the formation of non-equivalent Fe$^{II}$ and M$^{II}$ (M$^{II}$ = Pt, Pd) centres. The unsolvated **1$^{M}$** derivatives, constituted of homogeneously corrugated 2D layers with a minimum degree of distortion (maximum symmetry), feture only one crystallographic Fe$^{II}$ (and M$^{II}$) site and show the occurrence of similar one-step complete cooperative SCO for M$^{II}$ = Pt, Pd derivatives. In contrast, the inclusion of water distorts the layers generatinf two different centrosymmetric Fe$^{II}$ sites in **1$^{M}$·H$_2$O** with different degrees of octahedral $\sum$ and $\Theta$ distortions (see Table 2). The less distorted Fe1 site is more prone to exhibit SCO than that of Fe2 giving rise to the stabilization of an ordered intermediate mixed spin state ···LS(Fe1)-HS(Fe2)-LS(Fe1)···. The inclusion of MeOH or EtOH provokes further asymmetry in the **1$^{M}$·0.5MeOH** and **1$^{Pt}$·0.4EtOH** layers reflected on the occurrence of two crystallographically different [M(CN)$_4$]$^{2-}$ centres and the loss of centrosymmetry in the Fe1 and Fe2 sites. Consequently, the SCO conversion occurs at lower temperatures involving essentially 50% of the Fe$^{II}$ centres. Although the down-shift of the $T_c$ parallels the increase of the guest size, the electronic factors may also play an important role (*vide infra*). Surprisingly,

the Fe1 site, which undergoes SCO first in **$1^{M}\cdot H_2O$** remains HS in **$1^{M}\cdot$0.5MeOH/$1^{Pt}\cdot$0.4EtOH** even at 100K, in spite of being surrounded by a less distorted octahedron (Table 2).

However, the Fe2 site is SCO-active observing a complete HS → LS transition. In fact, pressure experiments carried out over **$1^{Pt}\cdot$0.5MeOH** demonstrate that whereas the $T_c$ value of the Fe2 centre increases markedly with pressure, the pressure dependence of the SCO experienced by the Fe1 site is more moderate being almost complete only with pressures above 1.76 kBar (Fig. S13). This singular situation can be associated with the fact that the oxygen aom of water and alcohol guests occupy different specific sites within the interlayer channels (Fig. 7). Indeed, the arrangement of methanol and ethanol molecules in the cavities tends to optimize the attractive interactions (H-bond) and minimize the repulsive contacts between the aliphatic part of the alcohol and the host network. Therefore, the water and the alcohol molecules display differences in the H-bond distances with the host 5-$NH_2$Pym ligands (Table 1). More precisely, the methanol and ethanol molecules afford stronger H-bonds (shorter distances) than the water molecule with the non-coordinated N2 atom of the pyrimidine moiety, which is directly connected to the Fe1 sites. This fact explains the higher affinity to alcohols suggested by the adsorption isotherms, time-dependent TGAs and the hysteretic behaviour defined by their desorption isotherms. Since this H-bond withdraws electron density from the pyrimidine ring, it is reasonable to infer a decrease of the ligand field strength around the Fe1 sites “deactivating” the SCO. Furthermore, there are additional steric reasons involving contacts between the C atom(s) of the MeOH/EtOH and the pyrimidine ring coordinatel to Fe1 [C(EtOH/MeOH)···C4(pym) and C(EtOH/MeOH)···N2(pym)] whose distances, shorter than the sum of the corresponding van der Waals radii, may also hamper the complete HS → LS transition stabilizing the mixed ···LS(Fe2)-HS(Fe1)-LS(Fe2)··· states. It is worthwhile emphasizing that the SCO behaviour of [Fe2$N_6$] site remains mostly unaltered presenting very similar SCO temperatures when interacting with water or methanol, however, they decrease markedly with ethanol. In the case of **$1^{Pd}\cdot$0.25EtOH**, the low quantity of adsorbed ethanol seems to affect only a small fraction of $Fe^{II}$ sites (*ca*. 32%) lowering their SCO temperature whereas the most part of the $Fe^{II}$ sites (47%) exhibit SCO temperatures reminiscent of the **$1^{Pd}$** unsolvated compound. This situation is reflecter when observing the powder X-Ray diffraction of **$1^{Pd}\cdot$0.25EtOH** soaked in ethanol, as the main intense peaks are those corresponding to the “empty” compound whereas only some less intense peaks correspond to the ehanol containing clathrate (Fig. S14)

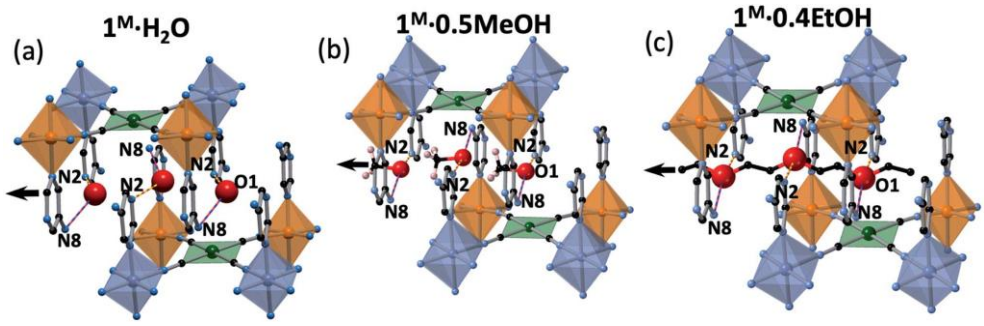


**Fig. 7.** View of a fragment of two consecutive layers emphasising the specific sites occupied by the guests, (a) $H_2O$, (b) MeOH and (c) EtOH, within the 1D channels which follow the orientation indicated by the black arrow. Hydrogen bonds are marked as bicolour blue-red lines for N8···O1 and yellow-red for N2···O1. Atom colour code: Fe1 (blue octahedrons), Fe2 (orange octahedrons), N (blue), M (green), C (black). Note that one out of two possible positions found for the MeOH is shown.

Finally, in order to qualitatively assess the selectivity properties of **$1^M$** against the adsorption of $H_2O$, MeOH and EtOH, freshly dehydrated **$1^M$·$H_2O$** samples were immersed overnight in solvent mixtures of $H_2O$ : MeOH, MeOH : EtOH or $H_2O$ : EtOH (1:1 in volume) and the SCO properties of the yielded solvates measured in the SQUID magnetometer. The results show that when soaking **$1^M$** either in $H_2O$ : MeOH or MeOH : EtOH mixtures the recorded SCO curves are reminiscent of those of **$1^M$·0.5MeOH** (Fig. S15) indicating a higher tendency to adsorb MeOH over the other molecules. On the other hand, the magnetic properties of **$1^M$**, recorded after being soaked in $H_2O$ : EtOH mixtures, display 2-stepped SCO profiles characteristic of **$1^M$·$H_2O$** derivatives (Fig. S15) suggesting that water moleculeshave been mostly adsorbed in this case. These results are in good agreement with that expected from the adsorption isotherms and X-ray diffraction data which predict higher chemical affinity to MeOH than $H_2O$ and higher selectivity of $H_2O$/MeOH against EtOH. The former observation may be associated to the stronger host-Guest interactions stablished with MeOH whereas the latter can be interpreted as a molecular size-based exclusion in which the adsorption of the larger EtOH molecules may be hampered by steric effects. Overall, the adsorption selectivity showed by **$1^M$** follows the tendency MeOH > $H_2O$ > EtOH.

## 2.5.- Conclusion

In conclusion, SCSC transformations in the new family of 2D HCPs formulated {Fe(5-NH2Pym)2[MII(CN)4]}·G (1M·G, M = Pt or Pd, G = H2O, MeOH or EtOH) have revealed reversible and controllable guest-dependent structural transformations coupled to drastic

SCO changes. The dual donor-acceptor nature of the 5-$NH_2$Pym axial ligands affords a singular array of intra-layer H-bond interactions. In the guest free **$1^M$** derivative, these interactions involve 50% of the amino groups and non-coordinated N atoms of the 5-$NH_2$Pym ligands coordinated to adjacent [$FeN_6$] sites, thereby conferring strong undulation to the layered structure. The remaining 50% of $NH_2$/N(pym) pairs, structurally disabled to define mutual H-bonds, generate functionalized void spaces potentially suitable for small ROH hydroxylic solvents. Indeed, the exposition of the essentially non-porous **$1^M$** derivatives to $H_2O$, MeOH or EtOH induces a gate-opening adsorption mechanism which involves important structural reorganizations including 180º rotation of the 5-$NH_2$Pym ligands, flattening of the layers and creation of host-guest H-bonds facilitating the migration of the trapped molecules. Importantly, the adsorption capabilities of **$1^M$** depend not only on the nature of the guest molecule and that of the host framework (M = Pt or Pd) conferring selectivity properties to the system, but also on their reciprocal interactions. These mutual interactions in turn affect the $Fe^{II}$ environments and determine varying and predictable SCO behaviours. The interplay between SCO and gate-opening adsorption, together with their likely suitability to be processed as nanometric thin films, as other related compounds,[21,27,30] evidence the potential of the reported 2D amino-funtionalized HCPs for sensing and/or gas separation applications.

## 2.6.- Experimental section

### Materials and reagents

All reagents and solvents used, including the 5-aminopyrimidine ligand, were obtained from commercial sources and used as received without further purification.

### Synthetic procedure

Single crystals of {Fe(5-$NH_2$pmd)$_2$[Pt(CN)$_4$]}·$H_2O$ and {Fe(5-$NH_2$pmd)$_2$[Pd(CN)$_4$]}·$H_2O$ (**$1^{Pt}$·$H_2O$** and **$1^{Pd}$·$H_2O$**) were grown by slow liquid diffusion in a double H-shaped tube. A small amount of Fe($BF_4$)2·6H2O (33.7 mg, 0.1 mmol) was deposited on one side, while the other positions were occupied by 5-aminopyrimidine (20.0 mg, 0.2 mmol) and $K_2$[Pd(CN)$_4$] or $K_2$[Pt(CN)$_4$] (34.1 mg or 43.1 mg, 0.1 mmol). The tube was filled with $H_2O$ (ca. 10 mL). The tube was then sealed and left undisturbed for 4 weeks, after that time yellow plate single crystals appeared in 70% yield. Elemental Analysis: Calculated for **$1^{Pt}$·$H_2O$** [$C_{12}H_{12}FeN_{10}OPt$ (563.23) (%)]: C 24.87, H 2.15, N 24.87 Found (%): C 25.24, H 2.21, N 24.09; Calculated for **$1^{Pd}$·$H_2O$** [$C_{12}H_{12}FeN_{10}OPd$ (474.6) (%)]: C 30.37, H 2.55, N 29.52. Found (%): C 30.71, H 2.63, N 29.11.

**$1^{Pt}$** and **$1^{Pd}$** desolvated compounds were obtained by introducing crystals of **$1^{Pt}$·H2O** and **$1^{Pd}$·H2O** in an oven at 400K for 30 minutes. **$1^{Pt}$·0.5MeOH**, **$1^{Pd}$·0.5MeOH**, **$1^{Pt}$·0.4EtOH** and **$1^{Pd}$·0.25EtOH** were achieved by submerging freshly prepared **$1^{Pt}$** and **$1^{Pd}$** compounds in a bath of the corresponding solvent for *ca*. 3 hours. In all cases the compounds are yellow plate crystals at room temperature and turn red (for hydrated and dehydrated compounds) or orange (for alcohol containing compounds) upon cooling at 100 K. Elemental Analysis: Calculated for **$1^{Pt}$·0.5MeOH** [$C_{12.5}H_{12}FeN_{10}O_{0.5}Pt$ (561.02) (%)]: C 26.75, H 2.16, N 24.96. Found (%): C 26.07, H 2.33, N 24.04; Calculated for **$1^{Pd}$·0.5MeOH** [$C_{12.5}H_{12}FeN_{10}O_{0.5}Pd$ (471.96) (%)]: C 31.77, H 2.56, N 29.64 Found (%): C 31.15, H 2.38, N 29.22; Calculated for **$1^{Pt}$·0.4EtOH** [$C_{12.8}H_{12.4}FeN_{10}O_{0.4}Pt$ (563.42) (%)]: C 27.28, H 2.22, N 24.85. Found (%): C 26.88, H 2.10, N 24.07; Calculated for **$1^{Pd}$·0.25EtOH** [$C_{12.4}H_{11.2}FeN_{10}O_{0.2}Pd$ (465.16) (%)]: C 31.98, H 2.42, N 30.07 Found (%): C 30.96, H 2.56, N 29.67.

**Physical characterization**

*Elemental analyses* (C, H, and N) were performed with a CE Instruments EA 1110 CHNS Elemental analyzer.

*Magnetic measurements* were performed with a Quantum Design MPMS-XL-5 SQUID magnetometer working in the 2 to 400 K temperature range with an applied magnetic field of 0.1 T. Experimental susceptibilities were corrected for diamagnetism of the constituent atoms using Pascal's constants.

*Calorimetric measurements* were performed using a differential scanning calorimeter Mettler Toledo DSC 821e. Low temperatures were obtained with an aluminium block attached to the sample holder, refrigerated with a flow of liquid nitrogen and stabilized at a temperature of 110 K. The sample holder was kept in a dry box under a flow of dry nitrogen gas to avoid water condensation. The measurements were carried out using around 15 mg of polycrystalline samples sealed in aluminium pans with a mechanical crimp. Temperature and heat flow calibrations were made with standard samples of indium by using its melting transition (429.6 K, 28.45 J $g^{-1}$). An overall accuracy of ±0.2 K in temperature and ±2% in the heat capacity is estimated. The uncertainty increases for the determination of the anomalous enthalpy and entropy due to the subtraction of an unknown baseline.

*Powder X-ray diffraction* measurements were performed on a PANalytical Empyrean X-ray powder diffractometer (monochromatic CuKα radiation) in capillary measurement mode. Due to the spontaneous rehydration of **$1^{Pt}$** and **$1^{Pd}$**, these samples were prepared by heating

the hydrated forms into open capillaries inside an oven at 120ºC during 1 hour and rapidly sealing them to avoid the entering of air.

*Single crystal X-ray measurements.* Single crystals were mounted on a glass fiber using a viscous hydrocarbon oil to coat the crystal and then transferred directly to the cold nitrogen stream for data collection. X-ray data were collected on a Supernova diffractometer equipped with a graphitemonochromated Enhance (Mo) X-ray Source (λ = 0.71073 Å). The program CrysAlisPro, Oxford Diffraction Ltd., was used for unit cell determinations and data reduction. Empirical absorption correction was performed using spherical harmonics, implemented in the SCALE3 ABSPACK scaling algorithm. The structures were solved by direct methods using SHELXS-2014 and refined by full matrix least-squares on $F^2$ using SHELXL-2014 (Sheldrick, G. M. Crystal Structure Refinement with SHELXL. Acta Crystallogr., Sect. C: Struct. Chem. 2015, 71, 3−8). Non-hydrogen atoms were refined anisotropically, and hydrogen atoms were placed in calculated positions refined using idealized geometries (riding model) and assigned fixed isotropic displacement parameters.

*Adsorption/desorption isotherms.* Vapor adsorption measurements were recorded on a Micromeritics 3Flex apparatus at relative pressures up to 1 bar and performed *ex situ* on **1$^{M}$**. Samples were degassed overnight at 150 ºC and 10-6 Torr prior to analysis assuring the presence of the totally desolvated **1$^{M}$** compounds. A Micromeritics' ISO Controller was used to keep the temperature constant at 293 K for the H2O, MeOH or EtOH adsorption measurements.

*TGA experiments* were carried out with a TA instruments TGA550 device equipped with a Pt/Rh oven (Tmax = 1000°C). The time dependent TGA experiments were performed by connecting the TGA apparatus to a flow mass controller. Thus, a controlled dry nitrogen flow (60 l/min) was passed through the desired solvent (water, methanol or ethanol) at room pressure and a temperature of 30°C and then the mixture (N2+solvent vapor) was driven until the TGA chamber where a previously desolvated sample **1$^{M}$** was mounted in a Pt pan.

## 2.7.- References

[1] (*a*) E. König, *Struct. Bond. (Berlin)*, 1991, **76**, 51-152; (*b*) P. Gütlich, A. Hauser and H. Spiering, *Angew. Chem. Int. Ed.*, 1994, **33**, 2024-2054; (*c*) J. A. Real, A. B. Gaspar, V. Niel and M. C. Muñoz, *Coord. Chem. Rev.*, 2003, **236**, 121-141; (*d*) P. Gütlich and G. Goodwin, Spin crossover in transition metal compound I-III, *Top. Curr. Chem.*, 2004, 233-235.

[2] J. A. Real, A. B. Gaspar and M. C. Muñoz, *Dalton Trans.*, 2005, 2062-2079.

[3] P. Gütlich, V. Ksenofontov and A. B. Gaspar, *Coord. Chem. Rev.*, 2005, **249**, 1811-1829.

[4] (*a*) S. Decurtins, P. Gütlich, P. C. Köhler, H. Spiering and A. Hauser, *Chem. Phys. Lett.*, 1984, **105**, 1-4; (*b*) A. Hauser, *Coord. Chem. Rev*., 1991, **111**, 275-290.

[5] C. Lefter, R. Tan, J. Dugay, S. Tricard, G. Molnár, L. Salmon, J. Carrey, W. Nicolazzi, A. Rotaru and A. Bousseksou, *Chem. Phys. Lett.*, 2016, **644**, 138-141.

[6] (*a*) M. C. Muñoz and J. A. Real, *Coord. Chm. Rev.*, 2011, **255**, 2068-2093; (*b*) Z.-L. Liu, Md. N. Hoque, W. Liu, J.-Y. Li, Y.-C. Chen and M.-L. Tong, *Coord. Chem. Rev.*, 2017, **335**, 28-43; (*c*) R. Ohtani and S. Hayami, *Chem.-Eur. J.*, **23**, 2236-2248.

[7] (*a*) M. D. Manrique-Juárez. S. Rat, L. Salmon, G. Molnár, C. M. Quintero, L. Nicu, H. J. Shepherd and A. Bousseksou, *Coord. Chem. Rev.*, 2016, **308**, 395-408; (*b*) K. S. Kumar and M. Ruben, *Angew. Chem. Int. Ed.*, DOI: 10.1002/ange.201911256.

[8] (*a*) M. Meneses-Sánchez, L. Piñeiro-López, T. Delgado, C. Bartual-Murgui, M. C. Muñoz, P. Chakraborty and J. A. Real, *J. Mater. Chem. C*, 202, **8**, 1623-1633; (*b*) T. Delgado, M. Meneses-Sánchez, L. Piñeiro-López, C. Barual-Murgui, M. C. Muñoz and J. A. Real, *Chem. Sci.*, 2018, **9**, 8446-8452; (*c*) B. Benaicha, K. Van Do, A. Yangui, N. Pittala, A. Lusson, M. Sy, G. Bouchez, H. Fourati, C. J. Gómez-García, S. Triki and K. Boukhedadden, *Chem. Sci.*, 2019, **10**, 6791-6798; (*d*) C. Lochenie, K. Schötz, F. Panzer, H. Kurz, B. Maier, F. Puchtler, S. Agarwal, A. Kö and B. Weber, *J. Am. Chem. Soc.*, 2018, **140**, 700-709; (*e*) C.-F. Wang, R.-F. Li, X.-Y. Chen, R.-J. Wei, L.-S. Zheng and J. Tao, *Angew. Chem.*, *Int. Ed.*, 2015, **54**, 1574-1577.

[9] O. Sato, Z.-Y. Li, Z.-S. Yao, S. Kang and S. Kanegawa, in *Spin-Crossover Materials*, John Wiley & Sons Ltd, 2013, pp. 303-319.

[10] (*a*) L. Piñeiro-López, M. Seredyuk, M. C. Muñoz and J. A. Real, *Eur. J. Inorg. Chem.*, 2020, 764-799; (*b*) J. -Y. Li, Y. C. Chen, Z. -M. Zhang, W. Liu, Z. -P. Ni and M. -L. Tong, *Chem.-Eur. J.*, 2015, **21**, 1645-1651; (*c*) J.-Y. Li, Z. Yan, Z.-P. Ni, Z.-M. Zhang, Y.-C. Chen, W. Liu and M.-L. Tong, *Inorg. Chem.*, 2014, **53**(8), 4039-4046; (*d*) C. Bartuel-Murgui, N. A. Ortega-Villar, H. J. Shepherd, M. C. Muñoz, L. Salmon, G. Molnár, A. Bousseksou and J. Antonio Real, *J. Mater. Chem.*, 2011, **21**, 7217-7222.

[11] J. A. Real, E. Andrés, M. C. Muñoz, M. Julve, T. Granier, A. Bousseksou and F. Varret, *Science*, 1995, **268**, 265-267.

[12] G. J. Halder, C. J. Kepert, B. Moubaraki, K. S. Murray and J. D. Cashion, *Science*, 2002, **298**, 1762-1765.

[13] Y. Garcia, V. Niel, M. C. Munoz and J. A. Real, *Top. Curr. Chem.*, 2004, **233**, 229-257.

[14] K. Otsubo, T. Haraguchi and H. Kitagawa, *Coord. Chem. Rev.*, 2017, **346**, 123-138.

[15] (*a*) Z.-P. Ni, J.-L. Liu, Md. N. Hoque, W. Liu, J.-Y. Li, Y.-C. Chen and M.-L. Tong, *Coord. Chem. Rev.*, 2017, **335**, 28-43; (*b*) R. Ohtani and S. Hayami, *Chem.-Eur. J.*, **23**, 2236-2248.

[16] M. Ohba, K. Yoneda, G. Agustí, M. C. Muñoz, A. B. Gaspar, J. A. Real, M. Yamasaki, H. Ando, Y. Nakao, S. Sakaki and S. Kitagawa, *Angew. Chem.*, *Int. Ed.*, 2009, **48**, 4767-4771.

[17] C. Bartual-Murgui, A. Akou, H. J. Shepherd, G. Molnar, J. A. Real, L. Salmon and A. Bousseksou, *Chem.-Eur. J.*, 2013, **19**, 15036-15043.

[18] (a) K. A. Zenere, S. G. Duyker, E. Trzop, E. Collet, B. Chan, P. W. Doheny, C. J. Kepert and S. M. Neville, *Chem. Sci.*, 2018, **9**, 5623; (*b*) M. M. Ndiaye, S. Pillet, E.-E. Bendeif, M. Marchivie, G. Chastanet, K. Boukheddaden and S. Triki, *Eur. J. Inorg. Chem.*, 2018, 305-313; (*c*) N. F. Sciortino, F. Ragon, Y. M. Klein, C. E. Housecroft, C. G. Davies, G. N. L. Jameson, G. Chastanet and S. M. Neville, *Inorg. Chem.*, 2018, **57**, 11068-11076; (*d*) N. F. Sciortino, K. A. Zenere, M. E. Corrigan. G. J. Halder, G. Chastanet, J.-F. Létard, C. J. Kepert and S. M. Neville, *Chem. Sci.*, 2017, **8**, 701; (*e*) M. J. Murphy. K. A. Zenere, F. Ragon, P. D. Southon, C. J. Kepert and S. M. Neville, *J. Am. Chem. Soc.*, 2017, **139**, 1330-1335; (*f*) E. Milin, V. Patinec, S. Triki, E.E. Bendeif, S. Pillet, M. Marchivie, G. Chastanet and K. Boukheddaden, *Inorg. Chem.*, 2016, **55**, 11652-11661; (*g*) N. F. Sciortino, F. Ragon, K. A. Zenere, P.D. Southon, G. J. Halder, K. W. Chapman, L. Piñeiro-Lopez, J. A. Real, C. J. Kepert and S. M. Neville, *Inorg. Chem*., 2016, **55**, 10490-10498; (*h*) Y. M. Klein, N. F. Sciortino, F. Ragon, C. E. Housecroft, C. J. Kepert and S. M. Neville, *Chem. Commun.*, 2014, **50**, 3838-3840.

[19] (*a*) F.-L. Liu and J. Tao, *Chem.-Eur. J.*, 2017, **23**, 18252-18257; (*b*) W. Liu, Y.-Y. Peng, S.-G. Wu, Y.-C. Chen, Md. N. Hoque, Z.-P. Ni, X.-M. Chen and M.-L. Tong, *Angew. Chem., Int. Ed.*, 2017, **56**, 14982-14986; (*c*) J. E. Clements, J. R. Price, S. M. Neville and C. J. Kepert, *Angew. Chem.*, *Int. Ed.*, 2016, **55**, 15105-15109; (*d*) N. F. Sciortino, K. R. Scherl-Gruenwald, G. Chastanet, G. J. Halder, K. W. Chapman, J.-F. Létard and C. J. Kepert, *Angew. Chem.*, *Int. Ed.*, 2012, **124**, 10301-10305; (*e*) G. J. Halder, K. W. Chapman, S. M. Neville, B. Moubaraki, K. S. Murray, J.-F. Létard and C. J. Kepert, *J. Am. Chem. Soc.*, 2008, **130**(51), 17552-17562.

[20] W. Liu, L. Wang, Y.-J. Su, Y.-C. Chen, J. Tucek, R. Zboril, Z.-P. Ni and M.-L. Tong, *Inorg. Chem.*, 2015, **54**, 8711-8716.

[21] C. Bartual-Murgui, V. Rubio-Giménez, M. Meneses-Sánchez, F. J. Valverde-Muñoz, S. Tatay, C. Martí-Gastaldo, M. C. Muñoz and J. A. Real, *ACS Appl. Mater. Interfaces*, 2020, **12**(26), 29461-29472.

[22] Q.-Y. Yang, P. Lama, S. Sen, M. Lusi, K.J. Chen, W.-Y. Gao, M. Shivanna, T. Pham, N. Hosono, S. Kusaka, J. J. Perry, S. Ma, B. Space, L. J. Barbour, S. Kitagawa and M. J. Zaworotko, *Angew. Chem.*, *Int. Ed.*, 2018, **57**, 5684-5689.

[23] S. Horike, D. Tanaka, K. Nakagawa and S. Kitagawa, *Chem. Commun.*, 2007, 3395-3397.

[24] M. Avrami, *J. Chem. Phys.*, 1939, **7**, 1103-1112.

[25] M. Nakaya, W. Kosaka, H. Miyasaka, Y. Komatsumaru, S. Kawaguchi, K. Sugimoto, Y. Zhang, M. Nakamura, L. F. Lindoy and S. Hayami, *Angew. Chem.*, *Int. Ed.*, 2020, **59**, 10658-10665.

[26] R. Ohtani. K. Shimayama, A. Mihima, M. Ohba, R. Ishikawa, S. Kawata, M. Nakamura, L. F. Lindoy and S. Hayami, *J. Mater. Chem. C*, 2015, **3**, 7865.7869.

[27] S. Sakaida, K. Otsubo, O. Sakata, C. SOng, A. Fujiwara, M. Takata and H. Kitagawa, *Nat. Chem.*, 2016, **8**, 377-383.

[28] L. A. Barrios, C. Bartual- Murgui, E. Peyrecave-Lleixà, B. Le Guennic, S. J. Teat, O. Roubeau and G. Aromí, *Inorg. Chem.*, 2016, **55**, 4110-4116.

[29] E. Coronado, M. Giménez-Marqués, G. Mínguez Espallargas, F. Rey and I. J. Vitórica-Yrezábal, *J. Am. Chem. Soc.*, 2013, **135**, 15986-15989.

[30] (*a*) V. Rubio-Giménez, C. Bartual-Murgui, M. Galbiati, A. Núñez-López, J. Catells-Gil, B. Quinard, P. Seneor, E. Otero, P. Ohresser, A. Cantarero, E. Coronado, E. Coronado, J. A. Real, R. Mattana, S. Tatay and C. Martí-Gastaldo, *Chem. Sci.*, 2019, **10**, 4038-4047; (*b*) V. Rubio-Giménez, G. Escorcia-Ariza, C. Bartual-Murgui, C. Sternemann, M. Galbiati, J. Castells-Gil, J. A. Real, S. Tatay and C. Martí-Gastaldo, *Chem. Mater.*, 2019, **31**, 7277-7728.

## 2.8.- Supporting Information

**Figure S1.** Thermogravimetric analyses of a)**$1^{Pt}\cdot H_2O$**, b) **$1^{Pd}\cdot H_2O$**, c) **$1^{Pt}\cdot 0.5MeOH$**, d) **$1^{Pd}\cdot 0.5MeOH$**, e) **$1^{Pt}\cdot 0.4EtOH$** and f) **$1^{Pd}\cdot 0.25EtOH$**

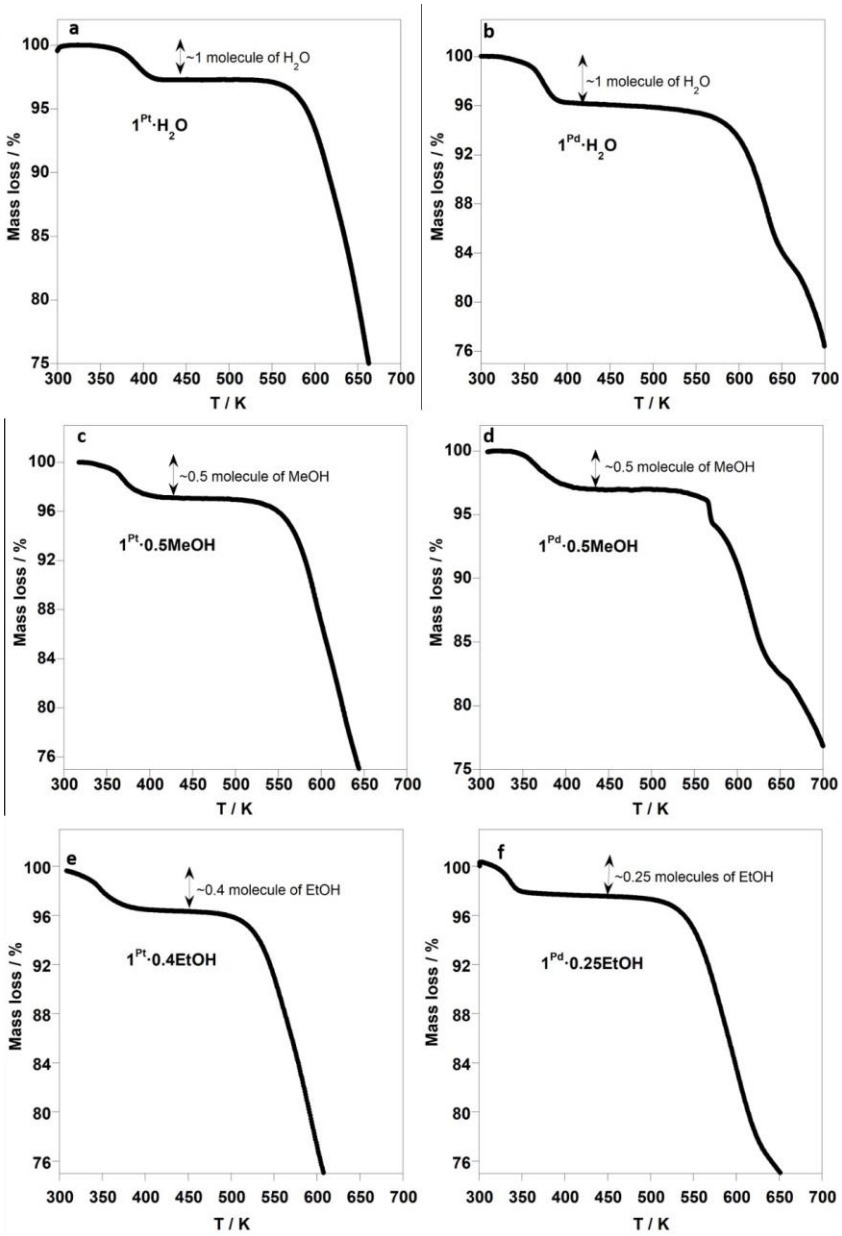

**Figure S2.** View along a) [001] and b) [100] directions of three stacked $\{Fe(5\text{-}NH_2Pym)_2[M(CN)_4]\}$ sheets in $\mathbf{1^M\cdot H_2O}$ (M = Pt or Pd). π-π interactions are highlighted with black dashed lines.

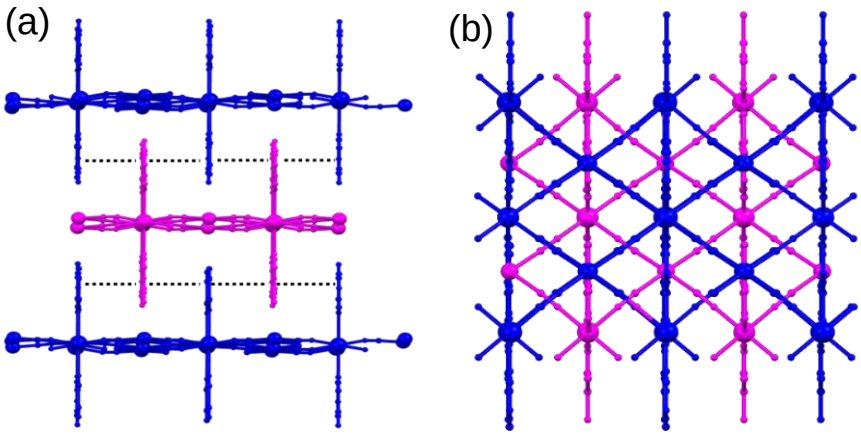


**Table S1.** Crystal data for $\mathbf{1^{Pt}\cdot H_2O}$ and $\mathbf{1^{Pt}}$ at the indicated temperatures.

| | $\mathbf{1^{Pt}\cdot H_2O}$_120K | $\mathbf{1^{Pt}\cdot H_2O}$_187K | $\mathbf{1^{Pt}\cdot H_2O}$_260K | $\mathbf{1^{Pt}}$_120K | $\mathbf{1^{Pt}}$_260K |
|---|---|---|---|---|---|
| Empirical formula | $C_{12}H_{11.6}N_{10}O_{0.8}PtFe$ | $C_{12}H_{11.6}N_{10}O_{0.8}PtFe$ | $C_{12}H_{10}N_{10}O_{0.8}PtFe$ | $C_{12}H_{10}N_{10}PtFe$ | $C_{12}H_{10}N_{10}PtFe$ |
| *Mr* | 559.65 | 559.65 | 558.04 | 545.24 | 545.24 |
| Crystal system | monoclinic | monoclinic | monoclinic | orthorhombic | orthorhombic |
| Space group | *C2/m* | *C2/m* | *C2/m* | *Pnma* | *Pnma* |
| *a* (Å) | 21.078(3) | 21.488(3) | 21.836(2) | 14.1282(6) | 14.5857(6) |
| *b* (Å) | 7.0587(9) | 7.1993(8) | 7.3747(6) | 7.1968(3) | 7.3650(4) |
| *c* (Å) | 14.488(3) | 14.671(2) | 14.8914(12) | 15.7460(7) | 15.9543(8) |
| *β* (°) | 131.352(3) | 131.584(3) | 131.952(3) | | |
| *V* (Å$^3$) | 1618.1(5) | 1697.6(3) | 1783.4(3) | 1601.02(12) | 1713.87(14) |
| *Z* | 4 | | | 4 | |
| *T (K)* | 120 | 187 | 260 | 120 | 260 |
| $D_c$ (mg cm$^{-3}$) | 2.297 | 2.190 | 2.078 | 2.262 | 2.113 |
| *F*(000) | 1056 | 1056 | 1050 | 1024 | 1024 |
| *μ* (Mo-$K_α$) (mm$^{-1}$) | 9.556 | 9.109 | 8.670 | 9.651 | 9.016 |
| Crystal size (mm) | 0.10x0.18x0.18 | | | | |
| No. of total reflections | 3046 | 2871 | 3361 | 2821 | 2164 |
| No. of reflections [$I>2\sigma(I)$] | 2106 | 2407 | 2601 | 2240 | 1596 |
| *R* [$I>2\sigma(I)$] | 0.0814 | 0.0737 | 0.0544 | 0.0470 | 0.0520 |
| *wR* [$I>2\sigma(I)$] | 0.1954 | 0.1674 | 0.1267 | 0.1059 | 0.1297 |
| *S* | 1.108 | 1.139 | 1.036 | 1.124 | 1.190 |

$R = \Sigma ||Fo| - |Fc|| / \Sigma |Fo|$; $wR = [\Sigma [w(Fo^2 - Fc^2)^2] / \Sigma [w(Fo^2)^2]]^{1/2}$.

$w = 1/ [\sigma^2(Fo^2) + (m\,P)^2 + n\,P]$ where $P = (Fo^2 + 2Fc^2) / 3$;

m = 0.1197 (**1**), 0.0265 (**2**), 0.0685 (**3**), 0.0000 (**4**), and 0.0523 (**5**);

n = 97.5723 (**1**), 170.7754 (**2**), 41.0043 (**3**), 52.1055 (**4**), and 43.7598 (**5**)

**Table S2.** Crystal data for $\mathbf{1^{Pd}\cdot H_2O}$ and $\mathbf{1^{Pd}}$ at the indicated temperatures.

| | $\mathbf{1^{Pd}\cdot H_2O\_120K}$ | $\mathbf{1^{Pd}\cdot H_2O\_180K}$ | $\mathbf{1^{Pd}\cdot H_2O\_260K}$ | $\mathbf{1^{Pd}\_120K}$ | $\mathbf{1^{Pd}\_260K}$ |
|---|---|---|---|---|---|
| Empirical formula | $C_{12}H_{12}N_{10}OPdFe$ | $C_{12}H_{12}N_{10}OPdFe$ | $C_{12}H_{10}N_{10}OPdFe$ | $C_{12}H_{10}N_{10}PdFe$ | $C_{12}H_{10}N_{10}PdFe$ |
| *M*r | 474.57 | 474.57 | 472.55 | 456.55 | 456.55 |
| Crystal system | monoclinic | monoclinic | monoclinic | orthorhombic | orthorhombic |
| Space group | *C*2/*m* | *C*2/*m* | *C*2/*m* | *Pnma* | *Pnma* |
| *a* (Å) | 21.092(3) | 21.454(3) | 21.770(3) | 14.1549(7) | 14.2723(10) |
| *b* (Å) | 7.0553(10) | 7.1986(8) | 7.3679(8) | 7.1808(4) | 7.3843(5) |
| *c* (Å) | 14.535(2) | 14.7221(16) | 14.951(3) | 15.6363(8) | 15.9189(12) |
| *β* (°) | 131.372(4) | 131.494(3) | 131.902(3) | | |
| *V* (Å$^3$) | 1623.1(4) | 1703.0(3) | 1784.9(5) | 1589.33(14) | 1677.7(2) |
| *Z* | 4 | | | 4 | |
| *T (K)* | 120 | 180 | 260 | 120 | 260 |
| $D_c$ (mg cm$^{-3}$) | 1.942 | 1.851 | 1.758 | 1.908 | 1.808 |
| *F*(000) | 936 | 936 | 928 | 896 | 896 |
| *μ* (Mo-K$_\alpha$) (mm$^{-1}$) | 2.027 | 1.932 | 1.843 | 2.061 | 1.953 |
| Crystal size (mm) | 0.05x0.15x0.20 | | | | |
| No. of total reflections | 2266 | 2496 | 2671 | 2347 | 2021 |
| No. of reflections [*I*>2*σ*(*I*)] | 1699 | 1942 | 2122 | 1759 | 1419 |
| *R* [*I*>2*σ*(*I*)] | 0.0654 | 0.0564 | 0.0526 | 0.0644 | 0.0902 |
| *wR* [*I*>2*σ*(*I*)] | 0.1332 | 0.1276 | 0.1292 | 0.1465 | 0.2291 |
| *S* | 1.042 | 1.051 | 1.104 | 1.117 | 1.176 |

$R = \Sigma ||Fo| - |Fc|| / \Sigma |Fo|$; $wR = [\Sigma [w(Fo^2 - Fc^2)^2] / \Sigma [w(Fo^2)^2]]^{1/2}$.

$w = 1/ [\sigma^2(Fo^2) + (m\,P)^2 + n\,P]$ where $P = (Fo^2 + 2Fc^2) / 3$;

m = 0.0176 (**1**), 0.0445 (**2**), 0.0674 (**3**), 0.0457 (**4**), and 0.0403 (**5**);

n = 78.1367 (**1**), 42.1677 (**2**), 24.3621 (**3**), 18.8066 (**4**), and 73.0831 (**5**)

**Figure S3.** Powder X-ray diffraction patterns of a) **$1^{M}\cdot H_2O$**, b) **$1^{M}\cdot$MeOH** and **$1^{M}\cdot$EtOH** and c) **$1^{M}$** series. Simulated patterns are also displayed for comparison.

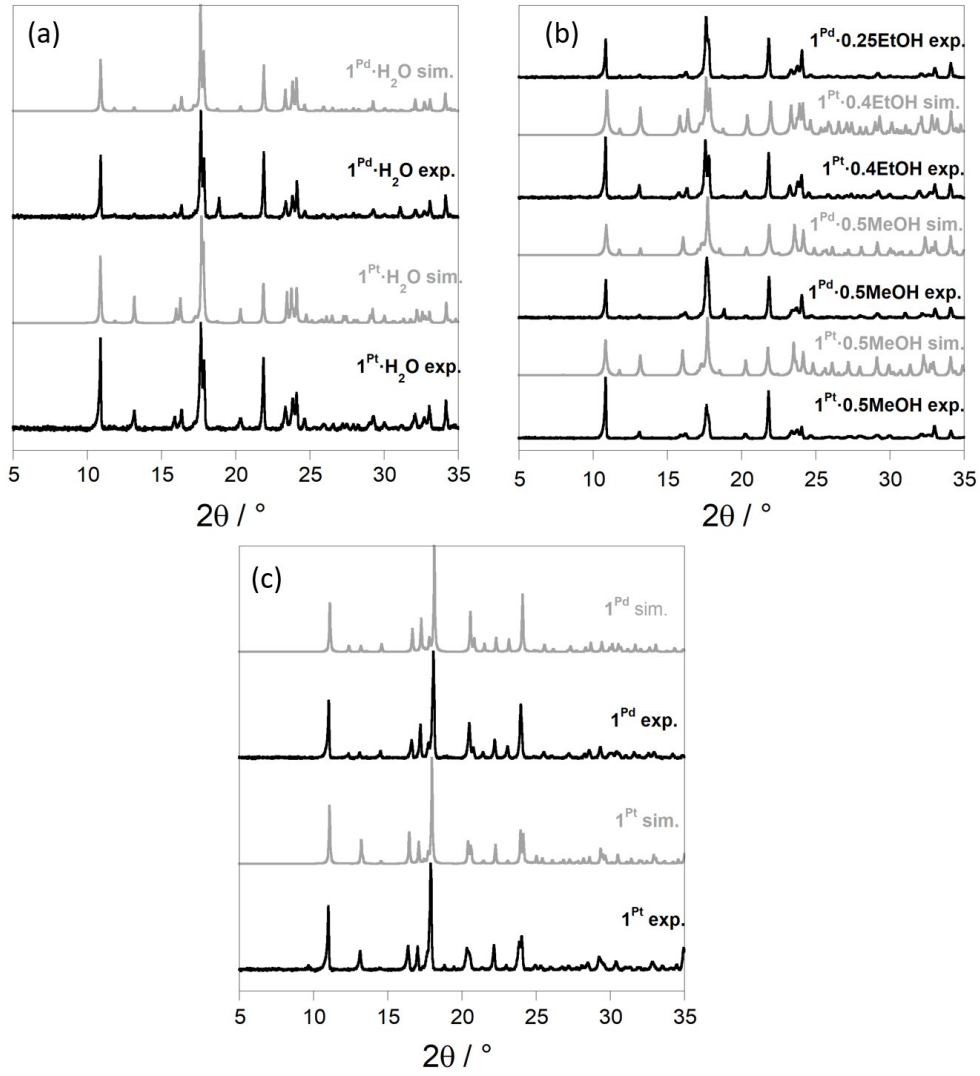

2.8.1.- Physical characterization

Kinetic water, methanol and ethanol adsorption experiments were performed through TGAmeasurements for activated **1$^{Pt}$** and **1$^{Pd}$** compounds (Figure S2a and S2b). As observed in Figure 2a, the tetracyanoplatinate derivative adsorbs 0.97/0.41/0.14 molecules of water/methanol/ethanol per Fe$^{II}$ ion. However, in the same conditions, the tetracyanopalladate network adsorbs a smaller fraction of guest molecules (0.91/0.25/0.01molecules of water/methanol/ethanol per Fe$^{II}$ ion) during the same range of time. In order to estimate the adsorption rates exhibited by each derivative for the different guests, the experimental isotherm curves were fitted with the kinetic Avrami equation:

$$\alpha = A(1 - exp\{-K_{av}t^{n}\})$$

where α is the adsorbed fraction at time t, A is the total amount of adsorbed guest at time ∞, $K_{av}$ is the rate constant, and n is the Avrami exponent which defines the cooperativity ofthe adsorption process. The kinetic parameters resulting from the fittings are gathered in Table S1. Whereas methanol adsorption curves show higher uptake rates, those of water exhibit higher n values reflecting a certain degree of cooperativity throughout the adsorption process. Besides, for a given guest, **1$^{Pt}$** displays higher kinetic constants and lower n values than**1$^{Pd}$**.

**Figure S4.** Time dependent TGA measurements registered during the adsorption of water, methanol and ethanol at room temperature and pressure. Solid lines correspond to the corresponding fittings following the Avrami's equation.

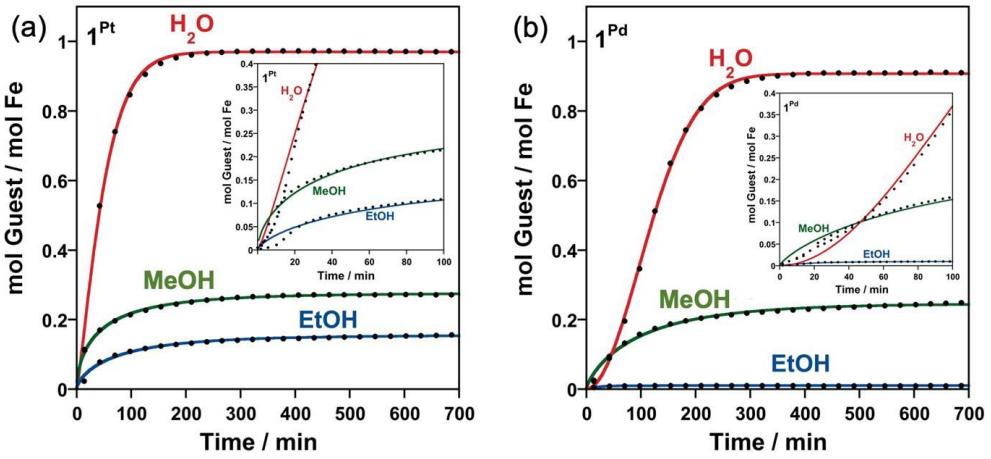

**Table S3.** Avrami parameters extracted from fitting of the experimental TGA curves depicted in Figure 4. **$1^{Pd}$·EtOH** has been excluded from fitting because it does not present significant adsorption at the studied conditions.

| | $K_{av}$ | $n$ | $A$ |
|---|---|---|---|
| **$1^{Pt}$+$H_2O$** | $7.00\times10^{-3}$ | 1.25 | 0.97 |
| **$1^{Pd}$+$H_2O$** | $6.35\times10^{-5}$ | 1.96 | 0.91 |
| **$1^{Pt}$+MeOH** | $9.38\times10^{-2}$ | 0.61 | 0.27 |
| **$1^{Pd}$+MeOH** | $2.43\times10^{-2}$ | 0.80 | 0.25 |
| **$1^{Pt}$+EtOH** | $4.45\times10^{-2}$ | 0.71 | 0.15 |

**Table S4.** Crystal data for **$1^{Pt}$·0.5MeOH** and **$1^{Pt}$·0.4EtOH** at the indicated temperatures.

| | **$1^{Pt}$·0.5MeOH _100K** | **$1^{Pt}$·0.5MeOH_260K** | **$1^{Pt}$·0.4EtOH_100K** | **$1^{Pt}$·0.4EtOH _260K** |
|---|---|---|---|---|
| Empirical formula | $C_{12.5}H_{12}N_{10}O_{0.5}PtFe$ | $C_{12.5}H_{12}N_{10}O_{0.5}PtFe$ | $C_{12.8}H_{10}N_{10}O_{0.4}PtFe$ | $C_{12.8}H_{10}N_{10}O_{0.4}PtFe$ |
| *Mr* | 561.26 | 561.26 | 561.25 | 561.25 |
| Crystal system | orthorhombic | | monoclinic | monoclinic |
| Space group | *Pbcm* | | *I*2/*m* | *I*2/*m* |
| *a* (Å) | 14.8631(7) | 14.9943(8) | 14.848(2) | 14.980(2) |
| *b* (Å) | 32.144(2) | 32.626(2) | 7.1717(7) | 7.3662(6) |
| *c* (Å) | 7.1639(4) | 7.3615(3) | 15.880(3) | 16.181(2) |
| *β* (°) | | | 92.699(11) | 91.922(9) |
| *V* (Å$^3$) | 3422.6(3) | 3601.3(3) | 1689.2(4) | 1784.5(3) |
| *Z* | 8 | 8 | 4 | 4 |
| *T (K)* | 100 | 260 | 100 | 260 |
| $D_c$ (mg cm$^{-3}$) | 2.178 | 2.070 | 2.207 | 2.089 |
| *F*(000) | 2120 | 2118 | 1056 | 1056 |
| *μ* (Mo-K$_\alpha$) (mm$^{-1}$) | 9.035 | 8.587 | 9.153 | 8.664 |
| Crystal size (mm) | 0.02x0.10x0.10 | 0.02x0.10x0.10 | 0.02x0.15x0.15 | 0.02x0.15x0.15 |
| No. of total reflections | 3804 | 4199 | 2079 | 2191 |
| No. of reflections [$I>2\sigma(I)$] | 3032 | 2751 | 1857 | 1902 |
| *R* [$I>2\sigma(I)$] | 0.0979 | 0.0869 | 0.1183 | 0.0693 |
| *wR* [$I>2\sigma(I)$] | 0.1933 | 0.1624 | 0.2800 | 0.1773 |
| *S* | 1.084 | 1.056 | 1.194 | 1.090 |

$R = \Sigma ||Fo| - |Fc|| / \Sigma |Fo|$; $wR = [\Sigma [w(Fo^2 - Fc^2)^2] / \Sigma [w(Fo^2)^2]]^{1/2}$.

$w = 1/ [\sigma^2(Fo^2) + (m\ P)^2 + n\ P]$ where $P = (Fo^2 + 2Fc^2) / 3$;

m = 0.0000 (**1**), 0.0333 (**2**), 0.1097 (**3**), and 0.1006 (**4**);

n = 553.5499 (**1**), 253.2535 (**2**), 251.023 (**3**), and 63.5736 (**4**)

**Table S5.** Crystal data for **$1^{Pt}$·0.5MeOH** at the indicated temperatures.

| | **FePd0.5(CH4O)_100K** | **FePd0.5(CH4O)_260K** |
|---|---|---|
| Empirical formula | $C_{12.5}H_{12}N_{10}O_{0.5}PdFe$ | $C_{12.5}H_{12}N_{10}O_{0.5}PdFe$ |
| *Mr* | 472.57 | 472.57 |
| Crystal system | orthorhombic | |
| Space group | *Pbcm* | |
| *a* (Å) | 14.9105(14) | 15.0184(12) |
| *b* (Å) | 32.021(2) | 32.516(2) |
| *c* (Å) | 7.1610(4) | 7.3514(4) |
| *V* (Å$^3$) | 3419.0(4) | 3589.9(4) |
| *Z* | 8 | 8 |
| *T (K)* | 120 | 260 |
| $D_c$ (mg cm$^{-3}$) | 1.836 | 1.749 |
| *F*(000) | 1864 | 1864 |
| $\mu$(Mo-K$_\alpha$) (mm$^{-1}$) | 1.922 | 1.830 |
| Crystal size (mm) | 0.03x0.12x0.12 | 0.03x0.12x0.12 |
| No. of total reflections | 3757 | 3897 |
| No. of reflections [$I>2\sigma(I)$] | 2486 | 1884 |
| $R$ [$I>2\sigma(I)$] | 0.1088 | 0.0816 |
| $wR$ [$I>2\sigma(I)$] | 0.2488 | 0.2037 |
| $S$ | 1.041 | 1.050 |

$R = \Sigma ||Fo| - |Fc|| / \Sigma |Fo|$; $wR = [\Sigma [w(Fo^2 - Fc^2)^2] / \Sigma [w(Fo^2)^2]]^{1/2}$.

$w = 1/ [\sigma^2(Fo^2) + (m\ P)^2 + n\ P]$ where $P = (Fo^2 + 2Fc^2) / 3$;

m = 0.0809 (**1**), and 0.0848(**2**);

n = 178.4426 (**1**), and 25.2612 (**2**)

**Figure S5.** X-ray diffraction pattern evolution indicating the structural reversibility throughout the **$1^{M}$·$H_2O$** → **$1^{M}$** → **$1^{M}$·$H_2O$** process [M = Pt (left) or Pd (right)]. The dehydration and rehydration processes were carried out through a thermal treatment at 400 K during 30 minutes and by exposing the sample to air, respectively.

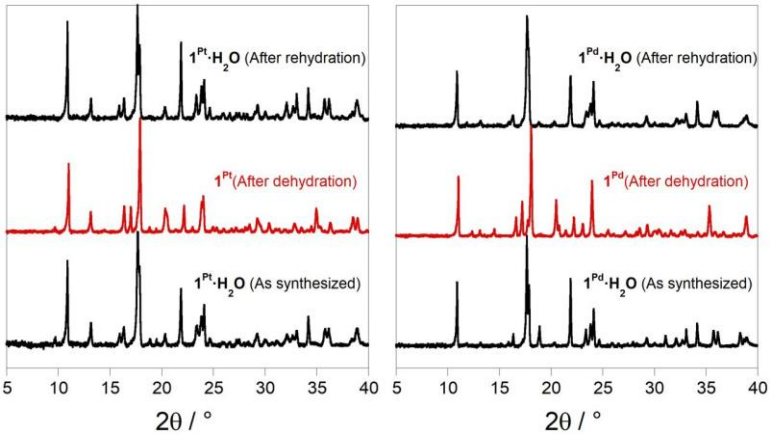

**Figure S6.** Asymmetric unit of **$1^{Pt}$·0.5MeOH** (isostructural to **$1^{Pd}$·0.5MeOH**). Hydrogen atoms have been omited for clarity.

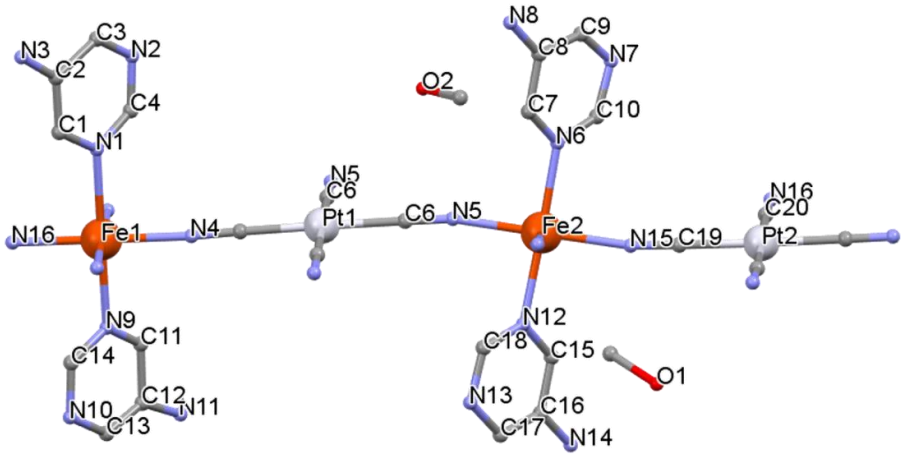


**Figure S7.** Fragment of the **$1^{M}$·0.5MeOH** structure displaying the packing of packing of the {Fe[M(CN)$_4$]} layers and the 1D chnnels where thr methanol guests are located. The N7···N3 and N11···N13 intralayer H bonds are represented by black dashed lines.

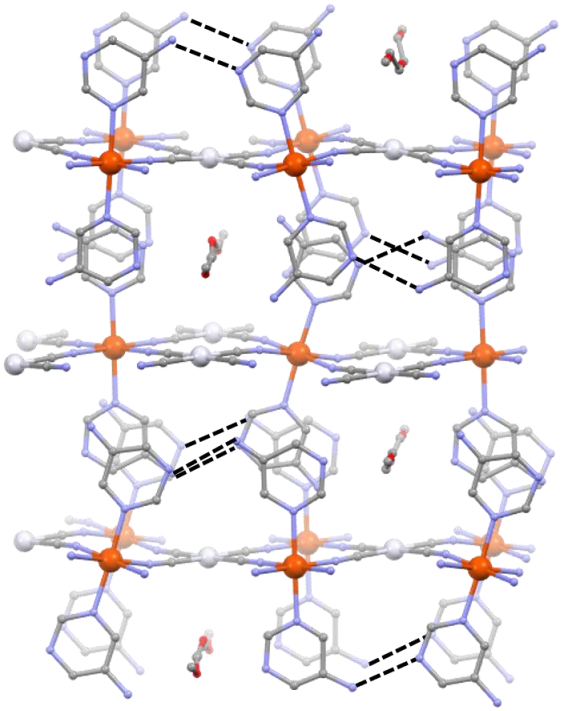

**Figure S8.** X-ray diffraction pattern evolution during the **$1^{M}\cdot H_2O \rightarrow 1^{M} \rightarrow 1^{M}\cdot 0.5MeOH$** guest exchange processes for M = a) Pt or b) Pd.

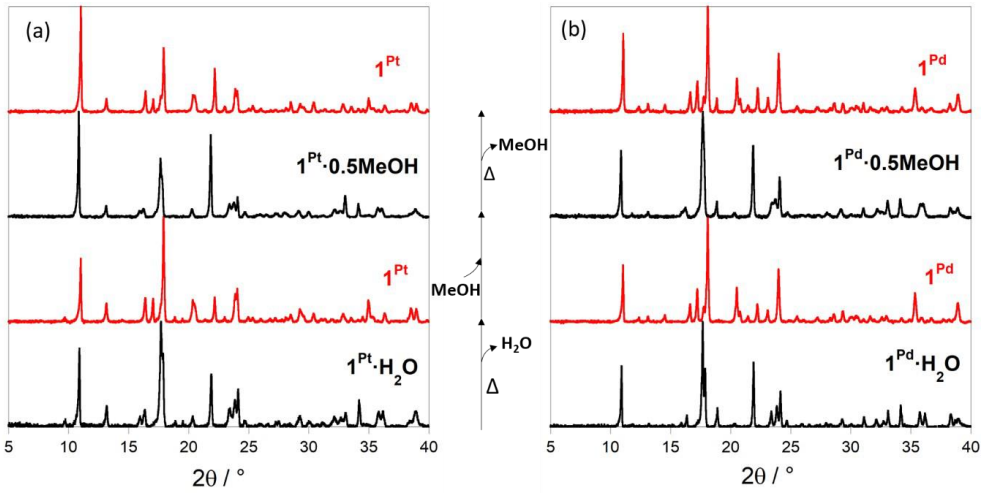

**Figure S9.** SCO properties recorded at 2K $min^{-1}$ of $\mathbf{1^{M}\cdot H_2O}$ (M = (a) Pt or (b) Pd) before heating (left), after heating at 400 K for 30 minutes (middle) and after exposure of $\mathbf{1^{Pt}}$ to air for 3 hours (right).

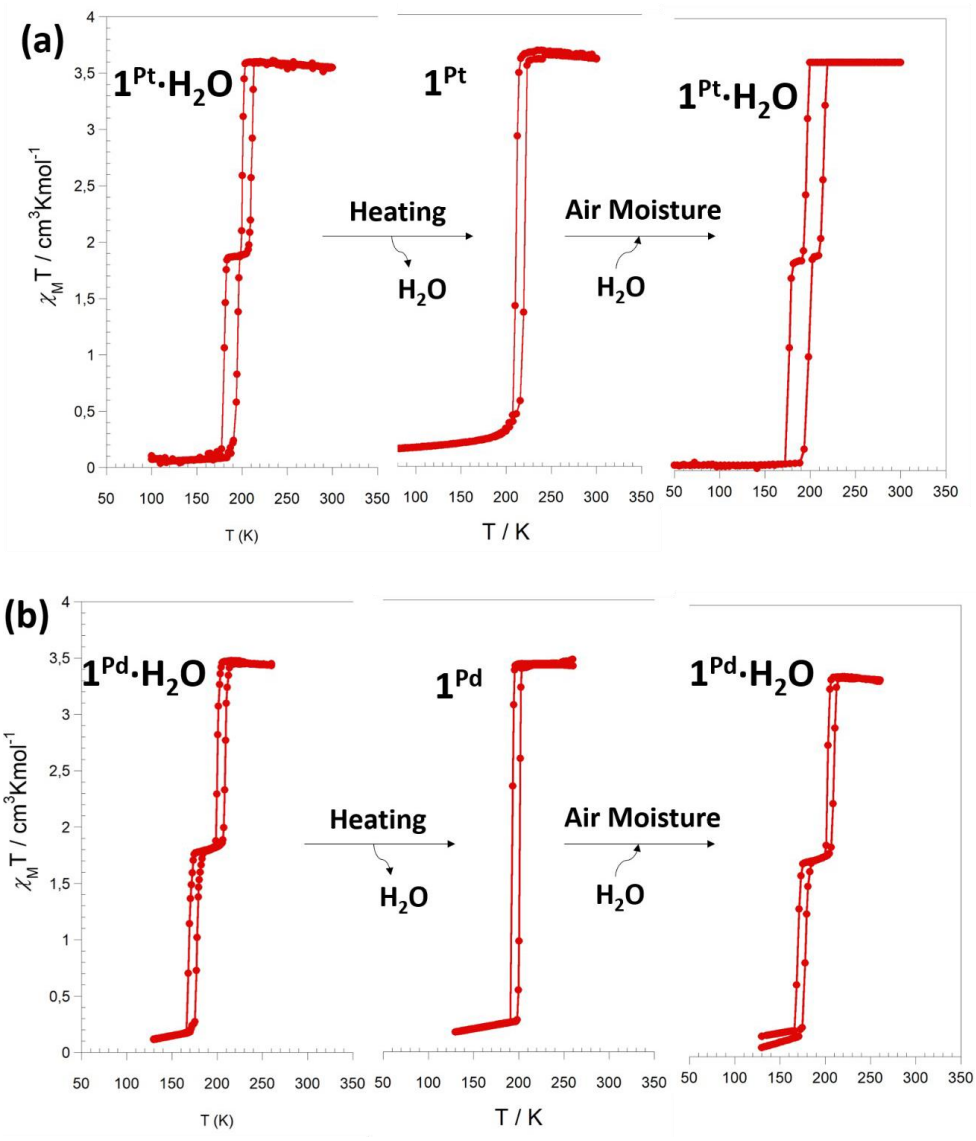

**Figure S10.** $X_M$T *vs* T curves measured at 2 K min$^{-1}$ of **1$^{Pt}$·0.4EtOH**, **1$^{Pd}$·0.5MeOH** and **1$^{Pt}$·0.5MeOH** in the 50-250 K range.

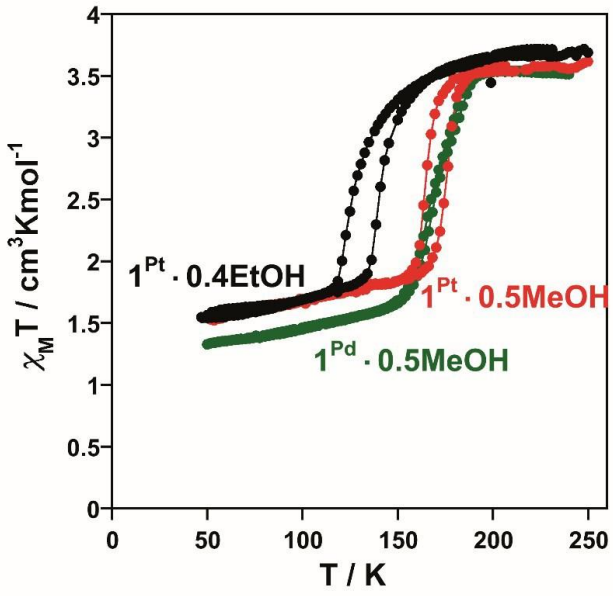


**Figure S11.** a) $X_M$T *vs* T curves measured at 2 K min$^{-1}$ of **1$^{Pd}$·0.25EtOH** ($X_M$T *vs* T curves of **1$^{Pt}$·0.4EtOH** and **1$^{Pd}$** are also represented for comparison) and b) corresponging TGA analyses of **1$^{Pd}$·0.25EtOH** and **1$^{Pt}$·0.4EtOH** revealing the presence of 0.25 and 0.42 molecules of EtOH per Fe$^{II}$ atom, respectively.

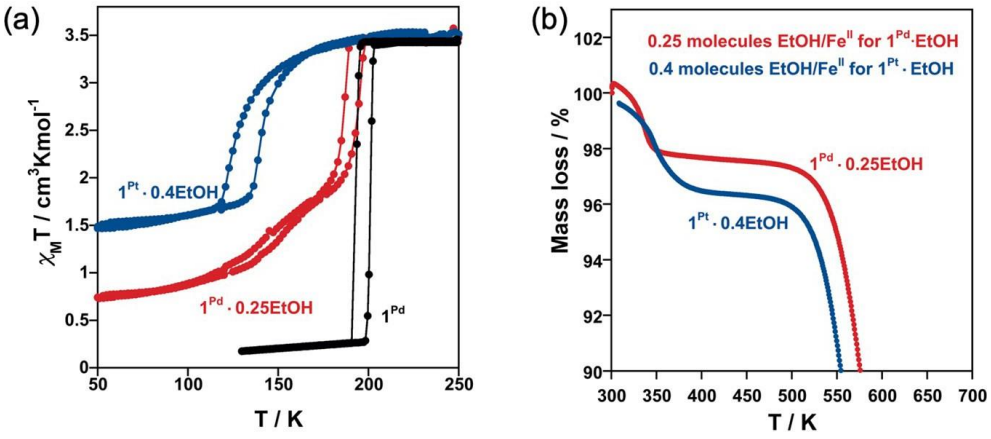

**Figure S12.** Calorimetric properties of $\mathbf{1^{M}}$, $\mathbf{1^{M}\cdot H_2O}$ and $\mathbf{1^{M}\cdot 0.5MeOH}$ (M = Pt, Pd). Blue and red dashed lines correspond to the cooling and heating modes, respectively. The SCO curve of each derivative is included as a reference (grey lines).

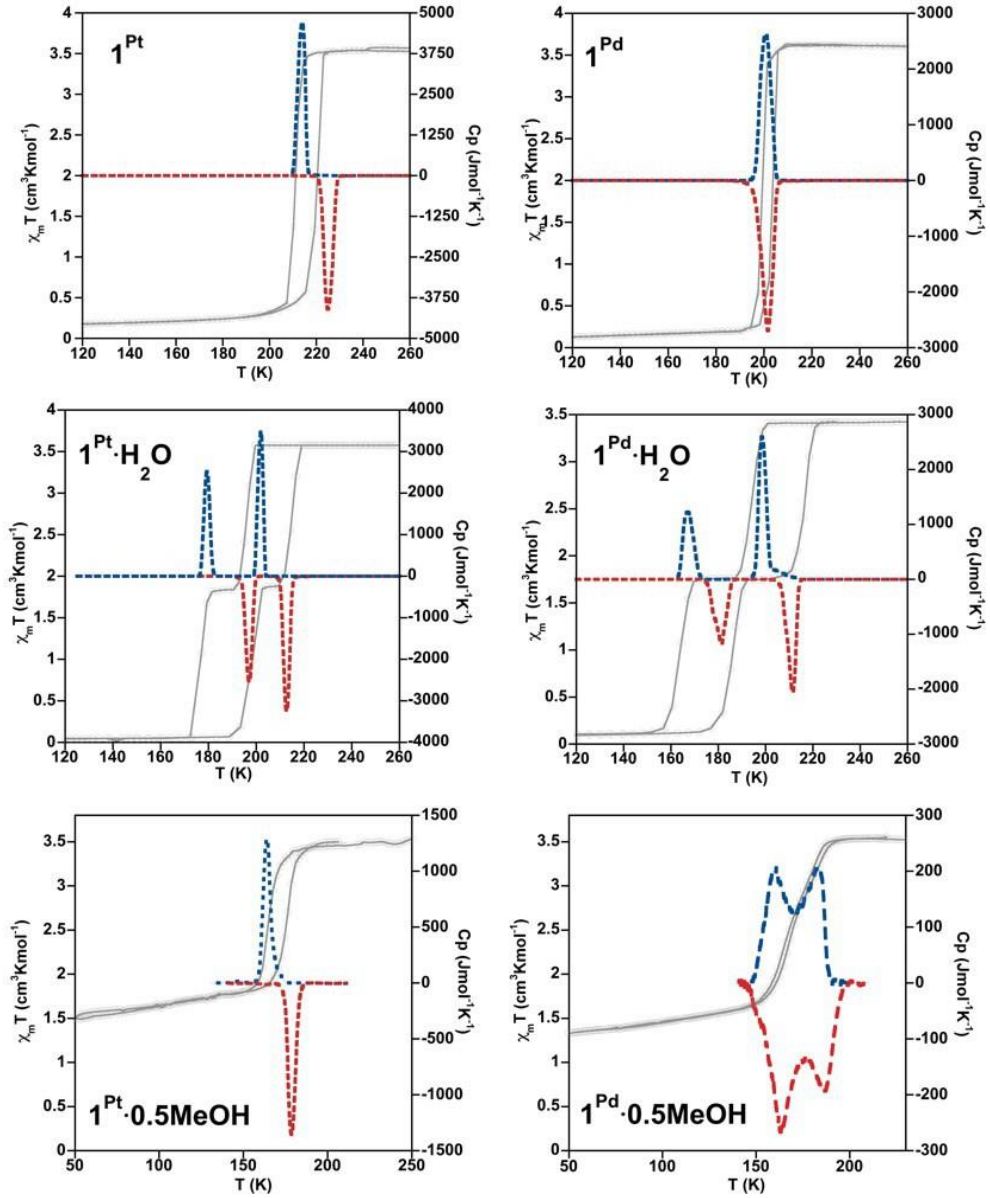

**Figure S13.** $X_M$T *vs* T plots for **$1^{Pt}$·0.5MeOH** at increasing pressures (scan rate 2 K $min^{-1}$).

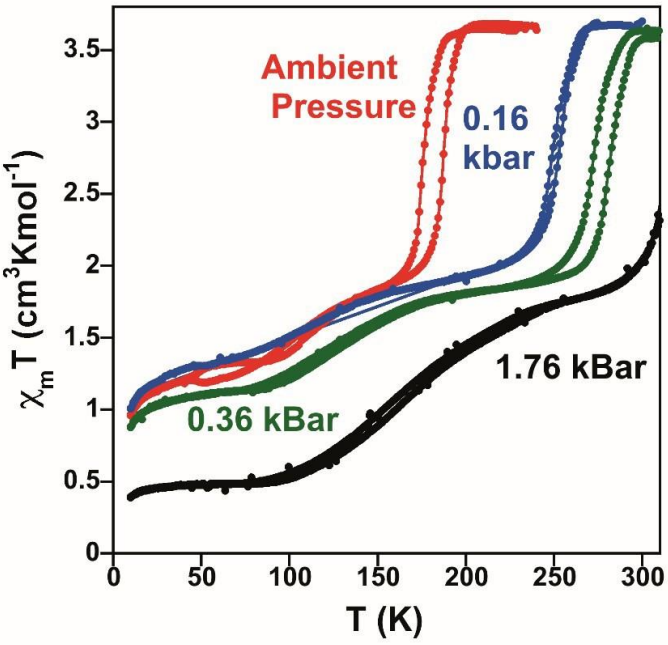


**Table S6.** Calculated accesible void volume (in Å$^3$) of the different clathrates for the different spin states.

| | $_1^M$ | | $1^M·H_2O$ | | | $1^M·0.5MeOH$ | | $1^M·xEtOH$ | |
|---|---|---|---|---|---|---|---|---|---|
| | HS | LS | HS-HS | HS-LS | LS-LS | HS-HS | HS-LS | HS-HS | HS-LS |
| M = Pt | No AVV observed | | 164 | 143 | 117 | 360 | 305 | 174 | 144 |
| M = Pd | | | 150 | 139 | 123 | 336 | 301 | | |

**Figure S14.** Powder X-ray diffraction patter of **$1^{Pd}$·EtOH** soaked in ethanol (blue line). Diffraction patterns of **$1^{Pd}$** (red line) and **$1^{Pt}$·EtOH** are showed for comparison. Three insets corresponding to the 2θ ranges delimited by the red dashed areas are depicted to see the spectra in more detail. As explained in the main text, the pattern of **$1^{Pd}$·EtOH** is very similar to that of **$1^{Pd}$** indicating that a low quantity of EtOH is adsorbed by **$1^{Pd}$** and consequently the spectrum is barely modified. However, the inset plots reveal some weak peaks (indicated by black arrows) which are reminiscent of the **$1^{Pd}$·EtOH**.

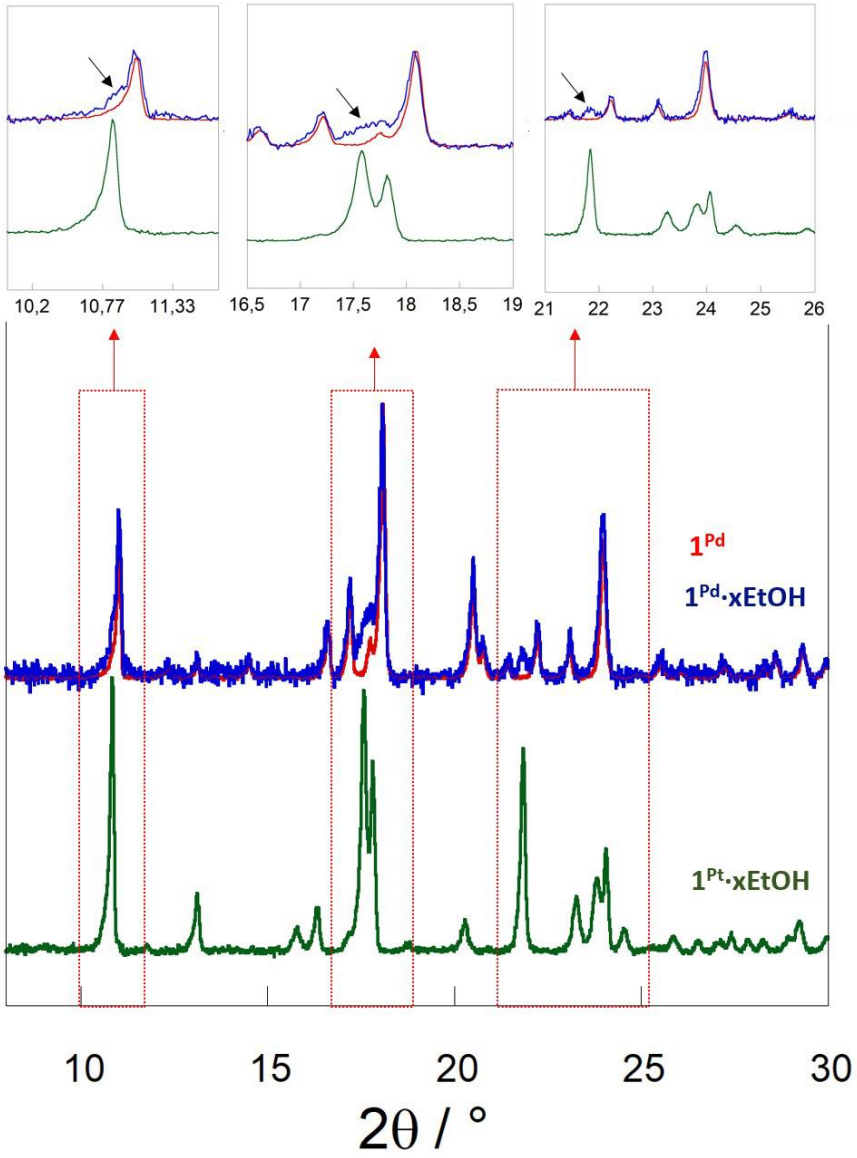

**Figure S15.** $X_M$T *vs* T curves measured at 2 K min$^{-1}$ for freshly dehydrated (a) **1$^{Pt}$** or (b) **1$^{Pd}$** compounds soaked in MeOH:EtOH, $H_2O$:MeOH or $H_2O$:EtOH (1:1) solvent mixtures. The curves of **1$^{M}$·H$_2$O**, **1$^{M}$·0.5MeOH** (M = Pt, Pd) and **1$^{Pt}$·0.4EtOH** compounds are displayed in grey for comparison.

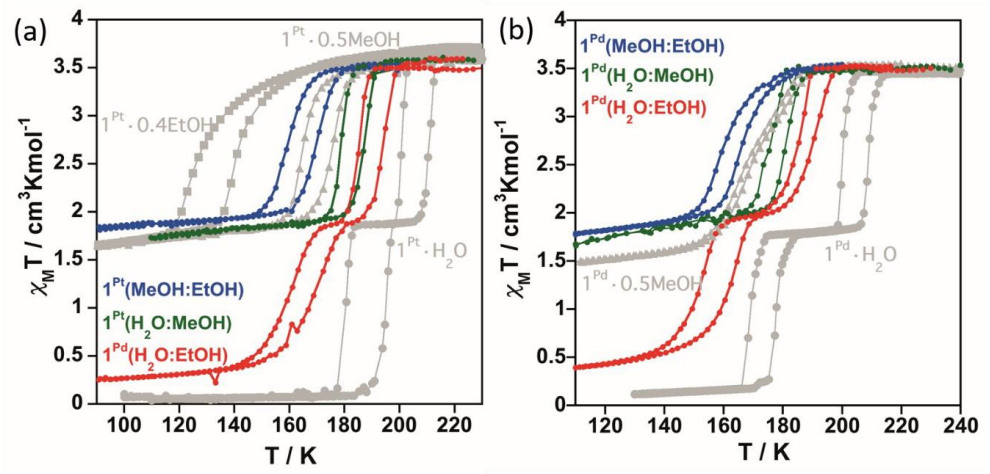

CAPÍTULO 3

# Bistable Hofmann-Type $Fe^{II}$ Spin-Crossover Two-Dimensional Polymers of 4-Alkyldisulfanylpyridine for Prospective Grafting of Monolayers on Metallic Surfaces

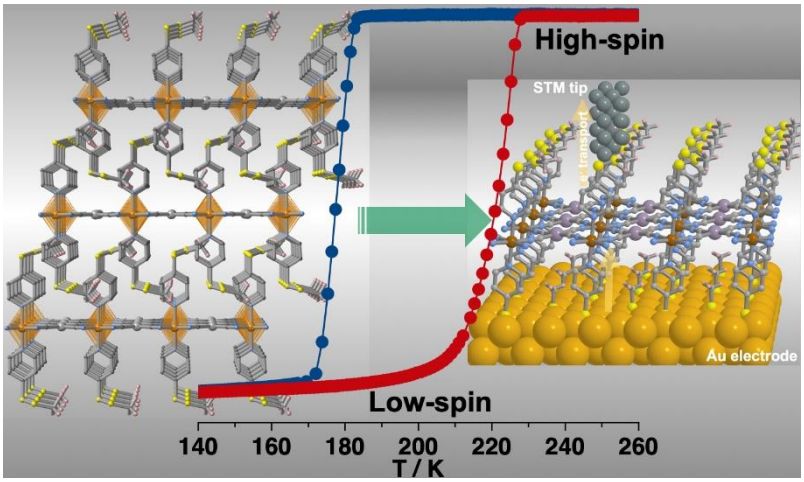


REVISTA: Inorganic Chemistry

ÍNDICE DE IMPACTO: 5.436

# CAPÍTULO 3

## Bistable Hofmann-Type $Fe^{II}$ Spin-Crossover Two-Dimensional Polymers of 4-Alkyldisulfanylpyridine for Prospective Grafting of Monolayers on Metallic Surfaces

### 3.1.- Abstract

Aiming at investigating the suitability of Hofmann-type two dimensional (2D) coordination polymers $\{Fe^{II}(L_{ax})_2[M^{II}(CN)_4]\}$ to be processed as single monolayers and probed as spin crossover (SCO) junctions in spintronic devices, the synthesis and characterication of the $M^{II}$ derivatives ($M^{II}$ = Pd and Pt) with sulfur-rich axial ligands ($L_{ax}$ = 4methyl- and 4-ethyl-disulfanylpyridine) have been conducted. The thermal dependence of the magnetic and calorimetric propertie confirmed the occurrence of strong cooperative SCO behavior in the temperature interval of 100-225 K, featuring hysteresis loops 44 and 32.5 K/21 K wide for $Pt^{II}$-methyl and $Pt^{II}/Pd^{II}$-ethyl derivatives, while the $Pd^{II}$-methyl derivative undergoes a much less cooperative multistep SCO. Excluding $Pt^{II}$-methyl, the remaining compounds display light-induced excited spin-state trapping at 10 K with $T_{LIESST}$ temperatures in the range of 50-70 K. Single-crystal studies performed in the temperature interval 100-250 K confirmed the layered structure and the occurrence of complete transformation between the high- and low-spin states of the $Fe^{II}$ center for the four compounds. Strong positional disorder seems to be the source of elastic frustration driving the multistep SCO observed for the $Pd^{II}$-methyl derivative. It is expected that the peripheral disulfanyl groups will favour anchoring and growing of the monolayer on gold substrates and optimal electron transport in the device.

### 3.2.- Introduction

Bistable molecular materials with switchable properties are appealing candidates for developing technological applications, e.g., sensors for information storage. Iron(II) spin crossover (SCO) complexes afford excellent examples of molecular bistability, because they reversibly switch between the high-spin (HS, $t_2g^4e_g^2$) and low-spin (LS, $t_2g^6e_g^0$) electronic states in response to a variety of external stimuli such as temperature, pressure, ligh, adsorption of analytes or extrinsic phase transitions. This is particularly true when the spin

changing centres are strongly couples to each other, since the spin state change manifests cooperatively conferring hysteretic behavior (memory effect) to the magnetic, optical, structural, mechanical and electric properties associated with the material.[1]

The SCO research is a very active and multidisciplinary field that spreads in many complementary directions. The synthesis and characterization of interesting mononuclear, polynuclear and one-dimensional to three-dimensional (1D-3D) polymeric SCO systems has increased exponentially during the last two decades, affording new SCO behaviors[2] wich, in turn, have inspired new sophisticated physical techniques and theoretical models.[1e,3] To engineer new multifunctional materials where the SCO synchronically interplays with other relevant physicochemical properties -e.g., porosity (host-guest chemistry), liquid crystalline properties, crystal-to-crystal phase transitions, lumniscence or chirality- in a synergetic fashion in the same crystal is one of the fundamental goals in the field. This requires a rational design of the synthesis at macroscopic scale and precise control of essential elusive SCO parameters, such as critical temperature ($T_c$), abruptness, hysteresis width and completeness, Relevant achievements of this strategy include the combination of SCO and nonlinear optical properties,[4] electronic conduction,[5] electroluminescence,[6] fluorescence,[7] liquid-crystalline properties,[8] porosity,[2d,g] molecular recognition[9], photoswitchable magnets,[10] chirality,[11] room-temperature photoisomers and reactions,[12] etc. The ultimate goal is the construction of sensing materials capable of acting as switchers in response to changes of ambient conditions (temperature, humidity, chemical contaminants, etc.). Furthermore, the potential implementation of SCO materials into electronic and spintronic devices is a new concept of paramount importance that has fuelled sophisticated studies aiming at controlling the electron transport (charge and spin) processing SCO materials as ultrathin films on surfaces.[13]

Two-dimensional (2D) Hofmann-type $Fe^{II}$ coordination polymers with general formula $\{Fe^{II}(L_{ax})_2[M^{II}(CN)_4]\}$ represent an important source of SCO compounds, where $M^{II}$ = $Pt^{II}$, $Pd^{II}$ or $Ni^{II}$ and $L_{ax}$ is a terminal monotopic axial ligand based on pyridine/pyridine-like[2d,14] and triazole rings.[15] The $Fe^{II}$ ions are equatorially connected through square-planar $[M^{II}(CN)_4]^{2-}$ anionic metalloligands affording robust infinite $[Fe^{II}[M^{II}(CN)_4]_\infty$ layers that are the origin of the cooperativity typically exhibited y these compounds. The layers stack on top of each other interdigitating the axial ligands $L_{ax}$ whose nature (length, donor-acceptor substituents, etc.) plays an important role in the modulation of the cooperativity through

changes in the interlayer spacing and flexibility of the layers (corrugation), fators that may influence the inclusion of guest molecules.

It has recently been shown that 2D Hofmann-type coordination polymers can be processed as ultrathin films under mild conditions (RT) by applying the layer-by-layer liquid phase epitaxy (LPE) methodology,[16-18] at variance of the homologous 3D derivatives, which require very low temperatures.[19-25] Processing of these materials as ultrathin films is a requirement to keep small electrode separation in vertical transport devices to ensure functional current flow but, obviously, it can seriously compromise the SCO properties. For example, synchrotron XAS studies showed that, for film thicknesses abose ca. 12nm, the 2D coordination polymer $\{Fe^{II}(pyridine)_2[Pt^{II}(CN)_4]\}$ presents a cooperative SCO behavior similar to that observed for the microcrystalline sample.[17] However, below this threshold value, the cooperativity and completeness of the spin transitions are exponentially attenuated since the films lose cohesion conferring to its structure a high degree of mosaicity constituted of practically unconnected nanoislands. The nature of the axial ligand and its dramatic influence on the coalescence of the thin film deposited on Au substrates has also been investigated for two new 2D Hofmann compounds $\{Fe^{II}(pyrimidine)_2[Pt^{II}(CN)_4]\}$ and $\{Fe^{II}(isoquinoline)_2[Pt^{II}(CN)_4]\}$, together with their transport properties.[18]

In the search for new $Fe^{II}$ Hofmann-type 2D coordination polymers, here, we report of the preparation, structural characterization, and spin crossover properties of four complexes generically formulated $\{Fe^{II}(pyS_2R)_2[M^{II}(CN)_4]\}_n$ (**MpyS$_2$R**, where $M^{II}$ = Pd, Pt and R = Me, Et), where the acial organic ligand $pyS_2R$ is 4-methyl/ethyldisulfanylpyridine (R = Me, Et). In contrast to the mentioned above multilayer studies based of the LPE technique, the axially coordinated pyridine ligand functionalized in 4-position with a reactive alkyldisulfanyl group opens the possibility to process the resulting 2d coordination polymers as robust single monolayer arrays of elastically coupled SCO centers deposited on suitable surfaces to be probed as SCO junctions. This approach was inspired by a relevant pioneer work by Mallouk et al. about the growth of thin films of the porous 3D Hofmann clathrate {Ni(4,4'-bipiridine)[Pt(CN)$_4$]} anchored through a monolayer of 4-pyridyl ethyldisulfide on gold substrates.[20] A similar strategi has recently led to the production of molecular monolayers prepared by simple inmersion of the substrate in highly diluted solutions of mononuclear $Fe^{II}$ SCO complexes on gold substrates and successfully tested as spintronic devices.[26]

## 3.3.- Results

### 3.3.1.- Synthesis

All the samples **MpyS₂R** (where M = Pt, Pd) and R = Me, Et) were prepared as singe crystals from slow diffusion techniques in water- methanol solutions (see the Experimental Section). According to chemical and thermogravimetric analyses (See Figure S1 in the supporting information), the single crystal resulted to be unsolvated and decompose above 420 K.

### 3.3.2.- Spin Crossover Properties

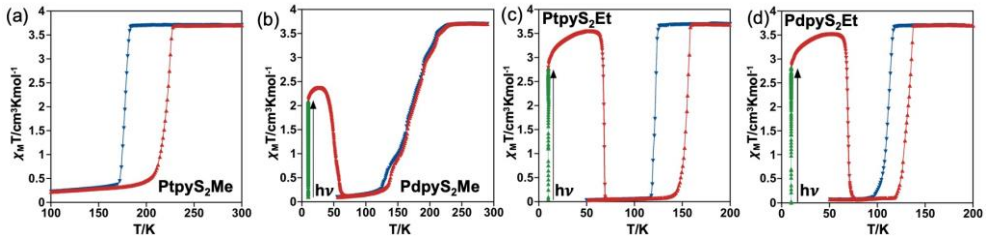


**Fig. 1.** Magnetic and photomagnetic properties of **MpyS₂Me** (M = Pt (a), Pd (b)) and **MpyS₂Et** (M = Pt (c), Pd (d)). Cooling, heating and photoswitching processes are represented in blue, red and green, respectively.

Figure 1 shows the magnetic and photomagnetic properties of the title compounds in the form of the product $\chi_M T$ *vs* $T$, where $\chi_M$ is the molar magnetic susceptibility and $T$ is the temperature. At 300 K, the $\chi_M T$ value is ca. 3.70 $cm^3$ K $mol^{-1}$ for the four derivatives consistently with a fully populated HS state with a strong orbital contribution. Upon cooling at 1 K/min, $\chi_M T$ remains constant down to 183 K for **PtpyS₂Me** and dcreases abruptly to 0.4 $cm^3$ K /mol in the interval 182-170 K, then decreases gradually to attain a value of 0.2 $cm^3$ K $mol^{-1}$ at 100K, where the LS state is practically fully populated. The profile of the $\chi_M T$ *vs* $T$ curve in the heating mode is similar to that of the cooling mode but shifted to high temperatures, defining a hysteresis loop $\Delta T$ = 44 K wide with the equilibrium temperatures, $T_c$, at which the populations of the HS and LS centers are equal at 0.5, equal to 180 K and 224 K for the cooling and heating branches, respectively. This strong cooperative SCO behavior contrasts dractically with that shown by the isostructural (vide infra) homologous **PdpyS₂Me** derivative. $\chi_M T$ *vs* $T$ = 3.70 $cm^3$ K $mol^{-1}$ remains constant down to 232 K;

however, below this temperature, it decreases gradually in a succession of sligthly marked steps, reaching a value of 0.15 $cm^3$ K $mol^{-1}$ at 100 K. Except for the lower step, which shows a small hysteresis between 130 K and 138 K, the cooling-heating profiles are practically superposed. The corresponding characteristic $T_c$ temperature is 170 K. The SCO profile for the **MpyS₂Et** derivatives is similar to that of **PtpyS₂Me**, featuring strong cooperative hysteretic behaviors with $T_c$ temperatures 121.5 and 154.0 K ($\Delta$T = 32.5 K) for M = Pt and 111.0 and 132.0 K ($\Delta$T = 21.0 K) for M = Pd, in the cooling and heating modes, respectively.

Photogeneration of the fully populated metastable HS* state, the so-called "light-induced excited spin state trapping (LIESST) experiment",[27] was performed by irradiating microcristalline samples of the title compounds with green light ($\lambda$ = 532 nm) at 10 K. Under these conditions, all the samples but **PtpyS₂Me** display the LIESST effect and saturate at $\chi_M T$ values of 2.08 $cm^3$ K $mol^{-1}$ for **PdpyS₂Me** and 2.80 $cm^3$ K $mol^{-1}$ for **MpyS₂Et** (M = Pt, Pd). Subsequently, the light was switched off and the temperature increased at a rate of 0.3 K/min inducing a gradual increase of $\chi_M T$ to a value of 2.36 $cm^3$ K $mol^{-1}$ at 26 K for **PdpyS₂Me** and 3.54 $cm^3$ K $mol^{-1}$ at ca. 48 K for **MpyS₂Et** (M = Pt, Pd), which corresponds to ca. 64% and 96% of the maximum value observed at 300 K, respectively. This increase in $\chi_M T$ reflects the thermal population of different microstates originated from the zero-field splitting of the HS* spin state. At higher temperatures, $\chi_M T$ decreases rapidly until joining the thermal SCO curve at ca. 65 K (**PdpyS₂Me**), 69 K (**PtpyS₂Et**) and 76 K (**PdpyS₂Et**), indicating that the metastable HS* state has relaxed back to the stable LS state. The corresponding $T_{LIESST}$ temperatures, evaluated as $\partial(\chi_M T)/\partial T$,[28] are 50.0 K (**PdpyS₂Me**) and 68-70 K (**MpyS₂Et**, M = Pt, Pd). These temperatures are consistent with the inverse-energy-gap law, i.e., the metastability of the photogenerated HS* species decreases as the stability of the LS increases, namely as $T_c$ increases.[29]

The SCO behavior was also investigated through the thermal dependence of the heat capacity at constant pressure, $\Delta C_p$, for **MpyS₂Me** (M =Pt, Pd) (Figure 2). The low SCO temperatures observed for both ethyl derivatives preventes us to evaluate their thermodynamic parameters. The average enthalpy $\Delta H$ and entropy $\Delta S$ (= $\Delta H/T_c$) are, respectively, 16.12 kJ $mol^{-1}$ and 79.89 J $K^{-1}$ $mol^{-1}$ for **PtpyS₂Me** and 7.68 kJ $mol^{-1}$ and 45.18 J $K^{-1}$ $mol^{-1}$ for **PdpyS₂Me**. The $\Delta H$ and $\Delta S$ values found for **PtpyS₂Me** are comparable to those reported for similar Hofmann-type coordination polymers with comparable cooperative SCO.[1b,2d] However, for **PdpyS₂Me** these values are considerably smaller due to the fact that ca. 27% of the SCO occurs out of the temperature window of our calorimeter, an

extrapolation to 100% gives $\Delta H$ = 10.5 kJ $mol^{-1}$ and $\Delta S$ = 62 J $K^{-1}$ $mol^{-1}$ (see also Figure S2 in the Supporting Information). These extrapolated values are still smaller than those observed for **PtpyS$_2$Me** but consistent with the much less cooperative gradual SCO and lower $T_c$ temperature of the homologous Pd derivative. The $T_c$ values obtained from the calorimetric measurements are virtually the same than those obtained from magnetism (see Figure S2). As it can be seen from Figure 2, the surprisingly distinct nature of both SCO behaviours, hysteretic versus multistepped, are clearly reflected in the $\Delta C_p$ vs $T$ plots.

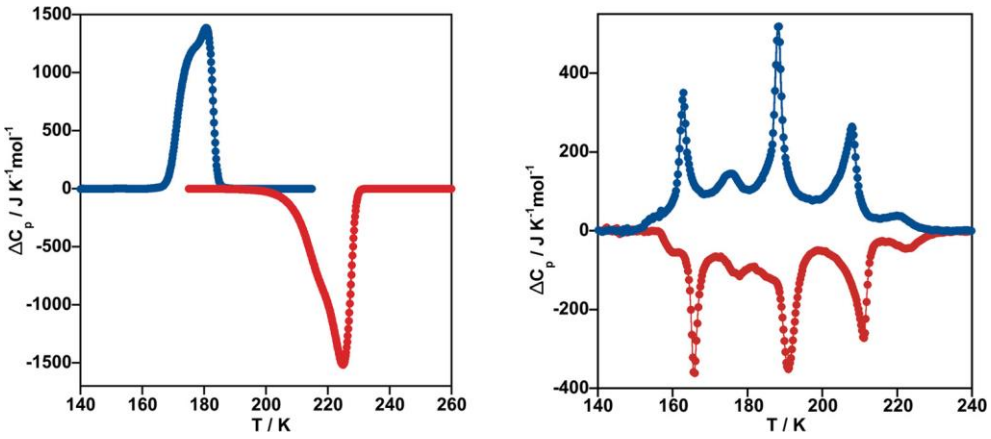


**Fig. 2.** Thermal dependence of $\Delta C_p$ *vs* $T$ for **PtpyS$_2$Me** (left) and **PdpyS$_2$Me** (right). Note that for the latter the step below 150 K could not be recorded (see text). Cooling and heating modes are represented in blue and red, respectively.

### 3.3.2.- Single-Crystal Struture Analysis

#### *3.3.2.1.- Structure of **MpyS$_2$Me***

The crystal structure of **MpyS$_2$Me** (M = Pt and Pd) was investigated at 120 and 250 K; it turned out to be isostructural and crystallized in the triclinic *P*-1 space group. A selection of relevant crystallographic data for **MpyS$_2$Me** (M = Pt, Pd) is given in Table S1 in the Supporting Information. At 120 K, the structure is characterized by a christallographically unique $Fe^{II}$ site lying in an inversion center defining a slightly elongated [$Fe^{II}N_6$] octahedron. A representative fragment of the structure including the atom numbering is shown in Figure 3 (left). Table 1 contains a selection of significant bond lengths and angles, together with the corresponding average angular distortion parameter $\sum^{Fe}$, which is defined as the sum of deviations from the ideal octahedron/tetrahedron of the 12 "cis" bond angles, $\sum_{i=1}^{i=12}|\theta_i - 90|$.

The equatorial positions are occupied by the N2 and N3 atoms of the CN groups belonging to the $[Pt^{II}(CN)_4]^{2-}$ bridging ligands, while the axial positions are occupied by the N1 atom of the pyridine group of the $pyS_2Me$ ligand. The average <Fe–N> bond length, 1.960(14) Å (M = Pt) and 1.957(3) Å (M = Pd), are typical of the $Fe^{II}$ site in the LS state and consistent with the magnetic data and the characteristic deep red color of the crystals at the same temperature. The $\sum^{Fe}$ parameter, almost 0 for the Pd derivative and relatively much larger for the Pt derivative, denote that the anfular distortion in both compounds is very small and practically independent of the spin state.

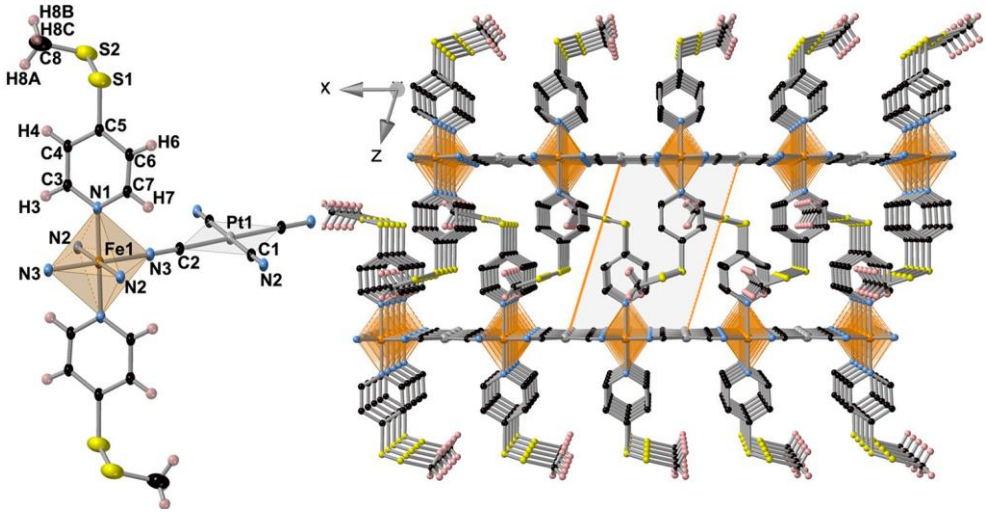


**Fig. 3.** (Left) Molecular fragment of **$PtpyS_2Me$** showing the atom numbering of the asymmetric unit. (Right) Packing of two consecutive layers (only one of the two possible orientations of the –S–S–Me moiety is shown).

Each $Fe^{II}$ site is bridged to four equivalent $Fe^{II}$ sites through four equivalent square planar $[Pt^{II}(CN)_4]^{2-}$ bridges defining 2D layers in which the equatorial planes of the $[Fe^{II}N_6]$ and $[Pt^{II}C_4]$ centers are strictly coplanar (Figure 3, right). Two consecutive layers interdigitate in such a way that the $pyS_2Me$ axial ligands of one layer point toward the center of the square windows of the adjacent layers, with the distance between the $\{Fe^{II}_2[M^{II}(CN)_4]_2\}_n$ layers being equal to 10.36 Å (M = Pt) and 10.75 Å (M = Pd). The S–S–$CH_3$ tails display positional disorder in two equivalent positions for the Pt derivatibe while the disorder is considerably more severe for the Pd derivative also involving the pyridine groups (see Figure S3 in the Supporting Information). At 250 K, the structures are essentially the

same, being the most significant differences, with respect to those at 120 K, the increase of the <Fe–N> bond length by 0.2 Å and the change of color of the crystals to yellow. Both facts are perfectly consistent with the full population of the $Fe^{II}$ HS state in agreement with the magnetic data. In addition, the change to the HS state in the Pt derivative is accompanied by a small degree of corrugation. The angle defined between the equatorial $Fe^{II}N_4$ and the $[Pt^{II}(CN)_4]^{2-}$ square planes is 7.64º. Consistently, the Fe–N2–C1 angle decreases 9º from 178(2)º in the LS state until 169(2)º in the HS state. Furthermore, the separation of two consecutive $[Fe_2M_2]_n$ layers increases by 0.38 Å until 10.95 Å (see Figure S2).

**Table 1.** Selected Bond Lengths and Angles for $MpyS_2Me$ (M = Pd, Pt).

| | **PdpyS Me, 120 K** | **PdpyS$_2$Me, 250 K** | **PtpyS$_2$Me, 120 K** | **PtpyS$_2$Me, 250 K** |
|---|---|---|---|---|
| | | **Selected Bond Lengths [Å]** | | |
| Fe–N(1) | 1.987(3) | 2.219(5) | 1.992(14) | 2.23(3) |
| Fe–N(2) | 1.942(3) | 2.132(4) | 1.943(14) | 2.13(2) |
| Fe–N(3) | 1.943(3) | 2.137(4) | 1.945(14) | 2.11(2) |
| Pd–C(1) | 1.991(3) | 1.991(4) | | |
| Pd–C(2) | 1.992(3) | 1.988(5) | | |
| Pt–C(1) | | | 1.975(17) | 1.97(2) |
| Pt–C(2) | | | 1.978(17) | 1.93(2) |
| C(1)–N(2) | 1.149(4) | 1.131(7) | 1.15(3) | 1.16(3) |
| C(2)–N(3) | 1.153(5) | 1.130(7) | 1.15(3) | 1.21(3) |
| | | **Selected Bond Angles (°)** | | |
| N(1)–Fe–N(2) | 90.06(12) | 90.1(2) | 90.7(6) | 91.6(11) |
| N(1)–Fe–N(3) | 90.13(12) | 90.0(2) | 90.5(6) | 91.0(11) |
| N(2)–Fe–N(3) | 90.01(10) | 90.04(14) | 91.0(6) | 90.2(6) |
| $\Sigma^{Fe}$ | 0.8 | 0.56 | 8.8 | 11.2 |
| C(1)–N(2)–Fe | 179.8(2) | 179.7(5) | 178(2) | 169(2) |
| C(2)–N(3)–Fe | 179.8(3) | 179.9(5) | 177(2) | 178(2) |

*3.3.2.1.- Structure of **MpyS$_2$Et***

The crystal structures of **MpyS$_2$Et**, M = Pt and Pd, were investigated at 100 and 250 K turning out to be isostructural. At 100 K, the red crystals of both derivatives display a monoclinic *I*2/*m* unit cell that changes to monoclinic *C*2/*m* at 250 K, where the crystals are tallow (see Table S2). Table 2 contains a selection of significant bond lengths and angles

including the distortion parameter $\sum^{Fe}$. The asymmetric unit contains one slightly distorted [$Fe^{II}N_6$] octahedral site defined by two distinct $pyS_2Et$ axial ligands coordinated, respectively via N1 and N2 and to distinct $[M(CN)_4]^{2-}$ groups coordinated, respectively, via N3 and N4 (Figure 4). The two pyridine rings of $pyS_2Et$ and the $Fe^{II}$ center lie in a reflection plane which bisects the equatorial N3-Fe-N3' and N4-Fe-N4' angles. At 100K, the <Fe–N> is 1.961(5) nd 1.968(4) Å for the Pt and Pd derivatives, respectively, are consistent with the $Fe^{II}$ centers in a fully populated LS state whereas, at 250 K, these average bond lengths increase by 0.20-0.21 Å attaining typical values for the $Fe^{II}$ in the HS state [2.166(9) and 2.179(9) Å, respectively]. The $\sum^{Fe}$ parameter is small (~20º) and remains almost constant upon SCO. There are two crystallographically distinct $[M^{II}(CN)_4]^{2-}$ groups and two pairs of them connect each $Fe^{II}$ center to four wquivalent atoms defining an irregularly corrugated layer. Indeed, at 100 K, the angle defined between the $[M1^{II}(CN)_4]^{2-}$/$[M2^{II}(CN)_4]^{2-}$ squares and the equatorial plane of the $Fe^{II}$ center is, respectively, 4.04º/4.24º and 20.47º/21.40º and increase by ca. 36% up to 6.22º–6.56º and 32.26º–35.82º for M = Pt/Pd at 250 K. The change of this angle occurs through the Fe–N3–C1, which decrease 10.9º (Pd) and 9º (Pt) when moving from the LS to the HS state. The separation between two consecutive layers, measured from the average plane defined by M1 and M2, is very similar for the two derivatives and practically does not change with temperature (11.15–11.52 Å).

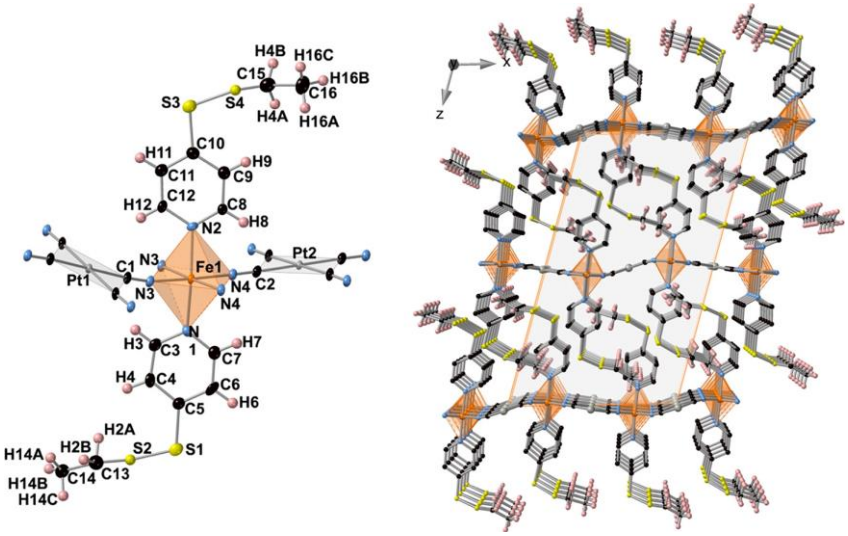


**Fig. 4.** (Left) Molecular fragment of **$PtpyS_2Et$** showing the atom numbering of the asymmetric unit. (Right) Packing of three consecutive layers (only one of the two possible orientations of the –S–S–Et moiety is shown).

**Table 2.** Selected Bond Lengths and Angles for $MpyS_2Me$ (M = Pd, Pt).

| | **$PdpyS_2Et$,100 K** | **$PdpyS_2Et$,250 K** | **$PtpyS_2Et$,100 K** | **$PtpyS_2Et$,250 K** |
|---|---|---|---|---|
| | | **Selected Bond Lengths [Å]** | | |
| Fe−N(1) | 2.001(5) | 2.218(8) | 1.997(7) | 2.205(7) |
| Fe−N(2 | 2.017(5) | 2.237(9) | 2.004(6) | 2.202(9) |
| Fe−N(3) | 1.946(4) | 2.170(5) | 1.940(5) | 2.162(5) |
| Fe−N(4) | 1.948(4) | 2.140(5) | 1.944(5) | 2.133(5) |
| Pd(1)−C(1) | 1.992(4) | 1.987(7) | | |
| Pd(2)−C(2) | 2.003(5) | 2.005(6) | | |
| Pt(1)−C(1) | | | 1.981(5) | 1.987(5) |
| Pt(2)−C(2) | | | 1.989(5) | 1.993(5) |
| C(1)−N(3) | 1.146(5) | 1.145(8) | 1.160(7) | 1.142(6) |
| C(2)−N(4) | 1.146(5) | 1.126(8) | 1.159(7) | 1.141(7) |
| | | **Selected Bond Angles [°]** | | |
| N(1)−Fe−N(3) | 91.29(14) | 90.7(2) | 91.4(2) | 90.5(2) |
| N(1)−Fe−N(4) | 90.72(14) | 91.3(2) | 90.6(2) | 91.2(2) |
| N(2)−Fe−N(3) | 86.83(14) | 86.7(2) | 86.6(2) | 86.6(2) |
| N(2)−Fe−N(4) | 91.18(14) | 91.2(2) | 91.5(2) | 91.7(2) |
| N(3)−Fe−N(4) | 88.43(14) | 88.3(2) | 88.3(2) | 88.5(2) |
| N(3)−Fe−N(3) | 91.9(2) | 90.4(3) | 92.0(3) | 90.2(3) |
| N(4)−Fe−N(4) | 91.2(2) | 93.0(3) | 91.3(3) | 92.7(3) |
| $\Sigma^{Fe}$ | 19.96 | 19.8 | 20.5 | 19.5 |
| C(1)−N(3)−Fe | 169.7(4) | 158.8(6) | 169.3(4) | 160.3(5) |
| C(2)−N(4)−Fe | 178.0(3) | 177.7(6) | 178.1(4) | 177.1(5) |

## 3.4.- Discussion

Since the first SCO Hofmann type 2D coordination polymer $\{Fe^{II}(pyridine)_2[M^{II}(CN)_4]\}$, $M^{II}$ = Ni,[30] and its isostructural $Pd^{II}$ and $Pt^{II}$ counterparts[31] were reported, this family of compounds has been steadily growing until recently (see refs 2d, g, 14, 15, 18). Despite their high insolubility, their synthesis based on formal replacement of the axial lpyridines with homologous N-donor ligands can be addressed in a straightforward manner to obtain samples constituted exclusively of single crystals by employing liquid-liquid slow diffusion techniques, which is the safes way to get pure samoles with reliable SCO properties for this type of compounds. The strong cooperative SCO behavior featuring well-shaped symmetric hysteresis loops expressed by many of these compounds is likely the most appealing aspect, which explains the interest and growth of this family of compounds. This cooperativity seems to be originated mainly from the robust nature of the $\{Fe^{II}[M^{II}(CN_4)]\}_n$ layers where all SCO centers are strongly coupled. Indeed, most of the $\{Fe^{II}(L)_2[M^{II}(CN)_4]\}$

compounds show hysteresis widths ranging in the interval of 10-30 K, but it has also been reported hysteresis close to 40 K[32a,18b] or even larger (50-65 K).[15g] It is reasonable to consider that the nature of the axial ligands and included guest molecules play an important role in the modulation of the observed cooperativity, however, this is a fact that generally has no obvious rationalization. In addition, it is also worth noting that the hysteresis width seems not to be correlated with the length of the axial ligand, namely, with the separation between the $\{Fe^{II}[M^{II}(CN)_4]\}_n$ layers. For example, interdigitation of the relatively long ligands L = 4-styrylpyridine (n = 0.5) and 4-(2-phenylethyl)pyridine (n = 0) in $\{Fe^{II}(L)_2[Pt^{II}(CN)_4]\}\cdot n$MeOH separates the $\{Fe^{II}[Pt^{II}(CN)_4]\}_n$ layers by ca. 13.85 Å and although both compounds display sharp SCO transitions they lack of hysteretic behavior.[32b] In contrast, the closely related axial ligands L = 3-phenylazopyridine and 4-phenylazopyridine in $\{Fe^{II}(L)_2[Pd^{II}(CN)_4]\}$ with similar interdigitation induce abrupt hysteretic spin transitions with $\Delta T_c$ = 12 and 17 K, respectively.[32c] An additional difficulty when dealing with this type of compounds is that the spin crossover nature ($T_c$, $\Delta T_c$, completeness, abruptness, etc.) may be strongly affected by the degree of crystallinity. A relevant example has been recently observed for $\{Fe^{II}(pyridine)_2[Pt^{II}(CN)_4]\}$ (separation between layers $\{Fe^{II}[Pt^{II}(CN)_4]\}_n$ ca. 7.6 Å). In its precipitated microcrystalline form, it displays a SCO centered at 212 K with a hysteresis 8 K wide, which is characterized by a remarkable residual fraction (15%-19%) of inactive HS centers. In contrast, the same compound exclusively constituted of single crystals shows a complete well-shaped SCO centered at 234 K and a hysteresis 42 K wide (see Figure S4 in the Supporting Information).[17] Rapid precipitation of these highly insoluble compounds usually produces microcrystalline samples consisting of submicrometric/nanometric crystallites, dramatically influencing the SCO via the increase of crystal defects, and hence consisting of the residual HS molar fraction in the LS phase, which, in turn is reflected on a decrease of the $T_c$, of cooperativity ($\Delta T_c$) and completeness of the SCO.

In the present study, the SCO behavior has been investigated for samples exclusively constituted of single crystals. Except for **PdpyS$_2$Me**, the SCO behavior of the title compouns **MpyS$_2$R** (R = Me, Et; M = Pd, Pt) retain the general features described for other Hofmann-type 2D polymers. Compound **PtpyS$_2$Me** undergoes a particularly stron cooperative transition with a hysteresis $\Delta T$ = 44 K wide, which, despite an interlayer distance increase of ~2–3 Å, because of the presence of the flexible –S–S–CH$_3$ moieties, it is virtually the same than the SCO observed for single crystals of $\{Fe^{II}(pyridine)_2[Pt^{II}(CN)_4]\}$. The only

noticeable difference is observed for the average $T_c^{av}$ value, which is 32 K less than that observed for the pyridine derivative. This result also supports the idea mentioned above that separation between the layers does not substantially affect the cooperativity.

Replacement of the methyl group by the ethyl group in **MpyS$_2$R** does not significantly change the separation between the layers but involves a considerable decrease in $T_c^{av}$ from 202 K to 138 K (64 K) for the Pt derivative. This fact could tentatively be correlated with a higher corrugation of the layers in the ethyl derivatives. This fact is clearly reflected in the decrease from 180º of one of the two Fe–N–C–Pt moieties. Fot **PtpyS$_2$Me**, the angle Fe–N2–C1(Pt) is 168.5º, whilethe equivalent angle for **PtpyS$_2$Et**, Fe–N3–C1(Pt), is 158.8º, both in the HS state, and they change to 178.0º and 169.6º in the LS state, respectively. Obviously the larger misalignment of the N–C–Pt moiety, with respect to the 3d orbitals of $Fe^{II}$ in the ethyl derivative, must necessarily decrease the σ and π overlaps, thereby desreasing the ligand field felt by the $Fe^{II}$ centers. Another important difference pointing to the same direction is that the angular distortion $\sum^{Fe}$ (see Tables 1 and 2) is significantly larger for **PtpyS$_2$Et** than for its methyl counterpart.

Surprisingly, even though both **MpyS$_2$Me** ( M = Pd, Pt) compounds are isostructural, their SCO properties are drastically different to each other. The Pd derivative shows a relatively gradual multistep behavior (ca. 6 steps) separated by very narrow plateaus, while the Pt derivative displays a sharp cooperative spin transition with large hysteresis. The most significant structural difference between them is the occurrence of positional disorder of the pyridine and S–S–$CH_3$`groups over four orientations in the Pd derivative, which remains in the HS and LS states. The behavior is reminiscent of that found, among others, for the 2D coordination polymer $\{Fe^{II}[Hg^{II}(SCN)_3]_2(4,4'\text{-bipy})_2\}_n$ where a sequence of different phases characterized by distict HS/LS fractions and symmetry breaking results from competition between SCO and structural 4,4'-bipy ligand ordering. For this system, it was possible to identify a correlation between the internal dihedral angle adopted by the 4,4'-bipy ligand and each particular step (spin state phase) as being responsible for the observedmultistability.[33] From a phenomenological point of view, thermally induced multistep SCO behavior is associated with elastic frustration,[3b,c] namely, the occurrence of subtle balances between opposed intramolecular interactions that drive the HS ↔ LS transformation in fractional steps consistent with different concentrations of HS and LS centers (with or without ordering). For **PdpyS$_2$Me**, the more conspicuous positional disorder may be the ource of subtle balances between interlayer interactions and/or distortions of the [$FeN_6$] centers.

However, to precisely identify the structural constraints favouring the steps, is for most of the known multistep SCO examples a major difficulty in particular when the steps are poorly defined.

## 3.5.- Conclusions

Here, we have described the synthesis, structure, magnetic, photomagnetic and calorimetric properties of four new Hofmann-type 2D SCO coordination polymers. Three of them show strong cooperative SCO properties, featuring wide thermal hysteresis, in particular compound **PtpyS$_2$Me**, while its isostructural Pd counterpart surprisingly displays a multistepped transition without hysteresis, most likely due to the occurrence of additional disorder in the structure. The **MpyS$_2$Et** derivatives, which have the lowest $T_c$ of the series, show a complete LIESST effect. In contrast, the LIESST effect is incomplete for **PdpyS$_2$Me** and vanishes completely for **PtpyS$_2$Me** because of their higher $T_c$ values.

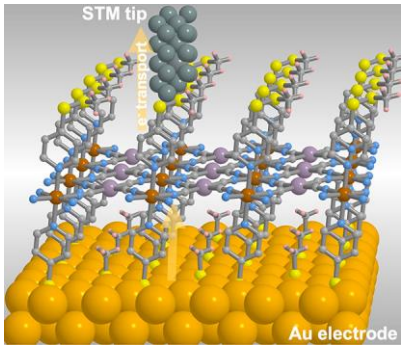


**Scheme 1.** Model of Device Constituted of a Monolayer of **MpyS$_2$Me** Deposited on an Au Substrate

The results here reported correspond to the first step in a more challenging work whose ultimate objective is to graft these Hofmann-type 2D SCO coordination polymers as monolayers on metallic surfaces (e.g., Au) to be probed as junctions for spintronic devices in which the switchable SCO centers can be used to modulate the junction conductance (see Scheme 1). The choice of 4-alkyldisulfanylpyridines as axial ligands was based on the well-known fact that S atoms ensure appropriate interaction between the molecular wires and the electrodes. Preliminary work on this second objective confirms its feasibility and definitive conclusions will be reported in due time.

## 3.6.- Experimental section

### Materials and Reagents.

$Fe(BF_4)_2 \cdot 6H_2O$, $K[Pt(CN)_4]$, $K[Pd(CN)_4]$, 4-mercaptopyridine and methyl methanethiosulfonate were purchased from commercial sources and used as received withour further purification. Ethyl methanethiosulfonate was synthesized following a literature procedure.[34]

Synthesis of Methyl/Ethyl(4-pyridyl)disulfide. The synthesis of methyl(4-pyridyl)disulfide was performed a method previously described.[35] Stoichiometric amounts of NaOH (5 mmol), 4-mercaptopyridine (5 mmol) and methylmethanethiosulfonate (5 mmol) were dissolved in water (10 mL). A white turbidness appears innmediately which slowly transforms to a yellow oil. The reaction mixture was stirred at room temperature for 30 min and then extracted with $CH_2Cl_2$. The organic phase was dried with $MgSO_4$ and subsequently evaporated to obtain a yellow oil, which was purified by $SiO_2$ column chromatography using a toluene-ethyl acetate mixture (80:20) as eluent. 300 Mhz, $CDCl_3$, δ/ppm: 8.49 (2H), 7.44 (2 H) 2.46 (3H). The same route was followed for the synthesis of ethyl(4-pyridyl)disulfide using the noncomercial precursor ethyl methanethiosulfonate. 300 MHz $^1$H-RMN, $CDCl_3$, δ/ppm: 8.47 (2H), 7.45 (2H), 2.77 (2H), 1.32 (3H).

Synthesis of Complexes **$MpyS_2R$** (M = Pt, Pd; R = Me, Et). All the samples were constituted of single crystals exclusively obtained through slow liquid-toliquid diffusion methods using a 10-mL-total-volume H-shaped tube. One arm of the tube was filled with 1 mL of $H_2O$:MeOH (1:1) solution containing a mixture of 33.7 mg of $Fe(BF_4)_2 \cdot 6H_2O$ (0.1 mmol) and 40/44 mg (0.25 mmol) of methyl/ethyl(4-pyridyl)disulfide, whereas the other was filled with an aqueous solution (1 mL) of 44/35 (0.1 mmol) of $K_2[M(CN)_4]$ (M = $Pt^{II}$/$Pd^{II}$). The rest of the tube was carefully filled with a methanol:water (1:1) solution, closed with parafilmd and left to stand at room temperature. Light yellow cubic single crystals of **$MpyS_2R$** were obtained after 2 weeks. Elemental analysis Calculated for $PtpyS_2Me$ [$C_{16}H_{14}N_6S_4FePt$ (669.5) (%)]: C 28.70; H 2.11; N 12.55. Found (%): C 29.11; H 2.08; N 12.78. Calculated for $PdpyS_2Me$ [$C_{16}H_{14}N_6S_4FePd$ (580.8) (%)]: C 33.09; H 2.43; N 14.47. Found (%): C 33.57; H 2.15; N 14.65. Calculated for $PtpyS_2Et$ [$C_{18}H_{18}N_6S_4FePt$ (697.6) (%)]: C 30.99; H 2.60; N 12.05. Found (%): C 30.52; H 2.52; N 12.35. Calculated for $PdpyS_2Et$ [$C_{18}H_{18}N_6S_4FePd$ (608.9) (%)]: C 35.51; H 2.98; N 13.80. Found (%): C 35.17; H 2.90; N 14.01.

**Physical Measurements.**

*Magnetic Measurements*. Variable temperature magnetic susceptibility data were recorded with a Quantum Design MPMS2 SQUID magnetometer equipped with a 7 T magnet, operating at 1 T and at temperatures of 1.8-400 K. Experimental susceptibilities were corrected for diamagnetism of the constituent atoms using Pascal's constants.

*Calorimetric Measurements*. DSC measurements were performed using a differential scanning calorimeter (Mettler Toledo, Model DSC 821e). Low temperatures were obtained with an alumninum block attached to the sample holder, refrigerated with a flow of liquid nitrogen and stabilized at a temperature of 110 K. The sample holder was kept in a drybox under a flow of dry nitrogen gas to avoid water condensation. The measurements were performed using ~15 mg of microcrystalline samples of **MpyS$_2$Me** (M = Pt, Pd) sealed in aluminum pans with a mechanical crimp. Temperature and heat flow calibrations were made with standard samples of indium by using its melting transition (429.6 K, 28.45 J g$^{-1}$). An overall accuracy of ±0.2 K in temperature and ±2% in the heat capacity is estimated. The uncertainty increases for the determination of the anomalous enthalpy and entropy due to the substraction of an unknown baseline.

*Single Crystal X-ray Diffraction.* Single crystal X-ray data were collected on an Oxford Diffraction Supernova diffractometer using a graphite monochromated Mo Kα radiation (λ = 0.71073 Å). A multiscan absorption correction was performed. The structures were solved by direct methods using SHELXS-2014 and refined by full matrix least squares on $F^2$ using SHELXL-2014.[36] Non-hydrogen atoms were refined anisotropically ad hydrogen atoms were placed in calculated positions refined using idealized geometries (riding model) and assigned fixed isotropic displacement parameters. CCDC 2072898 (100 K) and 2072899 (250 K) (**PdpyS$_2$Et**); 2072902 (129 K) and 2072901 (250 K) (**PdpyS$_2$Me**); 2072900 (100 K) and 2072905 (250 K) (**PtpyS$_2$Et**); and 2072903 (120 K) and 2072904 (250 K) (**PtpyS$_2$Me**) contain the supplementary crystallographic data for this article. These data can be obtained free of charge from The Cambridge Crystallographic Data Centre via www.ccdc.cam.ac.uk/data_request/cif.

## 3.7.- References

[1] (a) J. A. Real, A. B. Gaspar, V. Niel and M. C. Muñoz, *Coord. Chem. Rev.,* 2003, **236**, 121-141; (b) P. Gütlich and G. Goodwin, Spin crossover in transition metal compound I-III, *Top. Curr. Chem.*, 2004, 233-235; (c) J. A. Real, A. B. Gaspar and M. C. Muñoz, *Dalton Trans.,* 2005, 2062-2079; (d) A. Bousseksou, G. Molnár, L. Salmon and W. Nicolazzi, *Chem. Soc. Rev.* 2011, *40*, 3313-3335; (e) M. A. Halcrow (ed.), Spin-Crossover Materials: Properties and Applications; Wiley & Sons, 2013; (f) A. Bousseksou (ed.) Spin Crossover Phenomenon, *C. R. Chimie*, 2018, **21**, 1055-1299.

[2] (a) B. Weber, *Chem. Soc. Rev.* 2009, **253**, 2432-2449; (b) Y. Sunatsuki, R. Kawamoto, K. Fujita, H. Maruyama, T. Suzuki, H. Ishida, M. Kojima, S. Iijima and N. Matsumoto, *Coord. Chem. Rev.* 2010, **254**, 1871-1881; (c) G. Aromí, L. A. Barrios, O. Roubeau and P. Gamez, *Coord. Chem. Rev.* 2011, **255**, 485-546; (d) M. C. Muñoz, J. A. Real, *Coord. Chem. Rev*. 2011, **255**, 2068-2093; (e) M. Shatruk, H. Phan, B. A. Chrisostomo and A. Suleimenova, *Coord. Chem. Rev.* 2015, **289-290**, 62-73; (f) N. Ortega-Villar, M. C. Muñoz and J. A. Real, *Magnetochemistry* 2016, **2**, 16-22; (g) Z.-P. Ni, J.-L. Liu, M. N. Hoque, W. Liu, J.-Y Li, Y.-C Chen and M.-L. Tong. *Coord. Chem. Rev.*, 2017, **335**, 28-43; (h) R. W. Hogue, S. Singh and S. Brooker. *Chem. Soc. Rev.* 2018, **47**, 7303-7338; (i) Y.-C Chen, Y. Meng, Y.-J Dong, X.-W Song, G. Z. Huang, C.-L. Zhang, Z.-P Ni, J. Navarík, O. Malina, R. Zboril and M.-L. Tong, *Chem. Sci.* 2020, **11**, 3281-3289; (j) I. C. Berdiell, T. Hochdörffer, C. Desplanches, R. Kulmaczewski, N. Shahid, J. A. Wolny, S. L. Warriner, O. Cespedes, V. Schünemann, G. Chastanet and M. A. Halcrow, *J. Am. Chem. Soc.*, 2019, **141**, 18759-18770; (jj) S. Chorazy, T. Charytanowicz, D. Pinkowicz, J. Wang, K. Nakabayashi, S. Klimke, F. Renz, S.-I Ohkoshi and B. Sieklucka, *Angew. Chem. Int. Ed.*, 2020, **59**, 15741-15749.

[3] (a) R. Bertoni, M. Lorenç, A. Tissot, M.-L., Boillot and E. Collet, *Coord. Chem. Rev.*, 2015, **282-283**, 66-76; (b) M. Paez-Espejo, M. Sy and K. Boukheddaden, *J. Am. Chem. Soc.*, 2016, **138**, 3202-3210; (c) R. Traiche, M. Sy, K. Boukheddaden, *J. Phys. Chem. C*, 2018, **122**, 4083-4096.

[4] P. G. Lacroix, L. Malfant, J.-A. Real and V. Rodriguez, *Eur. J. Inorg. Chem.*, 2013, **2013**, 615-627.

[5] C. Lefter, V. Davesne, L. Salmon, G. Molnár, P. Demont, A. Rotaru, A. Bousseksou, *Magnetochemistry* 2016, **2**, 18.

[6] M. Matsuda, H. Isozaki and H. Tajima, *Thin Solid Films* 2008, **517**, 1465-1467.

[7] (a) J. Garcia, F. Robert, A. D. Naik, G. Zhou, B. Tinant, K. Robeyns, S. Michotte and L. Piraux, *J. Am. Chem. Soc.*, 2011, **133**, 15850-15853; (b) C. Lochenie, K. Schotz, F. Panzer, H. Kurz, B. Maier, F. Puchtler, S. Agarwal, A. Kohler and B. Weber, *J. Am. Chem. Soc.* 2018, **140**, 700-709; (c) T. Delgado, M. Meneses-Sánchez, L. Piñeiro-López, C. Bartual-Murgui, M. C. Muñoz and J. A. Real, *Chem. Sci.*, 2018, **9**, 8446-8452; (d) B. Benaicha, K. Van Do, A. Yangui, N. Pittala, A. Lusson, M. Sy, G. Bouchez, H. Fourati, C. J. Gómez-García, S. Triki and K. Boukheddaden, *Chem. Sci.* 2019, **10**, 6791-6798; (e) J.-Y Ge, Z. Chen, L Zhang, X. Liang, J. Su, M. Kurmoo and J.-L Zuo, *Angew. Chem., Int. Ed.* 2019, **58**, 8789-8793; (f) S. Ghosh, S. Kamilya, T. Pramanik, M. Rouzières, R. Herchel, S. Mehta and A. Mondal, *Inorg. Chem.* 2020, **59**, 13009-13013; (g) M. Meneses-Sánchez, L. Piñeiro-López, T. Delgado, C. Bartual-Murgui, M. C. Muñoz, P. Chakraborty and J. A. Real, *J. Mater. Chem. C*, 2020, **8**, 1623-1633.

[8] A. B. Gaspar and M. Seredyuk, *Coord. Chem. Rev.* 2014, **268**, 41-58.

[9] (a) Z. Ni and M. P. Shores, *J. Am. Chem. Soc*, 2009, **131**, 32-33; (b) M. Darawsheh, L. A. Barrios, O. Roubeau, S. J. Teat and G. Aromí, *Angew. Chem. Int. Ed.* 2018, **57**, 13509-13513.

[10] (a) S.-I. Ohkoshi, K. Imoto, Y. Tsunobuchi, S. Takano and H. Tokoro, *Nat. Chem.*, 2011, **3**, 564-569; (b) S.-I. Ohkoshi, S. Takano, K. Imoto, M. Yoshikiyo, A. Namai and H. Tokoro, *Nat. Photonics* 2014, **8**, 65-71.

[11] (a) C. Bartual-Murgui, L. Piñeiro-López, F. J. Valverde-Muñoz, M. C. Muñoz, M. Seredyuk and J. A. Real, *Inorg. Chem.* 2017, **56**, 13535-13546; (b) X.-P. Sun, Z. Tang, Z.-S. Yao and J. Tao, *Chem. Commun.* 2020, **56**, 133-136.

[12] (a) S. Venkataramani, U. Jana, M. Dommaschk, F. D. Sönnichsen, F. Tuczek and R. Herges, *Science* 2011, **331**, 445-448. (b) L.-F. Wang, W.-M. Zhuang, G.-Z. Huang, Y.-C. Chen, J.-Z. Qiu, Z.-P. Ni and M.-L. Tong, *Chem. Sci.* 2019, **10**, 7496-7502.

[13] (a) K. Senthil Kumar and M. Ruben, *Coord. Chem. Rev.* 2017, **346**, 176-205; (b) G. Molnar, S. Rat, L. Salmon, W. Nicolazzi and A. Bousseksou, *Adv. Mater.* 2018, **30**, 1703862; (c) A. Bellec, J. Lagoute and V. Repain, *C. R. Chim.* 2018, **21**, 1287-1299; (d) K. S. Kumar and M. Ruben, *Angew. Chem. Int. Ed.* 2021, **60**, 7502; (e) M. Gruber and R. Berndt, *Magnetochemistry* 2020, **6**, 35.

[14] For recent references, see: (a) W. Liu, L. Wang, Y.-J. Su, Y. C. Chen, J. Tucek, R. Zboril, Z.-P. Ni and M.-L. Tong, *Inorg. Chem.* 2015, **54**, 8711-8716; (b) O. I. Kucheriv, S. I. Shylin, V. Ksenofontov, S. Dechert, M. Haukka, I. O. Fritsky and I. A. Gural'skiy, *Inorg. Chem.* 2016, **55**, 4906-4914; (c) F. J. Valverde-Muñoz, M. Seredyuk, M. C. Muñoz, K. Znovjyak, I. O. Fritsky and J. A. Real, *Inorg. Chem.* 2016, **55**, 10654-10665; (d) F.-L Liu and J. Tao, *Chem – Eur. J*, 2017, **23**, 18252-18257; (e) I. A. Gural'skiy, S. I. Shylin, V. Ksenofontov and W. Tremel, *Eur. J. Inorg. Chem.* 2019, **2019**, 4532-4537; (f) V. M. Hiiuk, S. Shova, A. Rotaru, A. A. Golub, I. O. Fritsky and I. A. Gural'skiy, *Dalton Trans.* 2020, **49**, 5302-5311; (g) R. Turo-Cortés, C. Bartual-Murgui, J. Castells-Gil, M. C. Muñoz, C. Martí-Gastaldo and J. A. Real, *Chem. Sci.* 2020, **11**, 11224-11234.

[15] (a) Y. M. Klein, N. F. Sciortino, F. Ragon, C. E. Housecroft, C. J. Kepert and S. M. Neville, *Chem. Commun.* 2014, **50**, 3838-3840; (b) E. Milin, V. Patinec, S. Triki, E.-E. Bendeif, S. Pillet, M. Marchivie, G. Chastanet and K. Boukheddaden, *Inorg. Chem*. 2016, **55**, 11652-11661; (c) N. F. Sciortino, F. Ragon, K. A. Zenere, P. D. Southon, G. J. Halder, K. W. Chapman, L. Piñeiro-López, J. A. Real, C. J. Kepert and S. M. Neville, *Inorg. Chem.* 2016, **55**, 10490-10498; (d) N. F. Sciortino, K. A. Zenere, M. E. Corrigan, G. J. Halder, G. Chastanet, J.-F. Létard, C. J. Kepert and S. M. Neville, *Chem. Sci.* 2017, **8**, 701-707; (f) M. J. Murphy, K. A. Zenere, F. Ragon, P. D. Southon, C. J. Kepert and S. M. Neville, *J. Am. Chem. Soc.* 2017, **139**, 1330-1335; (g) K. A. Zenere, S. G. Duyker, E. Trzop, E. Collet, B. Chan, P. W. Doheny, C. J. Kepert and S. M. Neville, *Chem. Sci.* 2018, **9**, 5623-5629; (h) A. T. Brennan, K. A. Zenere, H. E. A. Brand, J. R. Price, M. M. Bhadbhade, G. F. Turner, S. A. Moggach, F. J. Valverde-Muñoz, J. A. Real, J. K. Clegg, C. J. Kepert and S. M. Neville, *Inorg. Chem.* 2020, **59**, 14296-14305.

[16] S. Sakaida, K. Otsubo, O. Sakata, C. Song, A. Fujiwara, M. Takata and H. Kitagawa, *Nat. Chem.* 2016, **8**, 377-383.

[17] V. Rubio-Giménez, C. Bartual-Murgui, M. Galbiati, A. Núñez-López, J. Castells-Gil, B. Quinard, P. Seneor, E. Otero, P. Ohresser, A. Cantarero, E. Coronado, J. A. Real, R. Mattana, S. Tatay and C. Martí-Gastaldo, *Chem. Sci.* 2019, **10**, 4038-4047.

[18] (a) V. Rubio-Giménez, G. Escorcia-Ariza, C. Bartual-Murgui, C. Sternemann, M. Galbiati, J. Castells-Gil, J. A. Real, S. Tatay and C. Martí-Gastaldo, *Chem. Mater.* 2019, **31**, 7277-7287; (b) C. Bartual-Murgui, V. Rubio-Giménez, M. Meneses-Sánchez, F. J. Valverde-Muñoz, S. Tatay, C. Martí-Gastaldo, M. C. Muñoz and J. A. Real, *ACS Appl. Mater. Interfaces*, 2020, **12**, 29461-29472.

[19] K. Otsubo, T. Haraguchi and H. Kitagawa, *Coord. Chem. Rev.* 2017, **346**, 123-138.

[20] C. M. Bell, M. F. Arendt, L. Gomez, R. H. Schomehl, T. E. Mallouk, *J. Am. Chem. Soc.* 1994, **116**, 8374-8375.

[21] S. Cobo, G. Molnár, J. A. Real and A. Bousseksou, *Angew. Chem., Int. Ed.* 2006, **45**, 5786-5789

[22] K. Otsubo, T. Haraguchi, O. Sakata, A. Fujiwara and H. Kitagawa, *J. Am. Chem. Soc.* 2012, **134**, 9605-9608.

[23] C. Bartual-Murgui, L. Salmon, A. Akou, C. Thibault, G. Molnár, T. Mahfoud, Z. Sekkat, J. A. Real and A. Bousseksou, *New. J. Chem.* 2011, **35**, 2089-2094.

[24] C. Bartual-Murgui, A. Akou, L. Salmon, G. Molnár, C. Thibault, J. A. Real, and A. Bousseksou, *Small* 2011, **7**, 3385-3391

[25] G. Agusti, S. Cobo, A. B. Gaspar, G. Molnár, N. O. Moussa, P. A. Szilagyi, V. Palfi, C. Vieu, M. C. Muñoz, J. A. Real and A. Bousseksou, *Chem. Mater.* 2008, **20**, 6721-6732.

[26] (a) A. C. Aragones, D. Aravena, J I. Cerda, Z. Acis-Castillo, H. Li, J. A. Real, F. Sanz, J. Hihath, E. Ruiz and I. Diez-Perez, *Nano Lett.* 2016, **16**, 218-226; (b) A. C. Aragonés, D. Aravena, F. J. Valverde-Muñoz, J. A. Real, F. Sanz, I. Díez-Pérez and E. Ruiz, *J. Am. Chem. Soc.* 2012, **139**, 5768-5778; (c) S. K. Karuppannan, A. Martín-Rodríguez, E. Ruiz, P. Harding, D. J. Harding, X. Yu, A. Tadich, B. Cowie, D. Qi and C. A. Nijhuis, *Chem. Sci.* 2021, **12**, 2381-2388.

[27] S. Decurtins, P. Gütlich, P. C. Köhler, H. Spiering and A. Hauser, *Chem. Phys. Lett.* 1984, **105**, 1-4

[28] J. F. Létard, P. Guionneau, L. Rabardel, J. A. K. Howard, A. E. Goeta, D. Chasseau and O. Kahn, *Inorg. Chem.* 1998, **37**, 4432-4441.

[29] (a) A. Hauser, *Coord. Chem. Rev.* 1991, **111**, 275-290; (b) A. Hauser, A. Vef and P. Adler, *J. Chem. Phys.* 1991, **95**, 8710-8717; (c) A. Hauser, C. Enachescu, M. L. Daku, A. Vargas and N. Amstutz, *Coord. Chem. Rev.* 2006, **250**, 1642-1652.

[30] T. Kitazawa, Y. Gomi, M, Takahashi, M. Takeda, M. Enemoto, A. Miyazaki and T. Enoki, *J. Mater. Chem.* 1996, **6**, 119-121.

[31] V. Niel, J. M. Martinez-Agudo, M. C. Muñoz, A. B. Gaspar and J. A. Real, *Inorg. Chem.* 2001, **40**, 3838-3839.

[32] (a) M. Seredyuk, A. B. Gaspar, V. Kseonofontov, M. Vergaguer, F. Villain and P. Gütlich, *Inorg. Chem.* 2009, **48**, 6130-6141; (b) R. Ohtani, M. Arai, H. Ohba, A. Hori, M. Takata, S. Kitagawa and M. Ohba, *Eur. J. Inorg. Chem.* 2013, **2013**, 738-744; (c) F. Ragon, K. Yaksi, N. F. Sciortino, G. Chastanet, J. F. Létard, D. M. D'Alessandro, C. J. Kepert and S. M. Neville, *Aust. J. Chem.* 2014, **67**, 1563-1573.

[33] (a) E. Trzop, D. Zhang, L. Piñeiro-Lopez, F. J. Valverde-Muñoz, M. C. Muñoz, L. Palatinus, L. Guerin, H. Cailleau, J. A. Real and E. Collet, *Angew. Chem., Int. Ed.* 2016, **55**, 8675-8679; (b) D. Zhang, E. Trzop, F. J. Valverde-Muñoz, L. Piñeiro-López, M. C. Muñoz, E. Collet and J. A. Real, *Cryst. Growth Des.* 2017, **17**, 2736-2745.

[34] M. Bentley, I. Douglass and J. A. Lacadie, *J. Org. Chem.* 1972, **37**, 333-334.

[35] T. M. Kitson and K. M. Loomes, *Anal. Biochem.* 1985, **146**, 429-430.

[36] G. M. Sheldrick, *Acta Crystallogr., Sect. C: Struct. Chem.* 2015, **71**, 3-8.

## 3.8.- Supporting Information

**Table S1.** Crystal data for **MpyS$_2$Me** (M = Pt, Pd).

| | **PdpyS$_2$Me_120K** | **PdpyS$_2$Me_250K** | **PtpyS$_2$Me_120K** | **PtpyS$_2$Me_250K** |
|---|---|---|---|---|
| Empirical formula | $C_{16}H_{14}N_6S_4PdFe$ | | $C_{16}H_{14}N_6S_4PtFe$ | $C_{16}H_8N_6S_4PtFe$ |
| *M*r | 580.82 | | 669.51 | 663.46 |
| Crystal system | triclinic | | | |
| Space group | *P*-1 | | | |
| *a* (Å) | 7.189(3) | 7.4283(4) | 6.9945(8) | 7.2382(8) |
| *b* (Å) | 7.192(3) | 7.4310(4) | 7.343(2) | 7.591(2) |
| *c* (Å) | 11.881(5) | 12.1476(8) | 11.065(2) | 11.372(3) |
| *α*(°) | 72.460(19) | 107.823(6) | 78.58(2) | 105.36(2) |
| *β*(°) | 72.419(14) | 107.831(5) | 73.11(2) | 101.31(2) |
| *γ* (°) | 89.946(13) | 89.990(4) | 89.902(13) | 90.05(2) |
| *V* (Å$^3$) | 555.6(4) | 604.45(7) | 532.1(2) | 589.9(2) |
| *Z* | 1 | | | |
| *T (K)* | 120 | 250 | 120 | 250 |
| $D_c$ (mg cm$^{-3}$) | 1.736 | 1.596 | 2.089 | 1.867 |
| *F*(000) | 288 | | 320 | 314 |
| *μ*(Mo-K$_α$) (mm$^{-1}$) | 1.852 | 1.702 | 7.655 | 6.903 |
| Crystal size (mm) | 0.01x0.08x0.08 | | 0.05x0.5x0.5 | |
| No.of total reflections | 2764 | 2433 | 2892 | 2378 |
| No. of reflections [*I*>2*σ*(*I*)] | 2685 | 2186 | 2669 | 1907 |
| *R* [*I*>2*σ*(*I*)] | 0.0341 | 0.0462 | 0.1234 | 0.1195 |
| *wR* [*I*>2*σ*(*I*)] | 0.0838 | 0.1013 | 0.3023 | 0.2940 |
| *S* | 1.109 | 1.051 | 1.265 | 1.154 |

$R = \Sigma ||Fo| - |Fc|| / \Sigma |Fo|$; $wR = [\Sigma [w(Fo^2 - Fc^2)^2] / \Sigma [w(Fo^2)^2]]^{1/2}$.

$w = 1/ [\sigma^2(Fo^2) + (m\ P)^2 + n\ P]$ where $P = (Fo^2 + 2Fc^2) / 3$; m = 0.0393 (**1**), 0.0502 (**2**), 0.2000 (**3**), and 0.2000 (**4**);

n = 0.7715 (**1**), 0.0000 (**2**), 0.0000 (**3**), and 0.0000 (**4**)

**Table S2.** Crystal data for **$MpyS_2Et$.** (M = Pt, Pd).

| | **$PdpyS_2Et$_100K** | **$PdpyS_2Et$_250K** | **$PtpyS_2Et$_100K** | **$PtpyS_2Et$_250K** |
|---|---|---|---|---|
| Empirical formula | $C_{18}H_{18}N_6S_4PdFe$ | | $C_{18}H_{18}N_6S_4PtFe$ | |
| *Mr* | 608.87 | | 697.56 | |
| Crystal system | monoclinic | | | |
| Space group | *I*2/*m* | *C*2/*m* | *I*2/*m* | *C*2/*m* |
| *a* (Å) | 13.8182(8) | 23.9683(14) | 13.8437(4) | 24.0228(10) |
| *b* (Å) | 7.3599(4) | 7.6791(2) | 7.3489(2) | 7.6448(2) |
| *c* (Å) | 23.201(2) | 13.8679(7) | 23.3286(8) | 13.9959(5) |
| *β* (°) | 106.079(7) | 106.053(5) | 106.218(3) | 106.485(4) |
| *V* ($Å^3$) | 2267.2(3) | 2452.9(2) | 2278.91(12) | 2464.7(2) |
| *Z* | 4 | | | |
| *T (K)* | 100 | 250 | 100 | 250 |
| $D_c$ (mg $cm^{-3}$) | 1.784 | 1.649 | 2.033 | 1.880 |
| *F*(000) | 1216 | 1216 | 1344 | 1344 |
| *μ*(Mo-$K_α$) ($mm^{-1}$) | 1.820 | 1.682 | 7.153 | 6.614 |
| Crystal size (mm) | 0.1x0.5x0.5 | | 0.1x0.7x0.7 | |
| No. of total reflections | 3166 | 3398 | 3272 | 3489 |
| No. of reflections [$I>2\sigma(I)$] | 2179 | 2052 | 2611 | 2588 |
| *R* [$I>2\sigma(I)$] | 0.0520 | 0.0707 | 0.0332 | 0.0369 |
| *wR* [$I>2\sigma(I)$] | 0.0862 | 0.1355 | 0.0832 | 0.0887 |
| *S* | 1.035 | 1.035 | 1.119 | 1.064 |

$R = \Sigma ||Fo| - |Fc|| / \Sigma |Fo|$; $wR = [\Sigma [w(Fo^2 - Fc^2)^2] / \Sigma [w(Fo^2)^2]]^{1/2}$.

$w = 1/ [\sigma^2(Fo^2) + (m\ P)^2 + n\ P]$ where $P = (Fo^2 + 2Fc^2) / 3$; m = 0.0275 (**1**), 0.0430 (**2**), 0.0346 (**3**), and 0.0422 (**4**);

n = 0.0000 (**1**), 23.1512 (**2**), 38.7639 (**3**), and 11.5730 (**4**)

**Figure S1.** Thermogravimetric analysis of **MpyS$_2$R**. (M = Pt, Pd; R = Me, Et)

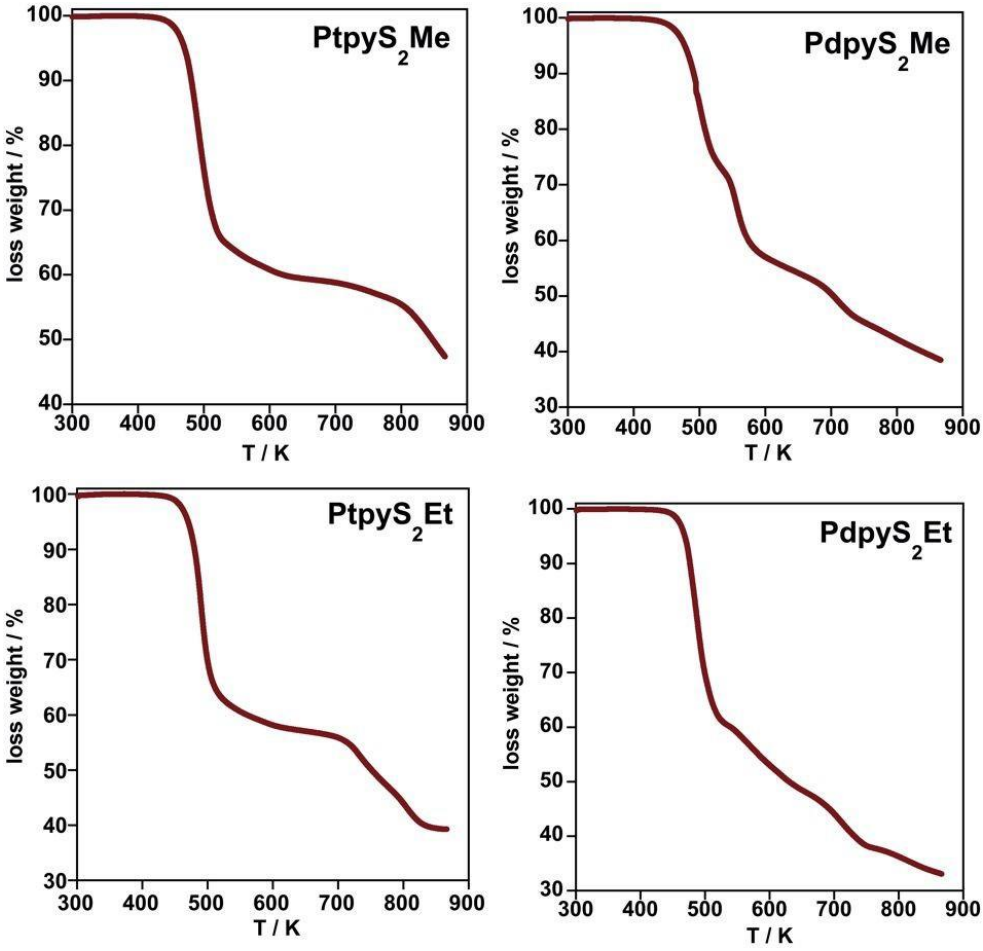

**Figure S2**. Comparison of the thermal dependence of $\Delta C_p$ and $\delta(X_M T)/\delta T$ curves for **PdpyS₂Me**. Note the excellent match between both curves and the lack in the $\Delta C_p$ vs T plot of the peak below 150 K due to experimental constraints.

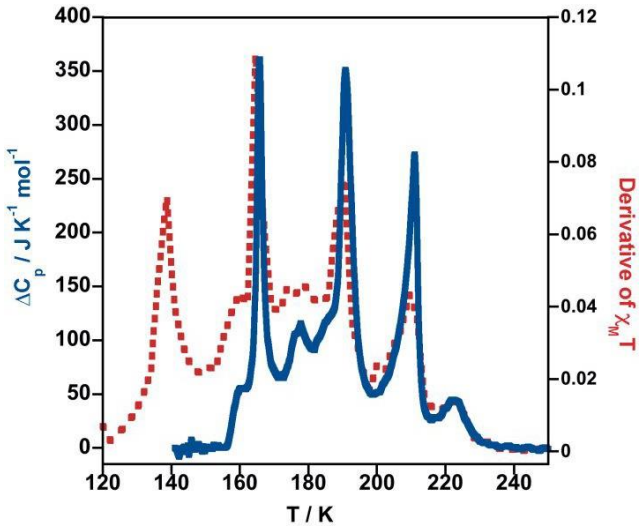


**Figure S3.** Perspective view of **PdpyS₂Me** at 250 K showing the perfectly flat $\{Fe(Pd(CN)_4]\}_n$ layers and the positional disorder of the $pyS_2Me$ ligands over four positions.

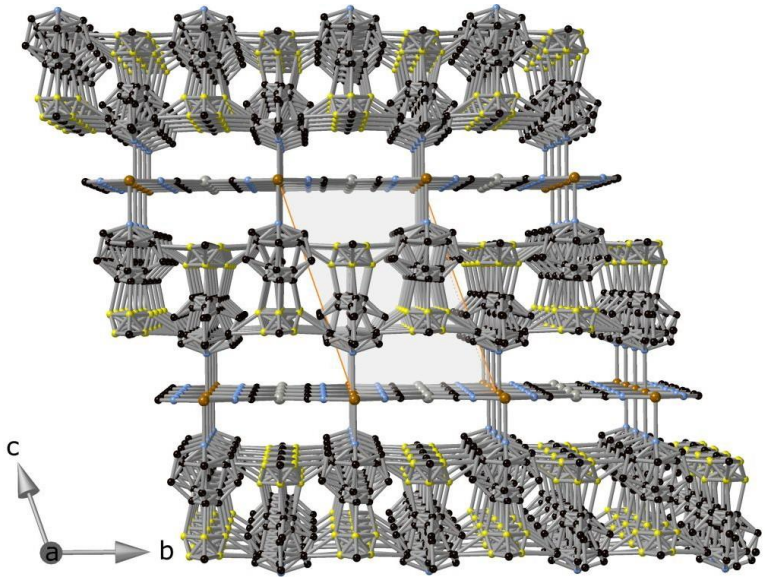

**Figure S4.** Comparison of the $X_MT$ vs T plots for {Fe(pyridine)$_2$[Pt(CN)$_4$]} obtained by direct precipitation as microcrystalline powder (blue) and by liquid-liquid slow diffusion as single crystals (red).

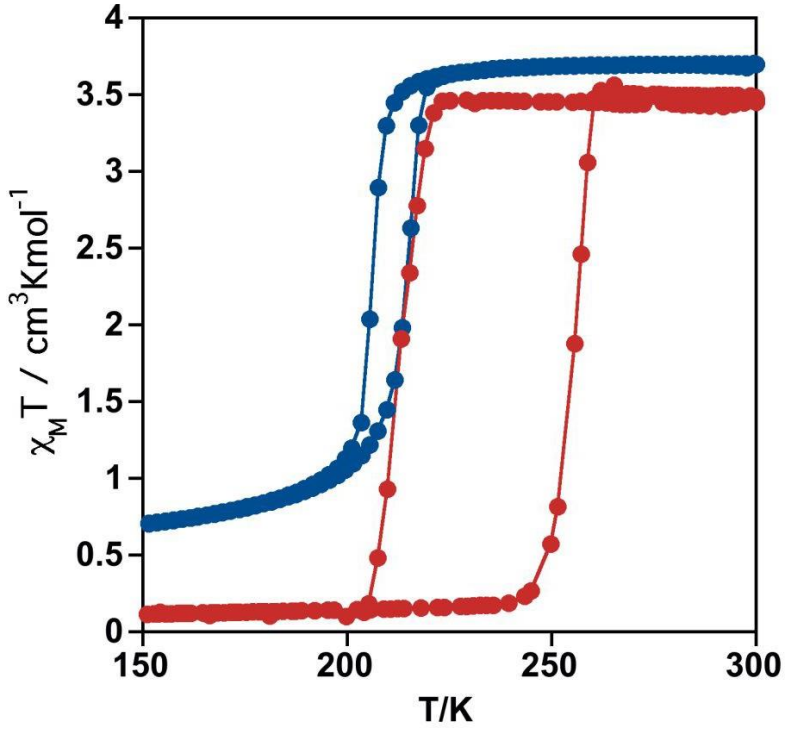

CAPÍTULO 4

# Coexistence of Luminiscence and Spin-Crossover in 2D Iron(II) Hofmann Clathrates Modulated Through Guest Encapsulation

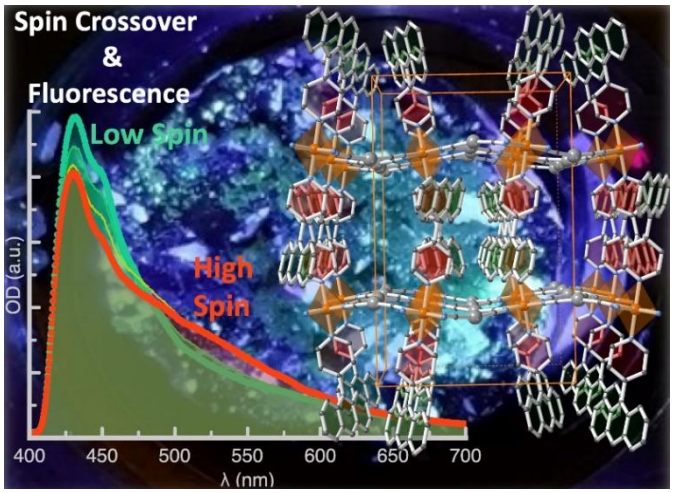


REVISTA: Journal of Materials Chemistry C

ÍNDICE DE IMPACTO: 8.067

# CAPÍTULO 4

## Coexistence of Luminiscence and Spin-Crossover in 2D Iron(II) Hofmann Clathrates Modulated Through Guest Encapsulation

### 4.1.- Abstract

The search for advanced multifunctional materials displaying two or more simultaneous and correlated physicochemical properties represents a key step in developing further practical applications. In this context, we report the synthesis and physical characterization of the unprecedented two dimensional Hofmann-type Coordination Polymers (HCPs) formulated as $\{Fe^{II}(AnPy)_2[M(CN)_2]_2\}\cdot XBz$ (AnPy = 4-anthracenepyridine; M = Ag, Au; XBz = substituted benzenic guest). These materials combine two functions, spin crossover (SCO) and fluorescence which arise, respectively, from the octahedrally coordinated Fe(II) ions and the anthracede based AnPy ligands. The thermal dependence of the magnetic and calorimetric properties, performed on microcrystalline samples, as well as single crystal UV-Vis absorption spectroscopy and structural studies, reflect a multi stepped nature of the SCO. The temperature at which the SCO takes place is markedly modulated by the nature of the XBz guests (X = I, Br, Cl, $NO_2$, $CH_3$) which are trapped within the interstitial spaces originated from the stacking of bimetallic layers. Two different crystallographic phases, one orthorhombic and another triclinic have been identified. The triclinic phase is not stable in air and transforms into the orthorhombic form likely prompted by the partial release of guest. Both phases afford new examples of symmetry breaking and spin-state ordering associated to the SCO. All compounds exhibit strong blue fluorescence that gradually vanishes as the temperature increases but they also present a prominent excimer/exciplex green fluorescence band for X = I (M = Ag, Au) and Cl (M = Au), whose intensity increases in parallel with the population of high-spin Fe(II) ions. Hence, the latter compounds represent new examples of synergy between SCO and luminescence.

### 4.2.- Introduction

The spin crossover phenomenon, displayed by certain transition metals ($3d^4$-$3d^7$) in octahedral environments, is a fascinating example of stimuli-driven molecular switching. It involves the controllable, detectable and reversible transition of the metal ion between the

high spin (HS) and the low spin (LS) electronic configurations leading to important changes of both the structure (volume and geometry) and physical properties (magnetic, electrical and optical) of the complex.[1-3] In the solid state, the structural changes drive the propagation of the spin state switch across the crystal more or less efficiently depending on the degree of interaction between the SCO centers. When these interactions are strong (*e.g.* covalently bonded SCO atoms), the volume change associated to the spin transition of a given SCO center elastically induces the switchin of the neighboring switchable metal ions.[4,5] For thermally induced SCO behaviours, this cooperative communication is macroscopically monitored as an abrupt change of the HS molar fraction ($\gamma_{HS}$) as a function of the temperature.[6,7] Furthermore, when the coupling between SCO ions is very strong, the observed $\gamma_{HS}$ vs T plot may exhibit hysteretic behaviour (memory effect)[8,9] which is an appealing situation for applicative purpouses. [10,11]

Bimetallic Fe(II) Hofmann-like coordination polymers [Fe(II)-HCPs] with general formula $\{Fe^{II}(L)_n[M^{II}(CN)_4]\}$ ($M^{II}$ = Ni, Pd, Pt) or $\{Fe^{II}(L)_n[M^{I}(CN)_2]_2\}$ ($M^{I}$ = Cu, Ag, Au) (being L an axial pyridinic-like ligand) are among the most investigated systems within the SCO community.[12-14] This is in part because they can be easily designed to generate void spaces where guest molecules can be accommodated, a fact which in turn affords the opportunity to modulate the SCO behaviour.[15] In the case of the $\{Fe(L)_n[M(CN)_4]\}$ HCPs, the use of monodentate L ligands (*n* = 2) produces 2D networks consisting of stacked cyanide-based bimetallic layers stabilized through the interdigitation of the axial L ligands. Although in principle this kind of structure is not porous, the appropriate functionalization of L can stimulate the occurrence of host-guest interactions affecting the SCO characteristics.[16-26] Besides, the use of ditopic pyridine-based ligands (*n* = 1) leads to the formation of intrinsically porous 3D networks, which promote the sorption/desorption of guest molecules in synergy with modulation of the SCO.[27] Regarding the $\{Fe(L)_n[M^{I}(CN)_2]_2\}$ derivatives, the lower coordination density of the heterometallic layers afforded by the $[M^{I}(CN)_2]$ bridging ligands with respect to the $[M(CN)_4]^{2-}$ homologues, together with the establishment of metallophilic (Ag···Ag or Au···Au) interactions, usually favor the formation of interpenetrated structures. In spite of this, most of the reported 3D (*n* = 1) dicyanometallate-based networks exhibit host-guest interactions which considerably impact the SCO properties.[28-39] In contrast, the presence of trapped guests in 2D (*n* = 2) $\{Fe(L)_2[M^{I}(CN)_2]_2\}$ networks is rare,[40,41] probably due to the efficient packing of the generated bilayered structures.[40,42-52]

In addition to the existence of host-guest interactions, the integration of fluorescence properties acting in synergy with the SCO is an exciting pathway for developing new advanced multifunctional materials.[53-59] In the case of $Fe^{II}$ based compounds, the interplay between fluorescence and SCO is based on the overlap between the fluorescent emission of the luminophore and the adsorption band of the $Fe^{II}$ in the LS state which vanishes in the HS state. In the case of 3D $Fe^{II}$-HCPs, the incorporation of fluorescent properties has been recently accomplished by following two strategies: (i) the use of a fluorophore as pillaring ligand[60] and (ii) the inclusion of a fluorescent guest into the structural cavities.[60,61] Whereas the first strategy led to the SCO compounds {Fe(Bpan)[$M^{I}(CN)_2]_2$} (M = Ag, Au; Bpan = 4-bis(pyridyl)anthracene), the second one yielded the SCO networks {Fe(bpb)[$M^{I}(CN)_2]_2$}·Pyr and {Fe(bpben)[$M^{I}(CN)_2]_2$·Pyr (bpb = bis((4-pyrirdyl)butadiyne; bpben = 1,4-bis(4-pyridyl)benzene); (M = Ag, Au) where the pyrede (Pyr) guests act as a luminophore (Scheme 1). Regardless of the used strategy, the corresponding SCO properties were successfully monitored as a modulation of the fluorescent signal confirming the synergy between both properties.

Although other types of 2D coordination polymers presenting synergies between luminescence and SCO have been recently reported,[62-64] up to date only one example of fluorescent 2D $Fe^{II}$-HCPs is known.[65] The interest of these laminar 2D $Fe^{II}$HCPs resides in the possibility of adjusting the layer-to-layer space designing interlayer cavities where a wide range of functional guests can actuate in synergy with both the SCO and fluorescence properties. Herein, we present the synthesis, structural characterization and SCO properties, derived from variable temperature, magnetic and calorimetric measurements on microcrystalline powders and optical absorption properties measured on single crystals, of an unprecedented family of 2D $Fe^{II}$-HCPs formulated {$Fe(AnPy)_2[M(CN)_2]_2$}·XBz (AnPy = 4-(anthracene)pyridine (Scheme 1); M = Ag (**AnPyAg·XBz**), Au (**AnPyAu·XBz**); XBz = substituted benzene (X = I, Br, Cl, $CH_3$ and $NO_2$)). Furthermore, these compounds exhibit fluorescence emission stemming from the anthracene moiety of the axial AnPy ligand (Scheme 1). The nature of the XBz aromatic guests, located within the large cavities originated between the bimetallic layers, noticeably modulates the SCO behaviour. New evidence of

synergy between SCO and fluorescence, namely modulation of the fluorescent signal as a function of the thermal dependence of the HS fraction is reported.

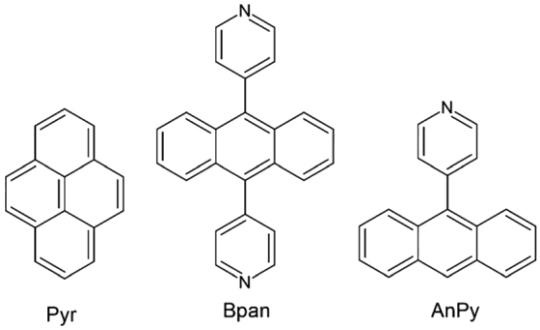


**Scheme 1.** Source of fluorescence used in ref. 60 and 61 (Pyrene (Pyr) as guest molecule, ref. 60 (Bpan as axial bridging ligand) and in this work (AnPy as axial terminal ligand).

## 4.3.- Results

### 4.3.1.- Synthesis chemical characterization

Single crystals of **AnPyM·*n*XBz** were prepared by slow liquid-to-liquid diffusion methods from a solution of $K^{I}[M^{I}(CN)_2]$ ($M^{I}$ = Au or Ag) in MeOH and another containing a mixture of Fe(*p*-OTs)$_2$ and AnPy dissolved in a MeOH : XBz (1:3) solution. The XBz solvent was intentionally included, on one hand, to facilitate the dissolution of the AnPy ligand and, on the other, to act as a template for the resulting structure. Both solutions were separated by a 1:3 MeOH : XBz interphase in a test tube (see experimental details in the SI). Yellow rhombohedral single crystals of {Fe(AnPy)$_2$[M(CN)$_2$]$_2$}·XBz (**AnPyM·XBz)** were obtained in good yields (*ca*. 60-70%) after *ca.* 4 weeks. For comparative reasons and using the same synthetic method, crystals of the non-SCO $Ni^{II}$ instead of $Fe^{II}$ (**NiAnPyAu·NO$_2$bz**) were also synthesized.

The composition of the crystals was characterized by elemental and thermogravimetric analyses (TGA) (see experimental section in SI and Fig. S1), single crystal and powder X-ray diffraction (SCXRD and PXRD). The X-ray diffraction studies demonstrated the presence of two distinct polymorphs/solvatomorphs for pristine crystals of **AnPyAu·XBz** (X = Cl, CH$_3$), the so-called triclinic metastable phase, which once removed from their mother liquor transforms in several hours into the stable orthorhombic form (Fig. S2, SI), characteristic of the whole family of the clathrate compounds **AnPyM·*n*Xbz** and **NiAnPyAu·NO$_2$Bz**. Indeed, the PXRD analysis carried out on air-dried crystals reveal that, regardless of the trapped guest, this

orthorhombic form is found for all derivatives (Fig. S3, SI). Likewise, the similarity between the PXRD patterns of the Ag and Au counterparts demonstrates that both analogues are isostructural. The PXRD patterns of the guest-free compounds **AnPyM** (M = Ag, Au), which were obtained from a thermal treatment (400K for one hour) of the $CH_3Bz$ and ClBz containing clathrates, indicates that the network retains the structure after guest desorption.

In general, the orthorhombic for accommodates about 1.6-2.0 molecules of XBz within the cavities of the structure and the TGA show that they remain adsorbed at temperatures below 380-430K depending on the derivative. The release of the benzenid guest, which correspons to the *ca.* 20-30% of the total mass is followed by the decomposition of the network at around 480K. This decomposition involves a total mass loss of *ca.* 45% corresponding well to 2 AnPy ligands and 4 CN unities being the remaining mass of *ca*. 30% consistent with Fe and Au/Ag residues. The crystal data analysis of the triclinic phases enabled us to infer a larger amount of guest in the clathrates, namely $n$ = 2 and 3 for ClBz and $CH_3Bz$, respectively, suggesting that the triclinic-to-orthorhombic crystal phase change is driven by the partial loss of guest molecules. Obviously, this transformation has direct consequences on the SCO properties of both derivatives (*vide infra*).

### 4.3.2.- Spin Crossover Properties

*4.3.2.1.- Magnetic, calorimetric and photomagnetic studies*

The thermal variation of the $\chi_M T$ product (where $\chi_M$ is the molar magnetic susceptibility and T is the temperature) was measured for the air-dried compounds **AnPyM·XBz** (orthorhombic phase) at 1K $min^{-1}$ in order to analyze the SCO properties (Fig. 1). At 260K, all samples exhibit a $\chi_M T$ value of *ca.* 3.5 $cm^3$ $mol^{-1}$ which indicates a fully populated HS state. Upon cooling, all **AnPyAg·XBz** derivatives undegro a similar four-step decrease of the $\chi_M T$ value revealing a complete HS-toLS state transformation. The steps are separated by more or less marked plateaus consistent with the stabilization of intemediate mixed spin states denoted $[HS_s:LS_j]$ following the sequence ($[HS_1:LS_0] \leftrightarrow [HS_{3/4}:LS_{1/4}] \leftrightarrow [HS_{1/2}:LS_{1/2}] \leftrightarrow [HS_{1/4}:LS_{3/4}] \leftrightarrow [HS_0:LS_1]$) taking place at around 2.6-2.5 $cm^3$ $mol^{-1}$ ($[HS_{3/4}:LS_{1/4}]$), 1.8-1.6 $cm^3$ $mol^{-1}$ ($[HS_{1/2}:LS_{1/2}]$) and 0.9-0.8 $cm^3$ $mol^{-1}$ ($[HS_{1/4}:LS_{3/4}]$). In the heating mode, the magnetic behaviour is overall superposed with that of the cooling mode altough a small hysteresis (2-5K) is observed for some of the transitions. Only the last step

observed for **AnPyAg·IBz** displays a remarkable hysteresis of 10K being the [$HS_{1/4}$:$LS_{3/4}$] state more stabilized. Altough this multi-stepped SCO behaviour is roughly reproduced for the Au counterparts, compounds **AnPyAu·IBz** and **AnPyAu·BrBz**/**AnPyAu·$CH_3$Bz** display incomplete transitions with only two and three steps, respectively, likely due to kinetic factors imposed by the lower temperatures involved. The critical SCO temperatures, $T_{ci}$, defined as the temperature at which 50% of the $Fe^{II}$ ions have switched from the HS to the LS state during the step I, are clearly dependent on the nature of the adsorbed guest (Table 1). Indeed, the $T_{ci}$ values increase in the order $T_{ci}$(IBz) < $T_{ci}$($CH_3$Bz) < $T_{ci}$(BrBz) < $T_{ci}$(ClBz) < $T_{ci}$($NO_2$Bz) for both the Ag and Au derivatives. Furthermore, a decrease of $T_{ci}$ is also observed when moving from the Ag to the Au derivatives (see Table 1).

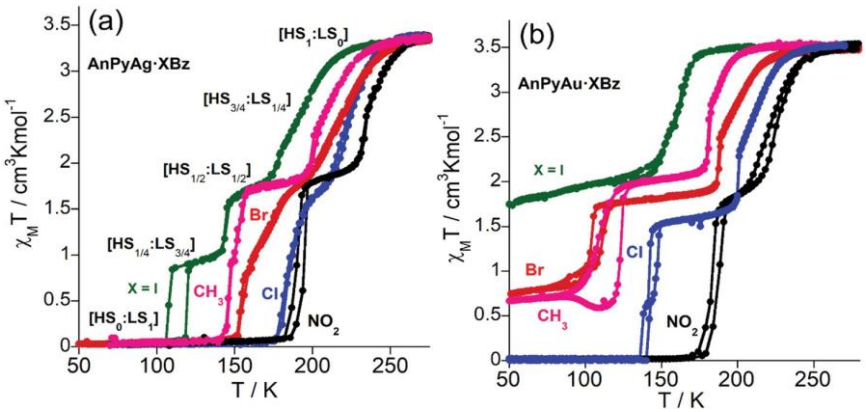


**Fig. 1.** Thermal dependence of $\chi_M T$ for (a) **AnPyAg·XBz** and (b) **AnPyAu·XBz** (X = I, $CH_3$, Br, Cl and $NO_2$) (orthorhombic phase) (1 K $min^{-1}$).

The magnetic behaviour of the triclinic phases (pristine crystals of **AnPyAu·ClBz** and **AnPyAu·$CH_3$Bz**) measured into their mother liquor displays incomplete and multi-stepped SCO curves with transitions shifted to low temperatures (Fig. S4, SI). However, the spin transition becomes more complete and shifts to higher temperatures when removing the crystals from the mother liquor driving to the SCO curves described above for the orthorhombic forms (Fig. S4, SI). These results reveal that the triclinic phases are not stable in air and evolve to the orthorhombic phase in good accord with the PXRD studies (Fig. S2, SI). In contrast to the guest-loaded clathrates, the SCO of the guest-free **AnPyAg** and **AnPyAu** compounds are markedly gradual, incomplete and take place in a unique step with $T_c$ values of 157 and 163K, respectively (Fig. S5, SI).

**Table 1.** $T_c$ values (in K) of the different steps obtained from the magnetic measurements of the different **AnPyM·XBz** compounds.

| | M | | | | | | | |
|---|---|---|---|---|---|---|---|---|
| | Ag | | | | Au | | | |
| X | $T_{c1}$ | $T_{c2}$ | $T_{c3}$ | $T_{c4}$ | $T_{c1}$ | $T_{c2}$ | $T_{c3}$ | $T_{c4}$ |
| I | 199 | 182 | 145 | 109[a] | 165 | 152 | — | — |
| $CH_3$ | 215 | 200 | 153 | 147 | 190 | 181 | 113[a] | — |
| Br | 231 | 210 | 173 | 156 | 200 | 187 | 104[a] | — |
| Cl | 233 | 219 | 190 | 181 | 215 | 201 | 143[a] | 138[a] |
| $NO_2$ | 246 | 234 | 193[a] | 188[a] | 228 | 215[a] | 184[a] | 180[a] |

[a] Temperature registered upon the cooling mode (measured at 1K $min^{-1}$).

The occurrence of a multi-stepped SCO behaviour of these clathrates is also reflected on the calorimetric measurements (recorded at 10K $min^{-1}$) characterized by a series of maxima/minima in the $C_p$ *vs* $T$ curves that determine the position of the steps in good accordance with the magnetic profiles (Fig. S6, SI). It is worth noting that only the **AnPyAg·XBz** (X = $NO_2$, Cl, Br and $CH_3$) and **AnPyAu·$NO_2$bz** species were studied since the temperature range where the spin-state change takes place in the rest of the derivatives is not achievable by our calorimeter. The estimated Δ$H$ and Δ$S$ variations (Table S1, SI) are common in $Fe^{II}$ spin crossover compounds. Light indiced excited spin state trapping (LIESST)[66] was observed for all the derivatives when irradiating with a green laser (λ = 532 nm, 40 mW) at 10K (Fig. S7, SI). The efficiency of the photoconversion from the LS to the metastable HS* state (green curves) is in the range 60-80% and 80-100% for Ag and Au derivatives, respectively. Then, once attained the saturation values and in the dark the photogenerated HS* state relaxes back (black curves) to the initial LS state increasing the temperature at a rate of 0.3K $min^{-1}$ obtaining the characteristic $T_{LIESST}$[67] of 33 ($NO_2$), 40 (Cl), 45 (Br), 46 (I) and 47K ($CH_3$) (in one step for the **AnPyAg·XBz**), 36/45 ($NO_2$), 49/66 (Cl) and 47/70K (Br) (in two steps for the **AnPyAu·XBz**) and 53 ($CH_3$) and 55K (I) (in one step for **AnPyAu·XBz**). These temperatures are consistent with the inverse-energy-gap law as the stability of the photogenerated HS* species decreases as the stability of the LS increases ($T_c$ increases).[68-70]

### 4.3.3.- Structural characterization

In order to follow the spin state change and evaluate the occurrence of symmetry breaking processes, the crystal structures of **AnPyM·XBz** (M = Au or Ag and X = $NO_2$, $CH_3$, Cl or Br) were studied at different temperatures according to the multi-stepped SCO behaviour observed through the magnetic measurements. Despite many efforts, the structures of **AnPyM·Ibz** (M = Au, Ag) and **NiAnPyAu·$NO_2$Bz** could not be resolved, although, as mentioned before, they are isostructural to the other members of the series adopting the stable orthorhombic form (Fig. S3, SI).

Compounds **AnPyAg·BrBz**, **AnPyAu·BrBz** and **AnPyAg·ClBz** exhibit the orthorhombic *Ccc*2 space group above 260K, but display symmetry breaking associated with spin-state changes at lower temperatures (*vide infra*). In contrast, compounds **AnPyAg·$CH_3$Bz** and **AnPyAg·$NO_2$Bz**/ **AnPyAg· $NO_2$Bz** crystallize in the orthorhombic *Pccn* and *Cccm* space groups, respectively, and remain in the same crystal phase upon SCO. Finally, both **AnPyAu·$CH_3$Bz** and **AnPyAu·ClBz** display the triclinic *P*-1 space group, the latter exhibiting symmetry breaking upon cooling also associated with the SCO behaviour. Due to their similarity, crystal structures presenting orthorhombic phases will be described together whereas the triclinic structures will be presented in a separated section. Crystal daya, structural parameters and a selection of relevant bond lengths and angles are gathered in Tables S2-S17 (SI).

*4.3.3.1.- Orthorhombic phases*

At 260-180K, the crystal structures of **AnPyAg·XBz** (X = Cl, Br, $NO_2$ or $CH_3$) and **AnPyAu·XBz** (X = Br or $NO_2$) contain a unique elongated octahedral [$Fe^{II}N_6$] site constituted of four equivalent equatorial $[M(CN)_2]^{-2}$ bridging units and two identical axial AnPy ligands (Fig. 2(a) with average bond lengths at T ≥ 260K in the interval 2.012(8)-2.140(4) Å and 2.212(9)-2.247(5) Å, respectively. The overall Fe-$N_{av}$ average bond-lengths, in the range 2.144-2.169 Å, are consistent with the FeII in the HS state as indicated by the magnetic measurements. Each equatorial $[M(CN)_2]$ unit bridges two [$Fe^{II}N_6$] centers therefore building up infinite $\{Fe(AnPy)_2[M(CN)_2]_2\}$ two-dimensional layers (Fig. 2(b)). The angle defined by two adjacent [$FeN_4$] equatorial planes is in the range 21-26º for the HS state and decreases by *ca*. 20-25% in the LS state. Furthermore, the $[M(CN)_2]$- bridging groups slightly depart from linearity by *ca*. 10º. Both facts, together with the symmetry, confer a homogeneous undulated character to the bimetallic layers. The layers stack along the *b* axis (*a* axis for

**AnPyAg·CH$_3$Bz**) (Fig. 2(b)) being the separation between two consecutive corrugated layers, measured as the distance between the planes defined by their respective Fe$^{II}$ centers, in the range 11.11–12.65 Å for T ≥ 260K. This separation remains almost constant at lower temperatures. The only exception was found for **AnPyAg·CH$_3$Bz** whose separation decreases by *ca*. 12% upon cooling at 120K. The stacking takes place in such a way that the [Fe$^{II}$N$_6$] sites of one layer project on the center of the {Fe$_4$[M(CN)$_2$]$_4$} windows of the adjacent layer. The resulting interdigitation between the AnPy ligands of adjacent layers favors the occurrence of some C–H···π and π···π interactions between the pyridine and the anthracene moieties (*e.g.*, anthracene···anthracene *d*[C20···C11'] = 3.469 Å, at 120 K). This packing mode generates channels running along the 001 direction (*c* axis) where the XBz molecules are hosted (Fig. 2(b) and Fig. S8, SI). Although modelling the trapped XBz molecules is not overall achievable due to the strong positional disorder of these molecules within the cavities, the most part of the electronic density is localized face-to-face to the anthracene moieties of the AnPy ligands suggesting the presence of π···π host–guest interactions. This was confirmed for **AnPyAg·CH$_3$Bz** at 120 K where the toluene was clearly identified (Fig. 2(b) and Fig. S9, SI) and stablishes short C···C contacts with the host framework, more precisely anthracene···toluene *d*[C15/C17···C24] = 3.485/3.444 Å and toluene···cyanide *d*[C25/C26···C1 = 3.483/3.426 Å]. A solvent mask was implemented for the rest of structures removing the electronic contribution of the disordered guest from the refine- ment and estimating the corresponding amount. The masked electron density is, for all the compounds, consistent with the quantity of guest inferred from TGA measurements (*i.e.* about 1.6-2.0 molecules per Fe$^{II}$ ion).

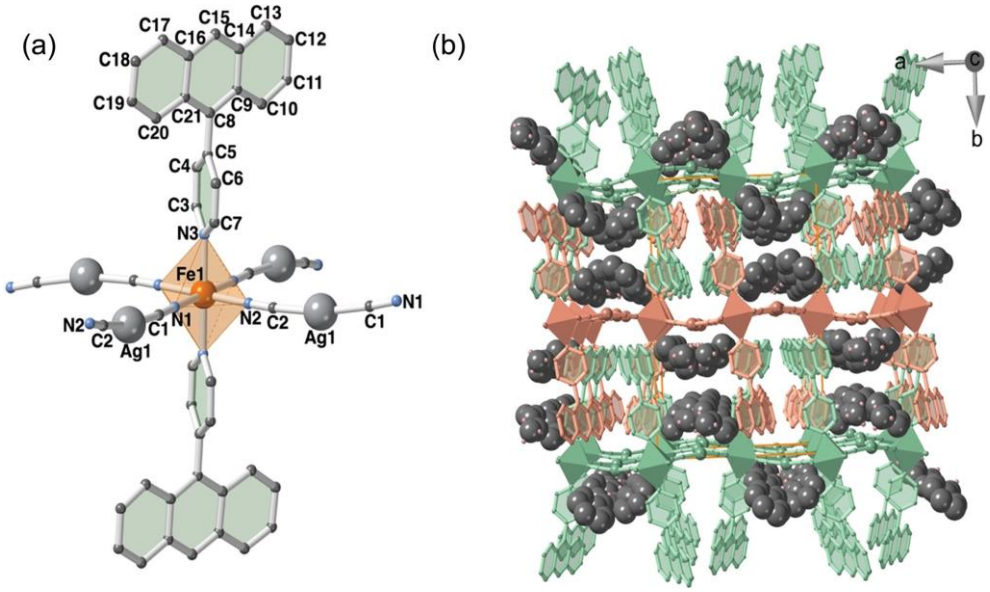


**Fig. 2.** (a) Typical $Fe^{II}$ environment displayed by **AnPy·Xbz** [M = Ag (X = Br, Cl, $CH_3$ and $NO_2$) or Au (X = Br and $NO_2$)] in the orthorhombic phase. (b) Packing of three consecutive layers (green and salmon) of the $CH_3$ derivative showing the interdigitation of the AnPy ligands and the channels where the guest molecules are located in **AnPyM·XBz**.

Upon cooling to 207, 192 and 165K, respectively, the structures of **AnPyAg·ClBz**, **AnPyAg·BrBz** and **AnPyAu·BrBz** undergo a symmetry breaking revealing a crystallographic phase change from the orthorhombic *Ccc*2 to the orthorhombic *Pmna* space group. This crystallographic transformation involves the generation of two structurally independent $Fe^{II}$ centers, one of them remaining mostly in the HS state and the other in the LS state, as indicated by the average bond lengths in the range 2.135-2.172 Å and 2.016-1.965 Å, respectively. This is in good accord with the $\chi_M T$ vs. *T* measurements and the stabilization of the $[HS_{1/2}:LS_{1/2}]$ state responsible for the marked plateau, halfway between the fully HS and LS states. This state is organized by alternating HS and LS centers running along the direction determined by the dicyanometallic bridging ligands (Fig. S10, SI). In contrast, no symmetry breaking was observed in the characteristic plateaus for **AnPyAg·$NO_2$Bz** (210K), **AnPyAg·$CH_3$Bz** (170K) and **AnPyAu·$NO_2$Bz** (200K) where the average bond lengths 2.048, 2.065 and 2.060 Å, respectively, reflect a 50% mixture of $Fe^{II}$ centers in the HS and LS states without detected ordering. After further cooling to 120K, **AnPyAg·ClBz** and **AnPyAg·BrBz** transform back to the initial *Ccc*2 space group with a single $Fe^{II}$ ion in the LS configuration (average bond lengths 1.958 and 1.967 Å, respectively) ($[HS_0:LS_1]$), which indicates,

consistently with the magnetic measurements, a complete HS-to-LS transformation. In contrast, the *Pmna* space group is retained for compound **AnPyAu·BrBz**, even at 90K, where the Fe-$N_{av}$ bond-lengths are 2.109 Å and 1.963 Å for each site. The former reflects a change of the HS Fe-$N_{av}$ bond length roughly approaching the mid-way between the HS and LS states and, although no ordering was observed, the overall spin-state change at 90K suggests that *ca*. 75% of the HS centers transform into the LS state defining a [$HS_{1/4}$:$LS_{3/4}$] plateau in good agreement with the corresponding magnetic measurements. According to the Fe-Nav bond length, the three remaining compounds that do not show symmetry breaking **AnPyAg·NO2Bz** (1.958 Å, 120K), **AnPyAg·CH3Bz** (1.966 Å, 120K) and A**nPyAu·NO2Bz** (1.947 Å, 200K) also attain a fully populated LS state at low temperatures. The *Ccc*2 (Cl, Br), *Pccn* ($CH_3$) and *Cmma* ($NO_2$) orthorhombic space groups differ basically in the dihedral angle (α) formed by the anthracene moieties of the two AnPy ligands bonded to a given $Fe^{II}$ center (Fig. S11, SI). Except for X = $CH_3$ in which the anthracene moieties are coplanar, a is in the interval 38.5-46.5º and slightly depends on the spin state of the FeII center. Furthermore, the anthracene and pyridine moieties of the AnPy ligand are oriented each other in an almost orthogonal fashion. The deviation from 90º is in the interval 15-23º depending on the clathrate and spin state (Fig. 2(a)).

*4.3.3.2.- Triclinic phases **AnPyAu·XBz** (X = $CH_3$ and Cl)*

Freshly prepared single crystals of compounds **AnPyAu·XBz** (X = $CH_3$ and Cl) crystallize in the triclinic *P*-1 space group, which is kept at all the studied temperatures. The asymmetric unit is con- stituted of two crystallographically independent [$Fe1N_6$] and [$Fe2N_6$] elongated octahedral sites. For the ClBz clathrate, both sites lay in an inversion center as well as the Fe2 site does for the $CH_3$Bz clathrate in contrast to its corresponding Fe1 site that lacks of symmetry (see Fig. 3(a) and (b)). This is the reason why the anthracenes of the latter site differ more markedly from coplanarity, by around 11.4º, in the temperature interval 260–95K. A small deviation of *ca*. 5º is also observed for the Fe2 site of the ClBz clathrate at 180K. At 260K, the dihedral angle defined by the pyridine and anthracene moieties depart from orthogonality by 32.41º/7.98º (X = Cl) and 13.81º/8.50º (X = $CH_3$) for sites Fe1/Fe2. The average axial Fe-N(pyridine) bond length is 2.201(6)/2.212(6) Å (X = Cl) and 2.225(4)/2.228(4) Å (X = $CH_3$) for Fe1/Fe2. A consequence of the asymmetric nature of the Fe1 nodes in the $CH_3$Bz derivative is the presence of four crystallographically independent $[Au(CN2)]^-$ equatorial bridging ligands while only two define the structure of the homologous

ClBz. Consequently, the resulting 2D bimetallic layers feature a different distribution of the Fe1 and Fe2 sites in each clathrate. For the ClBz derivative, the Fe1-Fe2 sites uniformly alternate each other along the two directions of the layer (Fig. 3(c)), while the pattern in the $CH_3Bz$ derivative is Fe1-Fe1-Fe2 (Fig. 3(d)). The equatorial Fe-$N_{av}$ bond lengths are 2.156(6)/2.163(6) Å (X = Cl) and 2.151(5)/2.144(4) Å (X = $CH_3$) for Fe1/Fe2. Then, the overall average Fe-Nav for the [$Fe1N_6$] and [$Fe2N_6$] octahedronsat 260K, found in the interval 2.170-2.179 Å, is consistent with the HS state for both $Fe^{II}$ sites.

At 260K, the angle defined by two adjacent [$FeN_4^{eq}$] equatorial squares is 22.59º for X = ClBz conferring a certain degree of corrugation to the layers, which are separated in average by 12.0 Å and stack following the *a* + *c* direction in the same way as described for the orthorhombic crystals (Fig. S12, SI). Although, in general, the packing of the $CH_3Bz$ homologue can be described in the same terms, the angle defined by the equatorial squares of two adjacent octahedrons is considerably much larger, 48.57º, resulting in a much more corrugate layer. The crystal packing of both clathrates, view down the *a* direction, shows that the layers widespread parallel to the bc plane and perfectly superpose defining two different channels (labeled 1 and 2) running along the a direction where, respectively, 2 and 3 molecules of ClBz and $CH_3Bz$ per $Fe^{II}$ ion are located (Fig. 4 and Fig. S12, SI). For **AnPyAu·CH3Bz**, the guest molecules are much more packed in channel 1 since the axial ligands do not protrude in them, in contrast to channel 2 where pairs of non-interacting guests are separated more than 8 Å. In channel 1, the largest separation between guests at 95K is *ca*. 4 Å and one of the two crystallographically distinct $CH_3Bz$ molecules interact via π···π with an equivalent one being the shortest intermolecular distance C75···C73' of 3.490 Å (see Fig. S13, SI). The other $CH_3Bz$ molecule is close to the C1 atom (CN group, 3.491 Å) and

C37 (anthracene, 3.484 Å). In channel 2 only a relatively short contact is observed at 95K between another CH3Bz molecule and the pyridine moiety *d*(C66···C30) = 3.495 Å.

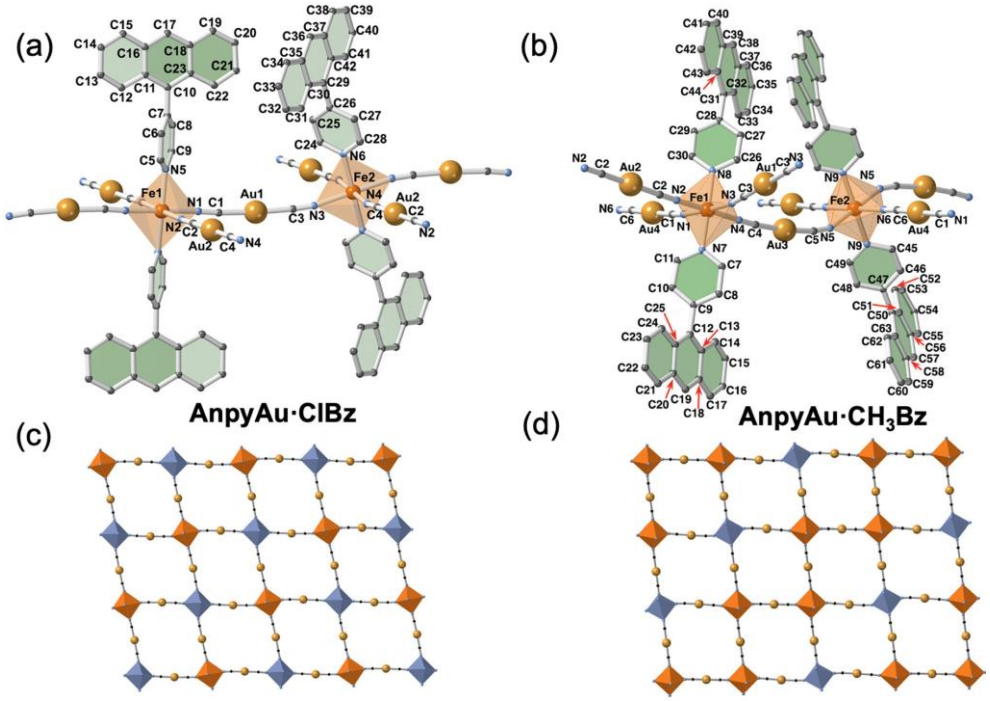


**Fig. 3.** Asymmetric unit for **AnPyAu·XBz**, X = Cl (a) and $CH_3$ (b). Distribution of the $Fe^{II}$ sites in the $\{Fe_4[Au(CN)_2]_4\}_n$ layers for X = Cl (c) and $CH_3$ (d), the axial ligands have been omitted for clarity.

The interdigitation of the AnPy ligands favours much more interlayer interactions in the two trigonal derivatives, particularly for the CH3Bz one due to its larger degree of corrugation. This may be a key factor influencing their metast- ability in favor of the orthorhombic form. Table S18 (SI) gathers a selection of interlayer contacts below 3.5 Å for the ClBz and CH3Bz derivatives.

When cooling down to 180K the overall structure of the ClBz clathrate remains the same but now three independent [$FeN_6$] centers are observed and, although the structure conserves the triclinic *P*-1 space group, the unit cell parameters are significantly modified (see Table S13, SI). The Fe-$N_{av}$ bond lengths are 1.964, 2.172 and 2.152 Å for [$Fe1N_6$], [$Fe2N_6$] and [$Fe3N_6$], respectively, indicating the occurrence of a complex LS-HS-HS state arising from the combination, in each layer, of interconnected $\{(Fe2)_2^{HS}(Fe3)_2^{HS}\}$, $\{(Fe1)_2^{LS}(Fe2)_2^{HS}\}$ and $\{(Fe1)_1^{LS}(Fe3)_1^{HS}(Fe2)_2^{HS}\}$ $\{Fe_4[Au(CN)_2]_4$ rhombuses as depicted in Fig. 5. The layers stack

along the *a* + *b* + *c* direction and the spin-state ordering can be described as defined by two alternating planes, running parallel to the a-direction, one defined by Fe1(LS)/Fe3(HS) centers and the other defined exclusively of Fe2(HS) centers laying perpendicular to the layers. Upon cooling to 110K, the Fe-N average distances change to 1.972 (Fe1), 1.955 (Fe2) and 2.168 (Fe3) Å defining a HS-LS-LS state. The ordering in this state is the same described for the LS-HS-HS state but now all the Fe2 centers are LS while the planes containing Fe1(LS) and Fe3(HS) remain identical. Both states are consistent with the magnetic behavior of the triclinic phase when the samples are measured in the mother liquor (see Fig. S4, SI).

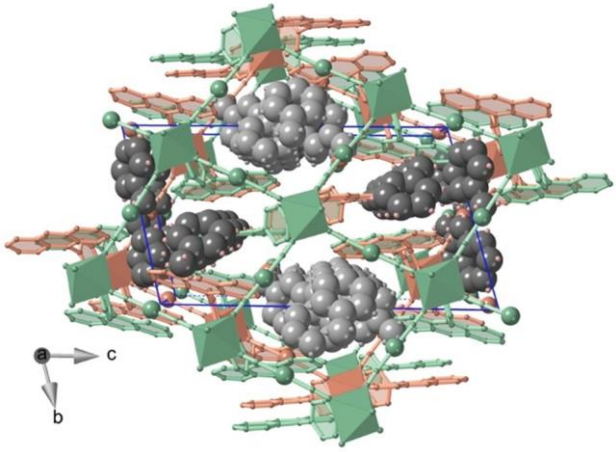


**Fig. 4.** Perspective view down the *a*-direction showing the superposition of three consecutive layers (green and salmon) of the triclinic **AnPyAu·$CH_3$Bz** and generation of two types of voids where the $CH_3$Bz guests (space filling) are located: light and grey channel 1 and 2, respectively. Blue lines define the unit cell.

Concerning the $CH_3$Bz derivative, the Fe1-$N_{av}$ and Fe2-$N_{av}$ bond-lengths decrease 0.108 Å (Fe1-$N_{av}$ = 2.068 Å) and 0.010 Å (Fe2-$N_{av}$ = 2.162 Å) upon cooling to 140K. Thus, considering that a complete spin state transformation involves a total bond length variation of ca. 0.2 Å, this indicates that whereas 50% of the Fe1 sites undergo spin transition, the Fe2 sites remain mainly in the HS state. Therefore, overall, only 25% of the $Fe^{II}$ ions present a HS - LS transition at 140K. An additional cooling to 95 K induces a further decrease of the Fe-$N_{av}$ bond lengths to 2.048 (Fe1) and 2.091 (Fe2) Å corresponding to a total Fe-$N_{av}$ bond length decrease of *ca*. 0.124 (Fe1) and 0.081 (Fe2) Å that correspond to *ca*. 50% spin transition. This structural change, which is consistent with that observed in the magnetic measurements (see Fig. S4, SI), slightly modifies the corrugation of the layers being now the angle between the equatorial planes of the Fe1 and Fe2 octahedrons 44.73º. In contrast

to the observed for the ClBz derivative, no symmetry breaking occurs during the SCO and hence no ordering of the HS and LS spin states was observed.

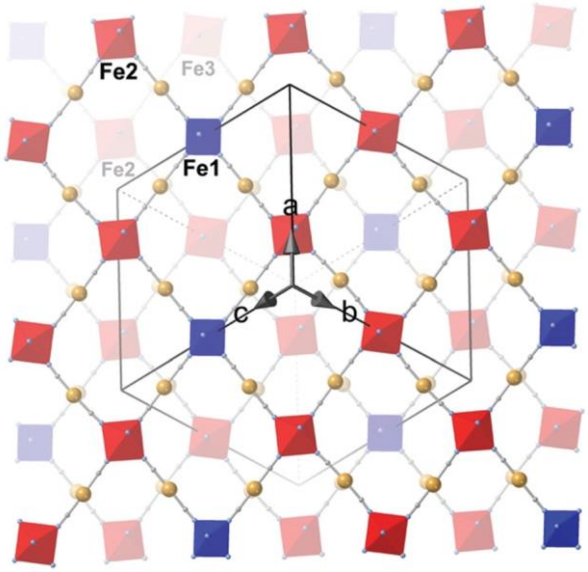


**Fig. 5.** Projection of two adjacent layers down the *a* + *b* + *c* direction showing the distribution of the HS (red octahedra) and LS (blue octahedra) centers. The axial ligands and ClBz guests have been omitted for clarity. The black lines correspond to the triclinic unit cell that relates the $Fe^{II}$ centers of both layers.

### 4.3.4.- Thermal SCO by single crystal UV-Vis absorption spectroscopy

The optical properties of **AnPyM·XBz** have been studied for individual single crystals in the temperature interval 10–300 K (see experimental section and SI). Herein, we will describe the results for **AnPyAg·IBz** as a representative example. The absorption spectrum of this compound has been recorded in the HS (300K) and LS (10K) states from 200 to 1200 nm (Fig. 6(a)). In the HS state the broad band centered at 830 nm, with optical density OD = 0.62, corresponds to the $^5T_2 \rightarrow {}^5E$ transition characteristic of the HS state ($\varepsilon$ = 12 $M^{-1}$ $cm^{-1}$). Below 700 nm, the HS spectrum is almost flat until 480 nm where a new band much higher in Fig. 6. (a) Complete absorption spectra at RT and 10K of a single crystal of **AnPyAg·IBz** and thermal evolution of the d–d $^1A_1 \rightarrow {}^1T_1$ band during (b) heating and (c) cooling, at 2 K $min^{-1}$ intensity appears and saturates at 415 nm, which corresponds to the tail of the metal-to-ligand charge transfer (MLCT) band. At 10 K the 830 nm band bleaches and instead a new relatively narrower and more intense band (OD = 3.92) centered at 532 nm appears, which corresponds to the $^1A_1 \rightarrow {}^1T_1$ transition of the LS state ($\varepsilon$ = 56 $M^{-1}$ $cm^{-1}$). Below 470 nm the tail of the MLCT

band appears and saturates below 438 nm. The change from the HS to LS state is accompanied by a drastic color change from pale-yellow to red (see inset in Fig. 6(a)). Similar features are found for the HS and LS bands of all **AnPyM·XBz** at room temperature and 10K (Fig. S14, SI). Likewise, the values of the corresponding extinction coefficients are relatively constant among the different crystals (Table S19, SI). Representative thermal evolution of the LS band intensity recorded in the heating-cooling modes at a scan rate of 2 K $min^{-1}$ is displayed in Fig. 6(b) and (c), respectively for the IBz clathrate. For the rest of compounds, the scan rate used was 10 K $min^{-1}$. Due to the difficulties to get good single crystals of **AnPyAu·$CH_3$Bz**, these measurements were performed on IR-like pellets by diluting the crystalline powder in KBr. In order to optically track the evolution of the HS molar fraction (γHS), we have used the thermal evolution of the difference between the maximum and minimum optical density (ΔOD) of the LS band. However, for the M = Au derivatives, displaying incomplete SCO, the residual gHS have been similarly estimated from the remaining HS band at low temperatures. As observed in Fig. 7, all the **AnPyM·XBz** compounds experience relatively abrupt and stepwise transitions with critical temperatures Tc and plateaus in good accord with the results obtained by magnetism (Fig. 1). The slight lower temperatures observed by absorption are attributed to the faster scan rate of the temperature (10 *vs*. 2 K $min^{-1}$). Indeed, aperture of the hysteresis has been observed for **AnPyM·XBz** upon faster scan rates of temperature (Fig. S15, SI). It is worth mentioning that an exception of the agreement with the magnetic data is found for **AnPyAu·$CH_3$Bz**. The thermal spin transition obtained optically for the semitransparent pellet is more gradual due to the grinding and pressuring process (Fig. S16, SI).[71]

#### 4.3.5.- Coexistence of SCO and fluorescence

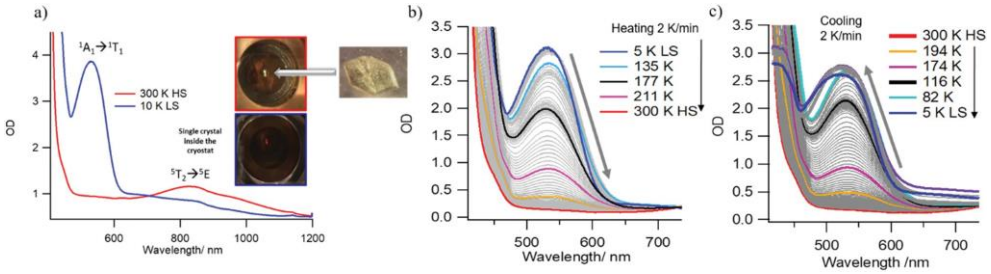


**Fig. 6.** (a)Complete absorption spectra at RT and 10K of a single crystal of **AnPyAg·IBz** and thermal evolution of the d-d $^1A_1 \rightarrow {}^1T_1$ band during (b) heating and (c) cooling, at 2 K $min^{-1}$.

The excitation and emission spectra of **AnPyM·XBz** have been recorded at room temperature in an ensemble of crystals glued to a cooper plate with silver paste to ensure thermal conductivity as shown in the Inset of Fig. S17 (SI). As an example, the excitation spectrum of **AnPyAg·IBz** is shown in Fig. S17a (SI).

It is characterized by two sets of peaks, one higher in intensity centered at 260 nm corresponding to the π-π* band of AnPy and another set split in four more structured excitation bands with origin in the different vibrational contributions between the ground and excited electronic states $S_0$ and $S_1$. The emission spectra of **AnPyAg·IBz** under excitation at 350 nm (Fig. S17b, SI) exhibit the emitting features of the $S_1$-$S_0$ transitions in addition to a less structured broader band centred at 500-550 nm associated with the excimer/exciplex. The excitation and emission spectra of the rest of **AnPyM·XBz** samples are almost identical in terms of peak position of the π-π* and $S_0$-$S_1$ transitions of AnPy ligand although the intensity of the emission band of the excimer/exciplex signals is very low and practically vanishes. As an exception, this latter band has been clearly identified in the case of **AnPyAu·IBz** and **AnPyAu·ClBz** (Fig. S18, SI). A relatively high QY value was obtained for the AnPy ligand (QY ≈ 25%, Fig. S19, SI), which is just slightly lower than for anthracene.[72] However, an important decrease of almost 50% is obtained when the ligand is part of the host structure of the non-spin-crossover material **NiAnPyAg·$NO_2$Bz** (QY ≈ 13%). The rigidity of the lattice and miss orientation of the AnPy ligands is expected to contribute to the decrease of non-radiative emissions leading to higher QY values. However, energy transfer from the ligand to the metals ($Ni^{II}$, $Ag^{I}$/$Au^{I}$) may play a relevant role in this case. Indeed, the QY values of the $Fe^{II}$ analogues decrease by around 25% more due to even stronger energy transfer from the ligand to the metals (QY ≈ 6%).

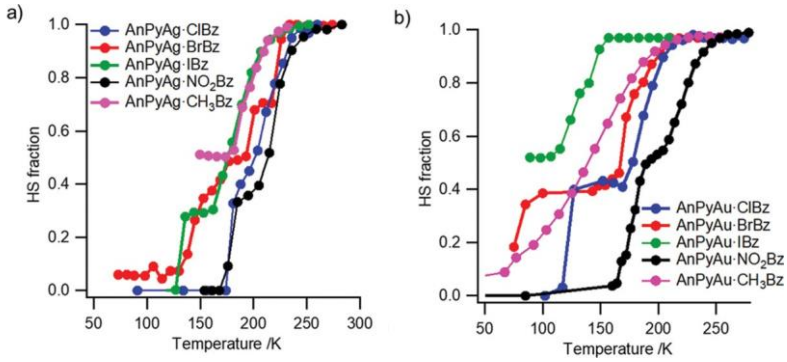


**Fig. 7.** Thermal dependence of $\gamma_{HS}$ of (a) **AnPyAg·XBz** and (b) **AnPyAu·XBz** obtained by single crystal absorption spectroscopy.

The thermal evolution of the fluorescence spectra (exc. 365 nm) was recorded for all the compounds including the $NO_2Bz$ clathrate of the non-SCO $Ni^{II}$ homologue and the free AnPy ligand as references. For the $Ni^{II}$ and AnPy derivatives the thermal dependence of the averaged intensity difference of all the peaks follows a straight line as expected due to thermal quenching (see Fig. S20, SI). This is also true for the monomer signal of the $Fe^{II}$ complexes but not for the excimer/exciplex signal observed for **AnPyAu·IBz** (Fig. 8(a) and (c)) and **AnPyAg·IBz** (Fig. 8(b) and (d)) centered around 520 nm whose signal increases with the temperature until approximately 250K. We associate this inversion of the trend with the LS to HS spin transition of the compounds and the lesser absorption of the fluorescence signal in the HS state (see absorption spectra of Fig. 6). Indeed, the temperature dependence of the HS fraction (γHS) extracted from the ratio between the monomer and excimer/exciplex signals matches reasonably well the spin transition curve obtained by magnetism and single crystal absorption for **AnPyM·IBz** (Fig. 8). Unfortunately, for the rest of **AnPyM·XBz** samples the signal of the excimer/exciplex is very weak and no change can be observed with the temperature (Fig. S21, SI). An exception is the case of **AnPyAu·ClBz** whose prominent excimer exciplex signal decreases in a non-linear fashion as temperature increases showing marked stabilization in the temperature interval where the spin transition takes place (Fig. S22, SI).

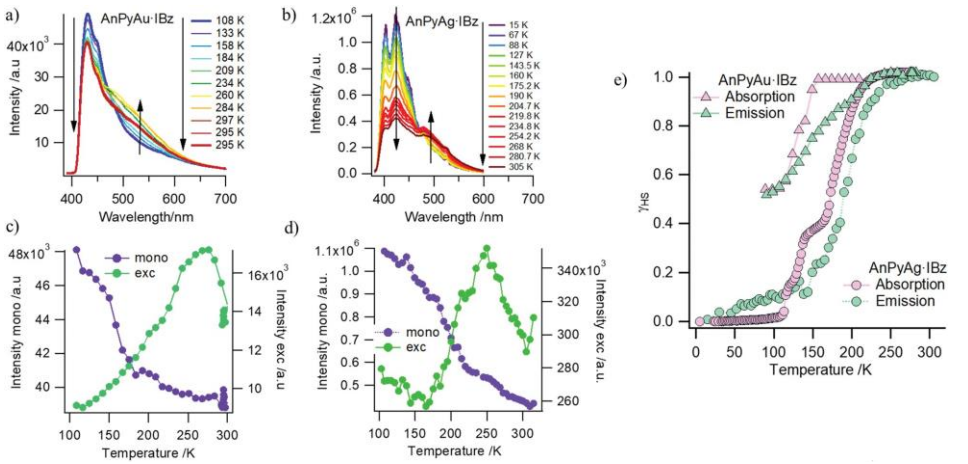


**Fig. 8.** Thermal evolution of the emission spectra after excitation at 365 nm of the ensemble of crystals of (a) **AnPyAu·IBz** and (b) **AnPyAg·IBz** upon heating ( 5 K $min^{-1}$). Corresponding variation of the monomer and excimer exciplex intensity with the temperature for (c) **AnPyAu·IBz** and (d) **AnPyAg·IBz** and (e) the comparison of the temperature dependence of the HS fraction extracted by the fluorescence and single crystal absorption.

## 4.4.- Discussion

The main objective of this paper is to delve into the design of new 2D metalorganic frameworks as new platforms for the study of synergies stemming from the coexistence of spin- crossover and luminescent properties. This has been achieved by assembling $Fe^{II}$, $[M(CN)_2]^-$ (M = Ag or Au) and the fluo- rescent AnPy ligands. Provided that the formation of the coordination polymer is carried out in the presence of a selected aromatic molecule XBz (X = $CH_3$, $NO_2$; Cl, Br, I), the resulting compounds present the formula $Fe(AnPy)_2[M(CN)_2]_2 \cdot XBz$ (**AnPyM·XBz**) where the XBz guests are trapped between the stacked bimetallic layers. The packing-mode of the most part of related dicyanometallate-based 2D networks is determined by interlayer metallophilic (Au···Au or Ag···Ag) interactions which lead to closed bilayered structures where no voids are accessible for hosting guest molecules. In such packing configuration, the pyridinic axial ligands, usually pointing toward the barycenter of the $[Fe_4(M(CN)_2)_4]$ windows of adjacent layers, prevent the inclusion of guests.[42–52] Nevertheless, the presence of a bulky axial ligand may inhibit the creation of metallophilic interactions avoiding the formation of a bilayered structure. This promotes the creation of open structures with the generation of interlayer porosity where the guest molecules can be incorpo- rated in a controlled way.[40,41] This strategy was implemented, for example, in the SCO network Fe[4-(3-Pentyl)pyridine]$_2$[Au(CN)$_2$]$_2$·Guest where the guests (chlorobenzene, *o*-dichlorobenzene, *m*-dichlorobenzene or *p*-dichlorobenzene) are intercalated between the bimetallic layers.[41] The authors concluded that the $T_c$ of each clathrate resulted to be influenced by the size of the aromatic guest via chemical pressure in a range of temperatures of 20-30 K.

In the present work, the introduction of the bulky anthracene group in the 4-position of the pyridine not only provides fluorescent properties but also confers enough void space between layers to permit the inclusion of a wide variety of template guests. Even if the different **AnPyM·XBz** clathrates are isostructural, the nature of the trapped guest strongly impacts on the resulting SCO properties. Indeed, the guest-free derivative, which conserves the same structure than the parent solvates, presents a gradual and incomplete SCO. In contrast, the guest-containing species present more or less abrupt and complete multi-stepped SCO behaviors. This observation reveals that the confined guest is a source of cooperativity activating and communicating the spin state change within the network. The trend of $T_c$ values ($T_c$(IBz) < $T_c$($CH_3$Bz) < $T_c$(BrBz) < $T_c$(ClBz) < $T_c$($NO_2$Bz)) does not correlate directly with the volume ($V$(IBz) > $V$(BrBz) > $V$($NO_2$Bz) > $V$(ClBz) > $V$($CH_3$Bz)) (see

Table S20, SI)[73] of the corresponding guest. Therefore, the $T_c$ modulation does not seem to be explained only by steric hindrance, acting against the network contraction during the spin transition and stabilizing the HS (lower $T_c$). Thus, it is reasonable to take also into consideration electronic factors related with subtle modifications of the ligand field strength of the AnPy ligand derived from its direct interaction with the guest molecules. Unfortunately, except for the CH3Bz derivatives at low temperatures, the strong disorder shown by the guest molecules prevented us from evaluating short host-guest contacts and hence directly assessing their potential steric and electronic influence on the AnPy ligand. Then, we only can prudently speculate with the electronic nature of XBz in order to afford some possible additional justification to the observed trend. As described for the X = $CH_3$ derivatives, it is expected the occurrence of π···π host-guest interactions. With this in mind, it is interesting to note that the highest $T_c$ value is observed for X = $NO_2$, in spite of being more voluminous than X = $CH_3$ or Cl (see Table S20, SI). This fact could be related to the strong electron-withdrawing character of X = $NO_2$, namely to the highest positive $\sigma_p$ Hammett[74,75] parameter of the XBz series (0.81), in contrast to the clathrate X = $CH_3$ ($\sigma_p$ = -0.17), which shows a $T_c$ significantly smaller. Consequently, the higher electron density of the $CH_3$Bz ring may weaken the attractive π···π interaction with the AnPy in contrast to the $NO_2$Bz-AnPy interaction. The latter interaction can indirectly enhance the π-accepting character of the ligand AnPy and hence increase subtly its ligand field strength. For IBz ($\sigma_p$ = 0.18), BrBz and ClBz ($\sigma_p$ = 0.23) with comparable $\sigma_p$ values, the $T_c$ of the corresponding clathrate ($T_c$(IBz) < $T_c$(BrBz) < $T_c$(ClBz)) seems to be directly correlated to the guest molecular volume $V$(IBz) > $V$(BrBz) > $V$(ClBz). Finally, the increase in $T_c$ when moving from **AnPyAu·XBz** to **AnPyAg·XBz**, and hence the stabilization of the LS state, is typically associated with the less donor character of the cyanide groups in $[Au(CN)_2]^-$ with respect to $[Ag(CN)_2]^-$ as a result of the higher electronegativity of the $Au^I$ against $Ag^I$ stemming from well-known relativistic effects.[76]

From an optical point of view, the single crystals of **AnPyM·XBz** display rather intense $Fe^{II}$ d-d bands in the LS state and thanks to the high quality and transparency of the crystals it has been possible to follow the thermal dependence of the optical density. For all the samples the absorption spectra show an isosbestic point indicating the presence of an equilibrium between the HS and LS populations as the thermal spin transition takes place. In general, the thermal dependence of the HS centers monitored optically is in good agreement with the magnetic data. Furthermore, the presence of the anthracene moiety in the AnPy ligand confers to the **AnPyM·XBz** crystals the property of luminescence. In

general, the crystals show a strong emission in the blue region and, in some cases, an additional less intense emission in the green region, which are associated with the monomer and excimer/exciplex signals, respectively. The monomer signal decreases linearly and bleaches with increasing temperatures due to thermal quenching. In contrast, the excimer/exciplex signal, only observed for **AnPyAg·IBz**, **AnPyAu·IBz** and **AnPyAu·ClBz**, increases or stabilizes in a concerted way as the amount of $Fe^{II}$ HS centers increases, due to their much weaker absorption compared to that of the LS centers in the same wavelengths window. Both contributions have also been previously described for the anthracene-bearing ditopic Bpan ligand used as pillar in the 3D SCO HCP $\{Fe(Bpan)[M^{I}(CN)_2]_2\}$ (so-called intrinsic fluorescence)[60] and, more markedly, in two other 3D SCO CPs $\{Fe(L)[M(CN)_2]_2\}\cdot Pyr$ with pyrene (Pyr) as guest fluorescent agent (L = bpb, bpben, extrinsic fluorescence) (M = Ag, Au).[60,61] All these compounds share a similar extinction coefficient of the $Fe^{II}$ d–d LS bands (≈50 $M^{-1}$ $cm^{-1}$), however, the efficiency of the energy transfer from the fluorophore to the $Fe^{II}$ seems to be proportional to the emission capacity of the former and hence to the quantum yield of the free fluorophore, being the highest for pyrene in the bpb and bpben based compounds (≈36%), followed by Bpan (≈32%) and finally AnPy (≈25%). This is the reason why the emission spectra of the AnPy derivatives are less efficient (less intense) than those of bpb, bpben and Bpan derivatives. It is also safe to state from this study that the presence of the guest XBz, which modulates the spin transition, does not contribute to the fluorescence in the UV region, although it could stabilize the excimer/exciplex. However, in spite of being isostructural, the excimer/exciplex emission has only been clearly observed for AnPyAg-IBz, AnPyAu-IBz and AnPyAu-ClBz although it is not an obvious matter to shed light on why the remaining members of the series, as well as the pure AnPy ligand, lack of this signal. It is commonly accepted that the precise orientation of the fluorophore ligands in the framework and in their interaction with the guests may be critical for the formation of the excimer/exciplex.[77] In this respect, the AnPy-based HCPs here described, keeping the isostructurality, present a number small relevant structural differences such as the degree of corrugation of the layers, the dihedral angle defined between the two anthracene moieties belonging to the same $Fe^{II}$ center, the dihedral angle defined between the anthracene and pyridine of the same AnPy, among others. Obviously, these differences also result from the inclusion of the different guests, which in addition do not display a favorable face-to-face stacking with the fluorophore as observed for the bpb, bpben and bpan-based 3D SCO HCPs.

## 4.5.- Conclusions

In summary, we have synthesized and characterized a novel family of multifunctional 2D HCPs formulated as $\{Fe(AnPy)_2[M(CN)_2]_2\}\cdot XBz$. This system is one of the first 2D Hofmann clathrates displaying concomitant multi-stepped SCO and fluorescent emission. These properties arise, respectively, from the presence of octahedrally coordinated $Fe^{II}$ ions and anthracene based AnPy ligands. Furthermore, the packing mode, consisting of stacking bimetallic layers, leads to large interlayer cavities where substituted benzenic guests are premeditatedly trapped and used as crystallization templates. Indeed, due to a combination of steric and electronic effects, this guest trapping impacts notably on the SCO behaviour modulating the $T_c$ as a function of the guest nature. The multi-stepped behaviour of the SCO has been evidenced also by single crystal X-ray diffraction which has allowed us to identify new examples of symmetry breaking and spin-state ordering associated to the spin state transition. The UV-visible absorption studies, carried out on individual single crystals, have revealed the HS ↔ LS equilibrium through the thermal evolution of the $Fe^{II}$ d-d bands, in good agreement with the thermal spin transition curves and $T_c$ modulation obtained from magnetism. Finally, new evidence of interplay between SCO and fluorescence functions has been unveiled in the case of X = I (M = Ag, Au) and X = Cl (M = Au). This interplay stems from the resonance between the $Fe^{II}$ LS-state d-d absorption band and the excimer/exciplex fluorescent emission band of the AnPy ligand in the green region. Therefore, as the $Fe^{II}$ LS-state d-d absorption band vanishes in the HS state the green emission increases with temperature allowing to monitor the spin conversion. These outcomes together with our previous observations of the SCO-fluorescence synergy in 3D SCO HCPs highlight the importance of the intrinsic emission capacity of the fluorophores involved and suggest that their precise orientation and packing in the structure as well as a relatively high compactness of the lattice is determinant to create and follow this synergy.

## 4.6.- Experimental section

### Materials and Reagents.

All reagents and solvents used, excluding the 4-(anthracene-9-yl)pyridine (AnPy) ligand and Iron(II) *p*-toluenesulfonate [$Fe^{II}(p\text{-}OTs)_2\cdot 6H_2O$], were obtained from commercial sources and used as received without further purifications.

The 4-(anthracene-9-yl)pyridine ligand was synthesized following a procedure previously described.[78]

Single crystals of **AnPyM·XBz** (M = Au, Ag; X = Cl, Br, I, CH3, NO2). were grown by slow liquid diffusion in test tubes. The iron salt Fe(*p*-OTs)$_2$·6H$_2$O (50.6 mg, 0.1 mmol) and 4-(anthracene-9-yl)pyridine (51.0 mg, 0.2 mmol) were dissolved in 4 mL of MeOH:Xbz (1:3) and added to the bottom of the tube. A spacer of 5 mL of MeOH:Xbz (2:1) was then carefully added. To complete the diffusion, a solution of M(CN)$_2$ (M = Ag (40.0 mg, 0.2 mmol), Au (57.6 mg, 0.2 mmol) in 2 mL of MeOH was added on top. The tube was then sealed and left in darkness for 4 weeks, after that time yellow rhombohedral crystals appear in 70% yield.
**AnPyM** was obtained by heating the derivative of choice up to the adequate temperature for the guest to leave the network. Check main manuscript and TGA for more information.
*Elemental Analysis*. Calculated for **AnPyAg** [$C_{42}H_{26}N_6FeAg_2$ (886.3) (%)]: C 56.92; H 2.96; N 9.48. Found (%): C 56.64; H 2.71; N 9.67. Calculated for **AnPyAg·NO$_2$Bz** [$C_{54.2}H_{36.2}N_8O_{4.1}FeAg_2$ (1136.2) (%)]: C 57.27; H 3.21; N 9.89. Found (%): C 57.03; H 3.36; N 9.95. Calculated for **AnPyAg·CH$_3$Bz** [$C_{53.8}H_{41.7}N_6FeAg_2$ (1066.8) (%)] C 60.52; H 3.95; N 7.87. Found (%): C 60.84; H 3.86; N 7.71. Calculated
for **AnPyAg·ClBz** [$C_{53.1}H_{35.3}N6Cl_{1.9}FeAg_2$ (1094.4) (%)]: C 58.27; H 3.25; N 7.68. Found (%): C 58.17; H 3.41; N 7.75. Calculated for **AnPyAg·BrBz** [$C_{53.3}H_{35.4}N_6Br_{1.9}FeAg_2$ (1181.4) (%)]: C 54.16; H 3.03; N 7.11. Found (%): C 53.96; H 2.97; N 7.27. Calculated for **AnPyAg·IBz** [$C_{51.6}H_{34}N_6I_{1.6}FeAg_2$ (1211.7) (%)]: C 51.10; H 2.83; N 2.83. Found (%): C 51.34; H 2.74; N 6.84. Calculated for **AnPyAu** [$C_{42}H_{26}N_6FeAu_2$ (1064.5) (%)]: C 47.39; H 1.46; N 7.89. Found (%): C 47.07; H 1.63; N 7.93. Calculated for **AnPyAu·NO$_2$Bz** [$C_{53.8}H_{35.8}N_8FeAu_2$ (1305.7) (%)]: C 49.45; H 2.77; N 8.53. Found (%): C 49.19; H 2.96; N 8.91. Calculated for **AnPyAu·CH$_3$Bz** [$C_{53.8}H_{41.7}N_6FeAu_2$ (1245.0) (%)]: C 51.86; H 3.38; N 6.75. Found (%): C 51.39; H 3.74; N 6.97. Calculated for **AnPyAu·ClBz** [$C_{51.6}H_{34}N_6Cl_{1.6}FeAu_2$ (1244.5) (%)]: C 49.80; H 2.76; N 6.75. Found (%): C 50.06; H 2.79; N 6.62. Calculated for **AnPyAu·ClBz** [$C_{51}H_{33.5}N_6Br_{1.5}FeAu_2$ (1300.0) (%)]: C 47.12; H 2.60; N 6.46. Found (%): C 46.97; H 2.71; N 6.23. Calculated for **AnPyAu·IBz** [$C_{50.5}H_{33.1}N_6I_{1.4}FeAu_2$ (1354.15) (%)]: C 44.81; H 2.47; N 6.20. Found (%): C 44.27; H 2.03; N 6.64.

**Physical Measurements.**

*Magnetic Measurements*. Variable temperature magnetic susceptibility data were recorded with a Quantum Design MPMS2 SQUID magnetometer equipped with a 7 T magnet,

operating at 1 T and at temperatures of 2-400 K at 1 K $min^{-1}$. Experimental susceptibilities were corrected for diamagnetism of the constituent atoms using Pascal's constants.

*Calorimetric Measurements*. Calorimetric measurements were performed using a differential scanning calorimeter (Mettler Toledo, Model DSC 821e). Low temperatures were obtained with an alumninum block attached to the sample holder, refrigerated with a flow of liquid nitrogen and stabilized at a temperature of 110 K. The sample holder was kept in a drybox under a flow of dry nitrogen gas to avoid water condensation. The measurements were performed at 10 K $min^{-1}$ using ~15 mg of microcrystalline samples of crystalline samples sealed in aluminum pans with a mechanical crimp. Temperature and heat flow calibrations were made with standard samples of indium by using its melting transition (429.6 K, 28.45 J $g^{-1}$). An overall accuracy of ±0.2 K in temperature and ±2% in the heat capacity is estimated. The uncertainty increases for the determination of the anomalous enthalpy and entropy due to the substraction of an unknown baseline.

*Single Crystal X-ray Diffraction.* Single crystal X-ray data were collected on an Oxford Diffraction Supernova diffractometer using a graphite monochromated Mo Kα radiation (λ = 0.71073 Å). A multiscan absorption correction was performed. The structures were solved by direct methods using SHELXS-2014 and refined by full matrix least squares on $F^2$ using SHELXL-2014.[79] Non-hydrogen atoms were refined anisotropically and hydrogen atoms were placed in calculated positions refined using idealized geometries (riding model) and assigned fixed isotropic displacement parameters. CCDC 2166356-2166379 contain the supplementary crystallographic data for this article. These data can be obtained free of charge from The Cambridge Crystallographic Data Centre via www.ccdc.cam.ac.uk/data_request/cif.

*TGA analysis*. TGA experiments were carried out with a TA instruments TGA550 device equipped with a Pt/Rh oven ($T_{max}$ = 1000°C). A flow of dry nitrogen gas was used as the atmosphere during the measurement. The samples were measured in a Pt pan.

*Absorption spectroscopy*. The single crystals are mounted in a copper plate with a previously made hole of the same size. To attach them, silver-nanoparticles paste (Agar scientific) is used to ensure the thermal conductivity. The spectra are recorded with the double beam UV/Vis/NIR spectrophotometer Varian Cary 6000. The temperature is tuned with a closed cycle cryostat with a cooling-heating rate of 10 K $min^{-1}$.

*Quantum yield*. A Quantum Efficiency Measurement System (EQE/IQE) (Newport QUANTX-300) was used to estimate the quantum yield of all the samples. As an excitation source a 365 nm LED (Thorlabs) was used.

*Fluorescence spectroscopy*. The room temperature fluorescence spectra of all samples were recorded in a fluorescence spectrophotometer Varian Cary Eclipse.
*Variable temperature emission spectra*. Fluorescence measurements at variable temperature were carried out using a closed-cycle He-flow cryostat (Sumitomo Cryogenics HC-4E) attached with a Lakeshore 340 temperature controller. The samples were cooled from room temperature to to 15K. The heating-cooling rate was set at 10 K $min^{-1}$. The excitation in most of the temperature cycles is a 365 nm LED (Thorlabs). A detection filter was used to cut the excitation source. The emission was detected with a CCD camera (Roper Pixis 100) coupled to a visible monochromator (Acton Spectra Pro, Princeton Instruments, 300 grooves per mm, centred at 600 nm). The emission intensity was integrated as a function of temperature.

## 3.7.- References


[1] E. König, *Nature and Dynamics of the Spin-State Interconversion in Metal Complexes*, 1991, pp. 51-152.

[2] A. Bousseksou (Ed.) Spin Crossover Phenomenon. *C. R. Chimie*, 2018, **21**, 1055-1299.

[3] P. Gütlich and G. Goodwin (Eds.), Spin crossover in transition metal compounds I-III, *Top. Curr. Chem.*, 2004, 233-235.

[4] B. Weber, *Coord. Chem. Rev.*, 2011, **40**, 2432-2449.

[5] M. A. Halcrow, *Chem. Soc. Rev.*, 2011, **40**, 4119-4142.

[6] V. Niel, M. C. Muñoz, A. B. Gaspar, A. Galet, G. Levchenko and J. A. Real, *Chem. – Eur. J.*, **8**, 2446-2453.

[7] P. Gütlich, A. Hauser and H. Spiering. *Angew. Chem., Int. Ed.*, 1994, **33**, 2024-2054.

[8] S. Brooker, *Chem. Soc. Rev.*, 2015, **44**, 2880-2892.

[9] M. A. Halcrow, *Chem. Lett.*, 2014 **43**, 1178-1188.

[10] M. A. Halcrow (Ed.) *Spin-Crossover materials: properties and applications*, Wiley-Blackwell, 2013.

[11] A. Bousseksou, G. Molnár, L. Salmon and W. Nicolazzi, *Chem. Soc. Rev.*, 2011, **40**, 3313-3335.

[12] O. I. Kucheriv, I. O. Fristsky and I. A. Gural'skiy, *Inorg. Chim, Acta*, 2021, **521**, 120303.

[13] M. C. Muñoz and J. A. Real, *Coord. Chem. Rev.*, 2011, **255**, 2068-2093.

[14] Y. Garcia, V. Niel, M. C. Muñoz and J. A. Real, Spin Crossover in 1D, 2D and 3D polymeric Fe(II) Networks, *Spin Crossover in Transition Metal Compounds I*, Springer, berlin, Heidelberg, 2004, 229-257.

[15] Z.-P Ni, J.-L Liu, M.-N Hoque, W. Liu, J.-Y Li, Y.-C. Chen and M. L. Tong, *Coord. Chem. Rev.*, 2017, **335**, 28-93.

[16] K. A. Zenere, S. G. Duyker, E. Trzop, E. Collet, B. Chan, P. W. Doheny, C. J. Kepert and S. M. Neville, *Chem. Sci.*, 2018, **9**, 5623-5629.

[17] N. F. Sciortino, F. Ragon, Y. M. Klein, C. E. Housecroft, C. G. Davies, C. G. Davies, G. N. L. Jameson, G. Chastanet and S. M. Neville, *Inorg. Chem.*, 2018, **57**, 11068-11076.

[18] E. Milin, V. Patinec, S. Triki, E. E. Bendeif, S. Pillet, M. Marchivie, G. Chastanet and K. Boukheddaden, *Inorg. Chem.*, **55**, 11652-11661.

[19] N. F. Sciortino, F. Ragon, K. A. Zenere, P. D. Southon, G. J. Halder, K. W. Chapman, L. Piñeiro-López, J. A. Real, C. J. Kepert and S. M. Neville, *Inorg. Chem.*, 2016, **55**, 10490-10498.

[20] A. T. Brennan, K. A. Zenere, C. J. Kepert, J. K. Clegg and S. M. Neville, *Inorg. Chem.*, 2020, **59**, 14296-14305.

[21] S. M. Neville, A. T. Brennan, K. A. Zenere, H. E. A. Brand, J. R. Price, M. M. Bhadbhade, G. F. Turner, S. A. Moggach, F. J. Valverde-Muñoz, J. A. Real, J. K. Clegg and C. J. Kepert, *Inorg. Chem.*, 2020, **59**, 14296-14305

[22] I. A. Gural-Skiy, S. I. Shylin, V. Ksenofontov and W. Tremel, *Eur. J. Inorg. Chem.*, 2019, 4532-4537.

[23] N. F. Sciortino, K. A. Zenere, M. E. Corrigan, G. J. Halder, G. Chastanet, J. F. Létard, C. J. Kepert and S. M. Neville, *Chem. Sci.*, 2016, **8**, 701-707.

[24] M. J. Murphy, K. A. Zenere, F. Ragon, P. D. Southon, C. J. Kepert and S. M. Neville, *J. Am. Chem. Soc.*, 2017, **139**, 1330-1335.

[25] Y. M. Klein, N. F. Sciortino, F. Ragon, C. E. Housecroft, C. J. Kepert and S. M. Neville, *Chem. Commun.*, 2014, **50**, 3838-3840.

[26] M. Meneses-Sánchez, R. Turo-Cortés, C. Bartual-Murgui, I. Da Silva, M. C. Muñoz and J. A. Real, *Inorg. Chem.*, 2021, **60**, 11866-11877.

[27] R. Ohtani and S. Hayami, *Chem. – Eur. J.*, 2017, **23**, 2236-2248.

[28] V. Niel, A. L. Thompson, M. C. Muñoz, A. Galet, A. E. Goeta and J. A. Real, *Angew. Chem., Int. Ed.*, 2003, **42**, 3760-3763.

[29] H. Xu, G. Juhász, K. Yoshizawa, M. Takahashi, S. Kanegawa and O. Sato, *CrystEngComm*, 2010, **12**, 4031-4034.

[30] K. Yoshida, D. Akahoshi, T. Kawasaki, T. Saito and T. Kitazawa, *Polyhedron*, 2013, **66**, 252-256.

[31] J.-Y. Li, Z. Yan, Z.-P. Ni, Z. M. Zhang, W. Liu, Z.-P. Ni and M. L. Tong, *Inorg. Chem.*, 2014, **53**, 4039-4046.

[32] J. Y. Li, Y. C. Chen, Z. M. Zhang, W. Liu, Z.-P. Ni and M. L. Tong, *Chem. Eur. J.*, 2015, **21**, 1645-1651.

[33] J. Y. Li, C.-T. He, Y. C. Chen, Z. M. Zhang, W. Liu, Z.-P. Ni and M. L. Tong, *J. Mater. Chem. C*, 2015, **3**, 7830-7835.

[34] J. E. Clements, J. R. Price, S. M. Neville and C. J. Kepert, *Angew. Chem., Int. Ed.*, 2014, **53**, 10164-10168.

[35] I. A. Gural'skiy, S. I. Shylin, B. O. Golub, V. Ksenofontov, I. O. Fritsky and W. Tremel, *New J. Chem.*, 2016, **40**, 9012-9016.

[36] M. L. Tong, W. Liu, Y.-Y. Peng, S.-G- Wu, Y.-C. Chen, N. Hoque, Z.-P. Ni and X.-M. Chen, *Angew. Chem., Int. Ed.*, 2017, **129**, 15178-15182.

[37] L. Piñeiro-López, F. J. Valverde-Muñoz, M. Seredyuk, M. C. Muñoz, M. Haukka and J. A. Real, *Inorg. Chem.*, 2017, **56**, 7038-7047.

[38] L. Piñeiro-López, F. J. Valverde-Muñoz, M. Seredyuk, C. Bartual-Murgui, M. C. Muñoz and J. A. Real, *Eur. J. Inog. Chem.*, 2018, 289-296.

[39] F. J. Valverde-Muñoz, C. Bartual-Murgui, L. Piñeiro-López, M. C. Muñoz and J. A. Real, *Inorg. Chem.*, 2019, **58**, 10038-10046.

[40] G. Agustí, M. C. Muñoz, A. B. Gaspar and J. A. Real, *Inorg. Chem.*, 2008, **47**, 2552-2561.

[41] Y. Ueki, J. Okabayashi and T. Kitazawa, *Chem. Lett.*, 2017, **46**, 747-749.

[42] T. Kosone, T. Kawasaki, I. Tomori and J. Okabayashi, *Inorganics*, 2017, 1-10.

[43] K. Yoshida, T. Kosone, C. Kanadani, T. Saito and T. Kitazawa, *Polyhedron*, 2011, **30**, 3062-3066

[44] S. Ueno, T. Kawasaki, J. Okabayashi and T. Kitazawa, *Bull. Chem. Soc. Jpn.*, 2015, **88**, 551-553.

[45] A. Sugaya, S. Ueno, J. Okabayashi and T. Kitazawa, *New J. Chem.*, 2014, **38**, 1955-1958.

[46] S. Ueno, T. Kawasaki, J. Okabayashi and T. Kitazawa, *Bull. Chem. Soc. Jpn.*, **89**, 581-583.

[47] Y. Meng, Q. Q. Sheng, M. N. Hoque, Y. C. Chen, S. G. Wu, J. Tucek, R. Zboril, T. Liu, Z.-P Ni and M. L. Tong, *Chem. – Eur. J.*, 2017, **23**, 10034-10037.

[48] J. Okabayashi, S. Ueno, T. Kawasaki and T. Kitazawa, *Inorg. Chim. Acta*, 2016, **445**, 1721.

[49] T. Kosone, I. Tomori, C. Kanadani, T. Saito, T. Mochida and T. Kitazawa, *Dalton Trans.*, 2010, **39**, 1719-1721,

[50] G. Agustí, A. B. Gaspar, M. C. Muñoz, P. G. Lacroix and J. A. Real, *Aust. J. Chem.*, 2009, **62**, 1155-1165.

[51] T. Kosone, C. Kachi-Terajima, C. Kanadani, T. Saito and T. Kitazawa, *Chem. Lett.*, 2008, **37**, 422-423.

[52] A. Galet, M. C. Muñoz, V. Martínez and J. A. Real, *Chem. Commun.*, 2004, 2268-2269.

[53] B. Benaicha, K. Van Do, A. Yangui, N. Pittala, A. Lusson, M. Sy, G. Bouchez, H. Fourati, C. J. Gómez-García, S. Triki and K. Boukheddaden, *Chem. Sci.*, 2019, **10**, 6791-6798.

[54] J. Yuan, S.-Q. Wu, M.-J. Liu, O. Sato and H.-Z Kou, *J. Am. Chem. Soc.*, 2018, **140**, 9426-9433.

[55] J.-L. Wang, Q. liu, Y.-S. Meng, X. liu, H. Zheng, Q. Shi, C.-Y. Duan and T. Liu, *Chem. Sci.*, 2018, **9**, 2892-2897.

[56] C. Lochenie, K. Schötz, F. Panzer, H. Kurz, B. Maier, F. Puchtler, S. Agarwal, A. Kö and B. Weber, *J. Am. Chem. Soc.*, 2018, **140**, 700-709.

[57] B. Schäfer, T. Bauer, I. Faus, J. A. Wolny, F. Dahms, O. Fuhr, S. Lebedkin, H.-C. Wille, K. Schlage, K. Chevalier, F. Rupp, R. Diller, V. Schünemann, M. M. Kappes and M. Ruben, *Dalton Trans.*, 2017, **46**, 2289-2302.

[58] H. J. Shepherd, C. M. Quintero, G. Molnár, L. Salmon and A. Bousseksou, *Spin crossover properties and applications* (M. Halcrow, ed.) 2013, 347-373.

[59] M. K. Javed, A. Sulaiman, M. Yamashita and Z.-Y Li, *Coord. Chem. Rev.*, 2022, **467,** 214625.

[60] M. Meneses-Sánchez, L. Piñeiro-López, T. Delgado, C. Bartual-Murgui, M. C. Muñoz, P. Chakraborty and J. A. Real, *J. Mater. Chem. C*, 2020, **8**, 1623-1633.

[61] T. Delgado, M. Meneses-Sánchez, L. Piñeiro-López, C. Bartual-Murgui, M. C. Muñoz and J. A. Real, *Chem. Sci.*, 2018, **9**, 8446-8452.

[62] J. Ge, Z. Chen, L. Zhang, X. Liang, J. Su, M. Kurmoo and J. Zuo, *Angew. Chem., Int. Ed.*, 2019, **131**, 8881-8885.

[63] S. Ghosh, S. Kamilyam T. Pramanik, M. Rouzières, R. Herchel, s. Mehta and A. Mondal, *Inorg. Chem.*, 2020, **59**, 13009-13013.

[64] Y. R. Qiu, L. Cui, J. Y. Ge, M. Kurmoo, G. Ma and J. Su, *Front. Chem.*, 2021, **9**, 692939.

[65] C. F. Wang, J. C. Wu and Q. Li, *Inorg. Chem. Front.*, 2022, 3251-3258.

[66] S. Decurtins, P. Gütlich, C. P. Köhler, H. Spiering and A. Hauser, *Chem. Phys. Lett.*, 1984, **105**, 1-4.

[67] J. F. Létard, P. Guionneau, L. Rabardel, J. A. K. Howard, A. E. Goeta, D. Chasseau and O. Kahn, *Inorg. Chem.*, 1998, **37**, 4432-4441.

[68] A. Hauser, *Coord. Chem. Rev.*, 1991, **111**, 275-290.

[69] A. Hauser, A. Vef and P. Adler, *J. Chem. Phys.*, 1991, **91**, 8710-8717.

[70] A. Hauser, C. Enachescu, M. L. Daku, A. Vargas, and N. Amstutz, *Coord. Chem. Rev.*, 2006, **250**, 1642-1652.

[71] T. Delgado, A. Tissot, C. Besnard, L. Guénée, P. Pattison and A. Hauser, *Chem. – Eur. J.*, 2015, **21**, 3664-3670.

[72] I. B. Berlman, *Handbook of fluorescence spectra of aromatic Molecules*, 1971, 473.

[73] Values of V were calculated were calculated with the software UCSF Chimera see E. F. Pettersen, T. D. Goddard, C. C. Huang, G. S. Couch, D. M. Greenblatt, E. C. Meng and T. E. Ferrin, UCSF Chimera-a visualization system for exploratory research and analysis, *J. Comput. Chem.*, 2004, **25**, 1605-1612.

[74] L. P. Hammett, *J. Am. Chem. Soc.*, 1937, **59**, 96-103.

[75] C. Hansch, A. Leo and R. W. Taft, *Chem. Rev.*, 1991, **91**, 165-195.

[76] P. Pyykkö, *Annu. Rev. Phys. Chem.*, 2012, **63**, 45-64.

[77] P. Samanta, S. Dutta and S. K. Ghosh, *Met. Org. Frameworks (MOFs) Environ. Appl.,* 2019, 231-283.

[78] W. J. Ramsay, F. T. Szczypiński, H. Weissman, T. K. Ronson, M. J. Smulders, B. Rybtchinski, J. R. Nitschke.

[79] G. M. Sheldrick, *Acta Scrystallographica Sect. A Found. Adv.*, 2015, **71**, 3-8.

## 3.8.- Supporting Information

**Fig. S1.** Thermogravimetric analysis for all the **AnPyM·XBz** derivatives.

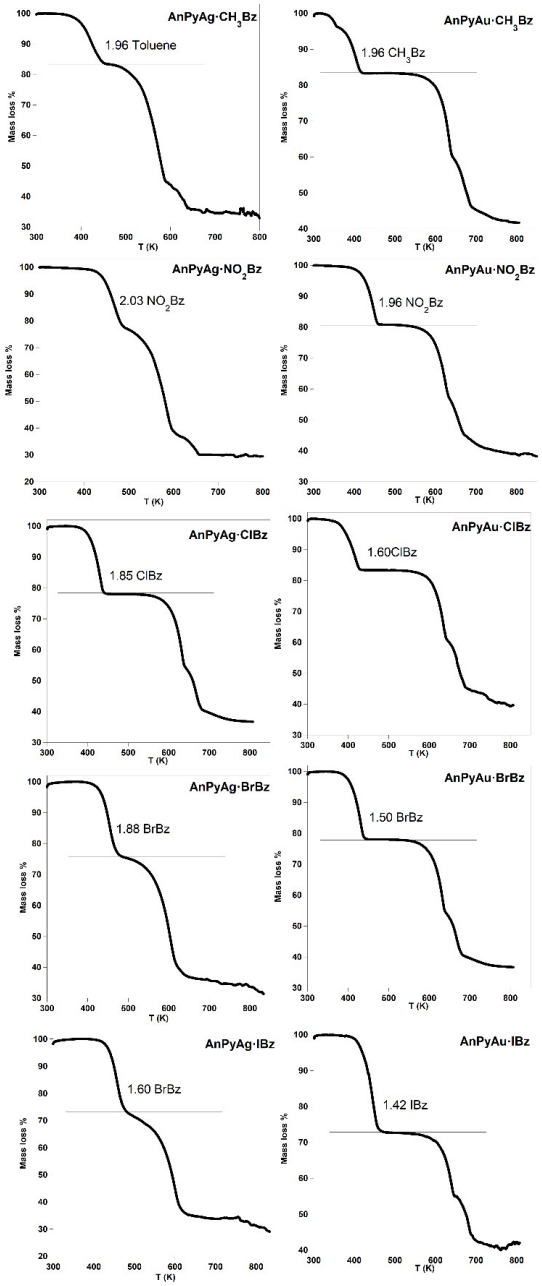

**Fig. S2.** PXRD patterns of (a) **AnPyAu·$CH_3$Bz** and (b) **AnPyAuClBz** measured in the mother liquor (green lines) and several hours after exposing to air (red lines) which shows the transformation from the triclinic to the orthorhombic structures, The patters simulated from the triclinic (top) and orthorhombic (bottom) structures are depicted (black lines) for comparison. In the case of the orthorhombic simulated patter, that obtained from **AnPyAu·BrBz** was used as reference.

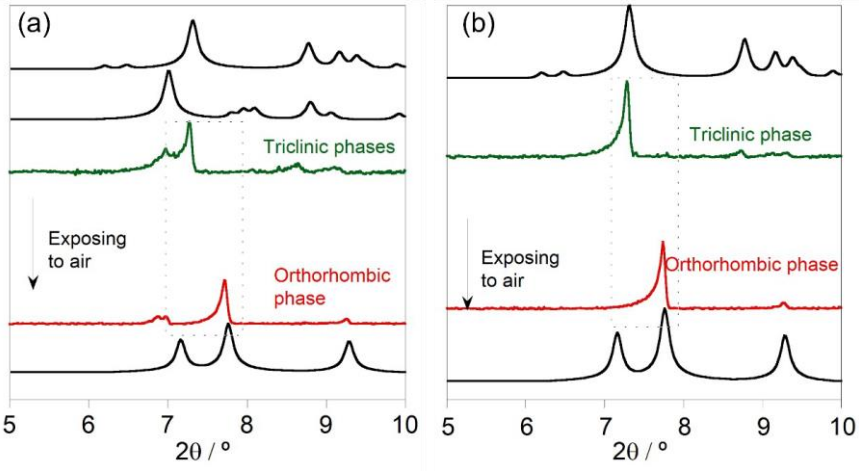


**Fig. S3.** PXRD patterns for the M = Ag (left) and Au (right) derivatives of the **AnPyM·XBz** family. The unsolvated counterparts (green lines), **NiAnPyAu·$NO_2$Bz** and typical simulated orthorhombic patters of **AnPyM·XBz** (black lines) are also displayed for comparison (the change in intensity ratio of peaks between 6-10º may be explained by preferential orientations of the measured crystals).

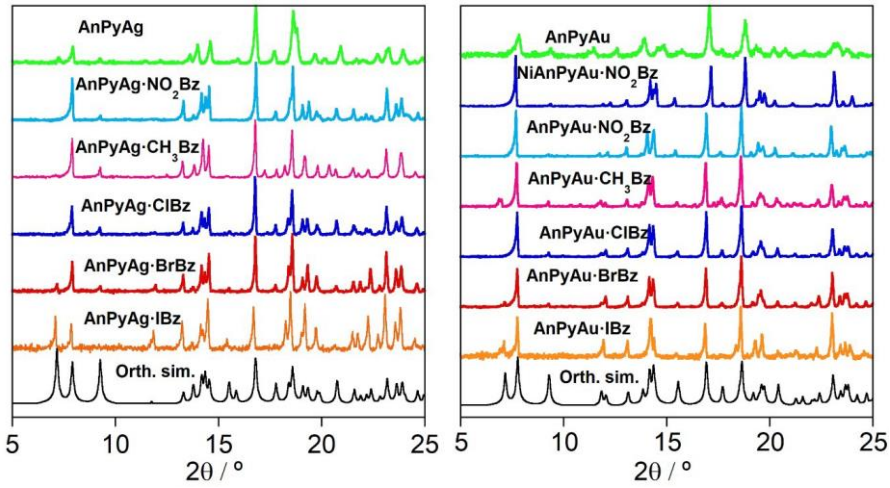

**Fig. S4.** Thermal magnetic behaviour of (a) **AnPyAu·$CH_3Bz$** and (b) **AnPyAu·ClBz** measured in the mother liquor (green lines) and several hours ater exposing to air (red lines).

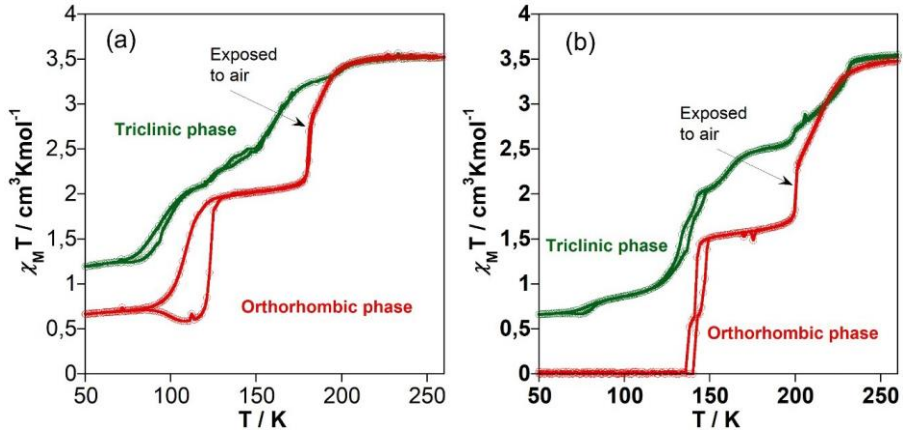


**Fig. S5.** Thermal dependence magnetic behavior of the **AnPyAg** and **AnPyAu** unsolvated counterparts.

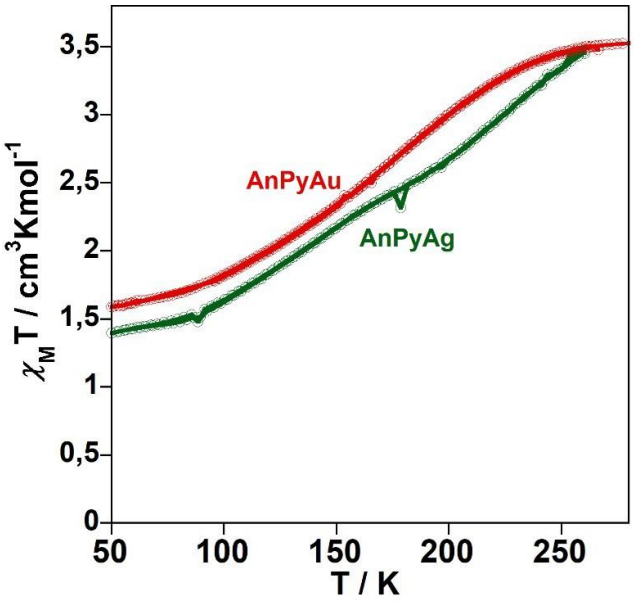

**Fig. S6.** DSC Curves for the compounds **AnPyAg·XBz** (X = Cl, Br, $CH_3$, $NO_2$) and **AnPyAu·$NO_2$Bz** measured at 10 K $min^{-1}$. The blue and red lines represent the cooling and heating modes, respectively. Magnetic curves are also represented for comparison.

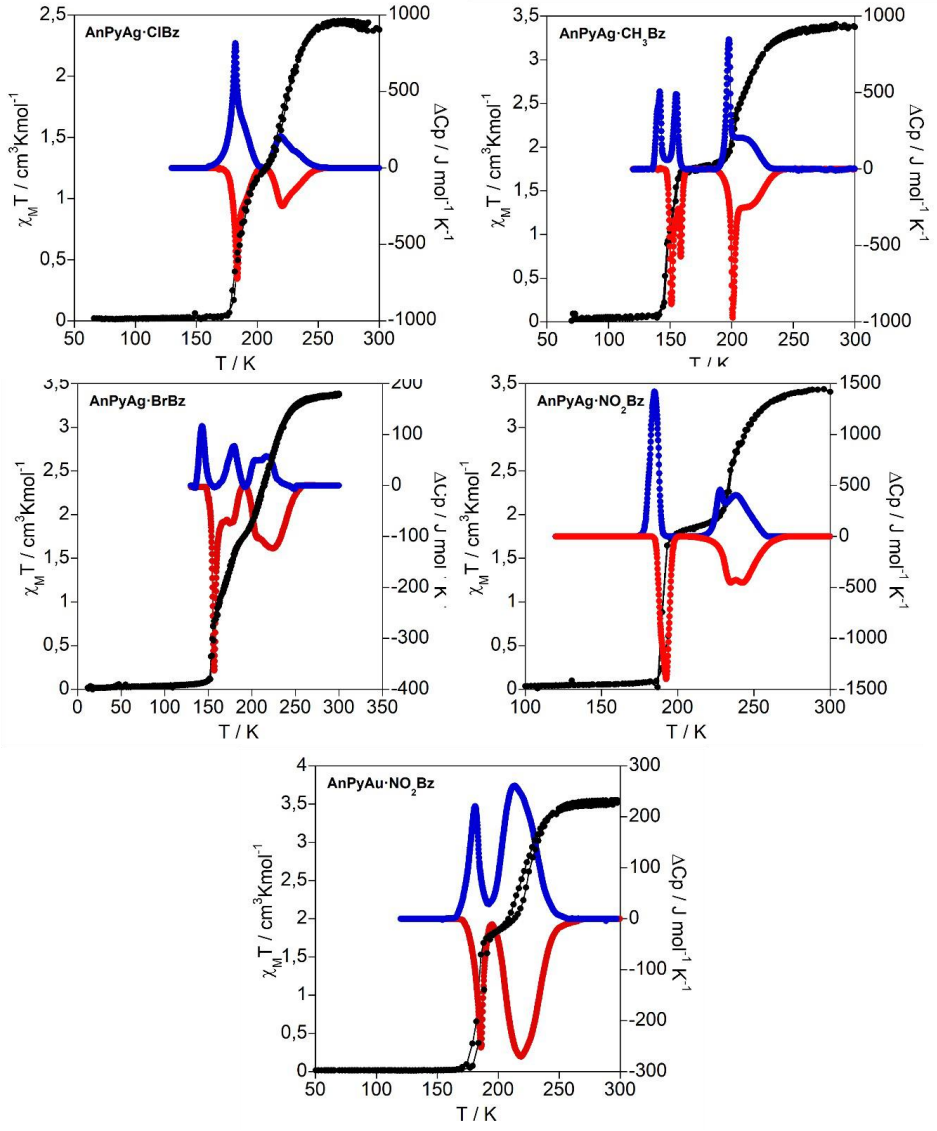

**Table S1.** Thermodinamic parameters extracted from the calorimetric measurements.

| | ΔH (kJ mol-1) | ΔS (J K-1 mol-1) |
|---|---|---|
| **AnPyAg·$CH_3$bz** | 14.35 | 81.41 |
| **AnPyAg·$NO_2$bz** | 18.66 | 78.81 |
| **AnPyAg·Clbz** | 11.47 | 58.70 |
| **AnPyAg·Brbz** | 5.90 | 30.64 |
| **AnPyAu·$NO_2$bz** | 10.20 | 51.13 |

**Fig. S7.** Thermal dependent magnetic [red (cooling 1 $Kmin^{-1}$) and black (heating after photoexcitation 0.3 3 K $min^{-1}$) lines] and photomagnetic properties [Green lines ($\lambda_{irrad}$ = 532 nm)] of the **AnPyM·XBz** derivatives.

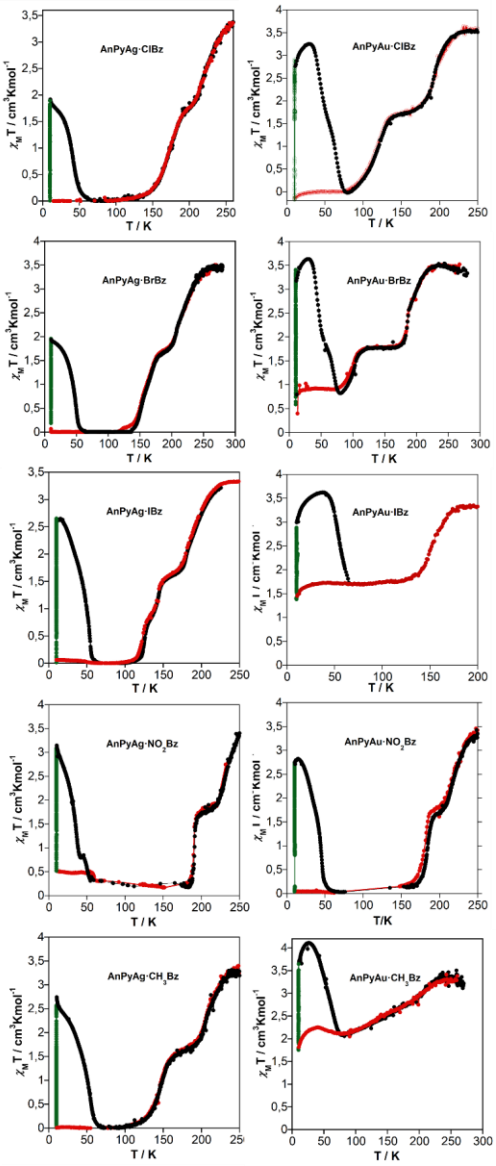

**Table S2.** Crystal data for **AnPyAg·$NO_2$Bz**

| | **$AgNO_2$Bz_120K** | **$AgNO_2$Bz_210K** | **$AgNO_2$Bz_290K** |
|---|---|---|---|
| Empirical formula | | $C_{52.8}H_{35}N_{7.8}O_{3.6}Ag_2Fe$ | |
| *M*r | | 1107.87 | |
| Crystal system | | orthorhombic | |
| Space group | | Cccm | |
| *a* (Å) | 14.0939(4) | 14.3894(11) | 14.7826(5) |
| *b* (Å) | 22.2731(7) | 22.2526(14) | 22.3755(6) |
| *c* (Å) | 14.7007(4) | 14.9826(7) | 15.0486(4) |
| *V* (Å$^3$) | 4614.8(2) | 4797.5(5) | 4977.6(3) |
| Z | | 4 | |
| $D_c$ (mg cm$^{-3}$) | 1.595 | 1.534 | 1.478 |
| *F*(000) | | 2221 | |
| μ (Mo-$K_\alpha$) (mm$^{-1}$) | 1.206 | 1.160 | 1.118 |
| Crystal size (mm) | | 0.05x0.10x0.20 | |
| No. of total reflections | 2518 | 3197 | 3480 |
| No. of reflections [I>2σ(I)] | 1888 | 1343 | 1758 |
| *R* [I>2σ(I)] | 0.0553 | 0.0804 | 0.0690 |
| *wR* [I>2σ(I)] | 0.1522 | 0.1997 | 0.1875 |
| S | 1.061 | 0.965 | 0.993 |

$R_1 = \Sigma \, ||Fo| - |Fc|| \, / \, \Sigma \, |Fo|$; $wR = [\, \Sigma \, [w(Fo2 - Fc2)2] \, / \, \Sigma \, [w(Fo^2)^2]]^{1/2}$.

$w = 1/ \, [\sigma^2(Fo^2) + (m \, P)^2 + n \, P]$ where $P = (Fo^2 + 2Fc^2) \, / \, 3$;

m = 0.0807 (**1**), 0.1032 (**2**) and 0.1153 (**3**);

n = 25.3803 (**1**), 0.0000 (**2**) and 0.0000 (**3**)

**Table S3.** Selected bon lengths (Å) and angles (º) for **AnPyAg·$NO_2$Bz**.

| | **$AgNO_2$Bz_120K** | **$AgNO_2$Bz_210K** | **$AgNO_2$Bz_290K** |
|---|---|---|---|
| Fe-N(1) | 1.932(4) | 2.038(6) | 2.139(5) |
| Fe-N(2) | 2.000(6) | 2.099(10) | 2.228(6) |
| Ag-C(1) | 2.053(5) | 2.063(8) | 2.058(6) |
| N(1)-Fe-N(2) | 90.8(2) | 88.9(3) | 88.6(2) |
| C(1)-Ag-C(1) | 171.2(3) | 170.3(5) | 170.6(3) |

**Table S4.** Crystal data for **AnPyAgCH$_3$Bz.**

| | AgCH3Bz_120K | AgCH3Bz_170K | AgCH3Bz_260K |
|---|---|---|---|
| Empirical formula | | $C_{54.6}H_{40.4}N_6Ag_2Fe$ | |
| *M*r | | 1052.12 | |
| Crystal system | | orthorhombic | |
| Space group | | *Pccn* | |
| *a* (Å) | 14.3993(3) | 14.6888(7) | 22.3526(10) |
| *b* (Å) | 22.2116(4) | 22.2043(7) | 14.9673(6) |
| *c* (Å) | 14.5770(4) | 14.7091(5) | 14.9037(6) |
| *V* (Å$^3$) | 4662.2(2) | 4797.4(3) | 4986.2(4) |
| Z | 4 | | |
| $D_c$ (mg cm$^{-3}$) | 1.499 | 1.457 | 1.402 |
| *F*(000) | | 2120 | |
| μ (Mo-K$_\alpha$) (mm$^{-1}$) | 1.182 | 1.149 | 1.106 |
| Crystal size (mm) | | 0.05x0.20x0.20 | |
| No. of total reflections | 6030 | 6381 | 6619 |
| No. of reflections [I>2σ(I)] | 3920 | 4037 | 2811 |
| *R* [I>2σ(I)] | 0.0550 | 0.0971 | 0.0565 |
| *wR* [I>2σ(I)] | 0.1140 | 0.1803 | 0.1089 |
| S | 1.037 | 1.100 | 0.920 |

$R_1$ = Σ ||*F*o| - |*F*c|| / Σ |*F*o|;

*wR* = [ Σ [w(*F*o2 - *F*c2)2] / Σ [*w*(*F*o$^2$)$^2$]]$^{1/2}$.

*w* = 1/ [σ$^2$(*F*o$^2$) + (m *P*)$^2$ + n *P*] where *P* = (*F*o$^2$ + 2*F*c$^2$) / 3;

m = 0.0454 (**1**), 0.0000 (**2**) and 0.0385 (**3**);

n = 5.6480 (**1**), 71.7043 (**2**) and 0.0000 (**3**)

**Table S5.** Selected bon lengths (Å) and angles (º) for **AnPyAg·CH$_3$Bz.**

| | AgCH$_3$Bz_120K | AgCH$_3$Bz_170K | AgCH$_3$Bz_260K |
|---|---|---|---|
| Fe-N(1) | 1.950(4) | 2.032(7) | 2.140(4) |
| Fe-N(2) | 1.944(4) | 2.044(7) | 2.144(4) |
| Fe-N(3) | 2.006(4) | 2.119(6) | 2.212(4) |
| Ag-C(1) | 2.073(5) | 2.058(9) | 2.058(5) |
| Ag-C(2) | 2.062(5) | 2.096(9) | 2.058(5) |
| | | | |
| N(1)-Fe-N(2) | 89.4(2) | 88.3(3) | 88.4(2) |
| N(1)-Fe-N(3) | 89.46(14) | 88.6(2) | 88.55(14) |
| N(2)-Fe-N(3) | 90.47(14) | 90.5(2) | 90.24(14) |
| C(1)-Ag-C(2) | 170.4(2) | 169.2(3) | 170.3(2) |

**Table S6.** Crystal data for **AnPyAg·ClBz**.

| | **AgClBz_120K** | **AgClBz_207K** | **AgClBz_280K** |
|---|---|---|---|
| Empirical formula | | $C_{51.6}H_{34}Cl_{1.6}N_6Ag_2Fe$ | |
| *M*r | | 1066.36 | |
| Crystal system | | orthorhombic | |
| Space group | Ccc2 | *Pmna* | *Ccc*2 |
| *a* (Å) | 14.1974(3) | 14.9087(3) | 14.707(7) |
| *b* (Å) | 22.2274(6) | 14.4938(3) | 22.230(11) |
| *c* (Å) | 14.7169(4) | 22.2153(5) | 15.113(7) |
| *V* (Å$^3$) | 4644.2(2) | 4800.4(2) | 4941(4) |
| Z | | 4 | |
| $D_c$ (mg cm$^{-3}$) | 1.525 | 1.475 | 1.434 |
| *F*(000) | | 2131 | |
| μ (Mo-$K_\alpha$) (mm$^{-1}$) | 1.277 | 1.235 | 1.200 |
| Crystal size (mm) | | 0.04x0.30x0.30 | |
| No. of total reflections | 8301 | 5153 | 5051 |
| No. of reflections [I>2σ(I)] | 8029 | 3143 | 3228 |
| *R* [I>2σ(I)] | 0.0267 | 0.0673 | 0.0969 |
| *wR* [I>2σ(I)] | 0.0685 | 0.1978 | 0.2337 |
| S | 1.065 | 1.067 | 1.024 |

$R_1 = \Sigma ||Fo| - |Fc|| / \Sigma |Fo|$; $wR = [\Sigma [w(Fo2 - Fc2)2] / \Sigma [w(Fo^2)^2]]^{1/2}$.

$w = 1/ [\sigma^2(Fo^2) + (m\ P)^2 + n\ P]$ where $P = (Fo^2 + 2Fc^2) / 3$;

m = 0.0321 (**1**), 0.1001 (**2**) and 0.1113 (**3**);

n = 6.1118 (**1**), 8.0766 (**2**) and 137.4962 (**3**)

**Table S7.** Selected bond lengths (Å) and angles (º) for **AnPyAg·ClBz**.

| | **AgClBz_120K** | **AgClBz_207K** | **AgClBz_280K** |
|---|---|---|---|
| Fe-N(1) | 1.933(2) | | 2.16(2) |
| Fe-N(2) | 1.936(2) | | 2.09(2) |
| Fe-N(3) | 2.006(2) | | 2.235(7) |
| Fe(1)-N(1) | | 1.987(4) | |
| Fe(1)-N(3) | | 2.075(6) | |
| Fe(2)-N(2) | | 2.113(4) | |
| Fe(2)-N(4) | | 2.181(6) | |
| Ag-C(1) | 2.040(3) | 2.065(5) | 2.01(2) |
| Ag-C(2) | 2.049(3) | 2.046(6) | 2.07(3) |
| | | | |
| N(1)-Fe-N(2) | 89.83(7) | | 89.6(7) |
| N(1)-Fe-N(3) | 90.28(10) | | 91.5(7) |
| N(2)-Fe-N(3) | 89.17(10) | | 91.3(7) |
| N(1)-Fe(1)-N(3) | | 89.0(2) | |
| N(2)-Fe(2)-N(4) | | 91.6(2) | |
| C(1)-Ag-C(2) | 171.34(9) | 171.4(2) | 169.8(8) |

**Table S8.** Crystal data for **AnPyAg·BrBz**.

| | **AgBrBz_120K** | **AgBrBz_192K** | **AgBrBz_280K** |
|---|---|---|---|
| Empirical formula | | $C_{52.8}H_{35}Br_{1.8}N_6Ag_2Fe$ | |
| *Mr* | | 1168.89 | |
| Crystal system | | orthorhombic | |
| Space group | *Ccc*2 | *Pmna* | *Ccc*2 |
| *a* (Å) | 14.3261(7) | 14.8634(6) | 14.7990(7) |
| *b* (Å) | 22.2063(9) | 14.5587(8) | 22.3435(10) |
| *c* (Å) | 14.6300(7) | 14.5587(8) | 15.0463(5) |
| *V* (Å$^3$) | 4654.2(4) | 4813.8(4) | 4975.2(4) |
| Z | | 4 | |
| $D_c$ (mg cm$^{-3}$) | 1.668 | 1.613 | 1.561 |
| *F*(000) | | 2307 | |
| μ (Mo-$K_\alpha$) (mm$^{-1}$) | 2.729 | 2.639 | 2.553 |
| Crystal size (mm) | | 0.05x0.20x0.40 | |
| No. of total reflections | 3919 | 5168 | 3943 |
| No. of reflections [I>2σ(I)] | 3488 | 3089 | 2860 |
| *R* [I>2σ(I)] | 0.0368 | 0.0751 | 0.0412 |
| *wR* [I>2σ(I)] | 0.0909 | 0.2134 | 0.0607 |
| S | 1.062 | 1.064 | 0.930 |

$R_1 = \Sigma \, ||Fo| - |Fc|| \, / \, \Sigma \, |Fo|$; $wR = [\, \Sigma \, [w(Fo2 - Fc2)2] \, / \, \Sigma \, [w(Fo^2)^2]]^{1/2}$.

$w = 1/ \, [\sigma^2(Fo^2) + (m \, P)^2 + n \, P]$ where $P = (Fo^2 + 2Fc^2) \, / \, 3$;

m = 0.0321 (**1**), 0.1001 (**2**) and 0.1113 (**3**);

n = 6.1118 (**1**), 8.0766 (**2**) and 137.4962 (**3**)

**Table S9.** Selected bond lengths (Å) and angles (º) for **AnPyAg·BrBz**.

| | **AgBrBz_120K** | **AgBrBz_192K** | **AgBrBz_280K** |
|---|---|---|---|
| Fe-N(1) | 1.995(6) | | 2.146(7) |
| Fe-N(2) | 1.894(6) | | 2.102(8) |
| Fe-N(3) | 2.012(4) | | 2.229(4) |
| Fe(1)-N(1) | | 2.137(5) | |
| Fe(1)-N(3) | | 2.200(6) | |
| Fe(2)-N(2) | | 1.964(5) | |
| Fe(2)-N(4) | | 2.042(6) | |
| Ag-C(1) | 2.015(7) | 2.067(6) | 2.048(9) |
| Ag-C(2) | 2.106(8) | 2.075(6) | 2.119(10) |
| | | | |
| N(1)-Fe-N(2) | 89.3(2) | | 88.0(2) |
| N(1)-Fe-N(3) | 87.2(2) | | 87.7(3) |
| N(2)-Fe-N(3) | 92.7(2) | | 93.8(3) |
| N(1)-Fe(1)-N(3) | | 91.1(2) | |
| N(2)-Fe(2)-N(4) | | 90.3(2) | |
| C(1)-Ag-C(2) | 171.3(2) | 170.9(3) | 170.9(2) |

**Table S10.** Crystal data for **AnPyAu·$NO_2$Bz**.

| | **$AuNO_2Bz$_150K** | **$AuNO_2Bz$_200K** | **$AuNO_2Bz$_280K** |
|---|---|---|---|
| Empirical formula | | $C_{50.4}H_{33}N_{7.4}O_{2.8}Au_2Fe$ | |
| *M*r | | 1236.82 | |
| Crystal system | | orthorhombic | |
| Space group | | Cccm | |
| *a* (Å) | 14.0279(3) | 14.2233(4) | 14.5414(5) |
| *b* (Å) | 22.9617(8) | 22.9389(6) | 22.9006(8) |
| *c* (Å) | 14.4747(3) | 14.8302(3) | 15.0008(6) |
| *V* (Å$^3$) | 4662.4(2) | 4838.6(2) | 4995.3(3) |
| Z | | 4 | |
| $D_c$ (mg cm$^{-3}$) | 1.762 | 1.698 | 1.645 |
| *F*(000) | | 2374 | |
| μ (Mo-$K_\alpha$) (mm$^{-1}$) | 6.634 | 6.392 | 6.192 |
| Crystal size (mm) | | 0.10x0.20x0.40 | |
| No. of total reflections | 2446 | 2540 | 2638 |
| No. of reflections [I>2σ(I)] | 2048 | 1988 | 1986 |
| *R* [I>2σ(I)] | 0.0394 | 0.0407 | 0.0454 |
| *wR* [I>2σ(I)] | 0.1027 | 0.1116 | 0.1241 |
| S | 1.077 | 1.067 | 1.059 |

$R_1 = \Sigma ||Fo| - |Fc|| / \Sigma |Fo|$; $wR = [\Sigma [w(Fo2 - Fc2)2] / \Sigma [w(Fo^2)^2]]^{1/2}$.

$w = 1/ [\sigma^2(Fo^2) + (m\ P)^2 + n\ P]$ where $P = (Fo^2 + 2Fc^2) / 3$;

m = 0.0458 (**1**), 0.0558 (**2**) and 0.0635 (**3**);

n = 76.5826 (**1**), 29.0573 (**2**) and 19.6285 (**3**)

**Table S11.** Selected bond lengths (Å) and angles (º) for **AnPyAu·$NO_2$Bz**.

| | **AuNO2Bz_150K** | **AuNO2Bz_200K** | **AuNO2Bz_280K** |
|---|---|---|---|
| Fe-N(1) | 1.917(5) | 2.027(5) | 2.144(5) |
| Fe-N(2) | 2.008(7) | 2.126(7) | 2.224(7) |
| Au-C(1) | 1.990(7) | 1.994(7) | 1.981(7) |
| | | | |
| N(1)-Fe-N(2) | 90.1(2) | 90.6(2) | 90.6(2) |
| C(1)-Au-C(1) | 176.4(3) | 175.8(3) | 176.1(4) |

**Table S12.** Crystal data for **AnPyAu·$CH_3Bz$**.

| | **$AuCH_3Bz$_95K** | **$AuCH_3Bz$_140K** | **$AuCH_3Bz$_260K** |
|---|---|---|---|
| Empirical formula | | $C_{60.67}H_{47.33}N_6Au_2Fe$ | |
| *M*r | | 1310.16 | |
| Crystal system | | triclinic | |
| Space group | | *P*-1 | |
| *a* (Å) | 13.2270(3) | 13.2644(4) | 13.3503(8) |
| *b* (Å) | 13.7058(4) | 13.7480(6) | 13.8787(9) |
| *c* (Å) | 23.1363(8) | 23.2743(8) | 23.5204(12) |
| *α*(°) | 74.044(3) | 74.165(3) | 74.237(5) |
| *β*(°) | 83.768(2) | 83.500(3) | 83.785(4) |
| *γ*(°) | 70.263(2) | 70.209(3) | 70.718(6) |
| *V* (Å$^3$) | 3795.2(2) | 3841.0(3) | 3958.0(4) |
| Z | | 3 | |
| $D_c$ (mg cm$^{-3}$) | 1.720 | 1.699 | 1.649 |
| *F*(000) | | 1912 | |
| μ (Mo-$K_\alpha$) (mm$^{-1}$) | 6.113 | 6.040 | 5.862 |
| Crystal size (mm) | | 0.10x0.20x0.20 | |
| No. of total reflections | 15063 | 15191 | 15371 |
| No. of reflections [I>2σ(I)] | 11469 | 11516 | 11633 |
| *R* [I>2σ(I)] | 0.0428 | 0.0474 | 0.0393 |
| *wR* [I>2σ(I)] | 0.0594 | 0.0658 | 0.0714 |
| S | 1.048 | 1.060 | 1.034 |

$R_1 = \Sigma \, ||Fo| - |Fc|| \, / \, \Sigma \, |Fo|$; $wR = [\, \Sigma \, [w(Fo2 - Fc2)2] \, / \, \Sigma \, [w(Fo^2)^2]]^{1/2}$.

$w = 1/ [\sigma^2(Fo^2) + (m\,P)^2 + n\,P]$ where $P = (Fo^2 + 2Fc^2) / 3$;

m = 0.0110 (**1**), 0.0045 (**2**) and 0.0237 (**3**);

n = 0.7800 (**1**), 4.3468 (**2**) and 2.2548 (**3**)

**Table S13.** Selected bond lengths (Å) and angles (º) for **AnPyAg·$CH_3Bz$**.

| | **$AuCH_3Bz$_95K** | **$AuCH_3Bz$_140K** | **$AuCH_3Bz$_260K** |
|---|---|---|---|
| Fe(1)-N(1) | 2.016(5) | 2.040(5) | 2.151(4) |
| Fe(1)-N(2) | 2.015(5) | 2.036(6) | 2.139(4) |
| Fe(1)-N(3) | 2.035(6) | 2.049(8) | 2.172(4) |
| Fe(1)-N(4) | 2.015(5) | 2.031(6) | 2.144(5) |
| Fe(1)-N(7) | 2.108(4) | 2.126(5) | 2.222(4) |
| Fe(1)-N(8) | 2.105(4) | 2.124(5) | 2.229(4) . |
| Fe(2)-N(5) | 2.079(5) | 2.151(5) | 2.154(5) |
| Fe(2)-N(6) | 2.056(5) | 2.122(5) | 2.135(4) |
| Fe(2)-N(9) | 2.141(5) | 2.213(5) | 2.228(4) |
| Au(1)-C(3) | 2.032(8) | 2.041(10) | 1.992(6) |
| Au(2)-C(2) | 1.981(6) | 1.980(7) | 2.001(6) |
| Au(3)-C(4) | 1.994(7) | 1.981(7) | 1.985(6) |
| Au(3)-C(5) | 1.979(6) | 1.982(7) | 1.975(6) |
| Au(4)-C(1) | 1.983(7) | 1.990(7) | 1.983(6) |
| Au(4)-C(6) | 1.991(7) | 2.004(7) | 1.994(6) |
| | | | |
| N(1)-Fe(1)-N(2) | 90.6(2) | 90.9(2) | 90.5(2) |
| N(1)-Fe(1)-N(3) | 176.2(2) | 175.6(2) | 175.9(2) |
| N(1)-Fe(1)-N(4) | 89.7(2) | 89.2(2) | 90.1(2) |
| N(1)-Fe(1)-N(7) | 88.3(2) | 88.0(2) | 87.9(2) |
| N(1)-Fe(1)-N(8) | 86.3(2) | 85.9(2) | 85.9(2) |
| N(2)-Fe(1)-N(3) | 89.1(2) | 89.2(2) | 89.8(2) |
| N(2)-Fe(1)-N(4) | 179.6(2) | 179.4(2) | 178.8(2) |
| N(2)-Fe(1)-N(7) | 91.2(2) | 91.0(2) | 90.9(2) |
| N(2)-Fe(1)-N(8) | 91.8(2) | 92.1(2) | 92.2(2) |
| N(3)-Fe(1)-N(4) | 90.6(2) | 90.7(2) | 89.8(2) |
| N(3)-Fe(1)-N(7) | 95.5(2) | 96.4(2) | 96.2(2) |
| N(3)-Fe(1)-N(8) | 89.9(2) | 89.7(2) | 90.0(2) |
| N(4)-Fe(1)-N(7) | 88.5(2) | 88.4(2) | 88.1(2) |
| N(4)-Fe(1)-N(8) | 88.6(2) | 88.5(2) | 88.9(2) |
| N(7)-Fe(1)-N(8) | 173.8(2) | 173.2(2) | 173.1(2) |
| N(5)-Fe(2)-N(6) | 89.5(2) | 89.2(2) | 88.5(2) |
| N(5)-Fe(2)-N(9) | 88.9(2) | 89.5(2) | 89.4(2) |
| N(6)-Fe(2)-N(9) | 87.3(2) | 87.0(2) | 87.5(2) |
| C(3)-Au(1)-C(3) | 180.0 | 180.0 | 180.0 |
| C(2)-Au(2)-C(2) | 180.0 | 180.0 | 180.0 |
| C(4)-Au(3)-C(5) | 173.9(2) | 174.5(3) | 174.5(2) |
| C(1)-Au(4)-C(6) | 177.9(2) | 178.4(3) | 177.6(2) |

**Table S14.** Crystal data for **AnPyAuClbz**.

| | **AuClBz_110K** | **AuClBz_180K** | **AuClBz_260K** |
|---|---|---|---|
| Empirical formula | | $C_{54}H_{36}N_6Cl_2Au_2Fe$ | |
| *M*r | | 1289.57 | |
| Crystal system | | triclinic | |
| Space group | | *P*-1 | |
| *a* (Å) | 15.3053(6) | 15.6161(5) | 13.4930(5) |
| *b* (Å) | 18.2506(6) | 18.2748(4) | 13.6762(4) |
| *c* (Å) | 19.4681(7) | 19.6811(5) | 15.6627(5) |
| *α*(°) | 90.757(3) | 90.508(2) | 86.165(2) |
| *β*(°) | 106.614(3) | 106.812(2) | 65.442(3) |
| *γ*(°) | 108.244(3) | 108.781(2) | 86.215(2) |
| *V* (Å$^3$) | 4917.4(3) | 5057.9(2) | 2620.6(2) |
| Z | | 4 | 2 |
| $D_c$ (mg cm$^{-3}$) | 1.742 | 1.693 | 1.634 |
| *F*(000) | | 2480 | 1240 |
| μ (Mo-$K_α$) (mm$^{-1}$) | 6.394 | 6.217 | 5.999 |
| Crystal size (mm) | | 0.10x0.20x0.30 | |
| No. of total reflections | 18975 | 20602 | 10916 |
| No. of reflections [I>2σ(I)] | 12498 | 14434 | 7873 |
| *R* [I>2σ(I)] | 0.0603 | 0.0497 | 0.0461 |
| *wR* [I>2σ(I)] | 0.1317 | 0.1097 | 0.1051 |
| S | 1.046 | 1.059 | 1.051 |

$R_1 = \Sigma \, ||Fo| - |Fc|| \, / \, \Sigma \, |Fo|$; $wR = [\, \Sigma \, [w(Fo2 - Fc2)2] \, / \, \Sigma \, [w(Fo^2)^2]]^{1/2}$.

$w = 1/ \, [\sigma^2(Fo^2) + (m \, P)^2 + n \, P]$ where $P = (Fo^2 + 2Fc^2) \, / \, 3$;

m = 0.0486 (**1**), 0.0455 (**2**) and 0.0468 (**3**);

n = 29.0248 (**1**), 16.8124 (**2**) and 8.5045 (**3**)

**Table S15.** Selected bond lengths (Å) and angles (º) for **AnPyAu·ClBz**.

| | **AuClBz_110K** | **AuClBz_180K** | **AuClBz_260K** |
|---|---|---|---|
| Fe(1)-N(1) | 1.962(8) | 1.938(6) | |
| Fe(1)-N(2) | 1.953(9) | 1.942(6) | |
| Fe(1)-N(9) | 2.003(9) | 2.011(6) | |
| Fe(2)-N(3) | 1.955(9) | 2.162(7) | |
| Fe(2)-N(4) | 1.958(9) | 2.156(6) | |
| Fe(2)-N(5) | 1.951(10) | 2.147(6) | |
| Fe(2)-N(6) | 1.963(9) | 2.161(6) | |
| Fe(2)-N(10) | 2.027(9) | 2.203(6) | |
| Fe(2)-N(11) | 2.021(9) | 2.203(6) | |
| Fe(3)-N(7) | 2.153(9) | 2.134(6) | |
| Fe(3)-N(8) | 2.167(10) | 2.129(7) | |
| Fe(3)-N(12) | 2.185(9) | 2.194(6) | |
| Au(1)-C(1) | 1.981(10) | 1.997(8) | |
| Au(1)-C(3) | 2.006(11) | 1.991(8) | |
| Au(2)-C(2) | 1.983(11) | 1.985(8) | |
| Au(2)-C(5) | 1.970(11) | 1.977(8) | |
| Au(3)-C(6) | 1.991(12) | 2.000(8) | |
| Au(3)-C(7) | 1.979(12) | 1.980(9) | |
| Au(4)-C(4) | 1.996(11) | 1.981(8) | |
| Au(4)-C(8) | 1.951(11) | 1.990(8) | |
| Fe(1)-N(1) | | | 2.154(6) |
| Fe(1)-N(2) | | | 2.158(6) |
| Fe(1)-N(5) | | | 2.201(6) |
| Fe(2)-N(3) | | | 2.165(6) |
| Fe(2)-N(4) | | | 2.162(6) |
| Fe(2)-N(6) | | | 2.212(6) |
| Au(1)-C(1) | | | 1.996(7) |
| Au(1)-C(3) | | | 2.003(8) |
| Au(2)-C(2) | | | 1.987(7) |
| Au(2)-C(4) | | | 1.987(7) |

**Table S15.(cont.)** Selected bond lengths (Å) and angles (º) for **AnPyAu·ClBz**.

| | | | |
|---|---|---|---|
| N(1)-Fe(1)-N(2) | 91.5(3) | 92.0(3) | |
| N(1)-Fe(1)-N(9) | 91.7(4) | 91.3(3) | |
| N(2)-Fe(1)-N(9) | 89.4(4) | 89.2(3) | |
| N(3)-Fe(2)-N(4) | 88.2(4) | 88.0(2) | |
| N(3)-Fe(2)-N(5) | 92.6(4) | 94.0(2) | |
| N(3)-Fe(2)-N(6) | 179.4(4) | 179.4(2) | |
| N(3)-Fe(2)-N(10) | 89.6(4) | 89.9(2) | |
| N(3)-Fe(2)-N(11) | 90.1(4) | 89.7(2) | |
| N(4)-Fe(2)-N(5) | 178.8(4) | 177.6(2) | |
| N(4)-Fe(2)-N(6) | 91.7(4) | 92.2(2) | |
| N(4)-Fe(2)-N(10) | 91.6(4) | 91.9(2) | |
| N(4)-Fe(2)-N(11) | 88.2(4) | 87.6(2) | |
| N(5)-Fe(2)-N(6) | 87.4(4) | 85.8(2) | |
| N(5)-Fe(2)-N(10) | 89.2(4) | 89.4(2) | |
| N(5)-Fe(2)-N(11) | 91.0(4) | 91.1(2) | |
| N(6)-Fe(2)-N(10) | 89.8(4) | 89.5(2) | |
| N(6)-Fe(2)-N(11) | 90.5(4) | 90.8(2) | |
| N(10)-Fe(2)-N(11) | 179.6(4) | 179.4(2) | |
| N(7)-Fe(3)-N(8) | 89.6(3) | 89.8(3) | |
| N(7)-Fe(3)-N(12) | 87.3(3) | 87.6(2) | |
| N(8)-Fe(3)-N(12) | 87.0(3) | 87.9(2) | |
| C(1)-Au(1)-C(3) | 175.1(4) | 175.1(3) | |
| C(2)-Au(2)-C(5) | 179.9(4) | 179.4(3) | |
| C(6)-Au(3)-C(7) | 173.9(5) | 173.7(3) | |
| C(4)-Au(4)-C(8) | 177.7(4) | 176.7(3) | |
| N(1)-Fe(1)-N(2) | | | 90.1(2) |
| N(1)-Fe(1)-N(5) | | | 92.0(2) |
| N(2)-Fe(1)-N(5) | | | 88.8(2) |
| N(3)-Fe(2)-N(4) | | | 93.1(2) |
| N(3)-Fe(2)-N(6) | | | 90.4(2) |
| N(4)-Fe(2)-N(6) | | | 88.7(2) |
| C(1)-Au(1)-C(3) | | | 175.8(3) |
| C(2)-Au(2)-C(4) | | | 178.4(3) |

**Table S16.** Crystal data for **AnPyAu·BrBz**.

| | **AuBrBz_90K** | **AuBrBz_165K** | **AuBrBz_260K** |
|---|---|---|---|
| Empirical formula | | $C_{49.8}H_{32.5}Br_{1.3}N_6Au_2Fe$ | |
| *M*r | | 1268.58 | |
| Crystal system | | orthorhombic | |
| Space group | *Pmna* | *Pmna* | *Ccc*2 |
| *a* (Å) | 14.6456(5) | 14.7380(5) | 14.6751(7) |
| *b* (Å) | 14.3001(6) | 14.3959(4) | 22.7556(9) |
| *c* (Å) | 22.5080(7) | 22.5898(6) | 14.9439(7) |
| *V* (Å$^3$) | 4713.9(3) | 4792.8(2) | 4990.4(4) |
| Z | | 4 | |
| $D_c$ (mg cm$^{-3}$) | 1.787 | 1.758 | 1.688 |
| *F*(000) | | 2411 | |
| μ (Mo-$K_\alpha$) (mm$^{-1}$) | 7.654 | 7.528 | 7.230 |
| Crystal size (mm) | | 0.10x0.30x0.30 | |
| No. of total reflections | 5643 | 5678 | 3880 |
| No. of reflections [I>2σ(I)] | 3485 | 3877 | 3236 |
| *R* [I>2σ(I)] | 0.1041 | 0.0848 | 0.0489 |
| *wR* [I>2σ(I)] | 0.2406 | 0.2117 | 0.1232 |
| S | 1.042 | 1.058 | 1.051 |

$R_1 = \Sigma \, ||Fo| - |Fc|| \, / \, \Sigma \, |Fo|$; $wR = [\, \Sigma \, [w(Fo2 - Fc2)2] \, / \, \Sigma \, [w(Fo^2)^2]]^{1/2}$.

$w = 1/ \, [\sigma^2(Fo^2) + (m \, P)^2 + n \, P]$ where $P = (Fo^2 + 2Fc^2) \, / \, 3$;

m = 0.0740 (**1**), 0.0788 (**2**) and 0.0614 (**3**);

n = 260.7764 (**1**), 124.1095 (**2**) and 16.4940 (**3**)

**Table S17.** Selected bond lengths (Å) and angles (º) for **AnPyAu·BrBz**.

| | AuBrBz_90 K | AuBrBz_165 K | AuBrBz_260 K |
|---|---|---|---|
| Fe-N(1) | | | 2.14(2) |
| Fe-N(2) | | | 2.11(2) |
| Fe-N(3) | | | 2.247(5) |
| Fe(1)-N(1) | 2.086(12) | 2.155(9) | |
| Fe(1)-N(3) | 2.15(12) | 2.206(13) | |
| Fe(2)-N(2) | 1.952(12) | 1.944(9) | |
| Fe(2)-N(4) | 2.01(2) | 2.007(13) | |
| Au-C(1) | 1.977(14) | 1.992(11) | 1.96(2) |
| Au-C(2) | 2.031(14) | 2.009(11) | 2.15(2) |
| | | | |
| N(1)-Fe-N(2) | | | 90.7(5) |
| N(1)-Fe-N(3) | | | 89.3(5) |
| N(2)-Fe-N(3) | | | 90.9(4) |
| N(1)-Fe(1)-N(3) | 89.5(5) | 88.9(3) | |
| N(2)-Fe(2)-N(4) | 89.7(5) | 89.7(4) | |
| C(1)-Au-C(2) | 175.4(6) | 175.2(5) | 170.0(7) |

**Fig. S8**. Views along the *c* and *a* directions of the orthorhombic **AnPyM·XBz** network showing the solvent accessible surface.

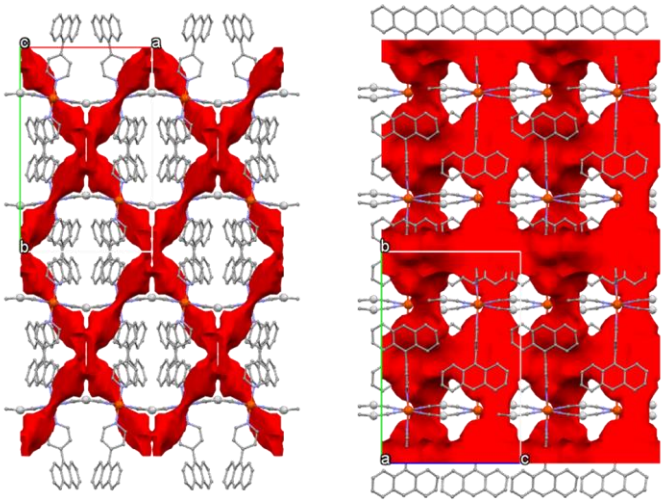

**Fig. S9.** Orthorhombic unit cell of **AnPyAg·$CH_3$Bz** at 120K showing the arrangement of the toluene guest molecules in the two parallel channels, running along *c* direction, generated by the interdigitation of the axial AnPy ligands of the 2D frameworks (excluded for simplicity).

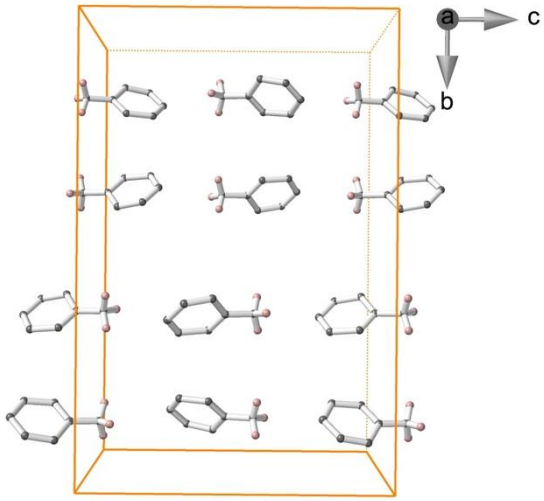


**Fig. S10.** Structural ordering of the HS (red) and LS (blue) states responsible for the symmetry breaking observed in the plateau at 50% of spin state conversion for **AnPyAg·ClBz**, **AnPyAg·BrBz** and **AnPyAu·BrBz**.

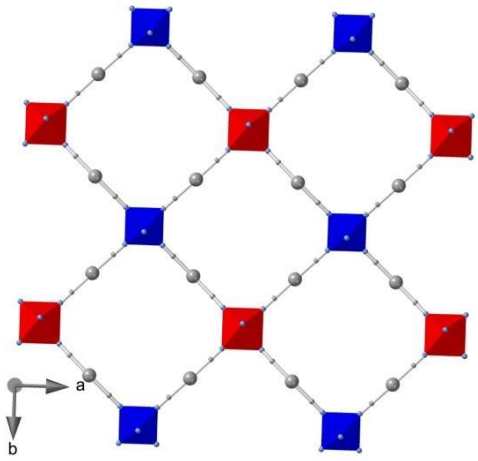

**Figure S11.** $Fe^{II}$ environments observed for **AnPyM·XBz** in the (a) *Ccc*2 [X = Cl (Ag), Br (Ag, Au)], (b) *Pccn* [X = $NO_2$ (Ag, Au)] and (c) *Cmma* [X = $CH_3$ (Ag)] space groups and the corresponding (d), (e) and (f) views.

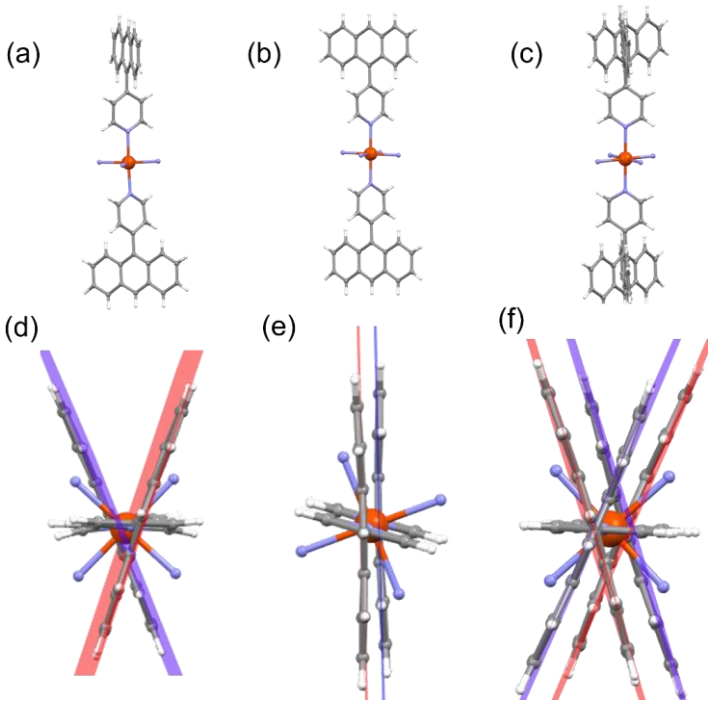


**Fig. S12.** Packing of four consecutive layers of **AnPyAu·ClBz** view along the *a*+*c* (left) / *b* (center, guest molecules omitted for clarity) and superposition of the layers on the *bc* plane (right)

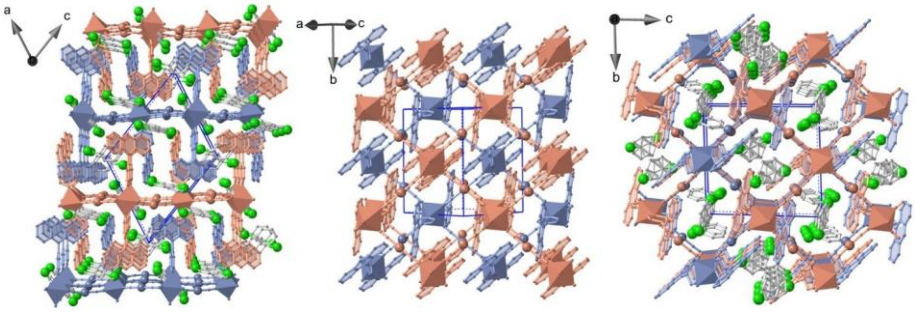

**Fig. S13.** Distribution of the $CH_3Bz$ guest molecules in the channels 1 and 2 defined by the packing of the 2D polymeric framework in the triclinic form of **AnPyAu·$CH_3Bz$**.

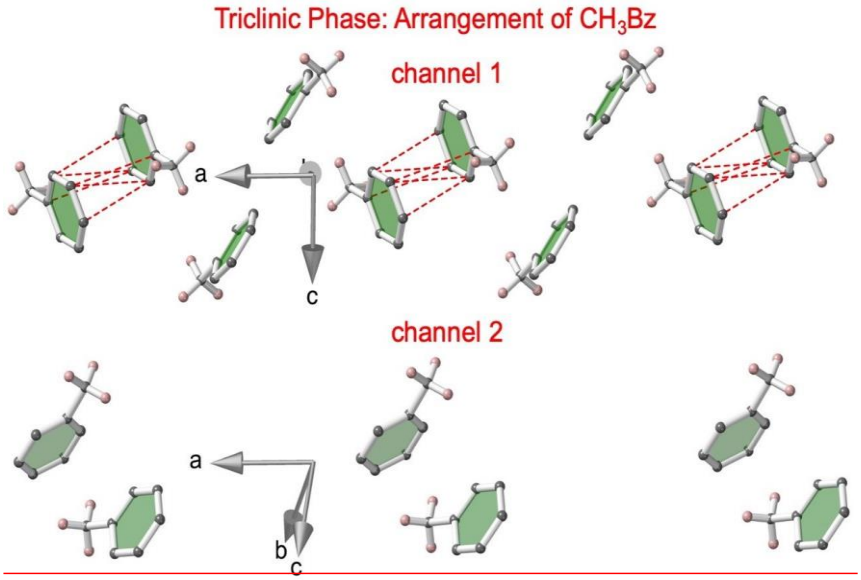

**Table S18.** Selection of short inter- and intra-layer distances for the triclinic forms of **AnPyAu·$CH_3$Bz** and **AnPyAu·ClBz**.

| **AnPyAu·$CH_3$Bz** (triclinic) | | | |
|---|---|---|---|
| T (K) | 95K | 140K | 260K |
| Anthracene···Anthracene (same layer) | | | |
| C36···C59 | 3.341 | 3.339 | 3.372 |
| C36···C58 | 3.434 | 3.417 | 3.490 |
| C37···C58 | 3.430 | 3.429 | 3.484 |
| C37···C57 | 3.479 | 3.480 | 3.530 |
| C38···C57 | 3.411 | 3.398 | 3.473 |
| Anthracene···Anthracene (adjacent layers) | | | |
| C20···C53 | 3.357 | 3.392 | 3.439 |
| C62···C61' | 3.498 | 3.517 | 3.572 |
| C24···C24' | 3.426 | 3.452 | 3.537 |
| Anthracene···Cyano (adjacent layers) | | | |
| C60···C6 | 3.356 | 3.363 | 3.433 |
| C45···C5 | 3.384 | 3.430 | 3.472 |

| **AnpyAu·ClBz** (triclinic) | | |
|---|---|---|
| T (K) | 110 K | 260 K |
| Anthracene···Anthracene (same layer) | | |
| C25···C38 | 3.414 | |
| C21···C34' | | 3.491 |
| Anthracene···Anthracene (adjacent layers) | | |
| C67···C37 | 3.313 | |
| C67···C38 | 3.307 | |
| C69···C17 | 3.431 | |
| C70···C18 | 3.351 | |
| C73···C16 | 3.319 | |
| C75···C13 | 3.469 | |
| C12···C12' | | 3.438 |
| C6···C34 | | 3.499 |
| Anthracene···Cyano (adjacent layers) | | |
| C18···C8 | 3.453 | |
| C75···C2 | 3.480 | |

**Fig. S14.** Thermal evolution of the *d-d* $^1A_1 \rightarrow {}^1T_1$ band in a single crystal during cooling at 2 K min$^{-1}$ of (a) **AnPyAg·ClBz**, (b) **AnPyAg·BrBz**, (c) **AnPyAg·IBz**, (d) **AnPyAg·$NO_2$Bz**, (e) **AnPyAg·$CH_3$Bz**, (f) **AnPyAu·ClBz**, (g) **AnPyAu·BrBz**, (h) **AnPyAu·IBz**, (i) **AnPyAu·$NO_2$Bz** and (j) **AnPyAu·$CH_3$Bz**. Notice that all of them exhibit an isosbestic point around 650 nm indicating the change between the LS and HS compositions.

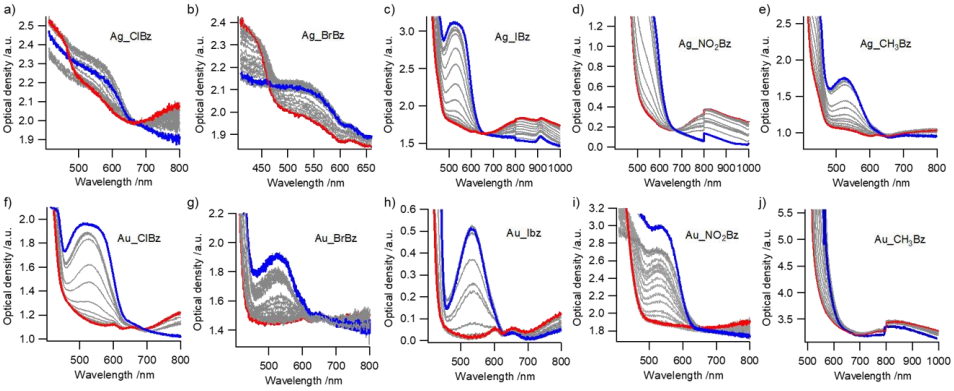


**Table S19.** Extinction coefficient of all the samples.

| Sample | [] (M) (LS /HS) | Thickness (µm) | λmax LS (nm) | OD LS (lmax-717nm) | ε LS (M-1cm-1) | OD HS (717-799 nm) | ε HS (M-1cm-1) |
|---|---|---|---|---|---|---|---|
| **Ag_ClBz** | 1.4302/1.3443 | 350 | (SAT) | 0.3604 (SAT) | 7.1998 | 0.0779 | 1.6557 |
| **Ag_BzBz** | 1.4271/1.3351 | 350 | (SAT) | 0.1981 (SAT) | 3.9660 | 0.0222 | 0.4751 |
| **Ag_IBz** | - | 350 | 530 | 1.5186 | - | 0.1225 | - |
| **Ag_CH3Bz** | 1.4247/1.3321 | 350 | 527 | 0.7768 | 15.578 | 0.0257 | 0.5512 |
| **Ag_NO2Bz** | 1.4393/1.3344 | 350 | (SAT) | 1.306 (SAT) | 25.925 | 0.1072 | 2.2953 |
| **Au_ClBz** | 1.3507/1.2673 | 350 | 522 | 0.8184 | 17.311 | 0.1118 | 2.5206 |
| **Au_BzBz** | 1.4091/1.3310 | 350 | 524 | 0.4943 | 10.023 | 0.0261 | 0.5603 |
| **Au_IBz** | - | 350 | 531 | 0.5014 | - | 0.0684 | - |
| **Au_CH3Bz** | 1.3126/1.2586 | 350 | (SAT) | SAT PELLET | - | 0.0877 | 1.9908 |
| **Au_NO2Bz** | 1.4246/1.3297 | 350 | 536 | 1.197 | 24.0064 | 0.0662 | 1.4225 |

**Fig. S15.** Broadening of the hysteresis loop at increasing scan rates [1 (red) *vs* 2 K $min^{-1}$ (blue)] for **AnPyAu·BrBz**. The fact that the thermal transition temperature depends on the scan rate indicates that the kinetics of the transition are slower than the scan rate applied.

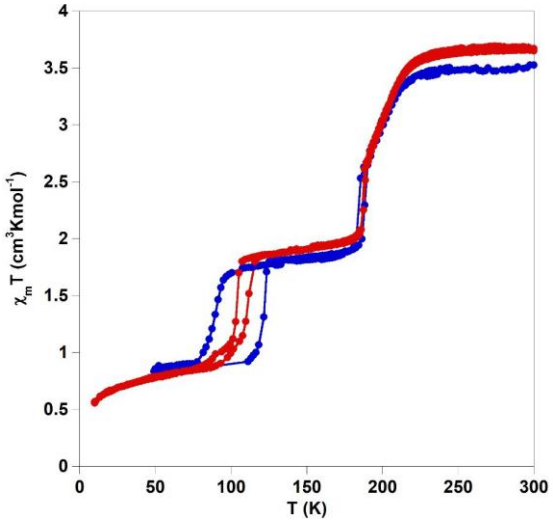


**Fig. S16.** The thermal spin transition obtained optically for the semitransparent pellet of **AnPyAu·$CH_3$Bz** is more gradual due to the grinding and pressuring process. In fact, this effect has been undoubtedly attributed thanks to the comparison of the transition in **AnPyAg·IBz** as a crystal (a) and as diluted powder in a pellet (b). The corresponding thermal evolution of $\gamma_{HS}$ is presented in (c).

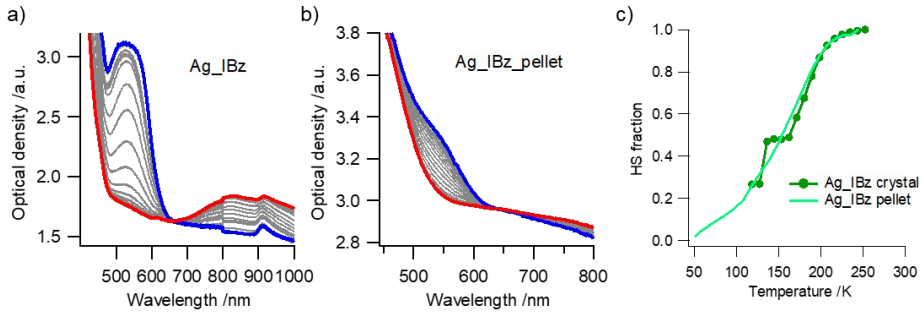

**Fig. S17.** Comparison of the (a) room temperature excitation spectra (Inset: crystals measured in a copper plate), and (b) room temperature and low temperature emission spectra at excitation 350 nm of an ensemble of **AnPyAg·IBz** crystals and of the previously studied fluorescent SCO compound {Fe(bpan)[Ag(CN)$_2$]$_2$} (bpan = bis(4-pyridyl)anthracene) (see ref. 60). Both ligands exhibit the same features in the excitationand emission but the excimer/exciplex signal is weaker in the case of the AnPy ligand.

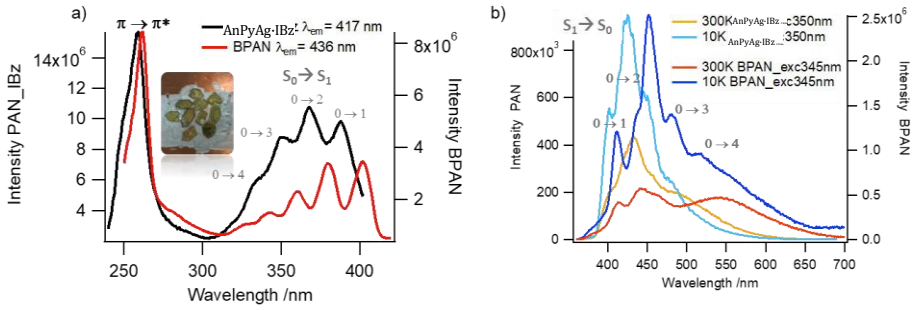


**Fig. S18.** Emission spectra of the **AnPyAg·XBz** (left) and **AnPyAu·XBz** (right) crystals at excitation 365 nm at 300K

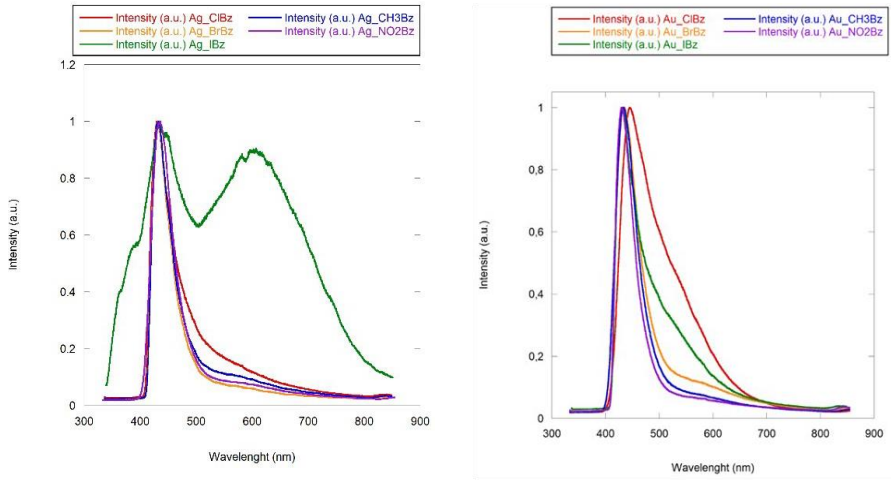

**Fig. S19.** Spectra used for quantum yield estimation by an integrating sphere for AnPy.

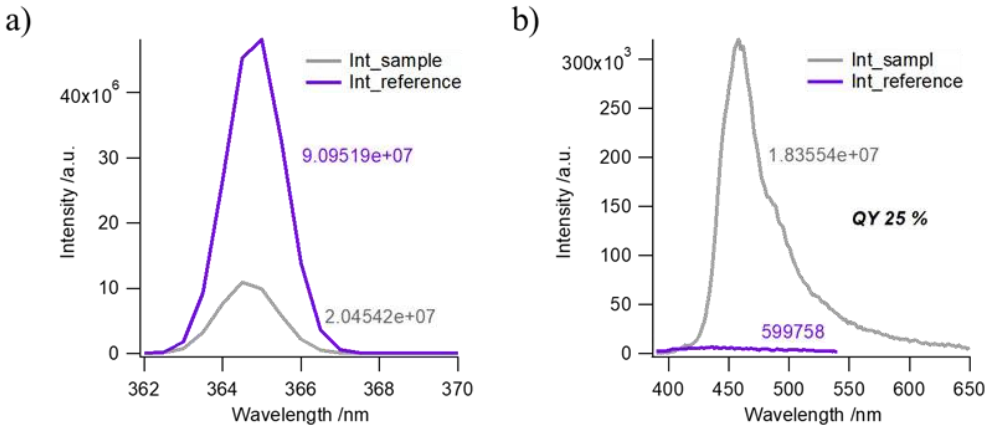


**Fig. S20.** Thermal evolution of the emission spectra after excitation at 365 nm of an ensemble of cristals of (a) AnPy and (b) **NiAnPyAg·NO$_2$Bz** during cooling at 5 K min$^{-1}$ with the corresponding variation of the intensity with the temperature for (c) AnPy and (d) **NiAnPyAg·NO$_2$Bz**.

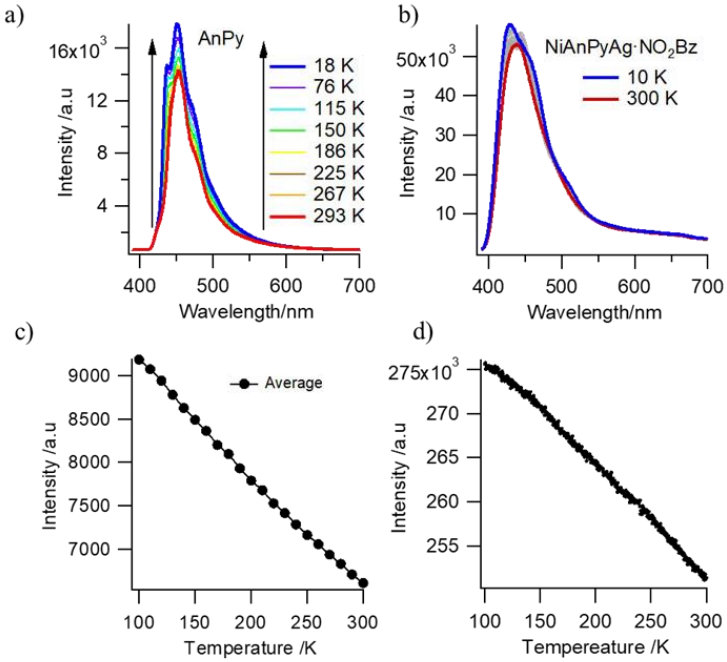

**Fig. S21.** Thermal evolution of the emission spectra during heating at 5 K $min^{-1}$ after excitation at 365 nm of an ensemble of crystals of (a) **AnPyAg·$CH_3$Bz**, (b) **AnPyAg·$NO_2$Bz**, (c) **AnPyAg·BrBz**, (d) **AnPyAg·ClBz**, (e) **AnPyAu·$CH_3$Bz**, (f) **AnPyAu·$NO_2$Bz** and (g) **AnPyAu·BrBz**

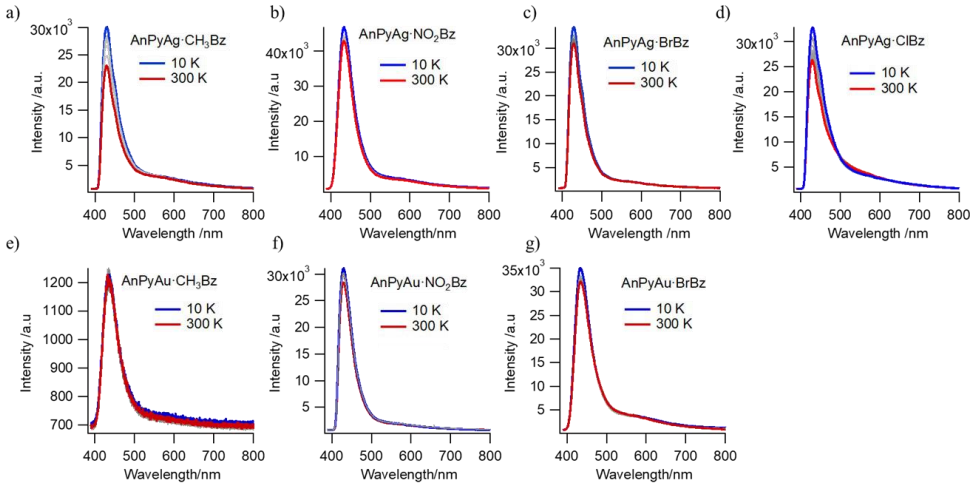


**Fig. S22.** (a) Thermal evolution of the emission spectra after excitation at 365 nm of an ensemble of crystals of **AnPyAu·ClBz** during heating at 5 K $min^{-1}$ (Inset: Image of the emission of the crystals at room temperature) and (b) the corresponding variation of the monomer and excimer/exciplex intensity with temperature.

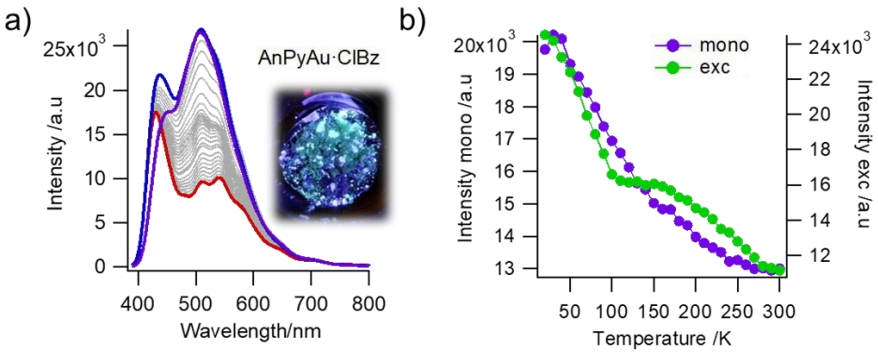

**Table S20.** Molecular volumes estimated through the Chimera software for the different studied guest molecules.

| Guest | V (Å$^3$) |
|---|---|
| $CH_3Bz$ | 87.9 |
| $NO_2Bz$ | 96.6 |
| ClBz | 96.4 |
| BrBz | 120.0 |
| IBz | 149.7 |

CAPÍTULO 5

# Conclusiones finales

# CAPÍTULO 5
# CONCLUSIONES FINALES

**Reversible guest-induced gate-opening with multiplex spin crossover responses in two dimendional Hofmann clathrates**

En el segundo capítulo de la presente tesis doctoral se ha descrito una nueva familia de clatratos de Hofmann 2D formulados $\{Fe(5\text{-}NH_2Pym)_2[M^{II}(CN)_4]\}\cdot G$ (**$1^{M}\cdot G$**, M = Pt or Pd, G = $H_2O$, MeOH o EtOH) que han revelado ser una excelente plataforma para analizar las transformaciones estructurables reversibles y controlables asociadas a las interacciones red anfitrióna-huésped que son el origen de los cambios observados en las propiedades SCO. La naturaleza dual dador-aceptor de los ligandos axiales 5-$NH_2$pmd favorece la formación de una matriz singular de enlaces de hidrógeno dentro de las capas. En el derivado desolvatado, **$1^{M}$,** estas interacciones son fruto de la complementariedad dador-aceptor N···HNH establecida entre dos ligandos 5-$NH_2$Pym coordinados a centros [$FeN_6$] adyacentes pertenecientes a la misma red 2D. Estas interacciones, que implican el 50% de los grupos amino y átomos de N no coordinados de los ligandos 5-$NH_2$Pym confieren una marcada ondulación a la estructura en capas. El 50% restante de los pares $NH_2$/N(Pym), desactivado estructuralmente para definir enlaces de hidrógeno mutuos, genera huecos funcionalizados potencialmente adecuados para albergar moléculas hidroxilicas ROH pequeñas. De hecho, la exposición de los derivados **$1^{M}$**, esencialmente no porosos, a moléculas como $H_2O$, MeOH o EtOH induce una adsorción basada en un mecanismo tipo “gate-opening” que implica importantes reorganizaciones estructurales que incluyen una rotación de 180º de los ligandos 5-$NH_2$Pym, la atenuación de la ondulación de las capas y la creación de enlaces de hidrógeno huésped-invitado con las moléculas atrapadas. Es importante destacar que la capacidad de adsorción de **$1^{M}$** depende no solo de la naturaleza del invitado y de la estructura del huésped (M = Pt o Pd), que confieren propiedades de selectividad al sistema, sino también de sus interacciones recíprocas. Estas interacciones mutuas a su vez afectan a los entornos del centro de $Fe^{II}$ y determinan comportamientos SCO variables y predecibles. La coexistencia del comportamiento SCO y la naturaleza cooperativa de la adsorción “gate opening” junto a la posibilidad de ser procesados en capas delgadas de espesor nanométrico, evidencian el potencial de los clatratos amino-funcionalizados 2D aquí descritos de cara a su aplicación en dispositivos sensores y de separación de moléculas hidroxílicas en fase vapor.

**Bistable Hofmann-Type $Fe^{II}$ Spin Crossover Two-Dimensional Polymers of 4-Alkyldisulfanylpyridine for Prospective Grafting of Monolayers on Metallic Surfaces**

En el tercer capítulo de la tesis doctoral se ha descrito la síntesis, estructura, propiedades magnéticas, fotomagnéticas y calorimétricas de cuatro nuevos polímeros de coordinación SCO 2D del tipo Hofmann formulados $\{Fe(PyS_2R)_2[M^{II}(CN)_4]\}$ (**$MPyS_2R$**, M = Pt or Pd, R = Me, Et). Tres de ellos muestran propiedades SCO fuertemente cooperativas caracterizadas por histéresis térmicas amplias, en particular el derivado **$PtpyS_2Me$**, mientras que su homólogo de Pd presenta inesperadamente una transición en varias etapas sin histéresis, hecho que muy probablemente se debe a la presencia del desorden posicional en los grupos periféricos -S-S-Me. Los derivados **$MpyS_2Et$**, que presentan las $T_c$ más bajas de la serie, exhiben efecto LIESST completo. En contraste el efecto LIESST es incompleto para **$PdpyS_2Me$** y desaparace por completo para **$PtpyS_2Me$** debido a sus valores más altos de $T_c$.

Los resultados aquí descritos pertenecen a la primera etapa de un proyecto más amplio cuyo objetivo último es el estudio de la deposición de estos polímeros de coordinación 2D en monocapas sobre superficies metálicas (por ejemplo, Au) para ser probadas como uniones en dispositivos espintrónicos en los que los centros SCO conmutables pueden usarse para modular la conductancia de la unión. La elección de estos ligandos axiales del tipo 4-alquildisulfanilpiridina se basó en el hecho bien conocido de que los atómos de azufre aseguran una interacción apropiada entre los cables moleculares y los electrodos.

**Coexistence of Luminiscence and Spin-Crossover in 2D Iron(II) Hofmann Clathrates Modulated Through Guest Encapsulation**

En el cuarto capítulo de la tesis se detalla la síntesis y caracterización de los nuevos polímeros de coordinación 2D multifuncionales formulados $\{Fe(AnPy)_2[M(CN)_2]_2\}\cdot XBz$ (**AnPyM·XBz** , M = Ag, Au; X = Cl, Br, I, $CH_3$, $NO_2$). Estos compuestos presentan comportamientos SCO en varias etapas asociados a los centros pseudo-octactaédricos de $Fe^{II}$ concomitantemente con la emisión fluorescente asociada al grupo antraceno del ligando axial AnPy. Además, el empaquetamiento cristalino, constituido por el apilamiento de las capas bimetálicas, conlleva la formación de grandes cavidades interlaminares que son ocupadas por moléculas invitadas derivadas del benceno las cuales median por efecto plantilla en el proceso de cristalización. Como consecuencia de la combinación de efectos estéricos y electrónicos, la presencia de estas moléculas invitadas afecta considerablemente

a las propiedades SCO, modulando así la temperatura característica $T_c$ del polímero 2D en función de la naturaleza del derivado bencénico. El análisis estructural de las diferentes etapas del comportamiento SCO ha permitido identificar sutiles roturas de simetría asociadas con el ordenamiento de los estados de espín en las diferentes etapas. Los estudios de absorción UV-Visible revelan la transformación HS-LS mediante la evolución térmica de las bandas d-d del $Fe^{II}$, en consonancia con la transición de espín térmica y la modulación de $T_c$ en función del invitado deducidas a partir de la evolución térmica de la susceptibilidad magnética. Para algunos derivados **AnPyM·XBz** (M = Ag; X = I y M = Au, X = I, $CH_3$) se ha observado un comportamiento sinérgico entre la propiedad SCO y la emisión fluorescente como resultado de la resonancia entre la absorción d-d del $Fe^{II}$ LS y la emisión excímero/exciplex del ligando AnPy en la región del espectro visible correspondiente al color verde. La emisión fluorescente es absorbida sustancialmente por la banda d-d característica del $Fe^{II}$ en el estado LS, pero a medida que se puebla paulatinamente el estado HS con el aumento de la temperatura, la emisión fluorescente aumenta paralelamente en intensidad hasta alcanzar un máximo, permitiendo la monitorización de la conversión de espín. Estos resultados, junto a estudios previos de la sinergia SCO-fluoresencia realizados en nuestro grupo resaltan la importancia de la capacidad de emisión intrínseca de los fluoróforos implicados y sugieren que su empaquetamiento y orientación precisa en la red es determinante para crear estas interaciones.

# CAPÍTULO 5
# CONCLUSIONS

## Reversible guest-induced gate-opening with multiplex spin crossover responses in two dimendional Hofmann clathrates

Chapter two introduces a new example of Single-Crystal to Single-Crystal transformations in the new family of 2D Hoffmann type Coordination polymers formulated $\{Fe(5\text{-}NH_2Pym)_2[M^{II}(CN)_4]\}\cdot G$ (**$1^{M}\cdot G$**, M = Pt or Pd, G = $H_2O$, MeOH o EtOH). These materials have revealed reversible and controllable guest-dependent structural transformations coupled to drastic SCO changes. The dual donor-acceptor nature of the 5-$NH_2$Pym axial ligands affords a singular array of intra-layer hydrogen bond interactions. In the guest-free **$1^{M}$** derivative, these interactions arise from the N···HNH donor-aceptor complementarity established between two 5-$NH_2$Pym ligands coordinated to adjacent [$FeN_6$] centres in each 2D layer. These interactions involve 50% of the amino groups and non-coordinated N atoms of the 5-$NH_2$Pym ligands and confer a a remarkable corrugation to the layered structure. The remaining 50% of $NH_2$/N(pym) pairs, struturally disabled to define mutual hydrogen bonds, generate functionalized void spaces potentially suitable for small ROH hydroxylic solvents. Indeed, exposition of the essentially non-porous **$1^{M}$** derivatives to $H_2O$, MeOH or EtOH induces a gate-opening adsorption mechanism which involves important structural reorganizations including 180º rotation of the 5-$NH_2$Pym ligands, flattening of the layers and creation of host-guest hydrogen bonds facilitating the migration of the trapped molecules. Importantly, the adsorption capabilities of **$1^{M}$** depend not only on the nature of the guest molecule and that of the host framework (M = Pt or Pd) conferring selectivity properties to the system, but also on their reciprocal interactions. These mutual interactions in turn affect the $Fe^{II}$ environments and determine varying and predictable SCO behaviours. The interplay between SCO and gate-opening adsorption, together with their likely suitability to be processed as nanometric thin films evidence the potential of the reported 2D amino-functionalized clathrates for the elaboration of devices for sensing and separation of hydroxilic molecules in gas phase.

**Bistable Hofmann-Type $Fe^{II}$ Spin Crossover Two-Dimensional Polymers of 4-Alkyldisulfanylpyridine for Prospective Grafting of Monolayers on Metallic Surfaces**

Chapter three describes the synthesis, structure, magnetic, photomagnetic and calorimetric properties of four new Hofmann-type 2D SCO coordination polymers formulated $\{Fe(PyS_2R)_2[M^{II}(CN)_4]\}$ (**MPyS₂R**, M = Pt or Pd, R = Me, Et). Three of them show strong cooperative SCO properties, featuring wide thermal hysteresis, in particular the compound **PtpyS₂Me**, while its isostructural Pd counterpart unexpectedly displays a multi-stepped transition without hysteresis, most likely due to the occurrence of positional disorder in the -S-S-Me peripheral groups. The **MpyS₂Et** derivatives, which exhibit the lowest $T_c$ of the series, show complete LIESST effect. In contrast, the LIESST effect is incomplete for **PdpyS₂Me** and vanishes completely for **PtpyS₂Me** due to their higher $T_{1/2}$ values.

The results here reported correspond to the first step in a more challenging project whose ultimate objective is to graft these Hofmann-type 2D SCO coordination polymers as monolayers on metallic surfaces (e.g., Au) to be probed as junctions for spintronic devices in which the switchable SCO centers can be used to modulate the junction conductance. The choice of the 4-alkyldisulfanylpyridines as axial ligands was based on the well-known fact that S atoms ensure appropriate interaction between the molecular wires and the electrodes.

**Coexistence of Luminiscence and Spin-Crossover in 2D Iron(II) Hofmann Clathrates Modulated Through Guest Encapsulation**

Chapter four describes the synthesis and characterization of the novel family of 2D Hofmann-type coordination polymers formulated as $\{Fe(AnPy)_2[M(CN)_2]_2\}\cdot Xbz$ (**AnPyMXbz**, M = Ag, Au; X = Cl, Br, I, $CH_3$, $NO_2$). These compounds display multi-stepped SCO, associated to the pseudo-octahedrally coordinated $Fe^{II}$ centres, concomitantly with fluorescent emission arising from the anthracene moiety of the AnPy axial ligand. Furthermore, the crystal packing, consisting of stacking bimetallic layers, leads to large interlayer cavities where substituted benzenic guests are premeditatedly trapped and used as crystallization templates. As a consequence of steric and electronic effects, the presence of these guest molecules greatly affects the SCO properties, modulating the $T_c$ of the 2D polymer depending on nature of the bencenic derivative. The structural analysis of the SCO steps has allowed to identify the subtle symmetry breakings associated with the ordering of the spin states at each step. The UV-Visible absorption studies have revealed the HS↔LS

transformation through the thermal evolution of the $Fe^{II}$ d-d bands, in good agreement with the thermal spin transition curves and the guest-induced $T_c$ modulation deduced from the thermal dependence of the magnetic susceptibility. For some derivatives **AnPyMXbz** (X = I; M = Ag, Au and X = Cl; M = Au) a synergy between SCO and fluorescent emission has been observed. This interplay between both phenomena stems from the resonance between the $Fe^{II}$ LS state d-d absorption band and the excimer/exciplex fluorescent emission band of the AnPy ligand in the green region of the visible spectra. The fluorescent emission is substantially absorbed by the characteristic d-d band of the $Fe^{II}$ in the LS state, but as the HS state gradually populates, with increasing temperature, the fluorescent emission increases parallel in intensity until a maximum is reached, allowing for the probing of the spin conversion. These outcomes, together with previous observations of the SCO-fluorescence synergy performed in our research group highlight the importance of the intrinsic emission capacity of the fluorophores involved and suggest that their precise orientation and packing is key to create this synergy.

# Apéndice

Chemical Science

ROYAL SOCIETY OF CHEMISTRY

EDGE ARTICLE

View Article Online
View Journal | View Issue

Check for updates

Cite this: *Chem. Sci.*, 2020, **11**, 11224

All publication charges for this article have been paid for by the Royal Society of Chemistry

Open Access Article. Published on 22 September 2020. Downloaded on 11/12/2021 10:39:38 AM.
This article is licensed under a Creative Commons Attribution 3.0 Unported Licence.

# Reversible guest-induced gate-opening with multiplex spin crossover responses in two-dimensional Hofmann clathrates†

Rubén Turo-Cortés, [a] Carlos Bartual-Murgui, *[a] Javier Castells-Gil, [a] M. Carmen Muñoz, [b] Carlos Martí-Gastaldo [a] and José Antonio Real *[a]

Spin crossover (SCO) compounds are very attractive types of switchable materials due to their potential applications in memory devices, actuators or chemical sensors. Rational chemical tailoring of these switchable compounds is key for achieving new functionalities in synergy with the spin state change. However, the lack of precise structural information required to understand the chemical principles that control the SCO response with external stimuli may eventually hinder further development of spin switching-based applications. In this work, the functionalization with an amine group in the two-dimensional (2D) SCO compound $\{Fe(5\text{-}NH_2Pym)_2[M^{II}(CN)_4]\}$ ($\mathbf{1}^{M}$, 5-$NH_2$Pym = 5-aminopyrimidine, $M^{II}$ = Pt ($\mathbf{1}^{Pt}$), Pd ($\mathbf{1}^{Pd}$)) confers versatile host–guest chemistry and structural flexibility to the framework primarily driven by the generation of extensive H-bond interactions. Solvent free $\mathbf{1}^{M}$ species reversibly adsorb small protic molecules such as water, methanol or ethanol yielding the $\mathbf{1}^{M}\cdot H_2O$, $\mathbf{1}^{M}\cdot 0.5MeOH$ or $\mathbf{1}^{M}\cdot x$EtOH ($x$ = 0.25–0.40) solvated derivatives. Our results demonstrate that the reversible structural rearrangements accompanying these adsorption/desorption processes ($\mathbf{1}^{M} \leftrightarrow \mathbf{1}^{M}\cdot$guest) follow a gate-opening mechanism whose kinetics depend not only on the nature of the guest molecule and that of the host framework ($\mathbf{1}^{Pt}$ or $\mathbf{1}^{Pd}$) but also on their reciprocal interactions. In addition, a predictable and reversible guest-induced SCO modulation has been observed and accurately correlated with the associated crystallographic transformations monitored in detail by single crystal X-ray diffraction.

Received 3rd August 2020
Accepted 21st September 2020

DOI: 10.1039/d0sc04246c

rsc.li/chemical-science

## Introduction

Hexa-coordinated iron(II) spin crossover (SCO) complexes are a singular class of materials featuring a labile and reversible electronic configuration change between the diamagnetic low-spin state $[t_{2g}^6e_g^0, S = 0]$ (LS) and the paramagnetic high spin state $[t_{2g}^4e_g^2, S = 2]$ (HS).[1] LS ↔ HS switching is an entropy-driven phenomenon which can be induced by a panoply of stimuli, *i.e.* a gradient of temperature[2] and/or pressure,[3] light irradiation,[4] application of an electric field[5] or even through interaction with analytes,[6] thereby effecting changes in the magnetic, electric, optical, mechanical and structural properties of the material. In the solid state, the profile of the spin-state switch depends on the elastic coupling (cooperativity) between active SCO $Fe^{II}$ centres. Gradual SCO spreading over a wide range of temperatures occurs when the elastic coupling is weak. On the contrary, strong elastic coupling favours sharp abrupt first order spin transitions which, in special cases, are accompanied by hysteretic behaviour conferring to the material bistability (memory effect). Materials exhibiting bistable SCO behaviour have attracted much interest because of their potential applications in memory devices, actuators or chemical sensors.[7]

In recent years, many studies have been devoted to the chemical design of SCO compounds in order to incorporate new functionalities acting in synergy with the purely thermal driven spin-state switching. These added properties include fluorescence,[8] electrical conductivity[9] or porosity,[10] among others. Indeed, combination of SCO and porosity has been one of the most exploited routes for achieving multifunctionality in part due to its high potential in molecular sensor applications. The first examples showing coexistence of both properties were the doubly-interpenetrated compounds with general formula $[FeL_2(SCN)_2]\cdot$Solv [L = 1,2-di-(4-pyridy1)-ethylene (tvp)[11] or *trans*-4-4′azopyridine (azpy)[12]]. These compounds display SCO properties which depend on the included solvent molecules. Later, Hofmann-type coordination polymers (HCPs) formulated $\{Fe(L)_y[M(CN)_x]\}$ {including non-interpenetrated [$x$ = 4; L = monodentate ($y$ = 2, 2D) or bis-monodentate ($y$ = 1, 3D) ligand; M = Pd, Pt, Ni] or interpenetrated [$x$ = 2, L =

[a]*Departamento de Química Inorgánica, Instituto de Ciencia Molecular (ICMol), Universidad de Valencia, Valencia, Spain. E-mail: carlos.bartual@uv.es; jose.a.real@uv.es*

[b]*Departamento de Física Aplicada, Universitat Politècnica de València, Camino de Vera s/n, E-46022, Valencia, Spain*

† Electronic supplementary information (ESI) available: Synthesis and characterization of samples, experimental and instrumental details. CCDC 2018378–2018393. For ESI and crystallographic data in CIF or other electronic format see DOI: 10.1039/d0sc04246c



This journal is © The Royal Society of Chemistry 2020

Open Access Article. Published on 22 September 2020. Downloaded on 11/12/2021 10:39:38 AM. This article is licensed under a Creative Commons Attribution 3.0 Unported Licence.

monodentate ($y$ = 2, 2D) or bis-monodentate ($y$ = 1, 3D) ligand; M = Ag, Au] compounds}[6a,13] gained increasing interest due to their demonstrated structural versatility and the possibility of being processed as thin-films or nano-objects.[14] The intrinsic structural porosity offered by this family of compounds has resulted in numerous reports studying synergies between SCO and host–guest chemistry.[15] Overall, modulation of the SCO through guest adsorption can be explained by steric and/or electronic effects. The first factor involves stabilization of the HS state by the guest due to the hindering of the framework contraction associated with the HS-to-LS process.[16] The second factor entails changes in the ligand field strength around the $Fe^{II}$ centre *via* host–guest interactions with the coordinated ligands.[17]

A suitable synthetic strategy for inducing guest inclusion-SCO synergies is the use of asymmetric ligands with hydrophilic functional groups. This type of ligands promotes intermolecular interactions leading to lattice asymmetries which originate inter-sheet cavities where the guest molecules are located. This structural model was exploited using a series of asymmetric triazole-type ligands substituted with various chemical groups leading, in all cases, to multi-stable SCO compounds.[18] Similar results were also obtained for pyridine donor asymmetric ligands.[19] Overall, the shape of the SCO curves in these systems depends not only on the selected pillaring ligand but also on the amount and nature of the adsorbed guest molecules. For example, the SCO of compound $\{Fe(bztrz)_2[Pd^{II}(CN)_4]\}\cdot G$ exhibits one, two or three steps when G = ($H_2O$,EtOH), $3H_2O$ or $\sim 2H_2O$, respectively, demonstrating that the elastic frustration which gives rise to multi-stability can be modulated by guest exchange.[18e] Unfortunately, with very rare exceptions,[18g] crystallinity of these 2D systems is partially or completely lost after total desorption of guest molecules preventing the evaluation of the involved structural modifications and their implication on the associated SCO changes. Moreover, the vanishing of crystallinity may also limit the accuracy of the structural characterization in a subsequent guest-dependent SCO study. The establishment of a dense network of host–host and host–guest intermolecular interactions (H-bonds, π–π stacking…) may be critical to overcome this limitation.

Recently, the analogous 2D compounds $\{Fe(3\text{-}NH_2Py)_2[M(CN)_4]\}$ and $\{Fe(Pym)_2[M(CN)_4]\}\cdot xH_2O$ [3-$NH_2$Py = 3-aminopyridine;[20] Pym = pyrimidine[21] (Scheme 1); M = Pt, Pd, Ni] were reported. The former displays host–host CH···N(amino) H-bonding interactions and hysteretic SCO for all the investigated derivatives, although no host–guest properties were described. In contrast, the latter exhibits guest-dependent cooperative spin transitions attributed to the H-bonds established between the non-coordinated nitrogen of the pyrimidine and the guest water molecules. However, the lack of detailed structural data after dehydration prevented the investigation of further precise magneto–structural correlations. In this work, the use of 5-aminopyrimidine (5-$NH_2$Pym, Scheme 1) ligand has led to 2D HCPs compounds $\{Fe(5\text{-}NH_2Pym)_2[M^{II}(CN)_4]\}\cdot H_2O$ [$M^{II}$ = Pt (**$1^{Pt}\cdot H_2O$**) or Pd (**$1^{Pd}\cdot H_2O$**)]. The combination of a donor amino group and an acceptor non-coordinated nitrogen in the 5-$NH_2$Pym axial ligand enables the coupling of contiguous [$FeN_6$] octahedrons, belonging to the same layer, through a robust network of H-bond interactions which is additionally reinforced by the inclusion of protic guest molecules. Indeed, this stiff H-bond network seems to be key for the persistence of crystallinity upon the loss of water molecules that gives rise to unsolvated derivatives **$1^{Pt}$** or **$1^{Pd}$**. These guest-free compounds are prone to re-adsorb water or other small molecules as methanol or ethanol also following reversible single-crystal-to-single-crystal (SCSC) transformations. This has enabled us to establish precise correlations between the wide variety of SCO behaviours presented by this family of compounds and the structural transformations upon guest exchange (**$1^{M}$** ↔ **$1^{M}\cdot$guest**). Interestingly, in agreement with the adsorption/desorption isotherm measurements, these crystallographic transformations follow a gate-opening mechanism which represents an unprecedented structural feature in combination with switchable 2D HCPs.

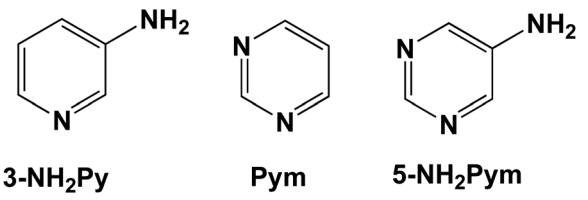


Scheme 1 Related axial ligands used for the synthesis of new 2D Hofmann-type SCO coordination polymers (see text).

## Results

### Synthesis, structure and SCO properties of $1^{Pt}\cdot H_2O$ and $1^{Pd}\cdot H_2O$

Single crystals of **$1^{Pt}\cdot H_2O$** and **$1^{Pd}\cdot H_2O$** were prepared by slow liquid-to-liquid diffusion methods from $Fe(BF_4)_2\cdot 6H_2O$, $K_2[M^{II}(CN)_4]$ ($M^{II}$ = $Pt^{II}$ or $Pd^{II}$) and 5-aminopyrimidine (5-$NH_2$Pym) aqueous solutions separated by a water interphase in a double-H shaped tube (see experimental section in ESI†). Yellow thin plate-shaped single crystals were obtained in good yields (*ca.* 60–70%) after 4 weeks.

Compounds **$1^{Pt}\cdot H_2O$** and **$1^{Pd}\cdot H_2O$** are isomorphous and crystallize in the monoclinic $C2/m$ space group. The asymmetric unit is constituted by two non-equivalent [$Fe^{II}1N_6$] and [$Fe^{II}2N_6$] pseudo-octahedral centres connected through their equatorial coordination sites by two equivalent $[M^{II}(CN)_4]^{2-}$ units ($M^{II}$ = Pt or Pd) (Fig. 1a), thereby defining cyano-bridged bimetallic $Fe^{II}$–$M^{II}$ layers (Fig. 1b). The axial positions of each $Fe^{II}$ ion are coordinated by two equivalent terminal 5-$NH_2$Pym ligands through one of its two heterocyclic N atoms. At 260 K, the average [Fe1$N_6$]/[Fe2$N_6$] bond lengths, 2.159 Å/2.164 Å for **$1^{Pt}\cdot H_2O$** and 2.168 Å/2.171 Å for **$1^{Pd}\cdot H_2O$**, are consistent with a fully populated HS state. Within a given $Fe^{II}$ centre, the apical 5-$NH_2$Pym ligands [hereafter labelled as 5-$NH_2$Pym(1) (coordinated to $Fe^{II}1$) and 5-$NH_2$Pym(2) (coordinated to $Fe^{II}2$)] are disposed in such a way that they adopt a *trans* conformation with respect to the orientation of the amino substituent. This enables the formation of two types of H-bonds within each

Open Access Article. Published on 22 September 2020. Downloaded on 11/12/2021 10:39:38 AM.
This article is licensed under a Creative Commons Attribution 3.0 Unported Licence.

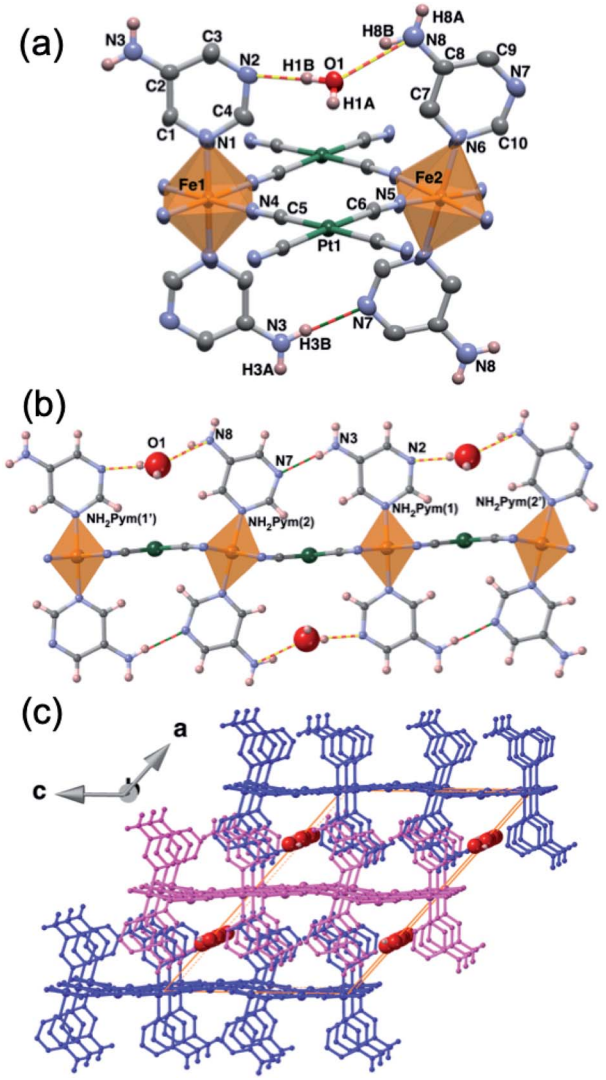


Fig. 1 (a) ORTEP view of the asymmetric unit of $\mathbf{1^{Pt}\cdot H_2O}$ at 260 K (isostructural to $\mathbf{1^{Pd}\cdot H_2O}$) showing 50% probability displacement ellipsoids (aromatic hydrogen atoms are omitted for clarity) and (b) view along the (010) direction of a $\mathbf{1^{M}\cdot H_2O}$ (M = Pt, Pd) layer (discontinuous yellow-red and red-green lines represent host–guest and host–host H-bonds, respectively). (c) 3D supramolecular fragment of $\mathbf{1^{M}\cdot H_2O}$ (M = Pt, Pd) displaying three successive pillared layers (distinguished in pink and blue). Red spheres represent the trapped water molecules within the 1D channels.

layer. One, a single H-bond between the N3 atom of the amino group of 5-$NH_2$Pym(1) and the uncoordinated N7 heteroatom of the adjacent 5-$NH_2$Pym(2) ligand. The other, a double H-bond involving the adjacent N2 and N8 atoms belonging to the heteroatom of 5-$NH_2$Pym(1) and the amino group of 5-$NH_2$-Pym(2′), respectively, mediated by the interaction with the guest water molecule (Fig. 1a and b). The trapped water molecule is located within two discrete equivalent positions modelled with an occupancy of 0.5 (0.4 in the case of Pt), hence the structure contains 1 (0.8 for Pt) molecule of water per $Fe^{II}$ ion in good agreement with the TGA studies (Fig. S1a and b†). The intralayer H-bond interactions define an array of parallel linear chains running along the (001) direction. As a result, the bimetallic layers are slightly corrugated (Fig. 1b) being the angles defined by the equatorial planes of the coordination Fe1–Fe2/Fe1–Pt(Pd)/Fe2–Pt(Pd) centres in the interval 14.8–15°/1.3–4.0°/16.2–18.8°, respectively. The layers are pillared in such a way that the apical 5-$NH_2$Pym ligands are interdigitated defining weak π–π interactions (Fig. S2a†) and the $M^{II}$ centres of one layer are on top the centre of the $[Fe_2M^{II}_2]$ windows of the adjacent layers (Fig. S2b†). The packing of the layers generates 1D channels where the water molecules are located (Fig. 1c). The interlayer distance based on the average plane defined by the Fe1–Fe2–Pt/Pd atoms is 8.17 and 8.14 Å for $\mathbf{1^{Pt}\cdot H_2O}$ and $\mathbf{1^{Pd}\cdot H_2O}$, respectively. Host–host and host–guest H-bond interactions found for $\mathbf{1^{Pt}\cdot H_2O}$ and $\mathbf{1^{Pd}\cdot H_2O}$ and for the rest of studied solvates are gathered in Table 1.

Upon cooling to 187 K (180 K for $\mathbf{1^{Pd}\cdot H_2O}$), the crystals become orange suggesting the occurrence of a HS-to-LS state change. The system retains the *C*2/*m* space group and the overall structure does not change significantly with respect to that at 260 K. However, whereas the average [Fe1$N_6$] bond length decreases by 0.194 Å for $\mathbf{1^{Pt}\cdot H_2O}$ and $\mathbf{1^{Pd}\cdot H_2O}$, that of [Fe2$N_6$] remains barely unaltered for both $\mathbf{1^{Pt}\cdot H_2O}$ (2.165 Å *vs.* 2.139 Å) and $\mathbf{1^{Pd}\cdot H_2O}$ (2.171 Å *vs.* 2.156 Å). These values reveal that whereas Fe1 centres undergo a complete HS-to-LS transition, those of Fe2 remain in the HS configuration. This defines a ···HS–LS··· ordered state within the linear H-bond chains mentioned above (Fig. 2a) that in turn results in an infinite ordered succession of HS and LS planes running along (001)

Table 1 Selected H-bond interactions (in Å) found for $\mathbf{1^{M}}$, $\mathbf{1^{M}\cdot H_2O}$, $\mathbf{1^{M}\cdot 0.5MeOH}$ and $\mathbf{1^{Pt}\cdot 0.4EtOH}$ at 260 K

| Interaction | $\mathbf{1^{Pt}}$ | $\mathbf{1^{Pd}}$ | $\mathbf{1^{Pt}\cdot H_2O}$ | $\mathbf{1^{Pd}\cdot H_2O}$ | $\mathbf{1^{Pt}\cdot 0.5MeOH}$ | $\mathbf{1^{Pd}\cdot 0.5MeOH}$ | $\mathbf{1^{Pt}\cdot 0.4EtOH}$ |
|---|---|---|---|---|---|---|---|
| **Host–host** | | | | | | | |
| N6(amino)···N7(het.) | 3.023 | 2.973 | — | — | — | — | — |
| N3(amino)···N7(het.) | — | — | 3.106 | 3.075 | — | — | 3.053 |
| N7(amino)···N3(het.) | — | — | — | — | 2.979 | 3.039 | — |
| N11(amino)···N13(het.) | | | — | — | 3.015 | 3.042 | — |
| **Host–guest** | | | | | | | |
| O1(guest)···N2(het.) | — | — | 2.885 | 2.842 | — | — | 2.795 |
| O1(guest)···N8(amino) | — | — | 3.053 | 3.035 | — | — | 2.963 |
| O1(MeOH)···N2(het.) | — | — | — | — | 2.724 | 2.771 | — |
| O2(MeOH)···N10(het.) | — | — | — | — | 2.805 | 2.781 | — |
| O1(MeOH)···N8(amino) | — | — | — | — | 2.900 | 2.914 | — |
| O2(MeOH)···N14(amino) | — | — | — | — | 2.979 | 2.908 | — |


This journal is © The Royal Society of Chemistry 2020

Open Access Article. Published on 22 September 2020. Downloaded on 11/12/2021 10:39:38 AM.
This article is licensed under a Creative Commons Attribution 3.0 Unported Licence.

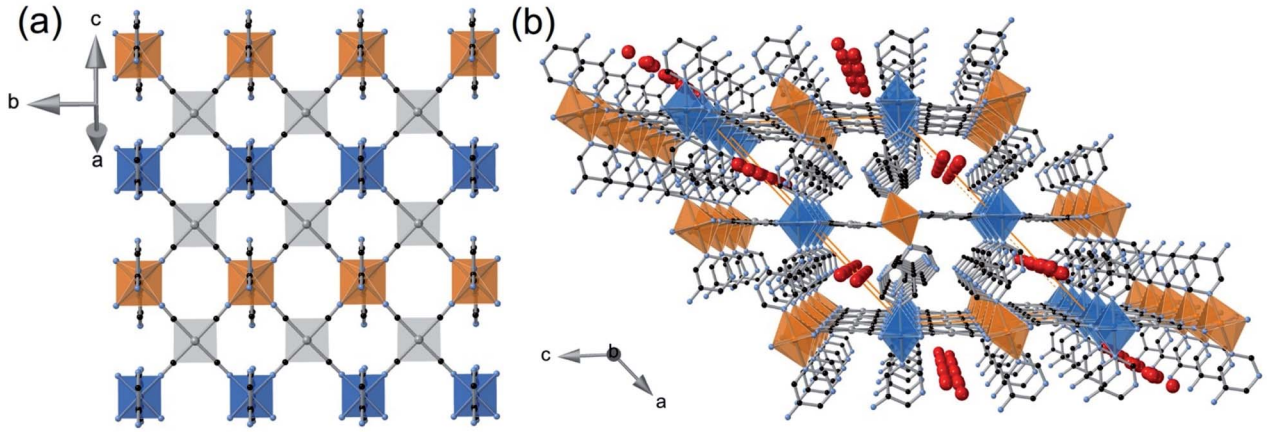


Fig. 2 Perspective views of $1^{Pt}\cdot H_2O$ at 187 K (structurally equivalent to $1^{Pd}\cdot H_2O$ at 180 K) displaying (a) a bimetallic layer in the ···HS–LS··· ordered intermediate state representing in blue the LS Fe1 sites and in orange the HS Fe2 sites and (b) three stacked layers showing the planes containing the HS or LS sites (hydrogen atoms are omitted for clarity).

(Fig. 2b). Further cooling to 120 K induces a complete spin transition as indicated by the Fe1–N/Fe2–N average distances of 1.948/1.955 and 1.961/1.963 Å for $\mathbf{1^{Pt}\cdot H_2O}$ and $\mathbf{1^{Pd}\cdot H_2O}$, respectively. These structural data are in perfect agreement with the magnetic measurements (*vide infra*). The HS → LS process is accompanied by a contraction of the interlayer distance by 0.3 Å and 0.2 Å for $\mathbf{1^{Pt}\cdot H_2O}$ and $\mathbf{1^{Pd}\cdot H_2O}$, respectively. Furthermore, the angles defined by the equatorial planes of Fe1–Fe2/Fe1–Pt(Pd)/Fe2–Pt(Pd) decrease by 0.7°/1.2°/2.0° when moving from the HS to the LS state for $\mathbf{1^{Pt}\cdot H_2O}$ and $\mathbf{1^{Pd}\cdot H_2O}$, consequently the undulation of the $\{Fe[M(CN)_4]\}_n$ planes is slightly less pronounced. The main crystallographic parameters of $\mathbf{1^{Pt}\cdot H_2O}$ and $\mathbf{1^{Pd}\cdot H_2O}$ are gathered in Tables S1 and S2,† respectively.

Fig. 3 shows the magnetic properties in the form of $\chi_M T$ *versus* $T$ plots ($\chi_M$ is the molar magnetic susceptibility and $T$ is the temperature) for $\mathbf{1^{Pt}\cdot H_2O}$ and $\mathbf{1^{Pd}\cdot H_2O}$. Samples of $\mathbf{1^{Pt}\cdot H_2O}$ and $\mathbf{1^{Pd}\cdot H_2O}$ and, consequently, those of their corresponding derivatives (*vide infra*) were constituted exclusively of single crystals which, according to the elemental analysis and powder X-ray diffraction studies (see experimental section and Fig. S3 in ESI†), corresponded to a single phase. At 290 K, the $\chi_M T$ value of the as-synthesized crystals of $\mathbf{1^{Pt}\cdot H_2O}$ and $\mathbf{1^{Pd}\cdot H_2O}$ was found to be about 3.5 $cm^3$ K $mol^{-1}$, which is consistent with the $Fe^{II}$ ion in the HS state. When cooling at 2 K $min^{-1}$, this value remains constant until it drops abruptly just below *ca.* 205 K in two marked steps, involving each one 50% of a complete HS-to-LS transformation. The average critical temperatures $T_c$ (calculated as $T_c = T_{ci}^{\uparrow} + T_{ci}^{\downarrow}/2$ where $T_{ci}^{\uparrow}$ and $T_{ci}^{\downarrow}$ ($i$ = 1, 2) are the transition temperatures in the respective heating and cooling modes) are $T_{c1}$ = 205.5 (204) K and $T_{c2}$ = 187.5 (173.5) K for $\mathbf{1^{Pt}\cdot H_2O}$ ($\mathbf{1^{Pd}\cdot H_2O}$) within the first and second step, respectively, and define hysteresis loops ($\Delta T_c = T_{ci}^{\uparrow} - T_{ci}^{\downarrow}$) of $\Delta T_{c1}$ = 9 (8) K and $\Delta T_{c2}$ = 15 (9) K for $\mathbf{1^{Pt}\cdot H_2O}$ ($\mathbf{1^{Pd}\cdot H_2O}$). Hence, the SCO curves of $\mathbf{1^{Pt}\cdot H_2O}$ and $\mathbf{1^{Pd}\cdot H_2O}$ define a plateau in the temperature range 184–205 K and 175–205 K, respectively, where, accordingly to the structural data, a HS–LS mixed state is present.

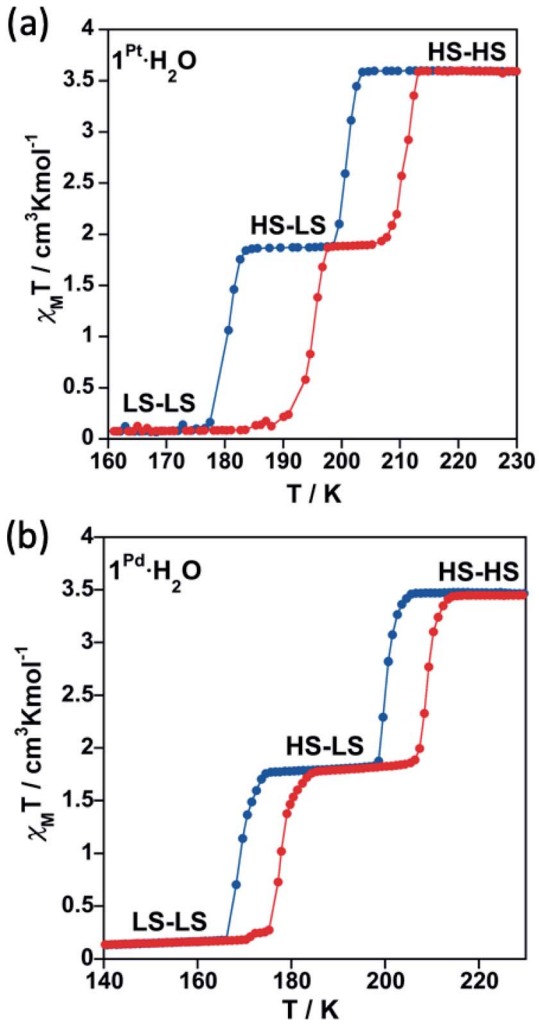


Fig. 3 SCO behaviour expressed as $\chi_M T$ *vs.* $T$ plots recorded at 2 K $min^{-1}$ for (a) $1^{Pt}\cdot H_2O$ and (b) $1^{Pd}\cdot H_2O$. Cooling and heating modes are highlighted in blue and red, respectively.

Open Access Article. Published on 22 September 2020. Downloaded on 11/12/2021 10:39:38 AM.
This article is licensed under a Creative Commons Attribution 3.0 Unported Licence.

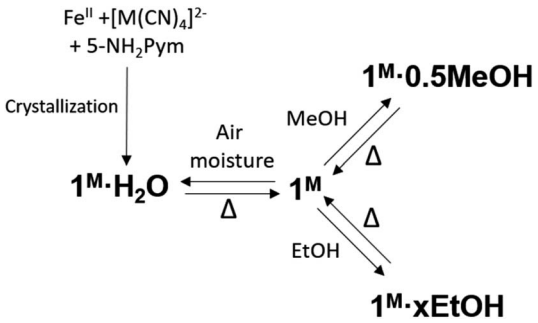


Scheme 2 Scheme of the main chemical transformations reported in this work.

### Guest exchange properties ($1^{M}\cdot H_2O \leftrightarrow 1^{M} \leftrightarrow 1^{M}\cdot$guest)

Based on the thermogravimetric analysis (TGA) (Fig. S1a and b†), $\mathbf{1^{Pt}}$ and $\mathbf{1^{Pd}}$ solvent-free single crystals were prepared by removing the included water molecule from the corresponding $\mathbf{1^{Pt}\cdot H_2O}$ and $\mathbf{1^{Pd}\cdot H_2O}$ counterparts through thermal treatment at 400 K for 30 minutes. The anhydrous derivatives spontaneously uptake water from atmospheric moisture yielding the primitive hydrated $\mathbf{1^{Pt}\cdot H_2O}$ and $\mathbf{1^{Pd}\cdot H_2O}$ derivatives (see Scheme 2). To in depth analyse this behaviour, water adsorption isotherms were performed for $\mathbf{1^{Pt}}$ and $\mathbf{1^{Pd}}$. These compounds do not show significant water adsorption below a value of relative pressure, $P/P_0$, equal to 0.02 for $\mathbf{1^{Pt}}$ and 0.08 for $\mathbf{1^{Pd}}$ (see Fig. 4a and c and the corresponding enlarged plots in Fig. 4b and d). Above this threshold value, a sigmoidal adsorption profile takes place first rapidly reaching a covering value of 0.83 and 0.90 mol $H_2O$/mol Fe for $\mathbf{1^{Pt}}$ and $\mathbf{1^{Pd}}$, respectively, and then more gradually to reach a value of *ca.* 1 mol $H_2O$/mol Fe at $P/P_0 = 0.6$. This result suggests a gate-opening mechanism in which the adsorption process is accompanied by a drastic cooperative crystallographic transformation. Indeed, the resulting curve corresponds to a Type F-IV adsorption profile typical for flexible compounds exhibiting non-porous to porous structural transitions.[22]

In subsequent SCSC transformations, desorbed $\mathbf{1^{Pt}}$ and $\mathbf{1^{Pd}}$ crystals soaked in MeOH or EtOH for a period of 3 h afforded crystals of $\mathbf{1^{M}\cdot 0.5MeOH}$ or $\mathbf{1^{M}\cdot x EtOH}$ (M = Pt, Pd, $x = 0.25$–$0.4$) (see Scheme 2). According to the corresponding TGA, a maximum of 0.5 molecules of methanol per $Fe^{II}$ are trapped within the structure of $\mathbf{1^{M}}$ whereas *ca.* 0.4 molecules of ethanol was included in $\mathbf{1^{Pt}}$ ($\mathbf{1^{Pt}\cdot 0.4EtOH}$). However, only 0.25 molecules of ethanol were found in $\mathbf{1^{Pd}}$ ($\mathbf{1^{Pd}\cdot 0.25EtOH}$) (Fig. S1c–f†). Given the non-porous nature of $\mathbf{1^{Pt}}$ and $\mathbf{1^{Pd}}$, and due to the larger molecular volume of MeOH, and especially of EtOH, their adsorption isotherms reflect much higher steric hindrance for these guests than for $H_2O$, thereby requiring higher $P/P_o$ values to include amounts close to the ones found for the soaked crystals. Interestingly, the MeOH adsorption isotherm for $\mathbf{1^{Pd}}$ also displays a clear sigmoidal shape with a threshold relative pressure of 0.04 $P/P_0$ (see Fig. 4d) reflecting a Type F-III adsorption profile ascribed to a gradual non-porous to porous structural switching.[22] Indeed, this threshold value is even lower than that of $H_2O$ and the same trend is observed for the Pt derivative (0.01 $P/P_0$ for MeOH *vs.* 0.02 for water) (Fig. 4b). In addition, the desorption isotherm profiles for the MeOH and EtOH derivatives are significantly different to the adsorption ones defining a marked hysteretic behaviour. This fact contrasts with the water uptake whose adsorption/desorption profiles are very close each other. All these observations suggest that the host clathrates exhibit higher chemical affinity for MeOH than for $H_2O$ at very low guest pressures and, although relatively strong interactions seem to be stablished with EtOH, its higher molecular volume may prevent an efficient adsorption. Similar results describing lower adsorption pressures for MeOH and EtOH than for $H_2O$ in a non-SCO 2D framework have been reported and ascribed to the presence of hydrophobic interactions.[23]

Time-dependent thermogravimetic studies of $\mathbf{1^{M}}$ under water, methanol or ethanol vapours are consistent with the results described above. With the aim of extracting the kinetic parameters associated with the adsorption processes, the quantity of adsorbed guest as a function of time was fitted to the Avrami equation[24] ($\alpha = A(1 - \exp\{-K_{av}t^{n}\})$) (see Fig. S4 and Table S3†). As expected regarding the adsorption isotherms, the Pt derivative presents higher amounts of adsorbed guest ($A$) and higher adsorption kinetic constants ($K_{av}$) than the Pd one. In addition, for a given activated derivative ($\mathbf{1^{Pt}}$ or $\mathbf{1^{Pd}}$), the adsorption kinetic constants are higher for MeOH and EtOH than for water suggesting a stronger affinity by the host framework for the formers. However, the $n$ parameter, which accounts for the cooperativity of the process, indicates that the adsorption event is more cooperative for water than for the alcohol molecules. Furthermore, for a given guest molecule, $n$ is higher for the Pd than for the Pt derivative.

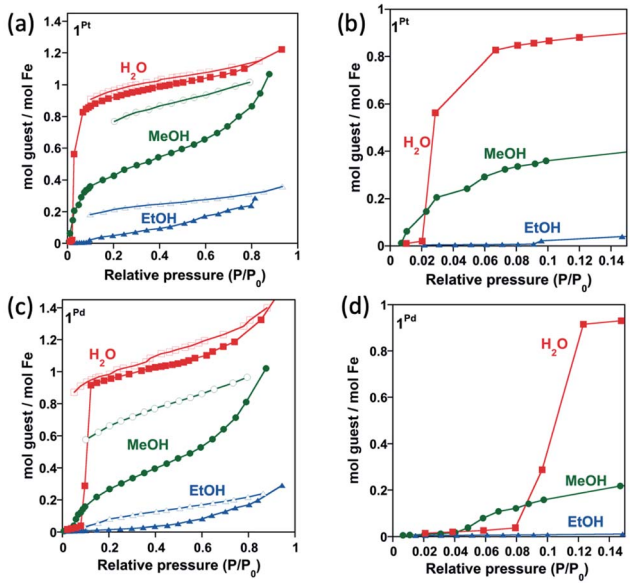


Fig. 4 Water, methanol and ethanol isothermal adsorption (full points) and desorption (open points) curves for $\mathbf{1^{Pt}}$ and $\mathbf{1^{Pd}}$ in (a and c) full scale and (b and d) the corresponding enlarged plots at low pressures range (desorption curves are omitted in the low pressures centred curves).


This journal is © The Royal Society of Chemistry 2020

Open Access Article. Published on 22 September 2020. Downloaded on 11/12/2021 10:39:38 AM.
This article is licensed under a Creative Commons Attribution 3.0 Unported Licence.

### Guest exchange-induced structural modifications

Single crystal X-ray diffraction measurements were performed in order to assess the structural modifications involved upon subsequent guest exchanges ($\mathbf{1^M \cdot H_2O} \leftrightarrow \mathbf{1^M} \leftrightarrow \mathbf{1^M \cdot guest}$). Furthermore, each compound was measured at temperatures in which the different spin states (HS, LS and/or mixed ⋯HS–LS⋯ ) manifest according to the magnetic properties (*vide infra*). Crystals of $\mathbf{1^{Pt} \cdot H_2O}$ and $\mathbf{1^{Pd} \cdot H_2O}$ were *in situ* heated in the diffractometer at 400 K in order to remove the guest water molecule, thereby yielding the corresponding $\mathbf{1^{Pt}}$ and $\mathbf{1^{Pd}}$ dehydrated phases. The water-free structures of $\mathbf{1^{Pt}}$ and $\mathbf{1^{Pd}}$ were then successfully determined at 260 K (HS) and 120 K (LS). In a subsequent step, $\mathbf{1^{Pt}}$ and $\mathbf{1^{Pd}}$ were loaded with MeOH to give $\mathbf{1^{Pt} \cdot 0.5MeOH}$ and $\mathbf{1^{Pd} \cdot 0.5MeOH}$ and the crystallographic data of freshly prepared crystals collected at 260 K (HS–HS) and 100 K (HS–LS). The ethanol derivatives were prepared in a similar way. In particular, $\mathbf{1^{Pt} \cdot 0.4EtOH}$ was analysed at 260 K (HS–HS) and 100 K (HS–LS). However, the low quantity of ethanol adsorbed by $\mathbf{1^{Pd}}$ led to mixed crystallographic phases that prevented the proper resolution of the structure of $\mathbf{1^{Pd} \cdot 0.25EtOH}$. The main crystallographic parameters of the discussed structures are displayed in Tables S1, S2, S4 and S5.†

### Structure of $\mathbf{1^{Pt}}$ and $\mathbf{1^{Pd}}$

Removal of the included water molecule from $\mathbf{1^M \cdot H_2O}$ ($\mathbf{1^M \cdot H_2O} \rightarrow \mathbf{1^M}$) involves a crystallographic phase transformation from the monoclinic *C*2/*m* to the orthorhombic *Pnma* space group. Although the layered structure of $\mathbf{1^M}$ is comparable to that of the hydrated monoclinic phase, the loss of water is accompanied by noticeable structural modifications (Fig. 5): (i) Only one type of $Fe^{II}$ ion, axially coordinated by two crystallographically distinct 5-$NH_2$Pym ligands, is now observed; (ii) one of the two axial 5-$NH_2$Pym is rotated 180° in such a manner that they adopt a *cis* conformation with respect to the orientation of the amine groups; (iii) the void space generated upon desorption of water molecules is minimized by subtle re-accommodation of the bimetallic layers whose undulated corrugation is more noticeable and regular. Indeed, the equatorial plane around Fe1 defines an angle with the $[M(CN)_4]^{2-}$ plane of 12.14° (M = Pt) and 14.95° (M = Pd) in the LS state but increases considerably up to 24.67° (M = Pt) and 29.59° (M = Pd) in the HS; (iv) the absence of included water molecules prevents the formation of the H-bonding chains observed for $\mathbf{1^{Pt} \cdot H_2O}$ and $\mathbf{1^{Pd} \cdot H_2O}$. Instead, only one intralayer H-bond interaction (N6⋯N7) is established between adjacent 5-$NH_2$Pym ligands (Fig. 5 and Table 1).

At 260 K, the $[FeN_6]$ average bond length [2.161 and 2.158 Å for $\mathbf{1^{Pt}}$ and $\mathbf{1^{Pd}}$, respectively] is consistent with 100% of the $Fe^{II}$ ions in the HS state. When cooling to 120 K, the structures remain in the *Pnma* space group but the $[FeN_6]$ average bond length decreases to 1.950 Å for $\mathbf{1^{Pt}}$ and 1.960 Å for $\mathbf{1^{Pd}}$, consistently with a complete HS-to-LS transition, also reflected by the observed yellow to red colour change. It is important to note that, according to the powder X-ray diffraction (Fig. S5†), the spontaneous readsorption of water from air moisture ($\mathbf{1^M} \rightarrow \mathbf{1^M \cdot H_2O}$) shows complete structural reversibility recovering the original $\mathbf{1^M \cdot H_2O}$ frameworks.

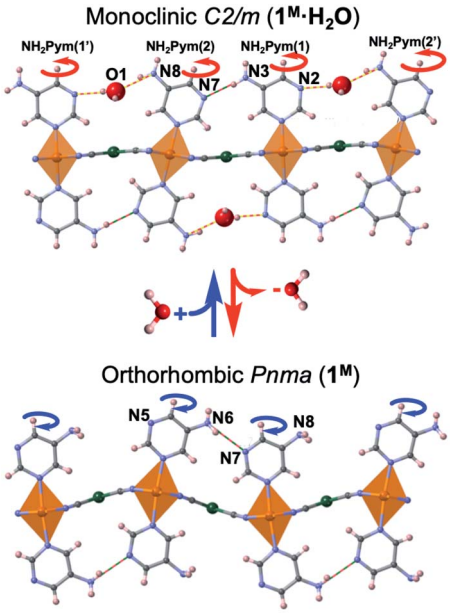


Fig. 5 Views along the (010) direction of a bimetallic layer of $\mathbf{1^M \cdot H_2O}$ (up) and $\mathbf{1^M}$ (down) at 260 K (M = Pt, Pd). Red/blue curved arrows indicate the 180° rotation of the 5-$NH_2$Pym ligands occurring along with the dehydration/hydration processes (discontinuous yellow-red and red-green lines represent host–guest and host–host H-bonds).

### Structure of $\mathbf{1^{Pt} \cdot 0.5MeOH}$ and $\mathbf{1^{Pd} \cdot 0.5MeOH}$

The $\mathbf{1^M} \rightarrow \mathbf{1^M \cdot 0.5MeOH}$ adsorption process involves a crystallographic phase change from the orthorhombic *Pnma* to the orthorhombic *Pbcm* space group. Overall, $\mathbf{1^{Pt} \cdot 0.5MeOH}$ and $\mathbf{1^{Pd} \cdot 0.5MeOH}$ present the same general structure as their water counterparts ($\mathbf{1^{Pt} \cdot H_2O}$ and $\mathbf{1^{Pd} \cdot H_2O}$) but the asymmetric unit is constituted, in addition to two different $[Fe^{II}N_6]$ centres, of two inequivalent 5-$NH_2$Pym per $Fe^{II}$ and two distinct $[M^{II}(CN)_4]^{2-}$ bridging units (Fig. S6†). As in $\mathbf{1^{Pt} \cdot H_2O}$ and $\mathbf{1^{Pd} \cdot H_2O}$, the two 5-$NH_2$Pym apical ligands coordinated to a given $Fe^{II}$ centre display a *trans* conformation with respect to the amine group orientation revealing that 50% of the axial ligands undergoes a 180° rotation upon MeOH adsorption. Similarly to $\mathbf{1^M \cdot H_2O}$, the bimetallic layers are slightly corrugated as shown by the angles defined between consecutive equatorial planes of the metallic centres [Fe1–M1/Fe2–M1/Fe1–M2/Fe2–M2] being equal to [1.96° (2.27°)/13.24° (17.59°)/1.01° (0.25°)/16.22° (15.07°)] for $\mathbf{1^{Pt} \cdot 0.5MeOH}$ and [1.43° (1.28°)/15.70° (14.15°)/1.25° (2.12°)/14.02° (17.56°)] for $\mathbf{1^{Pd} \cdot 0.5MeOH}$ in the LS and (HS) states, respectively. This irregular corrugation seems also to be guided by the formation of host–host and host–guest H-bonds. The bimetallic layers are now stacked along the (010) direction generating an array of two inequivalent 1D interlayer channels, running along the (001) direction and delimited by the $M^{II}(1)$ or $M^{II}(2)$ centres, respectively. These channels host an average of *ca.* 0.5 molecules of MeOH per $Fe^{II}$ (Fig. S7†) in good agreement with the thermogravimetric analysis (Fig. S1c and d†). The corresponding oxygen atom interacts *via* H-bonding with both the non-coordinated nitrogen heteroatom and the amino group of the apical 5-$NH_2$Pym ligands (Table 1). The much narrower channels created between the bimetallic layers are blocked by the (Pym)$NH_2$⋯N(Pym)$NH_2$ hydrogen bonds.

Open Access Article. Published on 22 September 2020. Downloaded on 11/12/2021 10:39:38 AM. This article is licensed under a Creative Commons Attribution 3.0 Unported Licence.

At 260 K, the average Fe1–N/Fe2–N bond lengths (2.174 Å/2.166 Å and 2.175 Å/2.173 Å for **1$^{Pt}$·0.5MeOH** and **1$^{Pd}$·0.5MeOH**, respectively) are consistent with a fully populated HS state. When cooling down to 100 K, the crystal retains the orthorhombic *Pbcm* space group and undergoes a yellow-to-dark orange color change indicating the occurrence of a HS-to-LS change. Indeed, although the Fe1 site remains in the HS state (Fe1–N average distance = 2.174 Å (260 K) *vs.* 2.164 Å (100 K)/2.175 Å (260 K) *vs.* 2.154 Å (100 K) for **1$^{Pt}$·0.5MeOH**/**1$^{Pd}$·0.5MeOH**), Fe2 undergoes a complete switch to the LS state (Fe2–N average distance = 2.166 Å (260 K) *vs.* 1.984 Å (100 K)/2.173 Å (260 K) *vs.* 1.985 Å (100 K) for **1$^{Pt}$·0.5MeOH**/**1$^{Pd}$·0.5MeOH**) giving rise to an ordered ···HS–LS··· state. The packing of the layers becomes slightly denser during the SCO event as it is reflected by the decrease of the distance between the average planes, defined by the undulated cyano-bridged bimetallic layers, from 8.197 Å/8.097 Å to 7.997 Å/7.987 Å for **1$^{Pt}$·0.5MeOH** and from 8.185 Å/8.138 Å to 8.070 Å/8.013 Å for **1$^{Pt}$·0.5MeOH**. Powder X-ray diffraction measurements have confirmed the structural reversibility of the methanol adsorption since the resulting pattern of the solid upon heating (**1$^{M}$·0.5MeOH** → **1$^{M}$**) coincides with that initially registered for the dehydrated compound (**1$^{M}$·H$_2$O** → **1$^{M}$**) (Fig. S8†).

### Structure of 1$^{Pt}$·0.4EtOH

The adsorption of ethanol in **1$^{Pt}$** provokes a crystallographic phase transition from the orthorhombic *Pnma* to the monoclinic *I*2/*m* space group. The structure of **1$^{Pt}$·0.4EtOH** is homologous to that of **1$^{M}$·H$_2$O** the main difference residing in the distinct nature of the included guests. Hence, in excellent accord with the TGA (Fig. S1e†), 0.4 molecules of ethanol are located within the 1D channels in such a way that they form hydrogen bonds with both the amino and the heterocyclic N atom of adjacent 5-NH$_2$Pym ligands (Table 1).

At 260 K, the Fe1–N/Fe2–N average distances are 2.164/2.168 Å, thereby reflecting a fully populated HS state. When cooling to 100 K, these distances change to 2.112/1.987 Å revealing that whereas the *ca.* 70% of the Fe1 centres remain in the HS state, the Fe2 centres undergo a complete transition to the LS state. Table 2 gathers the Fe–N average distances and the octahedral distortion parameters at each temperature for all the studied structures.

### Guest-dependent SCO properties of 1$^{M}$

Compounds **1$^{Pt}$·H$_2$O** and **1$^{Pd}$·H$_2$O** were dehydrated *in situ* in the SQUID chamber at 400 K for one hour to afford **1$^{Pt}$** and **1$^{Pd}$** and their $\chi_M T$ *vs.* $T$ curves subsequently recorded (see Fig. 6a and b, respectively). The resulting spin transitions remain abrupt and complete although they occur in a single step. In the case of the Pt derivative the critical temperature increases ($T_c$ = 218 K, $\Delta T_c$ = 10 K) with respect to those of the hydrated counterpart. In contrast, for **1$^{Pd}$**, the critical temperature ($T_c$ = 196.5, $\Delta T_c$ = 9 K) lie roughly in between the two hysteresis loops displayed by **1$^{Pd}$·H$_2$O**. Importantly, as mentioned above, **1$^{M}$** recover the water molecule when exposed to air moisture

Table 2 Octahedral distortion parameters ($\Theta$ and $\Sigma$) at different temperatures and the associated Fe–N average distances for 1$^{Pt}$·H$_2$O and 1$^{Pd}$·H$_2$O. ($\Theta$ is defined as $\sum_{i=1}^{i=24}(60-\theta_i)$ being $\theta_i$ the angle generated by superposition of two opposite faces of the octahedron there are four pairs of such superposition with six $\theta_i$ values each one). $\Sigma$ represents octahedron distortion defined as the sum of deviations from 90° of the 12 *cis* N–Fe–N angles in the coordination sphere $\sum_{i=1}^{i=12}(\varphi_i - 90)$

| Sample | **1$^{Pt}$** | | **1$^{Pt}$·H$_2$O** | | | | | |
|---|---|---|---|---|---|---|---|---|
| $T$ (K) | 260 | 120 | 260 | | 187 | | 100 | |
| Spin state | HS | LS | Fe1(HS) | Fe2(HS) | Fe1(LS) | Fe2(HS) | Fe1(LS) | Fe2(LS) |
| Fe–N (Å) | 2.161 | 1.950 | 2.159 | 2.164 | 1.965 | 2.140 | 1.948 | 1.955 |
| $\Theta/\Sigma$ | 39/17.9 | 20.1/8.4 | 22/11.6 | 39/22.8 | 21/12.0 | 43/29.6 | 17/14.0 | 30/20.4 |
| Sample | **1$^{Pd}$** | | **1$^{Pd}$·H$_2$O** | | | | | |
| $T$ (K) | 260 | 120 | 260 | | 180 | | 100 | |
| Spin state | HS | LS | Fe1(HS) | Fe2(HS) | Fe1(LS) | Fe2(HS) | Fe1(LS) | Fe2(LS) |
| Fe–N (Å) | 2.158 | 1.960 | 2.168 | 2.174 | 1.987 | 2.156 | 1.961 | 1.963 |
| $\Theta/\Sigma$ | 52/23 | 18.7/9.2 | 16/4.8 | 28/14.8 | 19/9.2 | 33/25.2 | 14/5.6 | 29/13.2 |
| Sample | **1$^{Pt}$·0.5MeOH** | | | | **1$^{Pd}$·0.5MeOH** | | | |
| T (K) | 260 | | 100 | | 260 | | 100 | |
| | Fe1(HS) | Fe2(HS) | Fe1(HS) | Fe2(LS) | Fe1(HS) | Fe2(HS) | Fe1(HS) | Fe2(LS) |
| Fe–N (Å) | 2.174 | 2.166 | 2.164 | 1.984 | 2.174 | 2.173 | 2.155 | 1.986 |
| $\Theta/\Sigma$ | 29/4.7 | 28/19.7 | 37/17.6 | 26/9.7 | 32/8.4 | 28/22.4 | 32/18.0 | 25/11.9 |
| Sample | | **1$^{Pt}$·0.4EtOH** | | | | | | |
| T (K) | | 260 | | | | 100 | | |
| | | Fe1(HS) | | Fe2(HS) | | Fe1(HS) | | Fe2(LS) |
| Fe–N (Å) | | 2.164 | | 2.166 | | 2.112 | | 1.986 |
| $\Theta/\Sigma$ | | 17/7.2 | | 36/22.8 | | 34/16.4 | | 22/15.6 |

 This journal is © The Royal Society of Chemistry 2020

Open Access Article. Published on 22 September 2020. Downloaded on 11/12/2021 10:39:38 AM.
This article is licensed under a Creative Commons Attribution 3.0 Unported Licence.

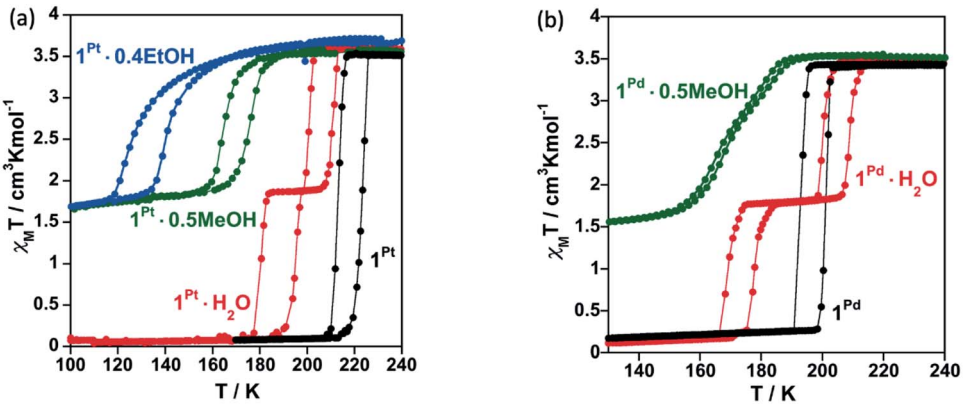


Fig. 6 SCO behaviour for (a) $1^{Pt}$, $1^{Pt}\cdot$0.5MeOH and $1^{Pt}\cdot$0.4EtOH and (b) $1^{Pd}$ and $1^{Pd}\cdot$0.5MeOH (scan rate: 2 K min$^{-1}$). Spin transitions curves of hydrated compounds ($1^{Pt}\cdot H_2O$ and $1^{Pd}\cdot H_2O$) are also displayed for comparison.

yielding the initial $\mathbf{1^{M}\cdot H_2O}$ compounds and showing full reversibility of the SCO properties (Fig. S9†).

The SCO properties of $\mathbf{1^{Pt}\cdot 0.5MeOH}$/$\mathbf{1^{Pt}\cdot 0.4EtOH}$ and $\mathbf{1^{Pd}\cdot 0.5MeOH}$ are displayed in Fig. 6a and b, respectively. The adsorption of MeOH induces a significant decrease of the SCO temperatures and whereas the transition remains cooperative displaying a one-step hysteretic curve ($\Delta T_c = 10$ K) with $T_c = 170$ K for $\mathbf{1^{Pt}\cdot 0.5MeOH}$, it exhibits a very subtle two-step behaviour centred at similar temperatures ($T_c$ = 170.5 K) with a narrow hysteresis ($\Delta T_c$ = 3 K) for $\mathbf{1^{Pd}\cdot 0.5MeOH}$. The inclusion of ethanol in $\mathbf{1^{Pt}}$ (compound $\mathbf{1^{Pt}\cdot 0.4EtOH}$) induces an even further decrease of the spin crossover temperatures than the methanol does ($T_c = 131.5$ K) while conserving a 13 K hysteresis wide. The $\chi_M T$ values recorded at 100 K (1.70/1.43/1.63 cm$^3$ K mol$^{-1}$ for $\mathbf{1^{Pt}\cdot 0.5MeOH}$/$\mathbf{1^{Pd}\cdot 0.5MeOH}$/$\mathbf{1^{Pt}\cdot 0.4EtOH}$) indicate, in good agreement with the structural data, that the presence of MeOH or EtOH blocks *ca.* 49/41/46% of the $Fe^{II}$ ions in the HS state. Despite further cooling to 50 K no additional spin transition events were observed for these compounds (Fig. S10†). In contrast, the $\chi_M T$ *vs.* $T$ curve of $\mathbf{1^{Pd}\cdot 0.25EtOH}$ displays a more complete two-step SCO behaviour (Fig. S11a†). The first step is characterized by a cooperative transition with $T_{c1} = 191$ K ($\Delta T_{c1}$ = 10 K) whereas the second one shows a gradual transition with $T_{c2} = 146.5$ K and ($\Delta T_{c2} = 9$ K). Among the *ca.* 79% of the $Fe^{II}$ centres that are SCO-active in $\mathbf{1^{Pd}\cdot 0.25EtOH}$, *ca.* 47% undergo the spin transition in the first step and *ca.* 32% in the second step. As shown by TGA (Fig. S1e, f and S11b†), the differences in the SCO properties between $\mathbf{1^{Pt}\cdot 0.4EtOH}$ and $\mathbf{1^{Pd}\cdot 0.25EtOH}$ are likely assignable to the lower effective quantity of ethanol present in the latter (0.4 *vs.* 0.25, respectively).

The SCO properties of $\mathbf{1^{Pt}}$, $\mathbf{1^{Pd}}$, $\mathbf{1^{Pt}\cdot H_2O}$, $\mathbf{1^{Pd}\cdot H_2O}$, $\mathbf{1^{Pt}\cdot 0.5MeOH}$ and $\mathbf{1^{Pd}\cdot 0.5MeOH}$ were also monitored through differential scanning calorimetry (DSC) at 10 K min$^{-1}$. $\mathbf{1^{Pt}\cdot 0.4EtOH}$ and $\mathbf{1^{Pd}\cdot 0.25EtOH}$ were not analysed by this technique since their corresponding spin transitions are out of the temperature window of our calorimeter. As depicted in Fig. S12,† DSC measurements reproduce very well the SCO behaviour observed for the different samples in the magnetic studies. For example, calorimetric curves of dehydrated ($\mathbf{1^{M}}$) and hydrated ($\mathbf{1^{M}\cdot H_2O}$) compounds show one and two singularities during both the heating and cooling modes confirming single and double stepped SCO behaviours, respectively. In addition, the $\Delta H/\Delta S$ (kJ mol$^{-1}$/J K$^{-1}$ mol$^{-1}$) parameters are 14.63/74.86, 18.06/82.32, 17.49/88.14 and 16.49/86.52 for $\mathbf{1^{Pt}}$, $\mathbf{1^{Pd}}$, $\mathbf{1^{Pt}\cdot H_2O}$ and $\mathbf{1^{Pd}\cdot H_2O}$, respectively, in good agreement with the values typically displayed by Hofmann-like $Fe^{II}$ compounds featuring cooperative and complete SCO behaviours.[4a] In contrast, $\mathbf{1^{Pt}\cdot 0.5MeOH}$ and $\mathbf{1^{Pd}\cdot 0.5MeOH}$ solvates present $\Delta H/\Delta S$ (kJ mol$^{-1}$/J K$^{-1}$ mol$^{-1}$) values of 7.64/40.09 and 7.10/41.40 consistent with a *ca.* 50% blocking of the spin transition as detected in the corresponding magnetic measurements.

## Discussion

The adsorption isotherms indicate different sorption capabilities for $\mathbf{1^{Pt}}$ and $\mathbf{1^{Pd}}$ derivatives. Indeed, under the same conditions, $\mathbf{1^{Pt}}$ adsorbs a higher amount of guest and with faster kinetics than $\mathbf{1^{Pd}}$ (see Fig. 4, S4 and Table S3†). It is worth mentioning that $\mathbf{1^{Pt}}$ and $\mathbf{1^{Pd}}$ desolvated forms do not present intrinsic porosity and, therefore, the uptake process occurs concomitantly to noticeable structural modifications which enable the entry of guests giving place to a gate-opening adsorption mechanism. Although related phenomena have been reported for 0D[25] and 1D[26] Co(II) SCO systems, the lack of precise structural data associated to the uptake processes prevented direct information about its origin. Kitagawa et *al.* showed a gate-opening effect on 2D nanometric thin films of {Fe(Pyridine)$_2$[Pt(CN)$_4$]} revealing that, upon adsorption, the guest molecules are hosted by inducing separation between the stacked 2D layers.[27] In contrast to the latter related example, our results here described disclose that the mechanism of structural reaccommodation upon guest sorption/desorption involves a 180° rotation of 50% of the 5-$NH_2$Pym axial ligands which seems to facilitate the diffusion of the guest throughout the channels. Similar "revolving door" effect has been observed in discrete[28] and 1D[29] SCO systems. Another relevant structural change accompanying the guest uptake involves breaking the N6···N7 H-bond operating between the amino group and the

Open Access Article. Published on 22 September 2020. Downloaded on 11/12/2021 10:39:38 AM.
This article is licensed under a Creative Commons Attribution 3.0 Unported Licence.

non-coordinated nitrogen of adjacent 5-$NH_2$Pym ligands (Fig. 5). Once the energy barrier of this rupture process is overcome the adsorption occurs in a cooperative one-step fashion revealing the gate-opening nature. Thus, the rupture of this interaction may determine the adsorption profile for each derivative. As a consequence, the slower adsorption regime of $\mathbf{1^{Pd}}$ with respect to $\mathbf{1^{Pt}}$ may be attributed to the stronger N6⋯N7 H-bond interaction of the former (Table 1). Furthermore, the accessible pore volumes calculated with PLATON for the corresponding $\mathbf{1^{M}}\cdot$**guest** structures (Table S6†) are slightly higher for Pt than for Pd derivatives, which probably facilitates the uptake and dissemination of guest molecules within the former.

The insertion of hydroxylic guest molecules in $\mathbf{1^{M}}$ promotes different degrees of local distortion in the 2D framework, which are responsible for the formation of non-equivalent $Fe^{II}$ and $M^{II}$ ($M^{II}$ = Pt, Pd) centres. The unsolvated $\mathbf{1^{M}}$ derivatives, constituted of homogeneously corrugated 2D layers with a minimum degree of distortion (maximum symmetry), feature only one crystallographic $Fe^{II}$ (and $M^{II}$) site and show the occurrence of similar one-step complete cooperative SCO for $M^{II}$ = Pt, Pd derivatives. In contrast, the inclusion of water distorts the layers generating two different centrosymmetric $Fe^{II}$ sites in $\mathbf{1^{M}\cdot H_2O}$ with different degrees of octahedral $\Sigma$ and $\Theta$ distortions (see Table 2). The less distorted Fe1 site is more prone to exhibit SCO than that of Fe2 giving rise to the stabilization of an ordered intermediate mixed spin state ⋯LS(Fe1)–HS(Fe2)–LS(Fe1)⋯. The inclusion of MeOH or EtOH provokes further asymmetry in the $\mathbf{1^{M}\cdot 0.5MeOH}$ and $\mathbf{1^{Pt}\cdot 0.4EtOH}$ layers reflected on the occurrence of two crystallograpically different $[M(CN)_4]^{2-}$ centres and the loss of centrosymmetry in the Fe1 and Fe2 sites. Consequently, the SCO conversion occurs at lower temperatures involving essentially 50% of the $Fe^{II}$ centres. Although the down-shift of the $T_c$ parallels the increase of the guest size, the electronic factors may also play an important role (*vide infra*). Surprisingly, the Fe1 site, which undergoes SCO first in $\mathbf{1^{M}\cdot H_2O}$, remains HS in $\mathbf{1^{M}\cdot 0.5MeOH}$/$\mathbf{1^{Pt}\cdot 0.4EtOH}$ even at 100 K, in spite of being surrounded by a less distorted octahedron (Table 2). However, the Fe2 site is SCO-active observing a complete HS → LS transition. In fact, pressure experiments carried out over $\mathbf{1^{Pt}\cdot 0.5MeOH}$ demonstrate that whereas the $T_c$ value of the Fe2 centre increases markedly with pressure, the pressure dependence of the SCO experienced by the Fe1 site is more moderate being almost complete only with pressures above 1.76 KBar (Fig. S13†). This singular situation can be associated with the fact that the oxygen atom of water and alcohol guests occupy different specific sites within the interlayer channels (Fig. 7). Indeed, the arrangement of methanol and ethanol molecules in the cavities tends to optimize the attractive interactions (H-bond) and minimize the repulsive contacts between the aliphatic part of the alcohol and the host network. Therefore, the water and the alcohol molecules display differences in the H-bond distances with the host 5-$NH_2$Pym ligands (Table 1). More precisely, the methanol and ethanol molecules afford stronger H-bonds (shorter distances) than the water molecule with the non-coordinated N2 atom of the pyrimidine moiety, which is directly connected to the Fe1 sites. This fact explains the higher affinity to alcohols suggested by the adsorption isotherms, time-dependent TGAs and the hysteretic behaviour defined by their desorption isotherms. Since this H-bond withdraws electron density from the pyrimidine ring, it is reasonable to infer a decrease of the ligand field strength around the Fe1 sites "deactivating" the SCO. Furthermore, there are additional steric reasons involving contacts between the C atom(s) of the MeOH/EtOH and the pyrimidine ring coordinated to Fe1 [C(EtOH/MeOH)⋯C4(pym) and C(EtOH/MeOH)⋯N2(pym)] whose distances, shorter than the sum of the corresponding van der Waals radii, may also hamper the complete HS → LS transition stabilizing the mixed ⋯LS(Fe2)–HS(Fe1)–LS(Fe2)⋯ states. It is worthwhile emphasizing that the SCO behaviour of [$Fe2N_6$] site remains mostly unaltered presenting very similar SCO temperatures when interacting with water or methanol, however, they decrease markedly with ethanol. In the case of $\mathbf{1^{Pd}\cdot 0.25EtOH}$, the low quantity of adsorbed ethanol seems to affect only a small fraction of $Fe^{II}$ sites (*ca.* 32%) lowering their SCO temperature whereas the most part of the

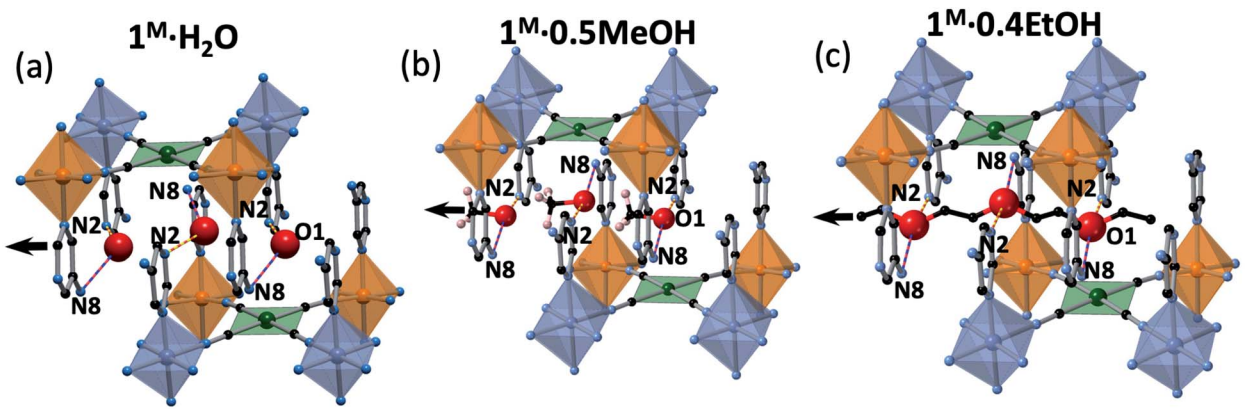


Fig. 7 View of a fragment of two consecutive layers emphasising the specific sites occupied by the guests, (a) $H_2O$, (b) MeOH and (c) EtOH, within the 1D channels which follow the orientation indicated by the black arrow. Hydrogen bonds are marked as bicolour blue-red lines for N8⋯O1 and yellow-red for N2⋯O1. Atom colour code: Fe1 (blue octahedrons), Fe2 (orange octahedrons), N (blue), M (green), C (black). Note that one out of two possible positions found for the MeOH is shown.

 This journal is © The Royal Society of Chemistry 2020

Open Access Article. Published on 22 September 2020. Downloaded on 11/12/2021 10:39:38 AM. This article is licensed under a Creative Commons Attribution 3.0 Unported Licence.

$Fe^{II}$ sites (47%) exhibit SCO temperatures reminiscent of the $\mathbf{1^{Pd}}$ unsolvated compound. This situation is reflected when observing the powder X-ray diffraction of $\mathbf{1^{Pd}\cdot 0.25EtOH}$ soaked in ethanol, as the main intense peaks are those corresponding to the "empty" compound whereas only some less intense peaks correspond to the ethanol containing clathrate (Fig. S14†).

Finally, in order to qualitatively assess the selectivity properties of $\mathbf{1^M}$ against the adsorption of $H_2O$, MeOH and EtOH, freshly dehydrated $\mathbf{1^M}\cdot H_2O$ samples were immersed overnight in solvent mixtures of $H_2O$ : MeOH, MeOH : EtOH or $H_2O$ : EtOH (1 : 1 in volume) and the SCO properties of the yielded solvates measured in the SQUID magnetometer. The results show that when soaking $\mathbf{1^M}$ either in $H_2O$ : MeOH or MeOH : EtOH mixtures the recorded SCO curves are reminiscent of those of $\mathbf{1^M\cdot 0.5MeOH}$ (Fig. S15†) indicating a higher tendency to adsorb MeOH over the other molecules. On the other hand, the magnetic properties of $\mathbf{1^M}$, recorded after being soaked in $H_2O$ : EtOH mixtures, display 2-stepped SCO profiles characteristic of $\mathbf{1^M\cdot H_2O}$ derivatives (Fig. S15†) suggesting that water molecules have been mostly adsorbed in this case. These results are in good agreement with that expected from the adsorption isotherms and X-ray diffraction data which predict higher chemical affinity to MeOH than $H_2O$ and higher selectivity of $H_2O$/MeOH against EtOH. The former observation may be associated to the stronger host–guest interactions stablished with MeOH whereas the latter can be interpreted as a molecular size-based exclusion in which the adsorption of the larger EtOH molecules is hampered by steric effects. Overall, the adsorption selectivity showed by $\mathbf{1^M}$ follows the tendency MeOH > $H_2O$ > EtOH.

## Conclusions

In conclusion, SCSC transformations in the new family of 2D HCPs formulated $\{Fe(5\text{-}NH_2Pym)_2[M^{II}(CN)_4]\}\cdot G$ ($\mathbf{1^M\cdot G}$, M = Pt or Pd, G = $H_2O$, MeOH or EtOH) have revealed reversible and controllable guest-dependent structural transformations coupled to drastic SCO changes. The dual donor–acceptor nature of the 5-$NH_2$Pym axial ligands affords a singular array of intra-layer H-bond interactions. In the guest-free $\mathbf{1^M}$ derivative, these interactions involve 50% of the amino groups and non-coordinated N atoms of the 5-$NH_2$Pym ligands coordinated to adjacent [$FeN_6$] sites, thereby conferring strong undulation to the layered structure. The remaining 50% of $NH_2$/N(pym) pairs, structurally disabled to define mutual H-bonds, generate functionalized void spaces potentially suitable for small ROH hydroxylic solvents. Indeed, exposition of the essentially non-porous $\mathbf{1^M}$ derivatives to $H_2O$, MeOH or EtOH induces a gate-opening adsorption mechanism which involves important structural reorganizations including 180° rotation of the 5-$NH_2$Pym ligands, flattening of the layers and creation of host–guest H-bonds facilitating the migration of the trapped molecules. Importantly, the adsorption capabilities of $\mathbf{1^M}$ depend not only on the nature of the guest molecule and that of the host framework (M = Pt or Pd) conferring selectivity properties to the system, but also on their reciprocal interactions. These mutual interactions in turn affect the $Fe^{II}$ environments and determine varying and predictable SCO behaviours. The interplay between SCO and gate-opening adsorption, together with their likely suitability to be processed as nanometric thin films, as other related compounds,[21,27,30] evidence the potential of the reported 2D amino-functionalized HCPs for sensing and/or gas separation applications.

## Conflicts of interest

There are no conflicts to declare.

## Acknowledgements

This work was supported by the Spanish Ministerio de Economia y Competitividad (MINECO)/Ministerio de Ciencia (MICINN) e Innovación FEDER (CTQ2016-78341-P/PID2019-106147GB-I00), Unidad de Excelencia Maria de Maeztu (MDM-2015-0538-18-2, CEX2019-000919-M), and the Generalitat Valenciana through PROMETEO/2016/147. R. T.-C. thanks MINECO for a predoctoral (FPI) grant. The gas analyzer used in this work was financed by the EU (ERC Stg Chem-fs-MOF 714122).

## Notes and references

1 (*a*) E. König, *Struct. Bond. (Berlin)*, 1991, **76**, 51–152; (*b*) P. Gütlich, A. Hauser and H. Spiering, *Angew. Chem., Int. Ed.*, 1994, **33**, 2024–2054; (*c*) J. A. Real, A. B. Gaspar, V. Niel and M. C. Muñoz, *Coord. Chem. Rev.*, 2003, **236**, 121–141; (*d*) P. Gütlich and G. Goodwin, Spin crossover in transition metal compound I-III, *Top. Curr. Chem.*, 2004, 233–235.

2 J. A. Real, A. B. Gaspar and M. C. Muñoz, *Dalton Trans.*, 2005, 2062–2079.

3 P. Gütlich, V. Ksenofontov and A. B. Gaspar, *Coord. Chem. Rev.*, 2005, **249**, 1811–1829.

4 (*a*) S. Decurtins, P. Gütlich, P. C. Köhler, H. Spiering and A. Hauser, *Chem. Phys. Lett.*, 1984, **105**, 1–4; (*b*) A. Hauser, *Coord. Chem. Rev.*, 1991, **111**, 275–290.

5 C. Lefter, R. Tan, J. Dugay, S. Tricard, G. Molnár, L. Salmon, J. Carrey, W. Nicolazzi, A. Rotaru and A. Bousseksou, *Chem. Phys. Lett.*, 2016, **644**, 138–141.

6 (*a*) M. C. Muñoz and J. A. Real, *Coord. Chem. Rev.*, 2011, **255**, 2068–2093; (*b*) Z.-P. Ni, J.-L. Liu, Md. N. Hoque, W. Liu, J.-Y. Li, Y.-C. Chen and M.-L. Tong, *Coord. Chem. Rev.*, 2017, **335**, 28–43; (*c*) R. Ohtani and S. Hayami, *Chem.–Eur. J.*, 2017, **23**, 2236–2248.

7 (*a*) M. D. Manrique-Juárez, S. Rat, L. Salmon, G. Molnár, C. M. Quintero, L. Nicu, H. J. Shepherd and A. Bousseksou, *Coord. Chem. Rev.*, 2016, **308**, 395–408; (*b*) K. S. Kumar and M. Ruben, *Angew. Chem., Int. Ed.* DOI: 10.1002/ange.201911256.

8 (*a*) M. Meneses-Sánchez, L. Piñeiro-López, T. Delgado, C. Bartual-Murgui, M. C. Muñoz, P. Chakraborty and J. A. Real, *J. Mater. Chem. C*, 2020, **8**, 1623–1633; (*b*) T. Delgado, M. Meneses-Sánchez, L. Piñeiro-López, C. Bartual-Murgui, M. C. Muñoz and J. A. Real, *Chem. Sci.*, 2018, **9**, 8446–8452; (*c*) B. Benaicha, K. Van Do, A. Yangui,

Open Access Article. Published on 22 September 2020. Downloaded on 11/12/2021 10:39:38 AM.
This article is licensed under a Creative Commons Attribution 3.0 Unported Licence.

N. Pittala, A. Lusson, M. Sy, G. Bouchez, H. Fourati, C. J. Gómez-García, S. Triki and K. Boukheddaden, *Chem. Sci.*, 2019, **10**, 6791–6798; (*d*) C. Lochenie, K. Schötz, F. Panzer, H. Kurz, B. Maier, F. Puchtler, S. Agarwal, A. Kö and B. Weber, *J. Am. Chem. Soc.*, 2018, **140**, 700–709; (*e*) C.-F. Wang, R.-F. Li, X.-Y. Chen, R.-J. Wei, L.-S. Zheng and J. Tao, *Angew. Chem., Int. Ed.*, 2015, **54**, 1574–1577.

9 O. Sato, Z.-Y. Li, Z.-S. Yao, S. Kang and S. Kanegawa, in *Spin-Crossover Materials*, John Wiley & Sons Ltd, 2013, pp. 303–319.

10 (*a*) L. Piñeiro-López, M. Seredyuk, M. C. Muñoz and J. A. Real, *Eur. J. Inorg. Chem.*, 2020, 764–799; (*b*) J. -Y. Li, Y. C. Chen, Z. -M. Zhang, W. Liu, Z. -P. Ni and M. -L. Tong, *Chem.–Eur. J.*, 2015, **21**, 1645–1651; (*c*) J.-Y. Li, Z. Yan, Z.-P. Ni, Z.-M. Zhang, Y.-C. Chen, W. Liu and M.-L. Tong, *Inorg. Chem.*, 2014, **53**(8), 4039–4046; (*d*) C. Bartual-Murgui, N. A. Ortega-Villar, H. J. Shepherd, M. C. Muñoz, L. Salmon, G. Molnár, A. Bousseksou and J. Antonio Real, *J. Mater. Chem.*, 2011, **21**, 7217–7222.

11 J. A. Real, E. Andrés, M. C. Muñoz, M. Julve, T. Granier, A. Bousseksou and F. Varret, *Science*, 1995, **268**, 265–267.

12 G. J. Halder, C. J. Kepert, B. Moubaraki, K. S. Murray and J. D. Cashion, *Science*, 2002, **298**, 1762–1765.

13 Y. Garcia, V. Niel, M. C. Munoz and J. A. Real, *Top. Curr. Chem.*, 2004, **233**, 229–257.

14 K. Otsubo, T. Haraguchi and H. Kitagawa, *Coord. Chem. Rev.*, 2017, **346**, 123–138.

15 (*a*) Z.-P. Ni, J.-L. Liu, Md. N. Hoque, W. Liu, J.-Y. Li, Y.-C. Chen and M.-L. Tong, *Coord. Chem. Rev.*, 2017, **335**, 28–43; (*b*) R. Ohtani and S. Hayami, *Chem.–Eur. J.*, 2017, **23**, 2236–2248.

16 M. Ohba, K. Yoneda, G. Agustí, M. C. Muñoz, A. B. Gaspar, J. A. Real, M. Yamasaki, H. Ando, Y. Nakao, S. Sakaki and S. Kitagawa, *Angew. Chem., Int. Ed.*, 2009, **48**, 4767–4771.

17 C. Bartual-Murgui, A. Akou, H. J. Shepherd, G. Molnar, J. A. Real, L. Salmon and A. Bousseksou, *Chem.–Eur. J.*, 2013, **19**, 15036–15043.

18 (*a*) K. A. Zenere, S. G. Duyker, E. Trzop, E. Collet, B. Chan, P. W. Doheny, C. J. Kepert and S. M. Neville, *Chem. Sci.*, 2018, **9**, 5623; (*b*) M. M. Ndiaye, S. Pillet, E.-E. Bendeif, M. Marchivie, G. Chastanet, K. Boukheddaden and S. Triki, *Eur. J. Inorg. Chem.*, 2018, 305–313; (*c*) N. F. Sciortino, F. Ragon, Y. M. Klein, C. E. Housecroft, C. G. Davies, G. N. L. Jameson, G. Chastanet and S. M. Neville, *Inorg. Chem.*, 2018, **57**, 11068–11076; (*d*) N. F. Sciortino, K. A. Zenere, M. E. Corrigan, G. J. Halder, G. Chastanet, J.-F. Létard, C. J. Kepert and S. M. Neville, *Chem. Sci.*, 2017, **8**, 701; (*e*) M. J. Murphy, K. A. Zenere, F. Ragon, P. D. Southon, C. J. Kepert and S. M. Neville, *J. Am. Chem. Soc.*, 2017, **139**, 1330–1335; (*f*) E. Milin, V. Patinec, S. Triki, E.-E. Bendeif, S. Pillet, M. Marchivie, G. Chastanet and K. Boukheddaden, *Inorg. Chem.*, 2016, **55**, 11652–11661; (*g*) N. F. Sciortino, F. Ragon, K. A. Zenere, P. D. Southon, G. J. Halder, K. W. Chapman, L. Piñeiro-Lopez, J. A. Real, C. J. Kepert and S. M. Neville, *Inorg. Chem.*, 2016, **55**, 10490–10498; (*h*) Y. M. Klein, N. F. Sciortino, F. Ragon, C. E. Housecroft, C. J. Kepert and S. M. Neville, *Chem. Commun.*, 2014, **50**, 3838–3840.

19 (*a*) F.-L. Liu and J. Tao, *Chem.–Eur. J.*, 2017, **23**, 18252–18257; (*b*) W. Liu, Y.-Y. Peng, S.-G. Wu, Y.-C. Chen, Md. N. Hoque, Z.-P. Ni, X.-M. Chen and M.-L. Tong, *Angew. Chem., Int. Ed.*, 2017, **56**, 14982–14986; (*c*) J. E. Clements, J. R. Price, S. M. Neville and C. J. Kepert, *Angew. Chem., Int. Ed.*, 2016, **55**, 15105–15109; (*d*) N. F. Sciortino, K. R. Scherl-Gruenwald, G. Chastanet, G. J. Halder, K. W. Chapman, J.-F. Létard and C. J. Kepert, *Angew. Chem., Int. Ed.*, 2012, **124**, 10301–10305; (*e*) G. J. Halder, K. W. Chapman, S. M. Neville, B. Moubaraki, K. S. Murray, J.-F. Létard and C. J. Kepert, *J. Am. Chem. Soc.*, 2008, **130**(51), 17552–17562.

20 W. Liu, L. Wang, Y.-J. Su, Y.-C. Chen, J. Tucek, R. Zboril, Z.-P. Ni and M.-L. Tong, *Inorg. Chem.*, 2015, **54**, 8711–8716.

21 C. Bartual-Murgui, V. Rubio-Giménez, M. Meneses-Sánchez, F. J. Valverde-Muñoz, S. Tatay, C. Martí-Gastaldo, M. C. Muñoz and J. A. Real, *ACS Appl. Mater. Interfaces*, 2020, **12**(26), 29461–29472.

22 Q.-Y. Yang, P. Lama, S. Sen, M. Lusi, K.-J. Chen, W.-Y. Gao, M. Shivanna, T. Pham, N. Hosono, S. Kusaka, J. J. Perry, S. Ma, B. Space, L. J. Barbour, S. Kitagawa and M. J. Zaworotko, *Angew. Chem., Int. Ed.*, 2018, **57**, 5684–5689.

23 S. Horike, D. Tanaka, K. Nakagawa and S. Kitagawa, *Chem. Commun.*, 2007, 3395–3397.

24 M. Avrami, *J. Chem. Phys.*, 1939, **7**, 1103–1112.

25 M. Nakaya, W. Kosaka, H. Miyasaka, Y. Komatsumaru, S. Kawaguchi, K. Sugimoto, Y. Zhang, M. Nakamura, L. F. Lindoy and S. Hayami, *Angew. Chem., Int. Ed.*, 2020, **59**, 10658–10665.

26 R. Ohtani, K. Shimayama, A. Mishima, M. Ohba, R. Ishikawa, S. Kawata, M. Nakamura, L. F. Lindoy and S. Hayami, *J. Mater. Chem. C*, 2015, **3**, 7865–7869.

27 S. Sakaida, K. Otsubo, O. Sakata, C. Song, A. Fujiwara, M. Takata and H. Kitagawa, *Nat. Chem.*, 2016, **8**, 377–383.

28 L. A. Barrios, C. Bartual-Murgui, E. Peyrecave-Lleixà, B. Le Guennic, S. J. Teat, O. Roubeau and G. Aromí, *Inorg. Chem.*, 2016, **55**, 4110–4116.

29 E. Coronado, M. Giménez-Marqués, G. Mínguez Espallargas, F. Rey and I. J. Vitórica-Yrezábal, *J. Am. Chem. Soc.*, 2013, **135**, 15986–15989.

30 (*a*) V. Rubio-Giménez, C. Bartual-Murgui, M. Galbiati, A. Núñez-López, J. Castells-Gil, B. Quinard, P. Seneor, E. Otero, P. Ohresser, A. Cantarero, E. Coronado, J. A. Real, R. Mattana, S. Tatay and C. Martí-Gastaldo, *Chem. Sci.*, 2019, **10**, 4038–4047; (*b*) V. Rubio-Giménez, G. Escorcia-Ariza, C. Bartual-Murgui, C. Sternemann, M. Galbiati, J. Castells-Gil, J. A. Real, S. Tatay and C. Martí-Gastaldo, *Chem. Mater.*, 2019, **31**, 7277–7728.

 This journal is © The Royal Society of Chemistry 2020

Inorganic Chemistry

pubs.acs.org/IC Article

# Bistable Hofmann-Type $Fe^{II}$ Spin-Crossover Two-Dimensional Polymers of 4-Alkyldisulfanylpyridine for Prospective Grafting of Monolayers on Metallic Surfaces

Rubén Turo-Cortés, Francisco Javier Valverde-Muñoz,* Manuel Meneses-Sánchez, M. Carmen Muñoz, Carlos Bartual-Murgui, and José Antonio Real*

Cite This: *Inorg. Chem.* 2021, 60, 9040−9049 Read Online

ACCESS | Metrics & More | Article Recommendations | Supporting Information

**ABSTRACT:** Aiming at investigating the suitability of Hofmann-type two-dimensional (2D) coordination polymers $\{Fe^{II}(L_{ax})_2[M^{II}(CN)_4]\}$ to be processed as single monolayers and probed as spin crossover (SCO) junctions in spintronic devices, the synthesis and characterization of the $M^{II}$ derivatives ($M^{II}$ = Pd and Pt) with sulfur-rich axial ligands ($L_{ax}$ = 4-methyl- and 4-ethyl-disulfanylpyridine) have been conducted. The thermal dependence of the magnetic and calorimetric properties confirmed the occurrence of strong cooperative SCO behavior in the temperature interval of 100−225 K, featuring hysteresis loops 44 and 32.5 K/21 K wide for $Pt^{II}$-methyl and $Pt^{II}/Pd^{II}$-ethyl derivatives, while the $Pd^{II}$-methyl derivative undergoes a much less cooperative multistep SCO. Excluding $Pt^{II}$-methyl, the remaining compounds display light-induced excited spin-state trapping at 10 K with $T_{LIESST}$ temperatures in the range of 50−70 K. Single-crystal studies performed in the temperature interval 100−250 K confirmed the layered structure and the occurrence of complete transformation between the high- and low-spin states of the $Fe^{II}$ center for the four compounds. Strong positional disorder seems to be the source of elastic frustration driving the multistep SCO observed for the $Pd^{II}$-methyl derivative. It is expected that the peripheral disulfanyl groups will favor anchoring and growing of the monolayer on gold substrates and optimal electron transport in the device.

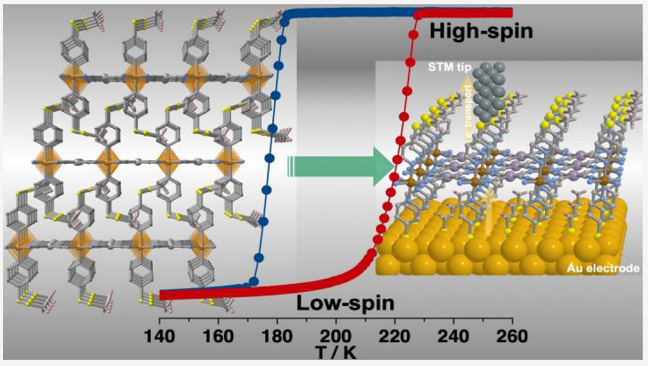


## INTRODUCTION

Bistable molecular materials with switchable properties are appealing candidates for developing technological applications, e.g., sensors for information storage. Iron(II) spin crossover (SCO) complexes afford excellent examples of molecular bistability, because they reversibly switch between the high-spin (HS, $t_{2g}^4e_g^2$) and low-spin (LS, $t_{2g}^6e_g^0$) electronic states in response to a variety of external stimuli such as temperature, pressure, light, adsorption of analytes or extrinsic phase transitions. This is particularly true when the spin changing centers are strongly coupled to each other, since the spin state change manifests cooperatively conferring hysteretic behavior (memory effect) to the magnetic, optical, structural, mechanical, and electric properties associated with the material.[1]

The SCO research is a very active and multidisciplinary field that spreads in many complementary directions. The synthesis and characterization of interesting mononuclear, polynuclear, and one-dimensional to three-dimensional (1D−3D) polymeric SCO systems has increased exponentially during the last two decades, affording new SCO behaviors[2] which, in turn, have inspired new sophisticated physical techniques and theoretical models.[1e,3] To engineer new multifunctional materials where the SCO synchronically interplays with other relevant physicochemical properties—e.g., porosity (host−guest chemistry), liquid crystalline properties, crystal-to-crystal phase transitions, luminescence or chirality—in a synergetic fashion in the same crystal is one of the fundamental goals in the field. This requires a rational design of the synthesis at macroscopic scale and precise control of essential elusive SCO parameters, such as critical temperature ($T_{1/2}$), abruptness, hysteresis width, and completeness. Relevant achievements of this strategy include the combination of SCO and nonlinear optical properties,[4] electronic conduction,[5] electroluminescence,[6] fluorescence,[7] liquid-crystalline properties,[8] porosity,[2d,g] molecular recognition,[9] photoswitchable magnets,[10] chirality,[11] room-temperature photoisomers and reactions,[12]

Received: April 1, 2021
Published: May 28, 2021

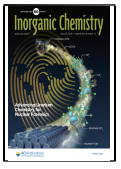

Downloaded via UNIV DE VALENCIA on January 10, 2022 at 14:57:47 (UTC).
See https://pubs.acs.org/sharingguidelines for options on how to legitimately share published articles.


© 2021 American Chemical Society

https://doi.org/10.1021/acs.inorgchem.1c01010
*Inorg. Chem.* 2021, 60, 9040−9049

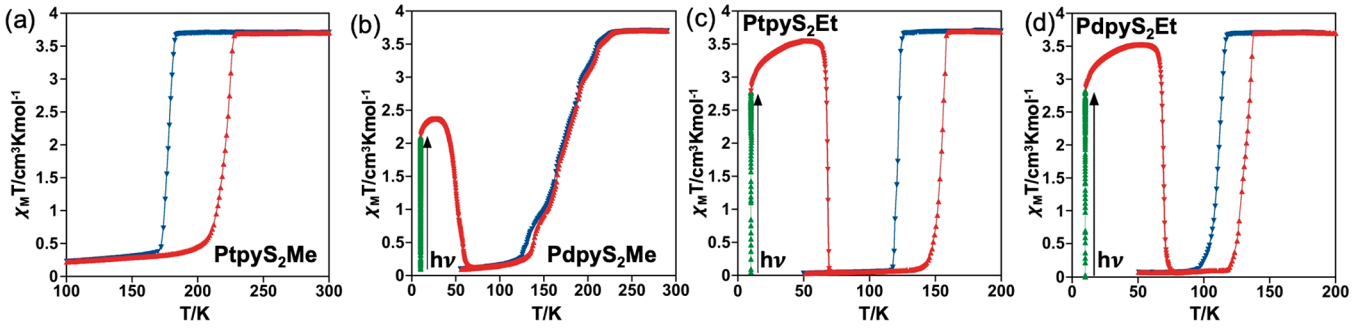


**Figure 1.** Magnetic and photomagnetic properties of **MpyS$_2$Me** (M = Pt (a), Pd (b)) and **MpyS$_2$Et** (M = Pt (c), Pd (d)). Cooling, heating and photoswitching processes are represented in blue, red, and green, respectively.

etc. The ultimate goal is the construction of sensing materials capable of acting as switchers in response to changes of ambient conditions (temperature, humidity, chemical contaminants, etc.). Furthermore, the potential implementation of SCO materials into electronic and spintronic devices is a new concept of paramount importance that has fuelled sophisticated studies aiming at controlling the electron transport (charge and spin) processing SCO materials as ultrathin films on surfaces.[13]

Two-dimensional (2D) Hofmann-type $Fe^{II}$ coordination polymers with general formula $\{Fe^{II}(L_{ax})_2[M^{II}(CN)_4]\}$ represent an important source of SCO compounds, where $M^{II}$ = $Pt^{II}$, $Pd^{II}$, or $Ni^{II}$ and $L_{ax}$ is a terminal monotopic axial ligand based on pyridine/pyridine-like[2d,14] and triazole rings.[15] The $Fe^{II}$ ions are equatorially connected through square-planar $[M^{II}(CN)_4]^{2-}$ anionic metalloligands affording robust infinite $[Fe^{II}[M^{II}(CN)_4]_\infty$ layers that are the origin of the cooperativity typically exhibited by these compounds. The layers stack on top each other interdigitating the axial ligands $L_{ax}$ whose nature (length, donor−acceptor substituents, etc.) plays an important role in the modulation of the cooperativity through changes in the interlayer spacing and flexibility of the layers (corrugation), factors that may influence the inclusion of guest molecules.

It has recently been shown that 2D Hofmann-type coordination polymers can be processed as ultrathin films under mild conditions (RT) by applying the layer-by-layer liquid phase epitaxy (LPE) methodology,[16−18] at variance of the homologous 3D derivatives, which require very low temperatures.[19−25] Processing of these materials as ultrathin films is a requirement to keep small electrode separation in vertical transport devices to ensure a functional current flow but, obviously, it can seriously compromise the SCO properties. For example, synchrotron XAS studies showed that, for film thicknesses above ca. 12 nm, the 2D coordination polymer $\{Fe^{II}(pyridine)_2[Pt^{II}(CN)_4]\}$ presents a cooperative SCO behavior similar to that observed for the microcrystalline sample.[17] However, below this threshold value, the cooperativity and completeness of the spin transition are exponentially attenuated since the films lose cohesion conferring to its structure a high degree of mosaicity constituted of practically unconnected nanoislands. The nature of the axial ligand and its dramatic influence on the coalescence of the thin film deposited on Au substrates has also been investigated for two new 2D Hofmann compounds $\{Fe^{II}(pyrimidine)_2[Pt^{II}(CN)_4]\}$ and $\{Fe^{II}(isoquinoline)_2[Pt^{II}(CN)_4]\}$, together with their transport properties.[18]

In the search for new $Fe^{II}$ Hofmann-type 2D coordination polymers, here, we report on the preparation, structural characterization, and spin crossover properties of four complexes generically formulated $\{Fe^{II}(pyS_2R)_2[M^{II}(CN)_4]\}_n$ (**MpyS$_2$R**, where $M^{II}$ = Pd, Pt and R = Me, Et), where the axial organic ligand $pyS_2R$ is 4-methyl/ethyldisulfanylpyridine (R = Me, Et). In contrast to the mentioned above multilayer studies based of the LPE technique, the axially coordinated pyridine ligand functionalized in 4-position with a reactive alkyldisulfanyl group opens the possibility to process the resulting 2D coordination polymers as robust single monolayer arrays of elastically coupled SCO centers deposited on suitable surfaces to be probed as SCO junctions. This approach was inspired by a relevant pioneer work by Mallouk et al. about the growth of thin films of the porous 3D Hofmann clathrate {Ni(4,4′-bipyridine)[Pt(CN)$_4$]} anchored through a monolayer of 4-pyridyl ethyldisulfide on gold substrates.[20] A similar strategy has recently led to the production of molecular monolayers prepared by simple immersion of the substrate in highly diluted solutions of mononuclear $Fe^{II}$ SCO complexes on gold substrates and successfully tested as spintronic devices.[26]

## RESULTS

**Synthesis.** All the samples **MpyS$_2$R** (where M = Pt, Pd and R = Me, Et) were prepared as single crystals from slow diffusion techniques in water−methanol solutions (see the Experimental Section). According to chemical and thermogravimetric analyses (see Figure S1 in the Supporting Information), the single crystals resulted to be unsolvated and decompose above 420 K.

**Spin Crossover Properties.** Figure 1 shows the magnetic and photomagnetic properties of the title compounds in the form of the product $\chi_M T$ vs $T$, where $\chi_M$ is the molar magnetic susceptibility and $T$ is the temperature. At 300 K, the $\chi_M T$ value is ca. 3.70 cm$^3$ K/mol for the four derivatives consistently with a fully populated HS state with a strong orbital contribution. Upon cooling at 1 K/min, $\chi_M T$ remains constant down to 183 K for **PtpyS$_2$Me** and decreases abruptly to 0.4 cm$^3$ K/mol in the interval 182−170 K, then decreases gradually to attain a value of 0.2 cm$^3$ K/mol at 100 K, where the LS state is practically fully populated. The profile of the $\chi_M T$ vs $T$ curve in the heating mode is similar to that of the cooling mode but shifted to high temperatures, defining a hysteresis loop $\Delta T$ = 44 K wide with the equilibrium temperatures, $T_{1/2}$, at which the populations of the HS and LS centers are equal at 0.5, equal to 180 K and 224 K for the cooling and heating branches, respectively. This strong cooperative SCO behavior contrasts drastically with that shown by the isostructural (vide infra) homologous **PdpyS$_2$Me** derivative. $\chi_M T$ = 3.70 cm$^3$ K/mol remains constant down to


https://doi.org/10.1021/acs.inorgchem.1c01010
Inorg. Chem. 2021, 60, 9040−9049

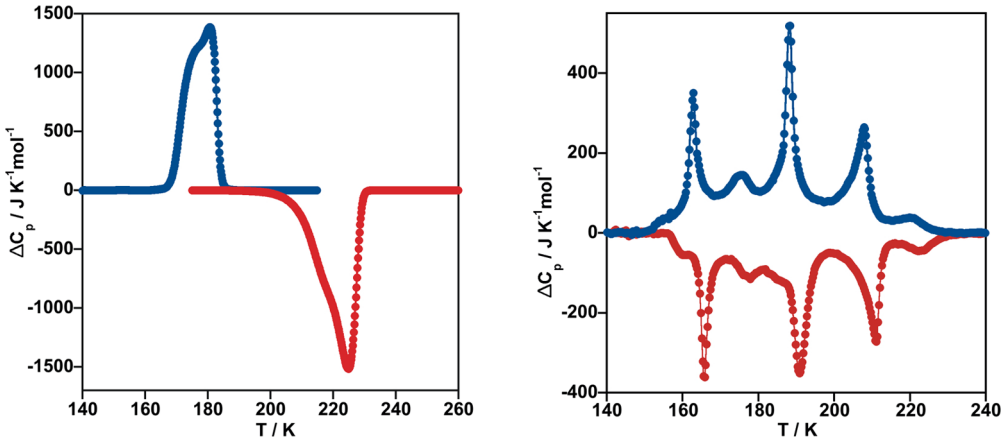


**Figure 2.** Thermal dependence of $\Delta C_p$ vs T for **PtpyS$_2$Me** (left) and **PdpyS$_2$Me** (right). Note that for the latter the step below 150 K could not be recorded (see text). Cooling and heating modes are represented in blue and red, respectively.

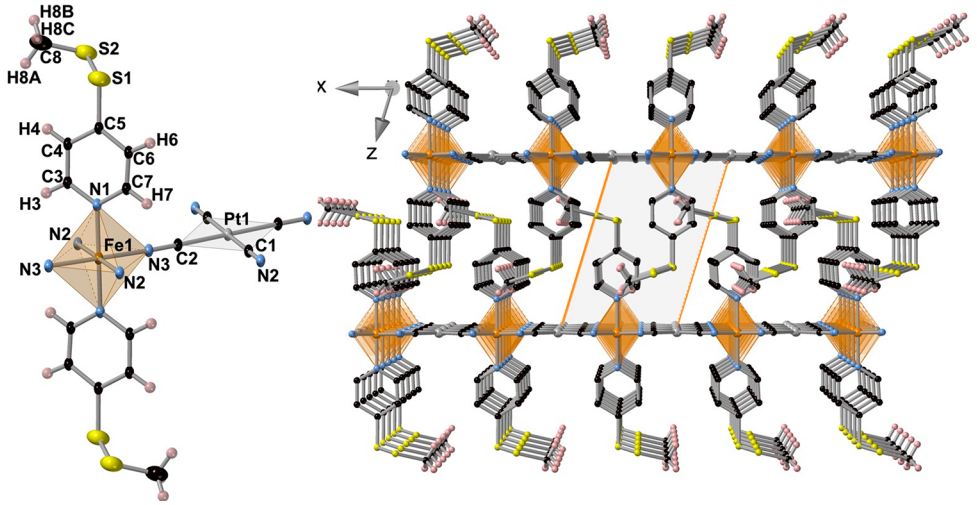


**Figure 3.** (Left) Molecular fragment of **PtpyS$_2$Me** showing the atom numbering of the asymmetric unit. (Right) Packing of two consecutive layers (only one of the two possible orientations of the −S−S−Me moiety is shown.

232 K; however, below this temperature, it decreases gradually in a succession of slightly marked steps, reaching a value of 0.15 cm$^3$ K/mol at 100 K. Except for the lower step, which shows a small hysteresis between 130 K and 138 K, the cooling−heating profiles are practically superposed. The corresponding characteristic $T_{1/2}$ temperature is 170 K. The SCO profile for the **MpyS$_2$Et** derivatives is similar to that of **PtpyS$_2$Me**, featuring strong cooperative hysteretic behaviors with $T_{1/2}$ temperatures 121.5 and 154.0 K ($\Delta T$ = 32.5 K) for M = Pt and 111.0 and 132.0 K ($\Delta T$ = 21.0 K) for M = Pd, in the cooling and heating modes, respectively.

Photogeneration of the fully populated metastable HS* state, the so-called "light-induced excited spin state trapping (LIESST) experiment",[27] was performed by irradiating microcrystalline samples of the title compounds with green light ($\lambda$ = 532 nm) at 10 K. Under these conditions, all the samples but **PtpyS$_2$Me** display the LIESST effect and saturate at $\chi_M T$ values of 2.08 cm$^3$ K/mol for **PdpyS$_2$Me** and 2.80 cm$^3$ K/mol for **MpyS$_2$Et** (M = Pt, Pd). Subsequently, the light was switched off and the temperature increased at a rate of 0.3 K/min inducing a gradual increase of $\chi_M T$ to a value of 2.36 cm$^3$ K/mol at 26 K for **PdpyS$_2$Me** and 3.54 cm$^3$ K/mol at ca. 48 K for **MpyS$_2$Et** (M = Pt, Pd), which corresponds to ca. 64% and 96% of the maximum value observed at 300 K, respectively. This increase in $\chi_M T$ reflects the thermal population of different microstates originated from the zero-field splitting of the HS* spin state. At higher temperatures, $\chi_M T$ decreases rapidly until joining the thermal SCO curve at ca. 65 K (**PdpyS$_2$Me**), 69 K (**PtpyS$_2$Et**), and 76 K(**PdpyS$_2$Et**), indicating that the metastable HS* state has relaxed back to the stable LS state. The corresponding $T_{LIESST}$ temperatures, evaluated as $\partial(\chi_M T)/\partial T$,[28] are 50.0 K (**PdpyS$_2$Me**) and 68−70 K (**MpyS$_2$Et**, M = Pt, Pd). These temperatures are consistent with the inverse-energy-gap law, i.e., the metastability of the photogenerated HS* species decreases as the stability of the LS increases, namely as $T_{1/2}$ increases.[29]

The SCO behavior was also investigated through the thermal dependence of the heat capacity at constant pressure, $\Delta C_p$, for **MpyS$_2$Me** (M = Pt, Pd) (Figure 2). The low SCO temperatures observed for both ethyl derivatives prevented us to evaluate their thermodynamic parameters. The average enthalpy $\Delta H$ and entropy variations $\Delta S$ (= $\Delta H/T_{1/2}$) are, respectively, 16.12 kJ/mol and 79.84 J/K mol for **PtpyS$_2$Me** and 7.68 kJ/mol and 45.18 J/K mol for **PdpyS$_2$Me**. The $\Delta H$ and $\Delta S$ values found for **PtpyS$_2$Me** are comparable to those reported for similar Hofmann-type coordination polymers with comparable cooperative SCO.[1b,2d] However, for **PdpyS$_2$Me** these values are considerably smaller due to the fact that ca.


https://doi.org/10.1021/acs.inorgchem.1c01010
Inorg. Chem. 2021, 60, 9040−9049

Table 1. Selected Bond Lengths and Angles for $MpyS_2Me$ (M = Pd, Pt)

| | $PdpyS_2Me$, 120 K | $PdpyS_2Me$, 250 K | $PtpyS_2Me$, 120 K | $PtpyS_2Me$, 250 K |
|---|---|---|---|---|
| **Selected Bond Lengths [Å]** | | | | |
| Fe−N(1) | 1.987(3) | 2.219(5) | 1.992(14) | 2.23(3) |
| Fe−N(2) | 1.942(3) | 2.132(4) | 1.943(14) | 2.13(2) |
| Fe−N(3) | 1.943(3) | 2.137(4) | 1.945(14) | 2.11(2) |
| Pd−C(1) | 1.991(3) | 1.991(4) | | |
| Pd−C(2) | 1.992(3) | 1.988(5) | | |
| Pt−C(1) | | | 1.975(17) | 1.97(2) |
| Pt−C(2) | | | 1.978(17) | 1.93(2) |
| C(1)−N(2) | 1.149(4) | 1.131(7) | 1.15(3) | 1.16(3) |
| C(2)−N(3) | 1.153(5) | 1.130(7) | 1.15(3) | 1.21(3) |
| **Selected Bond Angles (°)** | | | | |
| N(1)−Fe−N(2) | 90.06(12) | 90.1(2) | 90.7(6) | 91.6(11) |
| N(1)−Fe−N(3) | 90.13(12) | 90.0(2) | 90.5(6) | 91.0(11) |
| N(2)−Fe−N(3) | 90.01(10) | 90.04(14) | 91.0(6) | 90.2(6) |
| $\Sigma^{Fe}$ | 0.8 | 0.56 | 8.8 | 11.2 |
| C(1)−N(2)−Fe | 179.8(2) | 179.7(5) | 178(2) | 169(2) |
| C(2)−N(3)−Fe | 179.8(3) | 179.9(5) | 177(2) | 178(2) |

27% of the SCO occurs out of the temperature window of our calorimeter, an extrapolation to 100% gives $\Delta H$ = 10.5 kJ/mol and $\Delta S$ = 62 J/Kmol (see also Figure S2 in the Supporting Information). These extrapolated values are still smaller than those observed for **$PtpyS_2Me$** but consistent with the much less cooperative gradual SCO and lower $T_{1/2}$ temperature of the homologous Pd derivative. The $T_{1/2}$ values obtained from the calorimetric measures are virtually the same than those obtained from magnetism (see Figure S2). As it can be seen from Figure 2, the surprisingly distinct nature of both SCO behaviors, hysteretic versus multistepped, are clearly reflected in the $\Delta C_p$ vs $T$ plots.

**Single-Crystal Structure Analysis.** *Structure of* ***$MpyS_2Me$.*** The crystal structure of **$MpyS_2Me$** (M = Pt and Pd) was investigated at 120 and 250 K; it turned out to be isostructural and crystallized in the triclinic $P\bar{1}$ space group. A selection of relevant crystallographic data for **$MpyS_2Me$** (M = Pt, Pd) is given in Table S1 in the Supporting Information. At 120 K, the structure is characterized by a crystallographically unique $Fe^{II}$ site lying in an inversion center defining a slightly elongated $[Fe^{II}N_6]$ octahedron. A representative fragment of the structure including the atom numbering is shown in Figure 3 (left). Table 1 contains a selection of significant bond lengths and angles, together with the corresponding average angular distortion parameter $\Sigma^{Fe}$, which is defined as the sum of deviations from the ideal octahedron/tetrahedron of the 12 "cis" bond angles, $\sum_{12}^{i=1} |\theta_i - 90°|$. The equatorial positions are occupied by the N2 and N3 atoms of the CN groups belonging to the $[Pt^{II}(CN)_4]^{2-}$ bridging ligands, while the axial positions are occupied by the N1 atom of the pyridine group of the $pyS_2Me$ ligand. The average ⟨Fe−N⟩ bond length, 1.960(14) Å (M = Pt) and 1.957(3) Å (M = Pd), are typical of the $Fe^{II}$ site in the LS state and consistent with the magnetic data and the characteristic deep red color of the crystals at same temperature. The $\Sigma^{Fe}$ parameter, almost 0 for the Pd derivative and relatively much larger for the Pt derivative, denote that the angular distortion in both compounds is very small and practically independent of the spin state.

Each $Fe^{II}$ site is bridged to four equivalent $Fe^{II}$ sites through four equivalent square-planar $[Pt^{II}(CN)_4]^{2-}$ bridges defining 2D layers in which the equatorial planes of the $[Fe^{II}N_6]$ and $[Pt^{II}C_4]$ centers are strictly coplanar (Figure 3, right). Two consecutive layers interdigitate in such a way that the $pyS_2Me$ axial ligands of one layer point toward the center of the square windows of the adjacent layers, with the distance between the $\{Fe^{II}_2[M^{II}(CN)_4]_2\}_n$ layers being equal to 10.36 Å (M = Pt) and 10.75 Å (M = Pd). The S−S−$CH_3$ tails display positional disorder in two equivalent positions for the Pt derivative while the disorder is considerably more severe for the Pd derivative also involving the pyridine groups (see Figure S3 in the Supporting Information). At 250 K, the structures are essentially the same, being the most significant differences, with respect to those at 120 K, the increase of the ⟨Fe−N⟩ bond length by 0.2 Å and the change of color of the crystals to yellow. Both facts are perfectly consistent with the full population of the $Fe^{II}$ HS state in agreement with the magnetic data. In addition, the change to the HS state in the Pt derivative is accompanied by a small degree of corrugation. The angle defined between the equatorial $Fe^{II}N_4$ and the $[Pt^{II}(CN)_4]^{2-}$ square planes is 7.64°. Consistently, the Fe−N2−C1 angle decreases 9° from 178(2)° in the LS state until 169(2)° in the HS state. In addition, the separation of two consecutive $[Fe_2M_2]_n$ layers increases by 0.38 Å until 10.74 Å. In contrast, the layers remain perfectly flat for the Pd derivative while the separation between consecutive layers increases by 0.2 Å until 10.95 Å (see Figure S2).

*Structure of* ***$MpyS_2Et$.*** The crystal structures of **$MpyS_2Et$**, M = Pt and Pd, were investigated at 100 and 250 K turning out to be isostructural. At 100 K, the red crystals of both derivatives display a monoclinic $I2/m$ unit cell that changes to monoclinic $C2/m$ at 250 K, where the crystals are yellow (see Table S2). Table 2 contains a selection of significant bond lengths and angles including the angular distortion parameter $\Sigma^{Fe}$. The asymmetric unit contains one slightly distorted $[Fe^{II}N_6]$ octahedral site defined by two distinct $pyS_2Et$ axial ligands coordinated, respectively, via N1 and N2 and two distinct $[M(CN)_4]^{2-}$ groups coordinated, respectively, via N3 and N4 (Figure 4). The two pyridine rings of $pyS_2Et$ and the $Fe^{II}$ center lie in a reflection plane which bisects the equatorial N3−Fe−N3′ and N4−Fe−N4′ angles. At 100 K, the ⟨Fe−N⟩ is 1.961(5) and 1.968(4) Å for the Pt and Pd derivatives, respectively, are consistent with the $Fe^{II}$ centers in a fully populated LS state, whereas, at 250 K, these average bond lengths increase by 0.20−0.21 Å attaining typical values for the


https://doi.org/10.1021/acs.inorgchem.1c01010
Inorg. Chem. 2021, 60, 9040−9049

**Table 2. Selected Bond Lengths and Angles for $MpyS_2Et$ (M = Pd, Pt)**

| | $PdpyS_2Et$, 100 K | $PdpyS_2Et$, 250 K | $PtpyS_2Et$, 100 K | $PtpyS_2Et$, 250 K |
|---|---|---|---|---|
| **Selected Bond Lengths [Å]** | | | | |
| Fe−N(1) | 2.001(5) | 2.218(8) | 1.997(7) | 2.205(7) |
| Fe−N(2 | 2.017(5) | 2.237(9) | 2.004(6) | 2.202(9) |
| Fe−N(3) | 1.946(4) | 2.170(5) | 1.940(5) | 2.162(5) |
| Fe−N(4) | 1.948(4) | 2.140(5) | 1.944(5) | 2.133(5) |
| Pd(1)−C(1) | 1.992(4) | 1.987(7) | | |
| Pd(2)−C(2) | 2.003(5) | 2.005(6) | | |
| Pt(1)−C(1) | | | 1.981(5) | 1.987(5) |
| Pt(2)−C(2) | | | 1.989(5) | 1.993(5) |
| C(1)−N(3) | 1.146(5) | 1.145(8) | 1.160(7) | 1.142(6) |
| C(2)−N(4) | 1.146(5) | 1.126(8) | 1.159(7) | 1.141(7) |
| **Selected Bond Angles [°]** | | | | |
| N(1)−Fe−N(3) | 91.29(14) | 90.7(2) | 91.4(2) | 90.5(2) |
| N(1)−Fe−N(4) | 90.72(14) | 91.3(2) | 90.6(2) | 91.2(2) |
| N(2)−Fe−N(3) | 86.83(14) | 86.7(2) | 86.6(2) | 86.6(2) |
| N(2)−Fe−N(4) | 91.18(14) | 91.2(2) | 91.5(2) | 91.7(2) |
| N(3)−Fe−N(4) | 88.43(14) | 88.3(2) | 88.3(2) | 88.5(2) |
| N(3)−Fe−N(3) | 91.9(2) | 90.4(3) | 92.0(3) | 90.2(3) |
| N(4)−Fe−N(4) | 91.2(2) | 93.0(3) | 91.3(3) | 92.7(3) |
| Σ | 19.96 | 19.8 | 20.5 | 19.5 |
| C(1)−N(3)−Fe | 169.7(4) | 158.8(6) | 169.3(4) | 160.3(5) |
| C(2)−N(4)−Fe | 178.0(3) | 177.7(6) | 178.1(4) | 177.1(5) |

$Fe^{II}$ in the HS state [2.166(9) and 2.179(9) Å, respectively]. The $\Sigma^{Fe}$ parameter is small (~20°) and remains almost constant upon SCO. There are two crystallographically distinct $[M^{II}(CN)_4]^{2-}$ groups and two pairs of them connect each $Fe^{II}$ center to four equivalent atoms defining an irregularly corrugated layer. Indeed, at 100 K, the angle defined between the $[M1^{II}(CN)_4]^{2-}/[M2^{II}(CN)_4]^{2-}$ squares and the equatorial plane of the $Fe^{II}$ center is, respectively, 4.04°/4.24° and 20.47°/21.40° and increase by ca. 36% up to 6.22°−6.56° and 32.26°−35.82° for M = Pt/Pd at 250 K. The change of this angle occurs through the Fe−N3−C1, which decrease 10.9° (Pd) and 9° (Pt) when moving from the LS to the HS state. The separation between two consecutive the layers, measured from the average plane defined by M1 and M2, is very similar for the two derivatives and practically does not change with temperature (11.15−11.52 Å).

## DISCUSSION

Since the first SCO Hofmann type 2D coordination polymer $\{Fe^{II}(pyridine)_2[M^{II}(CN)_4]\}$, $M^{II}$ = Ni,[30] and its isostructural $Pd^{II}$ and $Pt^{II}$ counterparts[31] were reported, this family of compounds has been steadily growing until recently (see refs 2d, g, 14, 15, 18). Despite their high insolubility, their synthesis based on formal replacement of the axial pyridines with homologous N-donor ligands can be addressed in a straightforward manner to obtain samples constituted exclusively of single crystals by employing liquid−liquid slow diffusion techniques, which is the safest way to get pure samples with reliable SCO properties for this type of compounds. The strong cooperative SCO behavior featuring well-shaped symmetric hysteresis loops expressed by many of these compounds is likely the most appealing aspect, which explains the interest and growth of this family of compounds. This cooperativity seems to be originated mainly from the robust nature of the $\{Fe^{II}[M^{II}(CN)_4]\}_n$ layers where all SCO centers are strongly coupled. Indeed, most of the $[Fe^{II}(L)_2[M^{II}(CN)_4]$ compounds show hysteresis widths ranging in the interval of 10−30 K, but it has also been reported hysteresis close to 40 K[32a,18b] or even larger (50−65 K).[15g] It is reasonable to consider that the nature of the axial ligands and included guest molecules play an important role in the modulation of the observed cooperativity, however, this is a fact that generally has not obvious rationalization. In addition, it is also worth noting that the hysteresis width seems not to be correlated with the length of the axial ligand, namely, with the separation between the $\{Fe^{II}[M^{II}(CN)_4]\}_n$ layers. For example, interdigitation of the relatively long ligands L = 4-styrylpyridine ($n$ = 0.5) and 4-(2-phenylethyl)pyridine ($n$ = 0) in $[Fe^{II}(L)_2[Pt^{II}(CN)_4]\cdot n$MeOH separates the

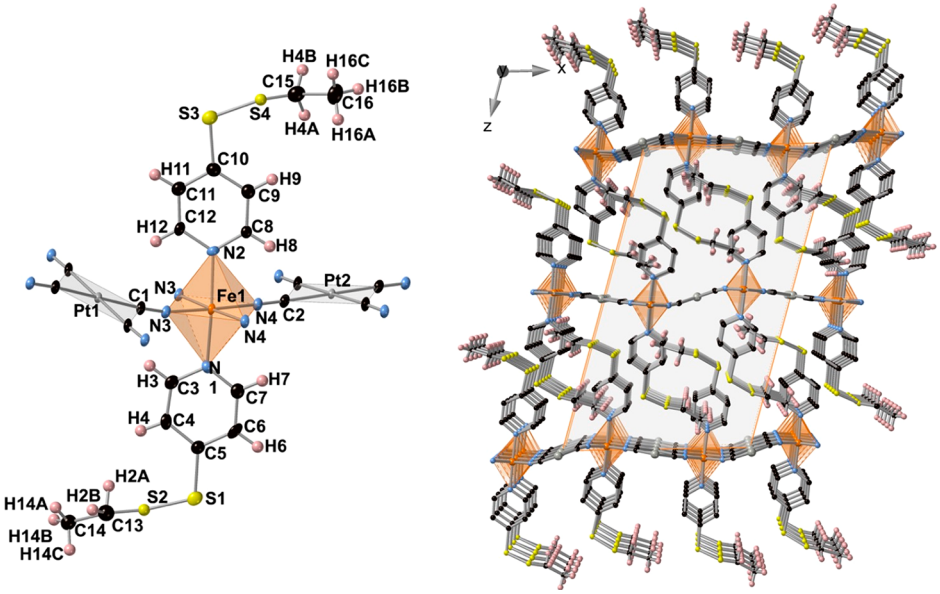


**Figure 4.** (Left) Molecular fragment of **$PtpyS_2Et$** showing the atom numbering of the asymmetric unit. (Right) Packing of three consecutive layers (only one of the two possible orientations of the −S−S−Et moiety is shown.


https://doi.org/10.1021/acs.inorgchem.1c01010
Inorg. Chem. 2021, 60, 9040−9049

$\{Fe^{II}[Pt^{II}(CN)_4]\}_n$ layers by ca. 13.85 Å and although both compounds display sharp SCO transitions they lack of hysteretic behavior.[32b] In contrast, the closely related axial ligands L = 3-phenylazo-pyridine and 4-phenylazopyridine in $[Fe^{II}(L)_2[Pd^{II}(CN)_4]$ with similar interdigitation induce abrupt hysteretic spin transitions with $\Delta T_{1/2}$ = 12 and 17 K, respectively.[32c] An additional difficulty when dealing with this type of compounds is that the spin crossover nature ($T_{1/2}$, $\Delta T_{1/2}$, completeness, abruptness, etc.) may be strongly affected by the degree of crystallinity. A relevant example has been recently observed for $\{Fe^{II}(pyridine)_2[Pt^{II}(CN)_4]\}$ (separation between layers $\{Fe^{II}[Pt^{II}(CN)_4]\}_n$ ca. 7.6 Å). In its precipitated microcrystalline form, it displays a SCO centered at 212 K with a hysteresis 8 K wide, which is characterized by a remarkable residual fraction (15%−19%) of inactive HS centers. In contrast, the same compound exclusively constituted of single crystals shows a complete well-shaped SCO centered at 234 K and a hysteresis 42 K wide (see Figure S4 in the Supporting Information).[17] Rapid precipitation of these highly insoluble compounds usually produces microcrystalline samples consisting of submicrometric/nanometric crystallites, dramatically influencing the SCO via the increase of crystal defects, and hence consisting of the residual HS molar fraction in the LS phase, which, in turn, is reflected on a decrease of the $T_{1/2}$, of cooperativity ($\Delta T_{1/2}$) and completeness of the SCO.

In the present study, the SCO behavior has been investigated for samples exclusively constituted of single crystals. Except for **PdpyS$_2$Me**, the SCO behavior of the title compounds **MpyS$_2$R** (R = Me, Et; M = Pd, Pt) retain the general features described for other Hofmann-type 2D coordination polymers. Compound **PtpyS$_2$Me** undergoes a particularly strong cooperative transition with a hysteresis $\Delta T$ = 44 K wide, which, despite an interlayer distance increase of ∼2−3 Å, because of the presence of the flexible −S−S−$CH_3$ moieties, it is virtually the same than the SCO observed for single crystals of $\{Fe^{II}(pyridine)_2[Pt^{II}(CN)_4]\}$. The only noticeable difference is observed for the average $T_{1/2}{}^{av}$ value, which is 32 K less than that observed for the pyridine derivative. This result also supports the idea mentioned above that separation between the layers does not substantially affect the cooperativity.

Replacement of the methyl group by the ethyl group in **MpyS$_2$R** does not change significantly the separation between the layers but involves a considerable decrease in $T_{1/2}{}^{av}$ from 202 K to 138 K (64 K) for the Pt derivative. This fact could tentatively be correlated with a higher corrugation of the layers in the ethyl derivatives. This fact is clearly reflected in the decrease from 180° of one of the two Fe−N−C−Pt moieties. For **PtpyS$_2$Me**, the angle Fe−N2−C1(Pt) is 168.5°, while the equivalent angle for **PtpyS$_2$Et**, Fe−N3−C1(Pt), is 158.8°, both in the HS state, and they change to 178.0° and 169.6° in the LS state, respectively. Obviously, the larger misalignment of the N−C−Pt moiety, with respect to the 3d orbitals of $Fe^{II}$ in the ethyl derivative, must necessarily decrease the $\sigma$ and $\pi$ overlaps, thereby decreasing the ligand field felt by the $Fe^{II}$ centers. Another important difference pointing to the same direction is that the angular distortion $\Sigma^{Fe}$ (see Tables 1 and 2) is significantly larger for **PtpyS$_2$Et** than for its methyl counterpart.

Surprisingly, even though both **MpyS$_2$Me** (M = Pd, Pt) compounds are isostructural, their SCO properties are drastically different to each other. The Pd derivative shows a relatively gradual multistep behavior (ca. 6 steps) separated by very narrow plateaus, while the Pt derivative displays a sharp cooperative spin transition with large hysteresis. The most significant structural difference between them is the occurrence of positional disorder of the pyridine and S−S−$CH_3$ groups over four orientations in the Pd derivative, which remains in the HS and LS states. This behavior is reminiscent of that found, among others, for the 2D coordination polymer $\{Fe^{II}[Hg^{II}(SCN)_3]_2(4,4'\text{-bipy})_2\}_n$ where a sequence of different phases characterized by distinct HS/LS fractions and symmetry breaking results from competition between SCO and structural 4,4′-bipy ligand ordering. For this system, it was possible to identify a correlation between the internal dihedral angle adopted by the 4,4′-bipy ligand and each particular step (spin state phase) as being responsible for the observed multistability.[33] From a phenomenological point of view, thermally induced multistep SCO behavior is associated with elastic frustration,[3b,c] namely, the occurrence of subtle balances between opposed intermolecular interactions that drive the HS ↔ LS transformation in fractional steps consistent with different concentrations of HS and LS centers (with or without ordering). For **PdpyS$_2$Me**, the more conspicuous positional disorder may be the source of subtle balances between interlayer interactions and/or distortions of the $[FeN_6]$ centers. However, to precisely identify the structural constraints favoring the steps, is for most of the known multistep SCO examples a major difficulty in particular when the steps are poorly defined.

## CONCLUSIONS

Here, we have described the synthesis, structure, magnetic, photomagnetic, and calorimetric properties of four new Hofmann-type 2D SCO coordination polymers. Three of them show strong cooperative SCO properties, featuring wide thermal hysteresis, in particular compound **PtpyS$_2$Me**, while its isostructural Pd counterpart surprisingly displays a multistepped transition without hysteresis, most likely due to the occurrence of additional disorder in the structure. The **MpyS$_2$Et** derivatives, which have the lowest $T_{1/2}$ of the series, show complete LIESST effect. In contrast, the LIESST effect is incomplete for **PdpyS$_2$Me** and vanishes completely for **PtpyS$_2$Me** because of their higher $T_{1/2}$ values.

The results here reported correspond to the first step in a more challenging work whose ultimate objective is to graft these Hofmann-type 2D SCO coordination polymers as monolayers on metallic surfaces (e.g., Au) to be probed as junctions for spintronic devices in which the switchable SCO centers can be used to modulate the junction conductance (see Scheme I). The choice of 4-alkyldisulfanylpyridines as axial ligands was based on the well-known fact that S atoms ensure appropriate interaction between the molecular wires and the electrodes. Preliminary work on this second objective confirms its feasibility and definitive conclusions will be reported in due time.

## EXPERIMENTAL SECTION

**Materials and Reagents.** Iron(II) tetrafluoroborate hexahydrate, potassium tetracyanoplatinate(II) trihydrate, potassium tetracyanopalladate(II) hydrate, 4-mercaptopyridine, and methyl methanethiosulfonate were obtained from commercial sources and used as received without further purification. Ethyl methanethiosulfonate was synthesized following a literature procedure.[34]

*Synthesis of Methyl/Ethyl(4-pyridyl)disulfide.* The synthesis of methyl(4-pyridyl)disulfide was performed using a method previously


https://doi.org/10.1021/acs.inorgchem.1c01010
Inorg. Chem. 2021, 60, 9040−9049

**Scheme I. Model of Device Constituted of a Monolayer of $MpyS_2Me$ Deposited on an Au Substrate**

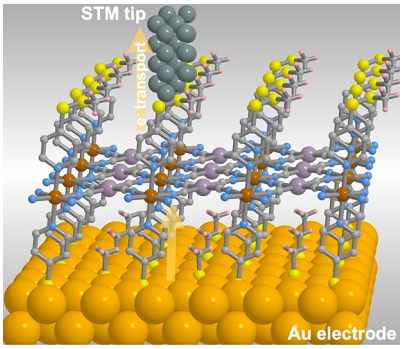


described.[35] Stoichiometric amounts of NaOH (5 mmol), 4-mercaptopyridine (5 mmol), and methylmethanethiosulfonate (5 mmol) were dissolved in water (10 mL). A white turbidness appears immediately which slowly transforms to a yellow oil. The reaction mixture was stirred at room temperature for 30 min and then extracted with $CH_2Cl_2$. The organic phase was dried with $MgSO_4$ and subsequently evaporated to obtain a yellow oil, which was purified by $SiO_2$ column chromatography using a toluene-ethyl acetate mixture (80:20) as eluent. 300 MHz, $CDCl_3$, $\delta$/ppm: 8.49 (2H), 7.44 (2H), 2.46 (3H). The same route was followed for the synthesis of ethyl(4-pyridyl)disulfide using the noncommercial precursor ethyl methanethiosulfonate. 300 MHz $^1$H-RMN, $CDCl_3$, $\delta$/ppm: 8.47 (2H), 7.45 (2H), 2.77 (2H), 1.32 (3H).

*Synthesis of Complexes* ***MpyS2R*** *(M = Pd, Pt; R = Me, Et).* All the samples were constituted of single crystals exclusively obtained through slow liquid-to-liquid diffusion methods using a 10-mL-total-volume H-shaped tube. One arm of the tube was filled with 1 mL of $H_2O$:MeOH (1:1) solution containing a mixture of 33.7 mg of $Fe(BF_4)_2{\cdot}6H_2O$ (0.1 mmol) and 40/44 mg (0.25 mmol) of methyl/ethyl(4-pyridyl)disulfide, whereas the other one was filled with an aqueous solution (1 mL) of 44/35 (0.1 mmol) of $K_2[M(CN)_4]$ (M = $Pt^{II}$/$Pd^{II}$). The rest of the tube was carefully filled with a methanol:water (1:1) solution, closed with parafilm and left to stand at room temperature. Light yellow cubic single crystals of **$MpyS_2R$** were obtained after 2 weeks. Elemental analysis: Calculated for **$PtpyS_2Me$** [$C_{16}H_{14}N_6S_4FePt$ (669.5) (%)]: C 28.70; H 2.11; N 12.55. Found (%): C 29.11; H 2.08; N 12.78. Calculated for **$PdpyS_2Me$** [$C_{16}H_{14}N_6S_4FePd$ (580.8) (%)]: C 33.09; H 2.43; N 14.47. Found (%): C 33.57; H 2.15; N 14.65. Calculated for **$PtpyS_2Et$** [$C_{18}H_{18}N_6S_4FePt$ (697.6) (%)]: C 30.99; H 2.60; N 12.05. Found (%): C 30.52; H 2.52; N 12.35. Calculated for **$PdpyS_2Et$** [$C_{18}H_{18}N_6S_4FePd$ (608.9) (%)]: C 35.51; H 2.98; N 13.80. Found (%): C 35.17; H 2.90; N 14.01.

**Physical Measurements.** *Magnetic Measurements.* Variable temperature magnetic susceptibility data were recorded with a Quantum Design MPMS2 SQUID magnetometer equipped with a 7 T magnet, operating at 1 T and at temperatures of 1.8−400 K. Experimental susceptibilities were corrected for diamagnetism of the constituent atoms by the use of Pascal's constants.

*Calorimetric Measurements.* DSC measurements were performed using a differential scanning calorimeter (Mettler Toledo, Model DSC 821e). Low temperatures were obtained with an aluminum block attached to the sample holder, refrigerated with a flow of liquid nitrogen, and stabilized at a temperature of 110 K. The sample holder was kept in a drybox under a flow of dry nitrogen gas to avoid water condensation. The measurements were performed using ∼15 mg of microcrystalline samples of **$MpyS_2Me$** (M = Pt, Pd) sealed in aluminum pans with a mechanical crimp. Temperature and heat flow calibrations were made with standard samples of indium by using its melting transition (429.6 K, 28.45 J $g^{-1}$). An overall accuracy of ±0.2 K in temperature and ±2% in the heat capacity is estimated. The uncertainty increases for the determination of the anomalous enthalpy and entropy due to the subtraction of an unknown baseline.

*Single Crystal X-ray Diffraction.* Single-crystal X-ray data were collected on an Oxford Diffraction Supernova diffractometer using graphite monochromated Mo K$\alpha$ radiation ($\lambda$ = 0.71073 Å). A multiscan absorption correction was performed. The structures were solved by direct methods using SHELXS-2014 and refined by full matrix least-squares on $F^2$ using SHELXL-2014.[36] Non-hydrogen atoms were refined anisotropically and hydrogen atoms were placed in calculated positions refined using idealized geometries (riding model) and assigned fixed isotropic displacement parameters. CCDC 2072898 (100 K) and 2072899 (250 K) (**$PdpyS_2Et$**); 2072901 (250 K) and 2072902 (129 K) (**$PdpyS_2Me$**); 2072900 (100 K) and 2072905 (250 K) (**$PtpyS_2Et$**); and 2072903 (120 K) and 2072904 (250 K) (**$PtpyS_2Me$**) contain the supplementary crystallographic data for this article. These data can be obtained free of charge from The Cambridge Crystallographic Data Centre via www.ccdc.cam.ac.uk/data_request/cif.

## ■ ASSOCIATED CONTENT

### Supporting Information

The Supporting Information is available free of charge at https://pubs.acs.org/doi/10.1021/acs.inorgchem.1c01010.

Relevant crystallographic data (Tables S1 and S2); thermogram for **$MpyS_2Me$** and **$MpyS_2Et$** (M = Pd, Pt) (Figure S1); comparison of the thermal dependence of $\Delta C_p$ and $\partial(\chi_M T)/\partial T$ curves for **$PdpyS_2Me$** (Figure S2); positional disorder of the $pyS_2Me$ ligands of **$PdpyS_2Me$** at 250 K (Figure S3); comparison of the $\chi_M T$ vs $T$ plots for {Fe(pyridine)$_2$[Pt(CN)$_4$]} obtained by direct precipitation and by slow diffusion as single crystals (Figure S4) (PDF)

### Accession Codes

CCDC 2072898−2072905 contain the supplementary crystallographic data for this paper. These data can be obtained free of charge via www.ccdc.cam.ac.uk/data_request/cif, or by emailing data_request@ccdc.cam.ac.uk, or by contacting The Cambridge Crystallographic Data Centre, 12 Union Road, Cambridge CB2 1EZ, UK; fax: +44 1223 336033.

## ■ AUTHOR INFORMATION

### Corresponding Authors

**Francisco Javier Valverde-Muñoz** − *Instituto de Ciencia Molecular/Departamento de Química Inorgánica, Universidad de Valencia, 46980 Paterna, Valencia, Spain;* orcid.org/0000-0003-3578-5445; Email: francisco.valverde@uv.es

**José Antonio Real** − *Instituto de Ciencia Molecular/Departamento de Química Inorgánica, Universidad de Valencia, 46980 Paterna, Valencia, Spain;* orcid.org/0000-0002-2302-561X; Email: jose.a.real@uv.es

### Authors

**Rubén Turo-Cortés** − *Instituto de Ciencia Molecular/Departamento de Química Inorgánica, Universidad de Valencia, 46980 Paterna, Valencia, Spain*

**Manuel Meneses-Sánchez** − *Instituto de Ciencia Molecular/Departamento de Química Inorgánica, Universidad de Valencia, 46980 Paterna, Valencia, Spain*

**M. Carmen Muñoz** − *Departamento de Física Aplicada, Universitat Politècnica de València, Valencia, Spain*

**Carlos Bartual-Murgui** − *Instituto de Ciencia Molecular/Departamento de Química Inorgánica, Universidad de Valencia, 46980 Paterna, Valencia, Spain;* orcid.org/0000-0003-1547-8018



https://doi.org/10.1021/acs.inorgchem.1c01010
*Inorg. Chem.* 2021, 60, 9040−9049

Complete contact information is available at:
https://pubs.acs.org/10.1021/acs.inorgchem.1c01010

### Notes

The authors declare no competing financial interest.

## ■ ACKNOWLEDGMENTS

This work was supported by the Spanish Ministerio de Ciencia e Innovación (MICINN) and FEDER founds (No. PID2019-106147GB-I00), Unidad de Excelencia María de Maeztu (Nos. MDM2015-0538-18-2, CEX2019-000919-M) and EU Framework FET-OPEN project COSMICS (Grant Agreement No. 766726). R.T.C. and M.M.S. thank the MICINN for a predoctoral grant.

## ■ REFERENCES

(1) (a) Real, J. A.; Gaspar, A. B.; Niel, V.; Muñoz, M. C. Communication between iron(II) building blocks in cooperative spin transition phenomena. *Coord. Chem. Rev.* **2003**, *236*, 121−141. (b) Gütlich, P.; Goodwin, G. Spin crossover in transition metal compound I−III. In *Topics in Current Chemistry*, Vol. *235*; Springer: Berlin, Heidelberg, Germany, 2004; pp 233−235, DOI: 10.1007/b96439. (c) Real, J. A.; Gaspar, A. B.; Muñoz, M. C. Thermal, pressure and light switchable spin-crossover materials. *Dalton Trans.* **2005**, 2062−2079. (d) Bousseksou, A.; Molnár, G.; Salmon, L.; Nicolazzi, W. Molecular spin crossover phenomenon: recent achievements and prospects. *Chem. Soc. Rev.* **2011**, *40*, 3313−3335. (e) Halcrow, M. A., Ed. In *Spin-Crossover Materials: Properties and Applications*; Wiley & Sons, Ltd., 2013. (f) Bousseksou, A., Ed. *Spin Crossover Phenomenon*, Vol. *21*; C. R. Chimie, 2018; pp 1055−1299.

(2) (a) Weber, B. Spin crossover complexes with $N_4O_2$ coordination sphere-The influence of covalent linkers on cooperative interactions. *Coord. Chem. Rev.* **2009**, *253*, 2432−2449. (b) Sunatsuki, Y.; Kawamoto, R.; Fujita, K.; Maruyama, H.; Suzuki, T.; Ishida, H.; Kojima, M.; Iijima, S.; Matsumoto, N. Structures and spin states of mono- and dinuclear iron(II) complexes of imidazole-4-carbaldehyde azine and its derivatives. *Coord. Chem. Rev.* **2010**, *254*, 1871−1881. (c) Aromí, G.; Barrios, L. A.; Roubeau, O.; Gamez, P. Triazoles and tetrazoles: Prime ligands to generate remarkable coordination materials. *Coord. Chem. Rev.* **2011**, *255*, 485−546. (d) Muñoz, M. C.; Real, J. A. Thermo-, piezo-, photo- and chemo-switchable spin crossover iron(II)-metallocyanate based coordination polymers. *Coord. Chem. Rev.* **2011**, *255*, 2068−2093. (e) Shatruk, M.; Phan, H.; Chrisostomo, B. A.; Suleimenova, A. Symmetry-breaking structural phase transitions in spin crossover complexes. *Coord. Chem. Rev.* **2015**, *289-290*, 62−73. (f) Ortega-Villar, N.; Muñoz, M. C.; Real, J. A. Symmetry breaking in iron(II) spin-crossover molecular crystals. *Magnetochemistry* **2016**, *2*, 16−22. (g) Ni, Z.-P.; Liu, J.-L.; Hoque, M. N.; Liu, W.; Li, J.-Y.; Chen, Y.-C.; Tong, M.-L. Recent advances in guest effects on spin-crossover behavior in Hofmann-type metal-organic frameworks. *Coord. Chem. Rev.* **2017**, *335*, 28−43. (h) Hogue, R. W.; Singh, S.; Brooker, S. Spin crossover in discrete polynuclear iron(II) complexes. *Chem. Soc. Rev.* **2018**, *47*, 7303−7338. (i) Chen, Y.-C.; Meng, Y.; Dong, Y.-J.; Song, X.-W.; Huang, G.-Z.; Zhang, C.-L.; Ni, Z.-P.; Navarík, J.; Malina, O.; Zboril, R.; Tong, M.-L. Light- and temperature-assisted spin state annealing: accessing the hidden multistability. *Chem. Sci.* **2020**, *11*, 3281−3289. (j) Berdiell, I. C.; Hochdörffer, T.; Desplanches, C.; Kulmaczewski, R.; Shahid, N.; Wolny, J. A.; Warriner, S. L.; Cespedes, O.; Schünemann, V.; Chastanet, G.; Halcrow, M. A. Supramolecular iron metallocubanes exhibiting site-selective thermal and light-induced spin-crossover. *J. Am. Chem. Soc.* **2019**, *141*, 18759−18770. (jj) Chorazy, S.; Charytanowicz, T.; Pinkowicz, D.; Wang, J.; Nakabayashi, K.; Klimke, S.; Renz, F.; Ohkoshi, S.-I.; Sieklucka, B. Octacyanidorhenate(V) ion as an efficient linker for hysteretic two-step iron(II) spin crossover switchable ny temperature light and pressure. *Angew. Chem., Int. Ed.* **2020**, *59*, 15741−15749.

(3) (a) Bertoni, R.; Lorenc, M.; Tissot, A.; Boillot, M.-L.; Collet, E. Femtosecond photoswitching dynamics and microsecond thermal conversion driven by laser heating in $Fe^{III}$ spin-crossover solids. *Coord. Chem. Rev.* **2015**, *282-283*, 66−76. (b) Paez-Espejo, M.; Sy, M.; Boukheddaden, K. Elastic frustration causing two-step and multistep transitions in spin-crossover solids: Emergence of complex antiferroelastic structures. *J. Am. Chem. Soc.* **2016**, *138*, 3202−3210. (c) Traiche, R.; Sy, M.; Boukheddaden, K. Elastic frustration in 1D spin-crossover chains: Evidence of multi-step transitions and self-organizations of the spin states. *J. Phys. Chem. C* **2018**, *122*, 4083−4096.

(4) Lacroix, P. G.; Malfant, I.; Real, J.-A.; Rodriguez, V. From magnetic to nonlinear optical switches in spin-crossover complexes. *Eur. J. Inorg. Chem.* **2013**, *2013*, 615−627.

(5) Lefter, C.; Davesne, V.; Salmon, L.; Molnár, G.; Demont, P.; Rotaru, A.; Bousseksou, A. Charge Transport and Electrical Properties of Spin Crossover Materials: Towards Nanoelectronic and Spintronic Devices. *Magnetochemistry* **2016**, *2*, 18.

(6) Matsuda, M.; Isozaki, H.; Tajima, H. Reproducible on−off switching of the light emission from the electroluminescent device containing a spin crossover complex. *Thin Solid Films* **2008**, *517*, 1465−1467.

(7) (a) Garcia, J.; Robert, F.; Naik, A. D.; Zhou, G.; Tinant, B.; Robeyns, K.; Michotte, S.; Piraux, L. Spin transition charted in a fluorophore-tagged thermochromic dinuclear iron(II) complex. *J. Am. Chem. Soc.* **2011**, *133*, 15850−15853. (b) Lochenie, C.; Schotz, K.; Panzer, F.; Kurz, H.; Maier, B.; Puchtler, F.; Agarwal, S.; Kohler, A.; Weber, B. Spin-crossover iron(II) coordination polymer with fluorescent properties: Correlation between emission properties and spin state. *J. Am. Chem. Soc.* **2018**, *140*, 700−709. (c) Delgado, T.; Meneses Sánchez, M.; Piñeiro-López, L.; Bartual-Murgui, C.; Muñoz, M. C.; Real, J. A. Thermo- and photo-modulation of exciplex fluorescence in a 3D spin crossover Hofmann-type coordination polymer. *Chem. Sci.* **2018**, *9*, 8446−8452. (d) Benaicha, B.; Van Do, K.; Yangui, A.; Pittala, N.; Lusson, A.; Sy, M.; Bouchez, G.; Fourati, H.; Gómez-García, C. J.; Triki, S.; Boukheddaden, K. Interplay between spin-crossover and luminescence in a multifunctional single crystal iron(II) complex: towards a new generation of molecular sensors. *Chem. Sci.* **2019**, *10*, 6791−6798. (e) Ge, J.-Y.; Chen, Z.; Zhang, L.; Liang, X.; Su, J.; Kurmoo, M.; Zuo, J.-L. A Two-Dimensional Iron(II) Coordination Polymer with Synergetic Spin-Crossover and Luminescent Properties. *Angew. Chem., Int. Ed.* **2019**, *58*, 8789−8793. (f) Ghosh, S.; Kamilya, S.; Pramanik, T.; Rouzières, M.; Herchel, R.; Mehta, S.; Mondal, A. ON/OFF Photoswitching and Thermoinduced Spin Crossover with Cooperative Luminescence in a 2D Iron(II) Coordination Polymer. *Inorg. Chem.* **2020**, *59*, 13009−13013. (g) Meneses-Sánchez, M.; Piñeiro-López, L.; Delgado, T.; Bartual-Murgui, C.; Muñoz, M. C.; Chakraborty, P.; Real, J. A. Extrinsic vs. intrinsic luminescence and their interplay with spin crossover in 3D Hofmann-type coordination polymers. *J. Mater. Chem. C* **2020**, *8*, 1623−1633.

(8) Gaspar, A. B.; Seredyuk, M. Spin crossover in soft matter. *Coord. Chem. Rev.* **2014**, *268*, 41−58.

(9) (a) Ni, Z.; Shores, M. P. Magnetic observation of anion binding in iron coordination complexes: Toward Spin-Switching Chemosensors. *J. Am. Chem. Soc.* **2009**, *131*, 32−33. (b) Darawsheh, M.; Barrios, L. A.; Roubeau, O.; Teat, S. J.; Aromi, G. Encapsulation of a $Cr^{III}$ single-ion magnet within an $Fe^{II}$ spin-crossover supramolecular host. *Angew. Chem., Int. Ed.* **2018**, *57*, 13509−13513.

(10) (a) Ohkoshi, S.-I.; Imoto, K.; Tsunobuchi, Y.; Takano, S.; Tokoro, H. Light-induced spin-crossover magnet. *Nat. Chem.* **2011**, *3*, 564−569. (b) Ohkoshi, S.-I.; Takano, S.; Imoto, K.; Yoshikiyo, M.; Namai, A.; Tokoro, H. 90-degree optical switching of output second-harmonic light in chiral photomagnet. *Nat. Photonics* **2014**, *8*, 65−71.

(11) (a) Bartual-Murgui, C.; Piñeiro-López, L.; Valverde-Muñoz, F. J.; Muñoz, M. C.; Seredyuk, M.; Real, J. A. Chiral and racemic spin crossover polymorphs in a family of mononuclear iron(II) compounds. *Inorg. Chem.* **2017**, *56*, 13535−13546. (b) Sun, X.-P.; Tang, Z.; Yao, Z.-S.; Tao, J. A homochiral 3D framework of

mechanically interlocked 1D loops with solvent-dependent spin-state switching behaviors. *Chem. Commun.* **2020**, *56*, 133−136.
(12) (a) Venkataramani, S.; Jana, U.; Dommaschk, M.; Sönnichsen, F. D.; Tuczek, F.; Herges, R. Magnetic bistability of molecules in homogeneous solution at room temperature. *Science* **2011**, *331*, 445−448. (b) Wang, L.-F.; Zhuang, W.-M.; Huang, G.-Z.; Chen, Y.-C.; Qiu, J.-Z.; Ni, Z.-P.; Tong, M.-L. Spin-crossover modulation via single-crystal to single-crystal photochemical [2 + 2] reaction in Hofmann-type frameworks. *Chem. Sci.* **2019**, *10*, 7496−7502.
(13) (a) Senthil Kumar, K.; Ruben, M. Emerging trends in spin crossover (SCO) based functional materials and devices. *Coord. Chem. Rev.* **2017**, *346*, 176−205. (b) Molnar, G.; Rat, S.; Salmon, L.; Nicolazzi, W.; Bousseksou, A. Spin crossover nanomaterials: from fundamental concepts to devices. *Adv. Mater.* **2018**, *30*, 1703862. (c) Bellec, A.; Lagoute, J.; Repain, V. Molecular electronics: Scanning tunneling microscopy and single-molecule devices electronique moléculaire: microscopie à effet tunnel et dispositifs à molécule unique. *C. R. Chim.* **2018**, *21*, 1287−1299. (d) Kumar, K. S.; Ruben, M. Sublimable spin-crossover complexes: from spin-state switching to molecular devices. *Angew. Chem., Int. Ed.* **2021**, *60*, 7502. (e) Gruber, M.; Berndt, R. Spin-crossover complexes in direct contact with surfaces. *Magnetochemistry* **2020**, *6*, 35.
(14) For recent references, see: (a) Liu, W.; Wang, L.; Su, Y.-J.; Chen, Y. C.; Tucek, J.; Zboril, R.; Ni, Z.-P.; Tong, M.-L. Hysteretic Spin Crossover in Two-Dimensional (2D) Hofmann-Type Coordination Polymers. *Inorg. Chem.* **2015**, *54*, 8711−8716. (b) Kucheriv, O. I.; Shylin, S. I.; Ksenofontov, V.; Dechert, S.; Haukka, M.; Fritsky, I. O.; Gural'skiy, I. A. Spin crossover in Fe(II)-M(II) cyanoheterobimetallic frameworks (M = Ni, Pd, Pt) with 2-substituted pyrazines. *Inorg. Chem.* **2016**, *55*, 4906−4914. (c) Valverde-Muñoz, F. J.; Seredyuk, M.; Muñoz, M. C.; Znovjyak, K.; Fritsky, I. O.; Real, J. A. Strong cooperative spin crossover in 2D and 3D $Fe^{II}$-$M^{I,II}$ Hofmann-like coordination polymers based on 2-fluoropyrazine. *Inorg. Chem.* **2016**, *55*, 10654−10665. (d) Liu, F.-L.; Tao, J. Hysteretic two-step spin-crossover behavior in two two-dimensional Hofmann-type coordination polymers. *Chem. - Eur. J.* **2017**, *23*, 18252−18257. (e) Gural'skiy, I. A.; Shylin, S. I.; Ksenofontov, V.; Tremel, W. Pyridazine-supported polymeric cyanometallates with spin transitions. *Eur. J. Inorg. Chem.* **2019**, *2019*, 4532−4537. (f) Hiiuk, V. M.; Shova, S.; Rotaru, A.; Golub, A. A.; Fritsky, I. O.; Gural'skiy, I. A. Spin crossover in 2D iron(II) phthalazine cyanometallic complexes. *Dalton Trans.* **2020**, *49*, 5302−5311. (g) Turo-Cortés, R.; Bartual-Murgui, C.; Castells-Gil, J.; Muñoz, M. C.; Martí-Gastaldo, C.; Real, J. A. Reversible guest-induced gate-opening with multiplex spin crossover responses in twodimensional Hofmann clathrates. *Chem. Sci.* **2020**, *11*, 11224−11234.
(15) (a) Klein, Y. M.; Sciortino, N. F.; Ragon, F.; Housecroft, C. E.; Kepert, C. J.; Neville, S. M. Spin crossover intermediate plateau stabilization in a flexible 2-D Hofmann-type coordination polymer. *Chem. Commun.* **2014**, *50*, 3838−3840. (b) Milin, E.; Patinec, V.; Triki, S.; Bendeif, E.-E.; Pillet, S.; Marchivie, M.; Chastanet, G.; Boukheddaden, K. Elastic frustration triggering photoinduced hidden hysteresis and multistability in a two-dimensional photoswitchable Hofmann-like spin-crossover metal-organic framework. *Inorg. Chem.* **2016**, *55*, 11652−11661. (c) Sciortino, N. F.; Ragon, F.; Zenere, K. A.; Southon, P. D.; Halder, G. J.; Chapman, K. W.; Piñeiro-López, L.; Real, J. A.; Kepert, C. J.; Neville, S. M. Exploiting pressure to induce a "guest-blocked" spin transition in a framework material. *Inorg. Chem.* **2016**, *55*, 10490−10498. (d) Sciortino, N. F.; Zenere, K. A.; Corrigan, M. E.; Halder, G. J.; Chastanet, G.; Létard, J.-F.; Kepert, C. J.; Neville, S. M. Four-step iron(II) spin state cascade driven by antagonistic solid state interactions. *Chem. Sci.* **2017**, *8*, 701−707. (f) Murphy, M. J.; Zenere, K. A.; Ragon, F.; Southon, P. D.; Kepert, C. J.; Neville, S. M. Guest programmable multistep spin crossover in a porous 2-D Hofmann-type material. *J. Am. Chem. Soc.* **2017**, *139*, 1330−1335. (g) Zenere, K. A.; Duyker, S. G.; Trzop, E.; Collet, E.; Chan, B.; Doheny, P. W.; Kepert, C. J.; Neville, S. M. Increasing spin crossover cooperativity in 2D Hofmann-type materials with guest molecule removal. *Chem. Sci.* **2018**, *9*, 5623−5629. (h) Brennan, A. T.; Zenere, K. A.; Brand, H. E. A.; Price, J. R.; Bhadbhade, M. M.; Turner, G. F.; Moggach, S. A.; Valverde-Muñoz, F. J.; Real, J. A.; Clegg, J. K.; Kepert, C. J.; Neville, S. M. Guest removal and external pressure variation induce spin crossover in halogen-functionalized 2D Hofmann frameworks. *Inorg. Chem.* **2020**, *59*, 14296−14305.
(16) Sakaida, S.; Otsubo, K.; Sakata, O.; Song, C.; Fujiwara, A.; Takata, M.; Kitagawa, H. Crystalline coordination framework endowed with dynamic gate-opening behaviour by being downsized to a thin film. *Nat. Chem.* **2016**, *8*, 377−383.
(17) Rubio-Giménez, V.; Bartual-Murgui, C.; Galbiati, M.; Núñez-López, A.; Castells-Gil, J.; Quinard, B.; Seneor, P.; Otero, E.; Ohresser, P.; Cantarero, A.; Coronado, E.; Real, J. A.; Mattana, R.; Tatay, S.; Martí-Gastaldo, S. Effect of nanostructuration on the spin crossover transition in crystalline ultrathin films. *Chem. Sci.* **2019**, *10*, 4038−4047.
(18) (a) Rubio-Giménez, V.; Escorcia-Ariza, G.; Bartual-Murgui, C.; Sternemann, C.; Galbiati, M.; Castells-Gil, J.; Real, J. A.; Tatay, S.; Martí-Gastaldo, C. Ultrathin films of 2D Hofmann-type coordination polymers: influence of pillaring linkers on structural flexibility and vertical charge transport. *Chem. Mater.* **2019**, *31*, 7277−7287. (b) Bartual-Murgui, C.; Rubio-Giménez, V.; Meneses-Sánchez, M.; Valverde-Muñoz, F. J.; Tatay, S.; Martí-Gastaldo, C.; Muñoz, M. C.; Real, J. A. Epitaxial thin-film vs single crystal growth of 2D Hofmann-type iron(II) materials: a comparative assessment of their bi-stable spin crossover properties. *ACS Appl. Mater. Interfaces* **2020**, *12*, 29461−29472.
(19) Otsubo, K.; Haraguchi, T.; Kitagawa, H. Nanoscale crystalline architectures of Hofmann-type metal−organic frameworks. *Coord. Chem. Rev.* **2017**, *346*, 123−138.
(20) Bell, C. M.; Arendt, M. F.; Gomez, L.; Schmehl, R. H.; Mallouk, T. E. Growth of lamellar Hofmann clathrate films by sequential ligand exchange reactions: assembling a coordination solid one layer at a time. *J. Am. Chem. Soc.* **1994**, *116*, 8374−8375.
(21) Cobo, S.; Molnár, G.; Real, J. A.; Bousseksou, A. Multilayer sequential assembly of thin films that display room-temperature spin crossover with hysteresis. *Angew. Chem., Int. Ed.* **2006**, *45*, 5786−5789.
(22) Otsubo, K.; Haraguchi, T.; Sakata, O.; Fujiwara, A.; Kitagawa, H. Step-by-step fabrication of a highly oriented crystalline three-dimensional pillared-layer-type metal-organic framework thin film confirmed by synchrotron X-Ray diffraction. *J. Am. Chem. Soc.* **2012**, *134*, 9605−9608.
(23) Bartual-Murgui, C.; Salmon, L.; Akou, A.; Thibault, C.; Molnár, G.; Mahfoud, T.; Sekkat, Z.; Real, J. A.; Bousseksou, A. High quality nano-patterned thin films of the coordination compound {Fe(Pyrazine)[Pt(CN)4]} deposited layer-by-layer. *New J. Chem.* **2011**, *35*, 2089−2094.
(24) Bartual-Murgui, C.; Akou, A.; Salmon, L.; Molnár, G.; Thibault, C.; Real, J. A.; Bousseksou, A. Guest effect on nanopatterned spin-crossover thin films. *Small* **2011**, *7*, 3385−3391.
(25) Agusti, G.; Cobo, S.; Gaspar, A. B.; Molnar, G.; Moussa, N. O.; Szilagyi, P. A.; Palfi, V.; Vieu, C.; Munoz, M. C.; Real, J. A.; Bousseksou, A. Thermal and light-induced spin crossover phenomena in new 3D Hofmann-like microporous metalorganic frameworks produced as bulk materials and nanopatterned thin films. *Chem. Mater.* **2008**, *20*, 6721−6732.
(26) (a) Aragones, A. C.; Aravena, D.; Cerda, J. I.; Acis-Castillo, Z.; Li, H.; Real, J. A.; Sanz, F.; Hihath, J.; Ruiz, E.; Diez-Perez, I. Large conductance switching in a single-molecule device through room temperature spin-dependent transport. *Nano Lett.* **2016**, *16*, 218−226. (b) Aragonés, A. C.; Aravena, D.; Valverde-Muñoz, F. J.; Real, J. A.; Sanz, F.; Díez-Pérez, I.; Ruiz, E. Metal-controlled magnetoresistance at room temperature in single molecule devices. *J. Am. Chem. Soc.* **2017**, *139*, 5768−5778. (c) Karuppannan, S. K.; Martín-Rodríguez, A.; Ruiz, E.; Harding, P.; Harding, D. J.; Yu, X.; Tadich, A.; Cowie, B.; Qi, D.; Nijhuis, C. A. Room temperature conductance switching in a molecular iron(III) spin crossover junction. *Chem. Sci.* **2021**, *12*, 2381−2388.


https://doi.org/10.1021/acs.inorgchem.1c01010
*Inorg. Chem.* 2021, 60, 9040−9049

(27) Decurtins, S.; Gütlich, P.; Köhler, P. C.; Spiering, H.; Hauser, A. Light-induced excited spin state trapping in a transition-metal complex: The hexa-1-propyltetrazole-iron (II) tetrafluoroborate spin-crossover system. *Chem. Phys. Lett.* **1984**, *105*, 1−4.
(28) Létard, J. F.; Guionneau, P.; Rabardel, L.; Howard, J. A. K.; Goeta, A. E.; Chasseau, D.; Kahn, O. Structural, magnetic, and photomagnetic studies of a mononuclear iron(II) derivative exhibiting an exceptionally abrupt spin transition. light-induced thermal hysteresis phenomenon. *Inorg. Chem.* **1998**, *37*, 4432−4441.
(29) (a) Hauser, A. Intersystem crossing in Fe(II) coordination compounds. *Coord. Chem. Rev.* **1991**, *111*, 275−290. (b) Hauser, A.; Vef, A.; Adler, P. Intersystem crossing dynamics in Fe(II) coordination compounds. *J. Chem. Phys.* **1991**, *95*, 8710−8717. (c) Hauser, A.; Enachescu, C.; Daku, M. L.; Vargas, A.; Amstutz, N. Low-temperature lifetimes of metastable high-spin states in spin-crossover and in low-spin iron(II) compounds: the rule and exceptions to the rule. *Coord. Chem. Rev.* **2006**, *250*, 1642−1652.
(30) Kitazawa, T.; Gomi, Y.; Takahashi, M.; Takeda, M.; Enomoto, M.; Miyazaki, A.; Enoki, T. Spin-crossover behaviour of the coordination polymer $Fe^{II}(C_5H_5N)_2Ni^{II}(CN)_4$. *J. Mater. Chem.* **1996**, *6*, 119−121.
(31) Niel, V.; Martinez-Agudo, J. M.; Muñoz, M. C.; Gaspar, A. B.; Real, J. A. Cooperative spin crossover behavior in cyanide-bridged Fe(II)-M(II) bimetallic 3D Hofmann-like networks (M = Ni, Pd, and Pt). *Inorg. Chem.* **2001**, *40*, 3838−3839.
(32) (a) Seredyuk, M.; Gaspar, A. B.; Ksenofontov, V.; Verdaguer, M.; Villain, F.; Gutlich, P. Thermal- and light-induced spin crossover in novel 2D Fe(II) metalorganic frameworks $\{Fe(4PhPy)_2[M^{II}(CN)_x]_y\}\cdot sH_2O$: Spectroscopic, Structural, and Magnetic Studies. *Inorg. Chem.* **2009**, *48*, 6130−6141. (b) Ohtani, R.; Arai, M.; Ohba, H.; Hori, A.; Takata, M.; Kitagawa, S.; Ohba, M. Modulation of the interlayer structures and magnetic behavior of 2D spin-crossover coordination polymers $[Fe^{II}(L)_2Pt^{II}(CN)_4]$. *Eur. J. Inorg. Chem.* **2013**, *2013*, 738−744. (c) Ragon, F.; Yaksi, K.; Sciortino, N. F.; Chastanet, G.; Létard, J. F.; D'Alessandro, D. M.; Kepert, C. J.; Neville, S. M. Thermal spin crossover behaviour of two-dimensional Hofmann-type coordination polymers incorporating photoactive ligands. *Aust. J. Chem.* **2014**, *67*, 1563−1573.
(33) (a) Trzop, E.; Zhang, D.; Piñeiro-Lopez, L.; Valverde-Muñoz, F. J.; Muñoz, M. C.; Palatinus, L.; Guerin, L.; Cailleau, H.; Real, J. A.; Collet, E. First step towards a devilÏs staircase in spin-crossover materials. *Angew. Chem., Int. Ed.* **2016**, *55*, 8675−8679. (b) Zhang, D.; Trzop, E.; Valverde-Muñoz, F. J.; Piñeiro-López, L.; Muñoz, M. C.; Collet, E.; Real, J. A. Competing phases involving spin-state and ligand structural orderings in a multistable two-dimensional spin crossover coordination polymer. *Cryst. Growth Des.* **2017**, *17*, 2736−2745.
(34) Bentley, M.; Douglass, I.; Lacadie, J. A. Silver-assisted displacements on sulfur. New thiolsulfonate ester synthesis. *J. Org. Chem.* **1972**, *37*, 333−334.
(35) Kitson, T. M.; Loomes, K. M. Synthesis of methyl 2- and 4-pyridyl disulfide from 2- and 4-thiopyridone and methyl methanethiosulfonate. *Anal. Biochem.* **1985**, *146*, 429−430.
(36) Sheldrick, G. M. Crystal Structure Refinement with SHELXL. *Acta Crystallogr., Sect. C: Struct. Chem.* **2015**, *71*, 3−8.


https://doi.org/10.1021/acs.inorgchem.1c01010
*Inorg. Chem.* 2021, 60, 9040−9049

Journal of Materials Chemistry C

ROYAL SOCIETY OF CHEMISTRY

PAPER

View Article Online
View Journal | View Issue

Check for updates

Cite this: J. Mater. Chem. C, 2022, 10, 10686

# Coexistence of luminescence and spin-crossover in 2D iron(II) Hofmann clathrates modulated through guest encapsulation†

Rubén Turo-Cortés, [a] Manuel Meneses-Sánchez,[a] Teresa Delgado, [b] Carlos Bartual-Murgui, *[a] M. Carmen Muñoz [c] and José Antonio Real *[a]

The search for advanced multifunctional materials displaying two or more simultaneous and correlated physicochemical properties represents a key step in developing further practical applications. In this context, here we report the synthesis and physical characterization of the unprecedented two-dimensional Hofmann-type Coordination Polymers (HCPs) formulated as $\{Fe^{II}(AnPy)_2[M^{I}(CN)_2]_2\}\cdot XBz$ (AnPy = 4-anthracenepyridine; M = Ag, Au; XBz = substituted benzenic guest). These materials combine two functions, spin crossover (SCO) and fluorescence which arise, respectively, from the octahedrally coordinated $Fe^{II}$ ions and the anthracene based AnPy ligands. The thermal dependence of the magnetic and calorimetric properties performed on microcrystalline samples, as well as single crystal UV-Vis absorption spectroscopy and structural studies reflect a multi-stepped nature of the SCO. The temperature at which the SCO takes place is markedly modulated by the nature of the XBz guests (X = I, Br, Cl, $NO_2$, $CH_3$) which are trapped within the interstitial spaces originating from the stacking of bimetallic layers. Two different crystallographic phases, one orthorhombic and another triclinic have been identified. The triclinic phase is not stable in air and transforms into the orthorhombic form likely prompted by the partial release of guests. Both phases afford new examples of symmetry breaking and spin-state ordering associated with the SCO. All compounds exhibit strong blue fluorescence that gradually vanishes as the temperature increases but they also present a prominent excimer/exciplex green fluorescence band for X = I (M = Ag, Au) and Cl (M = Au), whose intensity increases in parallel with the population of high-spin $Fe^{II}$ ions. Hence, the latter compounds represent new examples of synergy between SCO and luminescence.

Received 17th May 2022,
Accepted 2nd July 2022

DOI: 10.1039/d2tc02039d

rsc.li/materials-c

Published on 04 July 2022. Downloaded by Universitat de València on 2/3/2023 8:59:09 AM.

## Introduction

The spin crossover (SCO) phenomenon, displayed by certain transition metals ions ($3d^4$–$3d^7$) in octahedral environments, is a fascinating example of stimuli-driven molecular switching. It involves the controllable, detectable, and reversible transition of the metal ion between the high spin (HS) and the low spin (LS) electronic configurations leading to important changes of both the structure (volume and geometry) and physical properties (magnetic, electrical and optical) of the complex.[1–3] In the solid state, the structural changes drive the propagation of the spin state switch across the crystal more or less efficiently depending on the degree of interaction between the SCO centers. When these interactions are strong (*e.g.* covalently bonded SCO atoms), the volume change associated to the spin transition of a given SCO center elastically induces the switching of the neighboring switchable metal ions.[4,5] For thermally induced SCO behaviors, this cooperative communication is macroscopically monitored as an abrupt change of the HS molar fraction ($\gamma_{HS}$) as a function of the temperature.[6,7] Furthermore, when the coupling between SCO ions is very strong, the observed $\gamma_{HS}$ *vs.* $T$ plot may exhibit hysteretic behavior (memory effect)[8,9] which is an appealing situation for applicative purposes.[10,11]

Bimetallic $Fe^{II}$ Hofmann-like coordination polymers ($Fe^{II}$-HCPs) with general formula $\{Fe^{II}(L)_n[[M^{II}(CN)_4]]\}$ ($M^{II}$ = Ni, Pd, Pt) or $\{Fe^{II}(L)_n[[M^{I}(CN)_2]_2]\}$ ($M^{I}$ = Cu, Ag, Au) (L being an axial pyridinic-like ligand) are among the most investigated systems within the SCO community.[12–14] This is in part because they can

[a] Departamento de Química Inorgánica, Instituto de Ciencia Molecular (ICMol), Universidad de Valencia, Catedrático José Beltrán 2, 46980 Paterna, Spain. E-mail: carlos.bartual@uv.es, jose.a.real@uv.es
[b] PSL University, Chimie Paris Tech, IRCP-CNRS, Paris, 7505, France
[c] Departamento de Física Aplicada, Universitat Politècnica de València, Camino de Vera s/n, E-46022, Valencia, Spain

† Electronic supplementary information (ESI) available: Synthesis and characterization of samples, experimental and instrumental details. CCDC 2166356–2166379. For ESI and crystallographic data in CIF or other electronic format see DOI: https://doi.org/10.1039/d2tc02039d



This journal is © The Royal Society of Chemistry 2022

Published on 04 July 2022. Downloaded by Universitat de València on 2/3/2023 8:59:09 AM.

be easily designed to generate void spaces where guest molecules can be accommodated, a fact which in turn affords the opportunity to modulate the SCO behavior.[15] In the case of the $\{Fe(L)_n[M(CN)_4]\}$ HCPs, the use of monodentate L ligands ($n = 2$) produces 2D networks consisting of stacked cyanide-based bimetallic layers stabilized through the interdigitation of the axial L ligands. Although in principle this kind of structure is not porous, the appropriate functionalization of L can stimulate the occurrence of host–guest interactions affecting the SCO characteristics.[16–26] Besides, the use of a ditopic pyridine-based ligand ($n$ = 1) leads to the formation of intrinsically porous 3D networks, which promote the sorption/desorption of guest molecules in synergy with modulation of the SCO.[27] Regarding the $\{Fe(L)_n[[M^I(CN)_2]_2]\}$ derivatives, the lower coordination density of the heterometallic layers afforded by the $[M^I(CN)_2]^-$ bridging ligands with respect to the $[M(CN)_4]^{2-}$ homologues, together with the establishment of metallophilic (Ag···Ag or Au···Au) interactions, usually favor the formation of interpenetrated structures. In spite of this, most of the reported 3D ($n = 1$) dicyanometallate-based networks exhibit host–guest interactions which considerably impact the SCO properties.[28–39] In contrast, the presence of trapped guests in 2D ($n = 2$) $\{Fe(L)_2[[M^I(CN)_2]_2]\}$ networks is rare,[40,41] probably due to the efficient packing of the generated bilayered structures.[40,42–52]

In addition to the existence of host–guest interactions, the integration of fluorescence properties acting in synergy with the SCO is an exciting pathway for developing new advanced multifunctional materials.[58,5953–59] In the case of $Fe^{II}$ based compounds, the interplay between fluorescence and SCO is based on the overlap between the fluorescent emission of the luminophore and the absorption band of the $Fe^{II}$ in the LS state which vanishes in the HS state. In the case of 3D $Fe^{II}$-HCPs, the incorporation of fluorescent properties has been recently accomplished by following two strategies: (i) the use of a fluorophore as pillaring ligand[60] and (ii) the inclusion of a fluorescent guest into the structural cavities.[60,61] Whereas the first strategy led to the SCO compounds $\{Fe(Bpan)[M^I(CN)_2]_2\}$ (M = Ag, Au; Bpan = 4-bis(pyridyl)anthracene), the second one yielded the SCO networks $\{Fe(bpb)[M(CN)_2]_2\}\cdot$Pyr and $\{Fe(bpben)[M(CN)_2]_2\}\cdot$Pyr (bpb = bis(4-pyridyl)butadiyne; bpben = 1,4-bis(4-pyridyl)benzene); (M = Ag, Au) where the pyrene (Pyr) guests act as a luminophore (Scheme 1). Regardless of the used strategy, the corresponding SCO properties were successfully monitored as a modulation of the fluorescent signal confirming the synergy between both properties.

Although other types of 2D coordination polymers presenting synergies between luminescence and SCO have been recently reported,[62–64] up to date only one example of fluorescent 2D $Fe^{II}$-HCPs is known.[65] The interest of these laminar 2D $Fe^{II}$-HCPs resides in the possibility of adjusting the layer-to-layer space designing interlayer cavities where a wide range of functional guests can actuate in synergy with both the SCO and fluorescence properties. Herein, we present the synthesis, structural characterization and SCO properties, derived from variable temperature magnetic and calorimetric measurements on microcrystalline powders and optical absorption properties measured on single crystals, of an unprecedented family of 2D $Fe^{II}$-HCPs formulated $\{Fe(AnPy)_2[M(CN)_2]_2\}\cdot$XBz (AnPy = 4-(anthracene)-pyridine (Scheme 1); M = Ag (**AnPyAg·XBz**), Au (**AnPyAu·XBz**); XBz = substituted benzene (X = I, Br, Cl, $CH_3$, and $NO_2$)). Furthermore, these compounds exhibit fluorescence emission stemming from the anthracene moiety of the axial AnPy ligand (Scheme 1). The nature of the XBz aromatic guests, located within the large cavities originated between the bimetallic layers, noticeably modulates the SCO behavior. New evidence of synergy between SCO and fluorescence, namely modulation of the fluorescent signal as a function of the thermal dependence of the HS fraction is reported.

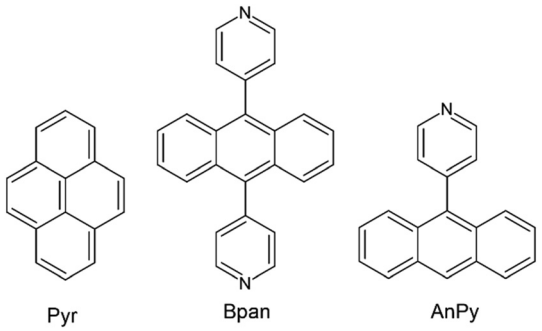


Scheme 1 Source of fluorescence used in ref. 60 and 61 (pyrene (Pyr) as guest molecule), ref. 60 (Bpan as axial bridging ligand) and in this work (AnPy as axial terminal ligand).

## Results

### Synthesis and chemical characterization

Single crystals of **AnPyM·*n*XBz** were prepared by slow liquid-to-liquid diffusion methods from a solution of $K[M^I(CN)_2]$ ($M^I$ = Au or Ag) in methanol and another containing a mixture of $Fe(BF_4)_2\cdot 6H_2O$ and AnPy dissolved in a methanol : XBz (1 : 3) solution. The XBz solvent was intentionally included, on one hand, to facilitate the dissolution of the AnPy ligand and, on the other, to act as a template for the resulting structure. Both solutions were separated by a 1 : 2 MeOH : XBz interphase in a test tube (see experimental details in the ESI†). Yellow rhombohedral single crystals of $\{Fe(AnPy)_2[M(CN)_2]_2\}\cdot$XBz (**AnPyM·XBz**) were obtained in good yields (*ca.* 60–70%) after *ca.* 4 weeks. For comparative reasons and using the same synthetic method, crystals of the non-SCO $Ni^{II}$ atom instead of $Fe^{II}$ (**NiAnPyAu·$NO_2$Bz**) were also synthesized.

The composition of the crystals was characterized by elemental and thermogravimetric analyses (TGA) (see experimental section in ESI† and Fig. S1), single crystal and powder X-ray diffraction (SCXRD and PXRD). The X-ray diffraction studies demonstrated the presence of two distinct polymorphs/solvatomorphs for pristine crystals of **AnPyAu·XBz** (X = Cl, $CH_3$), the so-called triclinic metastable phase, which once removed from their mother liquor transforms in several hours into the stable orthorhombic form (Fig. S2, ESI†), characteristic of the whole family of the clathrate compounds **AnPyM·*n*XBz** and of **NiAnPyAu·$NO_2$Bz**. Indeed, the PXRD analysis carried out on air-dried crystals reveal that,

Published on 04 July 2022. Downloaded by Universitat de València on 2/3/2023 8:59:09 AM.

regardless of the trapped guest, this orthorhombic form is found for all the derivatives (Fig. S3, ESI†). Likewise, the similarity between the PXRD patterns of the Ag and Au counterparts demonstrates that both analogues are isostructural. The PXRD patterns of the guest-free compounds **AnPyM** (M = Ag, Au), which were obtained from a thermal treatment (400 K for one hour) of the toluene or chlorobenzene containing clathrates, indicates that the network retains the structure after guest desorption.

In general, the orthorhombic form accommodates about 1.6–2 molecules of XBz within the cavities of the structure and the TGA show that they remain adsorbed at temperatures below 380–430 K depending on the derivative. The release of the benzenic guest, which corresponds to the *ca.* 20–30% of the total mass, is followed by the decomposition of the network at around 480 K. This decomposition involves a total mass loss of *ca.* 45% corresponding well to 2 AnPy ligands and 4 CN unities being the remaining mass of *ca.* 30% consistent with Fe and Ag/Au residues. The crystal data analysis of the triclinic phases enabled us to infer a larger amount of guest in the clathrates, namely $n = 2$ and 3 for ClBz and $CH_3Bz$, respectively, suggesting that the triclinic-to-orthorhombic crystal phase change is driven by the partial loss of guest molecules. Obviously, this transformation has direct consequences on the SCO properties of both derivatives (*vide infra*).

### Spin crossover properties

**Magnetic, calorimetric and photomagnetic studies.** The thermal variation of the $\chi_M T$ product (where $\chi_M$ is the molar magnetic susceptibility and T is the temperature) was measured for the air-dried compounds **AnPyM·XBz** (orthorhombic phase) at 1 K $min^{-1}$ in order to analyze the SCO properties (Fig. 1). At 260 K, all samples exhibit a $\chi_M T$ value of *ca.* 3.5 $cm^3$ $mol^{-1}$ which indicates a fully populated HS state. Upon cooling, all **AnPyAg·XBz** derivatives undergo a similar four-step decrease of the $\chi_M T$ value revealing a complete HS-to-LS state transformation. The steps are separated by more or less marked plateaus consistent with the stabilization of intermediate mixed spin states denoted $[HS_i{:}LS_j]$ following the sequence ($[HS_1{:}LS_0] \leftrightarrow [HS_{3/4}{:}LS_{1/4}] \leftrightarrow [HS_{1/2}{:}LS_{1/2}] \leftrightarrow [HS_{1/4}{:}LS_{3/4}] \leftrightarrow [HS_0{:}LS_1]$) taking place at around 2.6–2.5 $cm^3$ $mol^{-1}$ ($[HS_{3/4}{:}LS_{1/4}]$), 1.8–1.6 $cm^3$ $mol^{-1}$ ($[HS_{1/2}{:}LS_{1/2}]$) and 0.9–0.8 $cm^3$ $mol^{-1}$ ($[HS_{1/4}{:}LS_{3/4}]$). In the heating mode, the magnetic behavior is overall superposed with that of the cooling mode although a small hysteresis (2–5 K) is observed for some of the transitions. Only the last step observed for **AnPyAg**·IBz displays a remarkable hysteresis of 10 K being the $[HS_{1/4}{:}LS_{3/4}]$ state more stabilized. Although this multi-stepped SCO behavior is roughly reproduced for the Au counterparts, compounds **AnPyAu**·IBz and **AnPyAu·BrBz**/**AnPyAu·$CH_3$Bz** display incomplete transitions with only two and three steps, respectively, likely due to kinetic factors imposed by the lower temperatures involved. The critical SCO temperatures, $T_{ci}$, defined as the temperature at which 50% of the $Fe^{II}$ ions have switched from the HS to the LS state during the step i, are clearly dependent on the nature of the adsorbed guest (Table 1). Indeed, the $T_{ci}$ values increase in the order $T_{ci}$(IBz) < $T_{ci}$($CH_3$Bz) < $T_{ci}$(BrBz) < $T_{ci}$(ClBz) < $T_{ci}$($NO_2$Bz) for both the Ag and Au derivatives. Furthermore, a decrease of $T_{ci}$ is also observed when moving from the Ag to the Au derivatives (see Table 1).

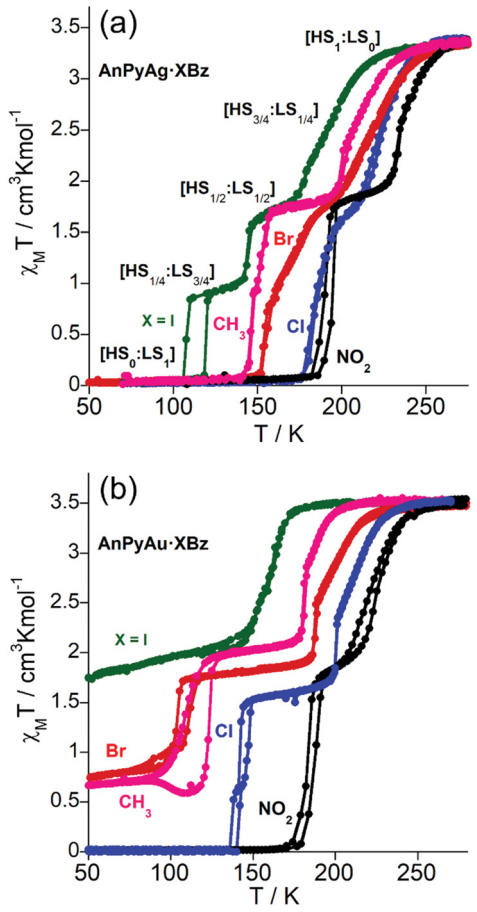


Fig. 1 Thermal dependence of $\chi_M T$ for (a) **AnPyAg·XBz** and (b) **AnPyAu·XBz** (X = I, $CH_3$, Br, Cl and $NO_2$) (orthorhombic phase) (1 K $min^{-1}$).

The magnetic behavior of the triclinic phases (pristine crystals of **AnPyAu·ClBz** and **AnPyAu·$CH_3$Bz**) measured into their mother liquor displays incomplete and multi-stepped SCO curves with transitions shifted to low temperatures (Fig. S4, ESI†). However, the spin transition becomes more complete and shifts to higher temperatures when removing the crystals from the mother liquor driving to the SCO curves described above for the orthorhombic forms (Fig. S4, ESI†). These results reveal that the triclinic phases are not stable in air

Table 1 $T_{ci}$ values (in K) of the different steps obtained from the magnetic measurements of the different **AnPyM·XBz** compounds

| | M | | | | | | | |
|---|---|---|---|---|---|---|---|---|
| | Ag | | | | Au | | | |
| X | $T_{c1}$ | $T_{c2}$ | $T_{c3}$ | $T_{c4}$ | $T_{c1}$ | $T_{c2}$ | $T_{c3}$ | $T_{c4}$ |
| I | 199 | 182 | 145 | 109[a] | 165 | 152 | — | — |
| $CH_3$ | 215 | 200 | 153 | 147 | 190 | 181 | 113[a] | — |
| Br | 231 | 210 | 173 | 156 | 200 | 187 | 104[a] | — |
| Cl | 233 | 219 | 190 | 181 | 215 | 201 | 143[a] | 138[a] |
| $NO_2$ | 246 | 234 | 193[a] | 188[a] | 228 | 215[a] | 184[a] | 180[a] |

[a] Temperature registered upon the cooling mode (measured at 1 K $min^{-1}$).

 This journal is © The Royal Society of Chemistry 2022

Published on 04 July 2022. Downloaded by Universitat de València on 2/3/2023 8:59:09 AM.

and evolve to the orthorhombic phase in good accord with the PXRD studies (Fig. S2, ESI†). In contrast to the guest-loaded clathrates, the SCO of the guest-free **AnPyAg** and **AnPyAu** compounds are markedly gradual, incomplete and take place in a unique step with $T_c$ values of 157 and 163 K, respectively (Fig. S5, ESI†).

The occurrence of the multi-stepped SCO behavior of these clathrates is also reflected on the calorimetric measurements (recorded at 10 K $min^{-1}$) characterized by a series of maxima/minima in the $C_p$ *vs.* $T$ curves that determine the position of the steps in good accordance with the magnetic profiles (Fig. S6, ESI†). It is worth noting that only the **AnPyAg·XBz** (X = $NO_2$, Cl, Br and $CH_3$) and[13] **AnPyAu·$NO_2$Bz** species were studied since the temperature range where the spin-state change takes place in the rest of derivatives is not achievable by our calorimeter. The estimated $\Delta H$ and $\Delta S$ variations (Table S1, ESI†) are common in $Fe^{II}$ spin-crossover compounds. Light induced excited spin state trapping (LIESST)[66] was observed for all the derivatives when irradiating with a green laser ($\lambda$ = 532 nm. 40 mW) at 10 K (Fig. S7, ESI†). The efficiency of the photoconversion from the LS to the metastable HS* state (green curves) is in the range 60–80% and 80–100% for Ag and Au derivatives, respectively. Then, once attained the saturation values and in the dark the photogenerated HS* state relaxes back (black curves) to the initial LS state increasing the temperature at a rate of 0.3 K $min^{-1}$ obtaining characteristic $T_{LIESST}$[67] of 33 ($NO_2$), 40 (Cl), 45 (Br), 46 (I), and 47 ($CH_3$) K (in one step for the **AnPyAg·XBz**), 36/45 ($NO_2$), 49/66 (Cl), 47/70 (Br) K, (in two steps for the **AnPyAu·XBz**) and 53 ($CH_3$) and 55 (I) K (in one step for **AnPyAu·XBz**). These temperatures are consistent with the inverse-energy-gap law as the stability of the photogenerated HS* species decreases as the stability of the LS increases ($T_c$ increases).[68–70]

### Structural characterization

In order to follow the spin state change and evaluate the occurrence of symmetry breaking processes, the crystal structures of **AnPyM·XBz** (M = Ag or Au and X = $NO_2$, $CH_3$, Cl or Br) were studied at different temperatures according to the multi-stepped SCO behavior observed through the magnetic measurements. Despite many efforts, the structures of **AnPyM·IBz** (M = Ag, Au) and **NiAnPyAu·$NO_2$Bz** could not be resolved although, as mentioned before, they are isostructural to the other members of the series adopting the stable orthorhombic form (Fig. S3, ESI†).

Compounds **AnPyAg·BrBz**, **AnPyAu·BrBz** and **AnPyAg·ClBz** exhibit the orthorhombic *Ccc*2 space group above 260 K but display symmetry breaking associated with spin-state changes at lower temperatures (*vide infra*). In contrast, compounds **AnPyAg·$CH_3$Bz** and **AnPyAg·$NO_2$Bz**/**AnPyAu·$NO_2$Bz** crystallize in the orthorhombic *Pccn* and *Cccm* space groups, respectively, and remain in the same crystal phase upon SCO. Finally, both **AnPyAu·$CH_3$Bz** and **AnPyAu·ClBz** display a triclinic $P\bar{1}$ space group, the latter exhibiting symmetry breaking upon cooling also associated with the SCO behavior. Due to their similarity, crystal structures presenting orthorhombic phases will be described together whereas the triclinic structures will be presented in a separated section. Crystal data, structural parameters and a selection of relevant bond lengths and angles are gathered in Tables S2–S17 (ESI†).

**Orthorhombic phases.** At 260–280 K, the crystal structures of **AnPyAg·XBz** (X = Cl, Br, $NO_2$ or $CH_3$) and **AnPyAu·XBz** (X = Br or $NO_2$) contain a unique elongated octahedral $[Fe^{II}N_6]$ site constituted of four equivalent equatorial $[M(CN)_2]^{2-}$ bridging units and two identical axial AnPy ligands (Fig. 2(a)) with average bond lengths at $T \geq 260$ K in the interval 2.012(8)–2.140(4) Å and 2.212(9)–2.247(5) Å, respectively. The overall $Fe–N_{av}$ average bond-lengths, in the range 2.144–2.169 Å, are consistent with the $Fe^{II}$ in the HS state as indicated by the magnetic measurements. Each equatorial $[M(CN)_2]^-$ unit bridges two $[Fe^{II}N_6]$ centers therefore building up infinite $\{Fe(AnPy)_2[M(CN)_2]_2\}$ two-dimensional layers (Fig. 2(b)). The angle defined by two adjacent $[FeN_4]$ equatorial planes is in the range 21–26° for the HS state and decreases by *ca.* 20–25% in the LS state. Furthermore, the $[M(CN)_2]^-$ bridging groups slightly depart from linearity by *ca.* 10°. Both facts, together with the symmetry, confer a homogeneous undulated character to the bimetallic layers. The layers stack along the *b* axis (*a* axis for **AnPyAg·$CH_3$Bz**) (Fig. 2(b)) being the separation between two consecutive corrugated layers, measured as the distance between the planes defined by their respective $Fe^{II}$ centers, in the range 11.11–12.65 Å for $T \geq 260$ K. This separation remains almost constant at lower temperatures. The only exception was found for **AnPyAg·$CH_3$Bz** whose separation decreases by *ca.* 12% upon cooling at 120 K. The stacking takes place in such a way that the $[Fe^{II}N_6]$ sites of one layer project on the center of the $\{Fe_4[M(CN)_2]_4\}$ windows of the adjacent layer. The resulting interdigitation between the AnPy ligands of adjacent layers favors the occurrence of some C–H···π and π···π interactions between the pyridine and the anthracene moieties (*e.g.* anthracene ···anthracene *d*[C20···C11′] = 3.469 Å, at 120 K). This packing mode generates channels running along the 001 direction (*c* axis) where the XBz molecules are hosted (Fig. 2(b) and Fig. S8, ESI†). Although modelling the trapped XBz molecules is not overall achievable due to the strong positional disorder of these molecules within the cavities, the most part of the electronic density is localized face-to-face to the anthracene moieties of the AnPy ligands suggesting the presence of π···π host–guest interactions. This was confirmed for **AnPyAg·$CH_3$Bz** at 120 K where the toluene was clearly identified (Fig. 2(b) and Fig. S9, ESI†) and stablishes short C···C contacts with the host framework, more precisely anthracene···toluene *d*[C15/C17···C24] = 3.485/3.444 Å and toluene···cyanide *d*[C25/C26···C1 = 3.483/3.426 Å]. A solvent mask was implemented for the rest of structures removing the electronic contribution of the disordered guest from the refinement and estimating the corresponding amount. The masked electron density is, for all the compounds, consistent with the quantity of guest inferred from TGA measurements (*i.e.* about 1.6–2 molecules per $Fe^{II}$ ion).

Upon cooling to 207, 192 and 165 K, respectively, the structures of **AnPyAg·ClBz**, **AnPyAg·BrBz** and **AnPyAu·BrBz** undergo a symmetry breaking revealing a crystallographic

Published on 04 July 2022. Downloaded by Universitat de València on 2/3/2023 8:59:09 AM.

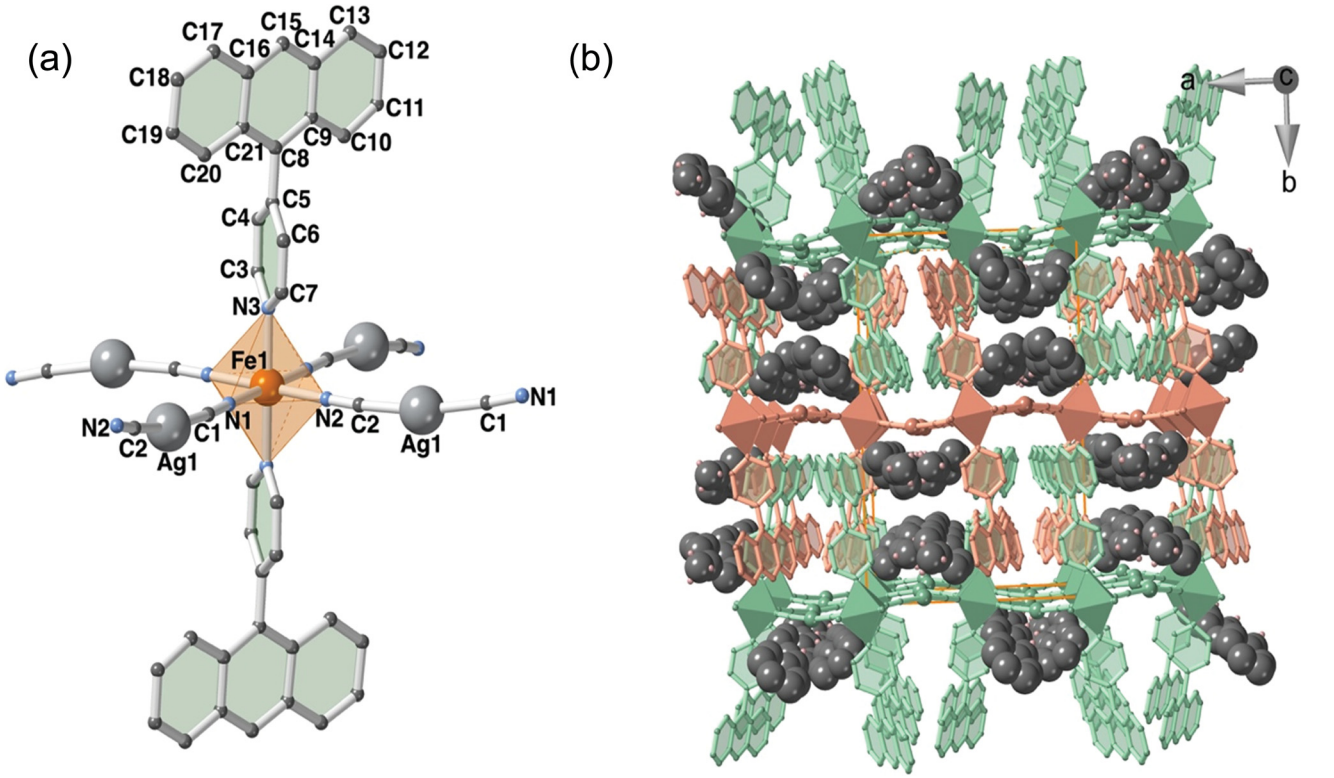


Fig. 2 Typical $Fe^{II}$ environment displayed by **AnPyM·XBz** (M = Ag (X = Br, Cl, $CH_3$, $NO_2$) or Au (X = Br, $NO_2$)) in the orthorhombic phase. (b) Packing of three consecutive layers (green and salmon) of the X = $CH_3$ derivative showing the interdigitation of the AnPy ligands and the channels where the guest molecules are located in **AnPyM·XBz**.

phase change from the orthorhombic *Ccc*2 to the orthorhombic *Pmna* space group. This crystallographic transformation involves the generation of two structurally independent $Fe^{II}$ centers, one of them remaining mostly in the HS state and the other in the LS state, as indicated by the average bond lengths in the range 2.135–2.172 Å and 2.016–1.965 Å, respectively. This is in good accord with the $\chi_M T$ *vs.* *T* measurements and the stabilization of the $[HS_{1/2}{:}LS_{1/2}]$ state responsible for the marked plateau, halfway between the fully HS and LS states. This state is organized by alternating HS and LS centers running along the direction determined by the dicyanometallic bridging ligands (Fig. S10, ESI†). In contrast, no symmetry breaking was observed in the characteristic plateaus for **AnPyAg·$NO_2$Bz** (210 K), **AnPyAg·$CH_3$Bz** (170 K) and **AnPyAu·$NO_2$Bz** (200 K) where the average bond lengths 2.048, 2.065 and 2.060 Å, respectively, reflect a 50% mixture of $Fe^{II}$ centers in the HS and LS states without detected ordering. After further cooling to 120 K, **AnPyAg·ClBz** and **AnPyAg·BrBz** transform back to the initial *Ccc*2 space group with a single $Fe^{II}$ ion in the LS configuration (average bond lengths 1.958 and 1.967 Å, respectively) ($[HS_0{:}LS_1]$), which indicates, consistently with the magnetic measurements, a complete HS-to-LS transformation. In contrast, the *Pmna* space group is retained for compound **AnPyAu·BrBz**, even at 90 K, where the Fe–$N_{av}$ bond-lengths are 2.109 Å and 1.963 Å for each site. The former reflects a change of the HS Fe–$N_{av}$ bond length roughly approaching the mid-way between the HS and LS states and, although no ordering was observed, the overall spin-state change at 90 K suggests that *ca.* 75% of the HS centers transform into the LS state defining a $[HS_{1/4}{:}LS_{3/4}]$ plateau in good agreement with the corresponding magnetic measurements. According to the Fe–$N_{av}$ bond length, the three remaining compounds that do not show symmetry breaking **AnPyAg·$NO_2$Bz** (1.958 Å, 120 K), **AnPyAg·$CH_3$Bz** (1.966 Å, 120 K) and **AnPyAu·$NO_2$Bz** (1.947 Å, 200 K) also attain a fully populated LS state at low temperatures. The *Ccc*2 (Cl, Br), *Pccn* ($CH_3$) and *Cmma* ($NO_2$) orthorhombic space groups differ basically in the dihedral angle ($\alpha$) formed by the anthracene moieties of the two AnPy ligands bonded to a given $Fe^{II}$ center (Fig. S11, ESI†). Except for X = $CH_3$ in which the anthracene moieties are coplanar, $\alpha$ is in the interval 38.5–46.5° and slightly depends on the spin state of the $Fe^{II}$ center. Furthermore, the anthracene and pyridine moieties of the AnPy ligand are oriented each other in an almost orthogonal fashion. The deviation from 90° is in the interval 15–23° depending on the clathrate and spin state (Fig. 2(a)).

**Triclinic phases AnPyAu·XBz (X = $CH_3$ and Cl).** Freshly prepared single crystals of compounds **AnPyAu·XBz** (X = $CH_3$ and Cl) crystallize in the triclinic $P\bar{1}$ space group, which is kept at all the studied temperatures. The asymmetric unit is constituted of two crystallographically independent [Fe1$N_6$] and [Fe2$N_6$] elongated octahedral sites. For the ClBz clathrate, both sites lay in an inversion center as well as the Fe2 site does for the $CH_3$Bz clathrate in contrast to its corresponding Fe1 site that lacks of symmetry (see Fig. 3(a) and (b)). This is the reason

 This journal is © The Royal Society of Chemistry 2022

Published on 04 July 2022. Downloaded by Universitat de València on 2/3/2023 8:59:09 AM.

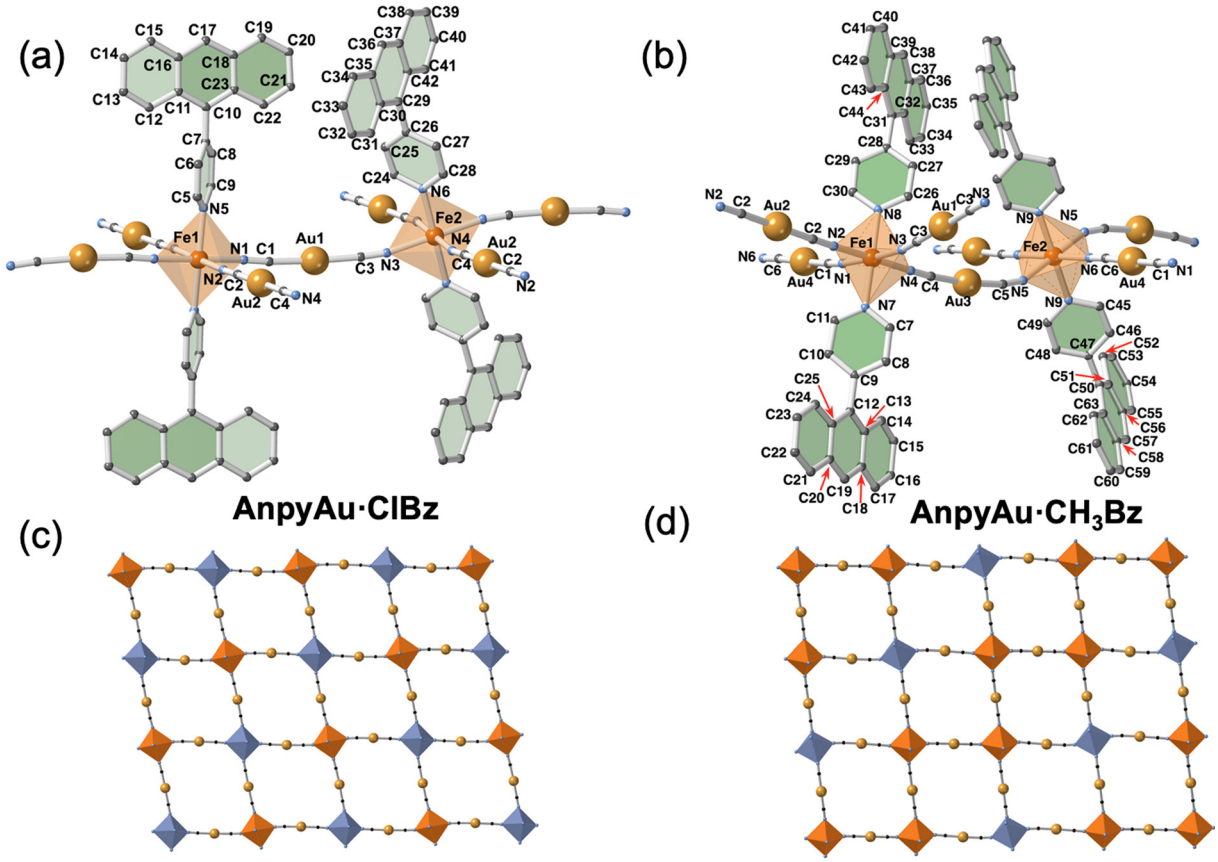


Fig. 3 Assymmetic unit for **AnPyAu·XBz**, X = Cl (a) and $CH_3$ (b). Distribution of the $Fe^{II}$ sites in the $\{Fe_4[Au(CN)_2]_4\}_n$ layers for X = ClBz (c) and $CH_3Bz$ (d) (the axial ligands have been omitted for clarity).

why the anthracenes of the latter site differ more markedly from coplanarity, by around 11.4°, in the temperature interval 260–95 K. A small deviation of *ca.* 5° is also observed for the Fe2 site of the ClBz clathrate at 180 K. At 260 K, the dihedral angle defined by the pyridine and anthracene moieties depart from orthogonality by 32.41°/7.98° (X = Cl) and 13.81°/8.50° (X = $CH_3$) for sites Fe1/Fe2. The average axial Fe–N(pyridine) bond length is 2.201(6)/2.212(6) Å (X = Cl) and 2.225(4)/2.228(4) Å (X = $CH_3$) for Fe1/Fe2. A consequence of the asymmetric nature of the Fe1 nodes in the $CH_3Bz$ derivative is the presence of four crystallographically independent $[Au(CN_2)]^-$ equatorial bridging ligands while only two define the structure of the homologous ClBz. Consequently, the resulting 2D bimetallic layers feature a different distribution of the Fe1 and Fe2 sites in each clathrate.

For the ClBz derivative, the Fe1–Fe2 sites uniformly alternate each other along the two directions of the layer (Fig. 3(c)), while the pattern in the $CH_3Bz$ derivative is Fe1–Fe1–Fe2 (Fig. 3(d)). The equatorial Fe–$N_{av}$ bond lengths are 2.156(6)/2.163(6) Å (X = Cl) and 2.151(5)/2.144(4) Å (X = $CH_3$) for Fe1/Fe2. Then, the overall average Fe–$N_{av}$ for the [Fe1$N_6$] and [Fe2$N_6$] octahedrons at 260 K, found in the interval 2.170–2.179 Å, is consistent with the HS state for both $Fe^{II}$ sites.

At 260 K, the angle defined by two adjacent [$FeN_4^{eq}$] equatorial squares is 22.59° for X = ClBz conferring a certain degree of corrugation to the layers, which are separated in average by 12.0 Å and stack following the $a + c$ direction in the same way as described for the orthorhombic crystals (Fig. S12, ESI†). Although, in general, the packing of the $CH_3Bz$ homologue can be described in the same terms, the angle defined by the equatorial squares of two adjacent octahedrons is considerably much larger, 48.57°, resulting in a much more corrugate layer. The crystal packing of both clathrates, view down the *a* direction, shows that the layers widespread parallel to the *bc* plane and perfectly superpose defining two different channels (labeled 1 and 2) running along the *a* direction where, respectively, 2 and 3 molecules of ClBz and $CH_3Bz$ per $Fe^{II}$ ion are located (Fig. 4 and Fig. S12, ESI†). For **AnPyAu·$CH_3$Bz**, the guest molecules are much more packed in channel 1 since the axial ligands do not protrude in them, in contrast to channel 2 where pairs of non-interacting guests are separated more than 8 Å. In channel 1, the largest separation between guests at 95 K is *ca.* 4 Å and one of the two crystallographically distinct $CH_3Bz$ molecules interact *via* π···π with an equivalent one being the shortest intermolecular distance C75···C73′ of 3.490 Å (see Fig. S13, ESI†). The other $CH_3Bz$ molecule is close to the C1 atom (CN group, 3.491 Å) and C37 (anthracene, 3.484 Å). In channel 2 only a relatively short contact is observed at 95 K between another $CH_3Bz$ molecule and the pyridine moiety *d*(C66···C30) = 3.495 Å.

The interdigitation of the AnPy ligands favors much more interlayer interactions in the two trigonal derivatives,

Published on 04 July 2022. Downloaded by Universitat de València on 2/3/2023 8:59:09 AM.

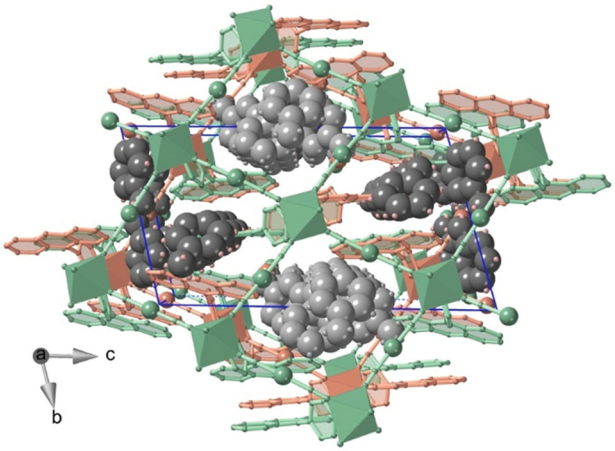


Fig. 4 Perspective view down the *a*-direction showing the superposition of three consecutive layers (green and salmon) of the triclinic **AnPyAu·CH$_3$Bz** and generation of two types of voids where the $CH_3Bz$ guests (space filling) are located: light- and dark-grey in channel 1 and 2, respectively. Blue lines define the unit cell.

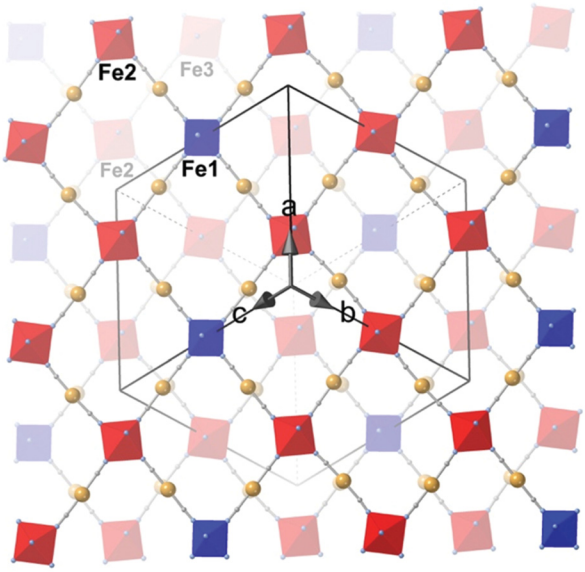


Fig. 5 Projection of two adjacent layers down the *a* + *b* + *c* direction showing the distribution of the HS (red octahedra) and LS (blue octahedra) centers. The axial ligands and the ClBz guests have been omitted for clarity. The black lines correspond to the triclinic unit cell that relates the $Fe^{II}$ centers of both layers.

particularly for the $CH_3Bz$ one due to its larger degree of corrugation. This may be a key factor influencing their metastability in favor of the orthorhombic form. Table S18 (ESI†) gathers a selection of interlayer contacts below 3.5 Å for the ClBz and $CH_3Bz$ derivatives.

When cooling down to 180 K the overall structure of the ClBz clathrate remains the same but now three independent [$FeN_6$] centers are observed and, although the structure conserves the triclinic $P\bar{1}$ space group, the unit cell parameters are significantly modified (see Table S13, ESI†). The Fe–$N_{av}$ bond lengths are 1.964, 2.172 and 2.152 Å for [$Fe1N_6$], [$Fe2N_6$] and [$Fe3N_6$], respectively, indicating the occurrence of a complex LS–HS–HS state arising from the combination, in each layer, of interconnected $\{(Fe2)_2^{HS}$-$(Fe3)_2^{HS}\}$, $\{(Fe1)_2^{LS}(Fe2)_2^{HS}\}$ and $\{(Fe1)_1^{LS}(Fe3)_1^{HS}(Fe2)_2^{HS}\}$ $\{Fe_4[Au(CN)_2]_4\}$ rhombuses as depicted in Fig. 5. The layers stack along the *a* + *b* + *c* direction and the spin-state ordering can be described as defined by two alternating planes, running parallel to the *a*-direction, one defined by Fe1(LS)/Fe3(HS) centers and the other defined exclusively of Fe2(HS) centers laying perpendicular to the layers. Upon cooling to 110 K, the Fe–N average distances change to 1.972 (Fe1), 1.955 (Fe2) and 2.168 (Fe3) Å defining a HS–LS–LS state. The ordering in this state is the same described for the LS–HS–HS state but now all the Fe2 centers are LS while the planes containing Fe1(LS) and Fe3(HS) remain identical. Both states are consistent with the magnetic behavior of the triclinic phase when the samples are measured in the mother liquor (see Fig. S4, ESI†).

Concerning the $CH_3Bz$ derivative, the Fe1–$N_{av}$ and Fe2–$N_{av}$ bond-lengths decrease 0.108 Å (Fe1–$N_{av}$ = 2.068 Å) and 0.010 Å (Fe2–$N_{av}$ = 2.162 Å) upon cooling to 140 K. Thus, considering that a complete spin state transformation involves a total bond length variation of *ca.* 0.2 Å, this indicates that whereas 50% of the Fe1 sites undergo spin transition, the Fe2 sites remain mainly in the HS state. Therefore, overall, only 25% of the $Fe^{II}$ ions present a HS → LS transition at 140 K. An additional cooling to 95 K induces a further decrease of the Fe–$N_{av}$ bond-lengths to 2.048 (Fe1) and 2.091 (Fe2) Å corresponding to a total Fe–$N_{av}$ bond length decrease of *ca.* 0.124 (Fe1) and 0.081 (Fe2) Å that correspond to *ca.* 50% spin transition. This structural change, which is consistent with that observed in the magnetic measurements (see Fig. S4, ESI†), slightly modifies the corrugation of the layers being now the angle between the equatorial planes of the Fe1 and Fe2 octahedrons 44.73°. In contrast to the observed for the ClBz derivative, no symmetry breaking occurs during the SCO and hence no ordering of the HS and LS spin states was observed.

### Thermal SCO by single crystal UV-Vis absorption spectroscopy

The optical properties of **AnPyM·XBz** have been studied for individual single crystals in the temperature interval 10–300 K (see experimental section and ESI†). Herein, we will describe the results for **AnPyAg·IBz** as a representative example. The absorption spectrum of this compound has been recorded in the HS (300 K) and LS (10 K) states from 200 to 1200 nm (Fig. 6(a)). In the HS state the broad band centered at 830 nm, with optical density OD = 0.62, corresponds to the $^5T_2 \rightarrow {}^5E$ transition characteristic of the HS state ($\varepsilon$ = 12 $M^{-1}$ $cm^{-1}$). Below 700 nm, the HS spectrum is almost flat until 480 nm where a new band much higher in Fig. 6. (a) Complete absorption spectra at RT and 10 K of a single crystal of **AnPyAg·IBz** and thermal evolution of the d–d $^1A_1 \rightarrow {}^1T_1$ band during (b) heating and (c) cooling, at 2 K $min^{-1}$ intensity appears and saturates at 415 nm, which corresponds to the tail of the metal-to-ligand charge transfer (MLCT) band. At 10 K the 830 nm band bleaches and instead a new relatively narrower and more intense band (OD = 3.92) centered at 532 nm appears, which

 This journal is © The Royal Society of Chemistry 2022

Published on 04 July 2022. Downloaded by Universitat de València on 2/3/2023 8:59:09 AM.

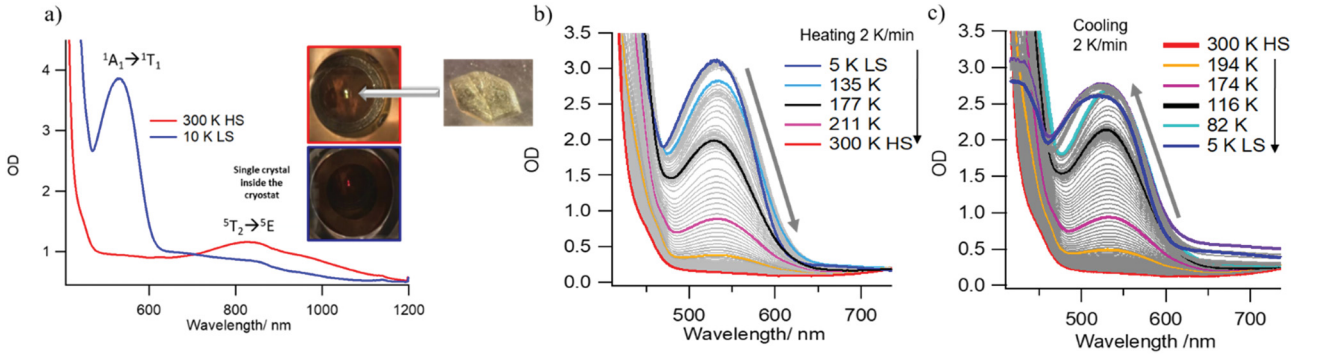


Fig. 6 (a) Complete absorption spectra at RT and 10 K of a single crystal of **AnPyAg·IBz** and thermal evolution of the d–d $^1A_1 \rightarrow {}^1T_1$ band during (b) heating and (c) cooling, at 2 K min$^{-1}$.

corresponds to the $^1A_1 \rightarrow {}^1T_1$ transition of the LS state ($\varepsilon$ = 56 M$^{-1}$ cm$^{-1}$). Below 470 nm the tail of the MLCT band appears and saturates below 438 nm. The change from the HS to LS state is accompanied by a drastic color change from pale-yellow to red (see inset in Fig. 6(a)). Similar features are found for the HS and LS bands of all **AnPyM·XBz** at room temperature and 10 K (Fig. S14, ESI†). Likewise, the values of the corresponding extinction coefficients are relatively constant among the different crystals (Table S19, ESI†). Representative thermal evolution of the LS band intensity recorded in the heating-cooling modes at a scan rate of 2 K min$^{-1}$ is displayed in Fig. 6(b) and (c), respectively for the IBz clathrate. For the rest of compounds, the scan rate used was 10 K min$^{-1}$. Due to the difficulties to get good single crystals of **AnPyAu·CH$_3$Bz**, these measurements were performed on IR-like pellets by diluting the crystalline powder in KBr. In order to optically track the evolution of the HS molar fraction ($\gamma_{HS}$), we have used the thermal evolution of the difference between the maximum and minimum optical density ($\Delta$OD) of the LS band. However, for the M = Au derivatives, displaying incomplete SCO, the residual $\gamma_{HS}$ have been similarly estimated from the remaining HS band at low temperatures. As observed in Fig. 7, all the **AnPyM·XBz** compounds experience relatively abrupt and stepwise transitions with critical temperatures $T_c$ and plateaus in good accord with the results obtained by magnetism (Fig. 1). The slight lower temperatures observed by absorption are attributed to the faster scan rate of the temperature (10 *vs.* 2 K min$^{-1}$). Indeed, aperture of the hysteresis has been observed for **AnPyM·XBz** upon faster scan rates of temperature (Fig. S15, ESI†). It is worth mentioning that an exception of the agreement with the magnetic data is found for **AnPyAu·CH$_3$Bz**. The thermal spin transition obtained optically for the semitransparent pellet is more gradual due to the grinding and pressuring process (Fig. S16, ESI†).[71]

### Coexistence of SCO and fluorescence

The excitation and emission spectra of **AnPyM·XBz** have been recorded at room temperature in an ensemble of crystals glued to a cooper plate with silver paste to ensure thermal conductivity as shown in the Inset of Fig. S17 (ESI†). As an example, the excitation spectrum of **AnPyAg·IBz** is shown in Fig. S17a (ESI†).

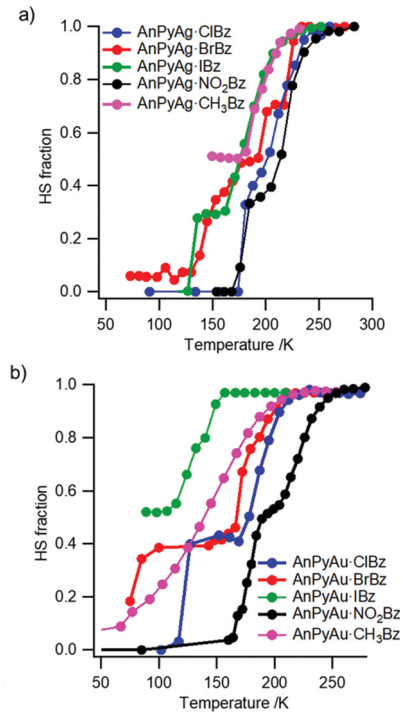


Fig. 7 Thermal dependence of $\gamma_{HS}$ of (a) **AnPyAg·XBz** and (b) **AnPyAu·XBz**, obtained by single crystal absorption spectroscopy.

It is characterized by two sets of peaks, one higher in intensity centered at 260 nm corresponding to the $\pi$–$\pi^*$ band of AnPy and another set split in four more structured excitation bands with origin in the different vibrational contributions between the ground and excited electronic states $S_0$ and $S_1$. The emission spectra of **AnPyAg·IBz** under excitation at 350 nm (Fig. S17b, ESI†) exhibit the emitting features of the $S_1$–$S_0$ transitions in addition to a less structured broader band centred at 500–550 nm associated with the excimer/exciplex. The excitation and emission spectra of the rest of **AnPyM·XBz** samples are almost identical in terms of peak position of the $\pi$–$\pi^*$ and $S_0$–$S_1$ transitions of AnPy ligand although the intensity of the emission band of the excimer/exciplex signals is very low and practically vanishes. As an exception, this latter band has been clearly

Published on 04 July 2022. Downloaded by Universitat de València on 2/3/2023 8:59:09 AM.

identified in the case of **AnPyAu·IBz** and **AnPyAu·ClBz** (Fig. S18, ESI†). A relatively high QY value was obtained for the AnPy ligand (QY ≈ 25%, Fig. S19, ESI†), which is just slightly lower than for anthracene.[72] However, an important decrease of almost 50% is obtained when the ligand is part of the host structure of the non-spin-crossover material **NiAnPyAg·NO$_2$Bz** (QY ≈ 13%). The rigidity of the lattice and miss orientation of the AnPy ligands is expected to contribute to the decrease of non-radiative emissions leading to higher QY values. However, energy transfer from the ligand to the metals ($Ni^{II}$, $Ag^{I}$/$Au^{I}$) may play a relevant role in this case. Indeed, the QY values of the $Fe^{II}$ analogues decrease by around 25% more due to even stronger energy transfer from the ligand to the metals (QY ≈ 6%).

The thermal evolution of the fluorescence spectra (exc. 365 nm) was recorded for all the compounds including the NO$_2$Bz clathrate of the non-SCO $Ni^{II}$ homologue and the free AnPy ligand as references. For the $Ni^{II}$ and AnPy derivatives the thermal dependence of the averaged intensity difference of all the peaks follows a straight line as expected due to thermal quenching (see Fig. S20, ESI†). This is also true for the monomer signal of the $Fe^{II}$ complexes but not for the excimer/exciplex signal observed for **AnPyAu·IBz** (Fig. 8(a) and (c)) and **AnPyAg·IBz** (Fig. 8(b) and (d)) centered around 520 nm whose signal increases with the temperature until approximately 250 K. We associate this inversion of the trend with the LS to HS spin transition of the compounds and the lesser absorption of the fluorescence signal in the HS state (see absorption spectra of Fig. 6). Indeed, the temperature dependence of the HS fraction ($\gamma_{HS}$) extracted from the ratio between the monomer and excimer/exciplex signals matches reasonably well the spin transition curve obtained by magnetism and single crystal absorption for **AnPyM·IBz** (Fig. 8). Unfortunately, for the rest of **AnPyM·XBz** samples the signal of the excimer/exciplex is very weak and no change can be observed with the temperature (Fig. S21, ESI†). An exception is the case of **AnPyAu·ClBz** whose prominent excimer/exciplex signal decreases in a non-linear fashion as temperature increases showing marked stabilization in the temperature interval where the spin transition takes place (Fig. S22, ESI†).

## Discussion

The main objective of this paper is to delve into the design of new 2D metalorganic frameworks as new platforms for the study of synergies stemming from the coexistence of spin-crossover and luminescent properties. This has been achieved by assembling $Fe^{II}$, $[M(CN)_2]^-$ (M = Ag or Au) and the fluorescent AnPy ligands. Provided that the formation of the coordination polymer is carried out in the presence of a selected aromatic molecule XBz (X = $CH_3$, $NO_2$; Cl, Br, I), the resulting compounds present the formula $Fe(AnPy)_2[M(CN)_2]_2$·XBz (**AnPyM·XBz**) where the XBz guests are trapped between the stacked bimetallic layers. The packing-mode of the most part of related dicyanometallate-based 2D networks is determined by interlayer metallophilic (Au···Au or Ag···Ag) interactions which lead to closed bilayered structures where no voids are accessible for hosting guest molecules. In such packing configuration, the pyridinic axial ligands, usually pointing toward the barycenter of the $[Fe_4(M(CN)_2)_4]$ windows of adjacent layers, prevent the inclusion of guests.[42–52] Nevertheless, the presence of a bulky axial ligand may inhibit the creation of metallophilic

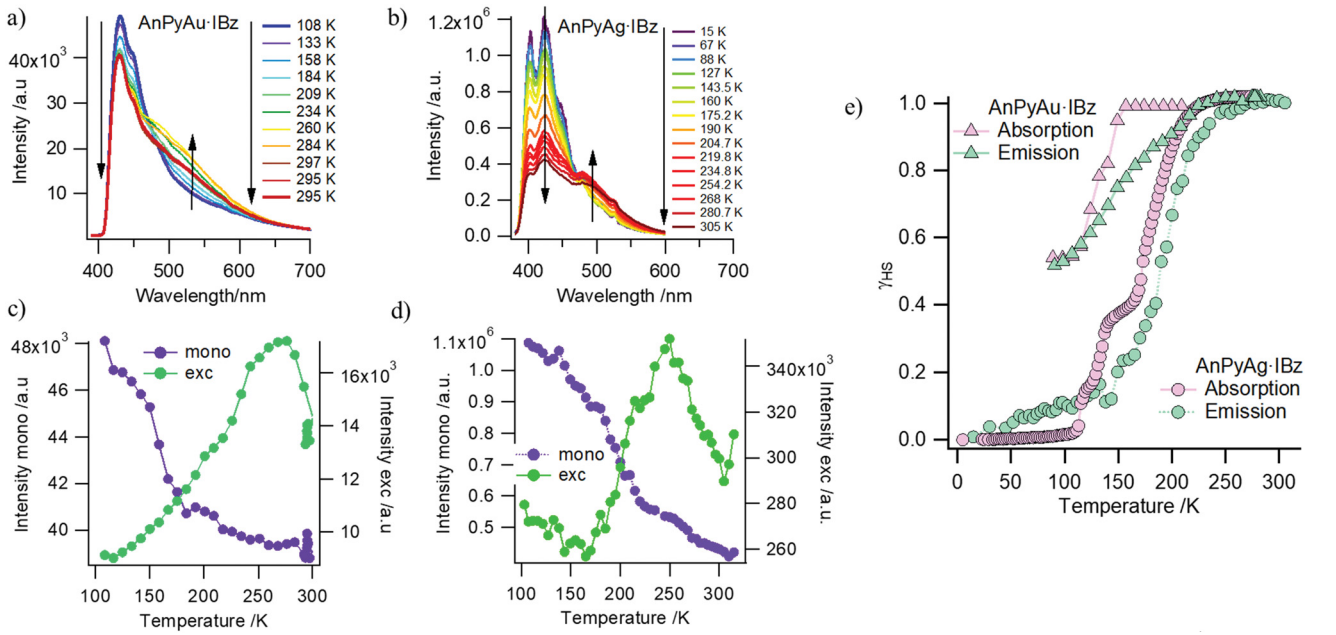


Fig. 8 Thermal evolution of the emission spectra after excitation at 365 nm of an ensemble of crystals of (a) **AnPyAu·IBz** and (b) **AnPyAg·IBz** upon heating (5 K min$^{-1}$). Corresponding variation of the monomer and excimer/exciplex intensity with the temperature for (c) **AnPyAu·IBz** and (d) **AnPyAg·IBz** and (e) the comparison of the temperature dependence of the high-spin fraction extracted by fluorescence and single crystal absorption.

 This journal is © The Royal Society of Chemistry 2022

Published on 04 July 2022. Downloaded by Universitat de València on 2/3/2023 8:59:09 AM.

interactions avoiding the formation of a bilayered structure. This promotes the creation of open structures with the generation of interlayer porosity where the guest molecules can be incorporated in a controlled way.[40,41] This strategy was implemented, for example, in the SCO network Fe[4-(3-Pentyl)pyridine]$_2$[Au(CN)$_2$]$_2$·Guest where the guests (chlorobenzene, *o*-dichlorobenzene, *m*-dichlorobenzene or *p*-dichlorobenzene) are intercalated between the bimetallic layers.[41] The authors concluded that the $T_c$ of each clathrate resulted to be influenced by the size of the aromatic guest *via* chemical pressure in a range of temperatures of 20–30 K.

In the present work, the introduction of the bulky anthracene group in the 4-position of the pyridine not only provides fluorescent properties but also confers enough void space between layers to permit the inclusion of a wide variety of template guests. Even if the different **AnPyM·XBz** clathrates are isostructural, the nature of the trapped guest strongly impacts on the resulting SCO properties. Indeed, the guest-free derivative, which conserves the same structure than the parent solvates, presents a gradual and incomplete SCO. In contrast, the guest-containing species present more or less abrupt and complete multi-stepped SCO behaviors. This observation reveals that the confined guest is a source of cooperativity activating and communicating the spin state change within the network. The trend of $T_c$ values ($T_c$(IBz) < $T_c$(CH$_3$Bz) < $T_c$(BrBz) < $T_c$(ClBz) < $T_c$(NO$_2$Bz)) does not correlate directly with the volume ($V$(IBz) > V(BrBz) > $V$(NO$_2$Bz) > V(ClBz) > $V$(CH$_3$Bz)) (see Table S20, ESI†)[73] of the corresponding guest. Therefore, the $T_c$ modulation does not seem to be explained only by steric hindrance, acting against the network contraction during the spin transition and stabilizing the HS (lower $T_c$). Thus, it is reasonable to take also into consideration electronic factors related with subtle modifications of the ligand field strength of the AnPy ligand derived from its direct interaction with the guest molecules. Unfortunately, except for the CH$_3$Bz derivatives at low temperatures, the strong disorder shown by the guest molecules prevented us from evaluating short host–guest contacts and hence directly assessing their potential steric and electronic influence on the AnPy ligand. Then, we only can prudently speculate with the electronic nature of XBz in order to afford some possible additional justification to the observed trend. As described for the X = CH$_3$ derivatives, it is expected the occurrence of π···π host–guest interactions. With this in mind, it is interesting to note that the highest $T_c$ value is observed for X = NO$_2$, in spite of being more voluminous than X = CH$_3$ or Cl (see Table S20, ESI†). This fact could be related to the strong electron-withdrawing character of X = NO$_2$, namely to the highest positive $\sigma_p$ Hammett[74,75] parameter of the XBz series (0.81), in contrast to the clathrate X = CH$_3$ ($\sigma_p$ = −0.17), which shows a $T_c$ significantly smaller. Consequently, the higher electron density of the CH$_3$Bz ring may weaken the attractive π···π interaction with the AnPy in contrast to the NO$_2$Bz–AnPy interaction. The latter interaction can indirectly enhance the π-accepting character of the ligand AnPy and hence increase subtly its ligand field strength. For IBz ($\sigma_p$ = 0.18), BrBz and ClBz ($\sigma_p$ = 0.23) with comparable $\sigma_p$ values, the $T_c$ of the corresponding clathrate ($T_c$(IBz) < $T_c$(BrBz) < $T_c$(ClBz)) seems to be directly correlated to the guest molecular volume $V$(IBz) > $V$(BrBz) > $V$(ClBz). Finally, the increase in $T_c$ when moving from **AnPyAu**·XBz to **AnPyAg·XBz**, and hence the stabilization of the LS state, is typically associated with the less donor character of the cyanide groups in [Au(CN)$_2$]$^-$ with respect to [Ag(CN)$_2$]$^-$ as a result of the higher electronegativity of the Au$^I$ against Ag$^I$ stemming from well-known relativistic effects.[76]

From an optical point of view, the single crystals of **AnPyM·XBz** display rather intense Fe$^{II}$ d–d bands in the LS state and thanks to the high quality and transparency of the crystals it has been possible to follow the thermal dependence of the optical density. For all the samples the absorption spectra show an isosbestic point indicating the presence of an equilibrium between the HS and LS populations as the thermal spin transition takes place. In general, the thermal dependence of the HS centers monitored optically is in good agreement with the magnetic data. Furthermore, the presence of the anthracene moiety in the AnPy ligand confers to the **AnPyM·XBz** crystals the property of luminescence. In general, the crystals show a strong emission in the blue region and, in some cases, an additional less intense emission in the green region, which are associated with the monomer and excimer/exciplex signals, respectively. The monomer signal decreases linearly and bleaches with increasing temperatures due to thermal quenching. In contrast, the excimer/exciplex signal, only observed for **AnPyAg·IBz**, **AnPyAu·IBz** and **AnPyAu·ClBz**, increases or stabilizes in a concerted way as the amount of Fe$^{II}$ HS centers increases, due to their much weaker absorption compared to that of the LS centers in the same wave-lengths window. Both contributions have also been previously described for the anthracene-bearing ditopic Bpan ligand used as pillar in the 3D SCO HCP {Fe(Bpan)[M$^I$(CN)$_2$]$_2$} (so-called intrinsic fluorescence)[60] and, more markedly, in two other 3D SCO CPs {Fe(L)[M(CN)$_2$]$_2$}·Pyr with pyrene (Pyr) as guest fluorescent agent (L = bpb, bpben, extrinsic fluorescence) (M = Ag, Au).[60,61] All these compounds share a similar extinction coefficient of the Fe$^{II}$ d–d LS bands (≈50 M$^{-1}$ cm$^{-1}$), however, the efficiency of the energy transfer from the fluorophore to the Fe$^{II}$ seems to be proportional to the emission capacity of the former and hence to the quantum yield of the free fluorophore, being the highest for pyrene in the bpb and bpben based compounds (≈36%), followed by Bpan (≈32%) and finally AnPy (≈25%). This is the reason why the emission spectra of the AnPy derivatives are less efficient (less intense) than those of bpb, bpben and Bpan derivatives. It is also safe to state from this study that the presence of the guest XBz, which modulates the spin transition, does not contribute to the fluorescence in the UV region, although it could stabilize the excimer/exciplex. However, in spite of being isostructural, the excimer/exciplex emission has only been clearly observed for **AnPyAg·IBz**, **AnPyAu·IBz** and **AnPyAu·ClBz** although it is not an obvious matter to shed light on why the remaining members of the series, as well as the pure AnPy ligand, lack of this signal. It is commonly accepted that the precise orientation of the fluorophore ligands in the framework and in their interaction with the guests may be critical for the formation of the excimer/exciplex.[77] In this respect, the

Published on 04 July 2022. Downloaded by Universitat de València on 2/3/2023 8:59:09 AM.

AnPy-based HCPs here described, keeping the isostructurality, present a number of small relevant structural differences such as the degree of corrugation of the layers, the dihedral angle defined between the two anthracene moieties belonging to the same $Fe^{II}$ center, the dihedral angle defined between the anthracene and pyridine of the same AnPy, among others. Obviously, these differences also result from the inclusion of the different guests, which in addition do not display a favorable face-to-face stacking with the fluorophore as observed for the bpb, bpben and bpan-based 3D SCO HCPs.

## Conclusions

In summary, we have synthesized and characterized a novel family of multifunctional 2D HCPs formulated as $\{Fe(AnPy)_2[M(CN)_2]_2\}\cdot XBz$. This system is one of the first 2D Hofmann clathrates displaying concomitant multi-stepped SCO and fluorescent emission. These properties arise, respectively, from the presence of octahedrally coordinated $Fe^{II}$ ions and anthracene based AnPy ligands. Furthermore, the packing mode, consisting of stacking bimetallic layers, leads to large interlayer cavities where substituted benzenic guests are premeditatedly trapped and used as crystallization templates. Indeed, due to a combination of steric and electronic effects, this guest trapping impacts notably on the SCO behaviour modulating the $T_c$ as a function of the guest nature. The multi-stepped behaviour of the SCO has been evidenced also by single crystal X-ray diffraction which has allowed us to identify new examples of symmetry breaking and spin-state ordering associated to the spin state transition. The UV-visible absorption studies, carried out on individual single crystals, have revealed the HS $\leftrightarrow$ LS equilibrium through the thermal evolution of the $Fe^{II}$ d–d bands, in good agreement with the thermal spin transition curves and $T_c$ modulation obtained from magnetism. Finally, new evidence of interplay between SCO and fluorescence functions has been unveiled in the case of X = I (M = Ag, Au) and X = Cl (M = Au). This interplay stems from the resonance between the $Fe^{II}$ LS-state d–d absorption band and the excimer/exciplex fluorescent emission band of the AnPy ligand in the green region. Therefore, as the $Fe^{II}$ LS-state d–d absorption band vanishes in the HS state the green emission increases with temperature allowing to monitor the spin conversion. These outcomes together with our previous observations of the SCO-fluorescence synergy in 3D SCO HCPs highlight the importance of the intrinsic emission capacity of the fluorophores involved and suggest that their precise orientation and packing in the structure as well as a relatively high compactness of the lattice is determinant to create and follow this synergy.

## Author contributions

Rubén Turo-Cortés: investigation, methodology, writing – review & editing; Manuel Meneses-Sánchez: investigation, writing-review & editing; Teresa Delgado: investigation, writing-review & editing; Carlos Bartual-Murgui: supervision, writing – original draft, investigation; M. Carmen Muñoz: supervision, writing – review & editing, funding acquisition; J. Antonio Real: funding acquisition, supervision, writing – review & editing.

## Conflicts of interest

There are no conflicts to declare.

## Acknowledgements

This work was supported by: Grant PID2019-106147GB-I00 funded by (MCIN/AEI/10.13039/501100011033) and Unidad de Excelencia María de Maeztu (CEX2019-000919-M). We thank the Swiss National Science Foundation (Postdoc Mobility P400P2_191108/1) and Dr Viana for discussion and constructive feedback. R. T.-C. and M. M.-S. thank MCIN and FSE invierte en tu futuro for the predoctoral (FPI) grants PRE2018-084918 and BES2017-081393, respectively. We thank Juan Aragó for his hepfull contribution regarding the molecular volume calculations with Chimera software.

## Notes and references

1 E. König, *Nature and Dynamics of the Spin-State Interconversion in Metal Complexes*, 1991, pp. 51–152.
2 Spin Crossover Phenomenon, *C. R. Chimie*, ed. A. Bousseksou, 2018, vol. 21, pp. 1055–1299.
3 Spin crossover in transition metal compound I–III, *Topics in Current Chemistry*, ed. P. Gütlich and G. Goodwin, Springer, 2004, pp. 233–235.
4 B. Weber, *Coord. Chem. Rev.*, 2009, **253**, 2432–2449.
5 M. A. Halcrow, *Chem. Soc. Rev.*, 2011, **40**, 4119.
6 V. Niel, M. C. Muñoz, A. B. Gaspar, A. Galet, G. Levchenko and J. A. Real, *Chem. – Eur. J.*, 2002, **8**, 2446–2453.
7 P. Gütlich, A. Hauser and H. Spiering, *Angew. Chem., Int. Ed. Engl.*, 1994, **33**, 2024–2054.
8 S. Brooker, *Chem. Soc. Rev.*, 2015, **44**, 2880–2892.
9 M. A. Halcrow, *Chem. Lett.*, 2014, **43**, 1178–1188.
10 M. A. Halcrow, *Spin-crossover materials: properties and applications*, Wiley-Blackwell, 2013.
11 A. Bousseksou, G. Molnár, L. Salmon and W. Nicolazzi, *Chem. Soc. Rev.*, 2011, **40**, 3313.
12 O. I. Kucheriv, I. O. Fritsky and I. A. Gural'skiy, *Inorg. Chim. Acta*, 2021, **521**, 120303.
13 M. C. Muñoz and J. A. Real, *Coord. Chem. Rev.*, 2011, **255**, 2068–2093.
14 Y. Garcia, V. Niel, M. C. Muñoz and J. A. Real, Spin Crossover in 1D, 2D and 3D Polymeric Fe(II) Networks, *Spin Crossover in Transition Metal Compounds I*, Springer, Berlin, Heidelberg, 2004, pp. 229–257.
15 Z.-P. Ni, J.-L. Liu, M. N. Hoque, W. Liu, J.-Y. Li, Y.-C. Chen and M.-L. Tong, *Coord. Chem. Rev.*, 2017, **335**, 28–43.
16 K. A. Zenere, S. G. Duyker, E. Trzop, E. Collet, B. Chan, P. W. Doheny, C. J. Kepert and S. M. Neville, *Chem. Sci.*, 2018, **9**, 5623–5629.

 This journal is © The Royal Society of Chemistry 2022

Published on 04 July 2022. Downloaded by Universitat de València on 2/3/2023 8:59:09 AM.

17 N. F. Sciortino, F. Ragon, Y. M. Klein, C. E. Housecroft, C. G. Davies, G. N. L. Jameson, G. Chastanet and S. M. Neville, *Inorg. Chem.*, 2018, **57**, 44.
18 E. Milin, V. Patinec, S. Triki, E. E. Bendeif, S. Pillet, M. Marchivie, G. Chastanet and K. Boukheddaden, *Inorg. Chem.*, 2016, **55**, 11652–11661.
19 N. F. Sciortino, F. Ragon, K. A. Zenere, P. D. Southon, G. J. Halder, K. W. Chapman, L. Piñeiro-López, J. A. Real, C. J. Kepert and S. M. Neville, *Inorg. Chem.*, 2016, **55**, 10490–10498.
20 A. T. Brennan, K. A. Zenere, C. J. Kepert, J. K. Clegg and S. M. Neville, *Inorg. Chem.*, 2021, **60**, 3871–3878.
21 S. M. Neville, A. T. Brennan, K. A. Zenere, H. E. A. Brand, J. R. Price, M. M. Bhadbhade, G. F. Turner, S. A. Moggach, F. J. Valverde-Munoz, J. A. Real, J. K. Clegg and C. J. Kepert, *Inorg. Chem.*, 2020, **59**, 14296–14305.
22 I. A. Gural'skiy, S. I. Shylin, V. Ksenofontov and W. Tremel, *Eur. J. Inorg. Chem.*, 2019, 4532–4537.
23 N. F. Sciortino, K. A. Zenere, M. E. Corrigan, G. J. Halder, G. Chastanet, J. F. Létard, C. J. Kepert and S. M. Neville, *Chem. Sci.*, 2016, **8**, 701–707.
24 M. J. Murphy, K. A. Zenere, F. Ragon, P. D. Southon, C. J. Kepert and S. M. Neville, *J. Am. Chem. Soc.*, 2017, **139**, 1330–1335.
25 Y. M. Klein, N. F. Sciortino, F. Ragon, C. E. Housecroft, C. J. Kepert and S. M. Neville, *Chem. Commun.*, 2014, **50**, 3838–3840.
26 M. Meneses-Sánchez, R. Turo-Cortés, C. Bartual-Murgui, I. Da Silva, M. C. Muñoz and J. A. Real, *Inorg. Chem.*, 2021, **60**, 11866–11877.
27 R. Ohtani and S. Hayami, *Chem. – Eur. J.*, 2017, **23**, 2236–2248.
28 V. Niel, A. L. Thompson, M. C. Muñoz, A. Galet, A. E. Goeta and J. A. Real, *Angew. Chem., Int. Ed.*, 2003, **42**, 3760–3763.
29 H. Xu, G. Juhász, K. Yoshizawa, M. Takahashi, S. Kanegawa and O. Sato, *CrystEngComm*, 2010, **12**, 4031–4034.
30 K. Yoshida, D. Akahoshi, T. Kawasaki, T. Saito and T. Kitazawa, *Polyhedron*, 2013, **66**, 252–256.
31 J.-Y. Li, Z. Yan, Z.-P. Ni, Z.-M. Zhang, Y.-C. Chen, W. Liu and M.-L. Tong, *Inorg. Chem.*, 2014, **53**, 4039–4046.
32 J. Y. Li, Y. C. Chen, Z. M. Zhang, W. Liu, Z. P. Ni and M. L. Tong, *Chem. – Eur. J.*, 2015, **21**, 1645–1651.
33 J.-Y. Li, C.-T. He, Y.-C. Chen, Z.-M. Zhang, W. Liu, Z.-P. Ni and M.-L. Tong, *J. Mater. Chem. C*, 2015, **3**, 7830–7835.
34 J. E. Clements, J. R. Price, S. M. Neville and C. J. Kepert, *Angew. Chem., Int. Ed.*, 2014, **53**, 10164–10168.
35 I. A. Gural'skiy, S. I. Shylin, B. O. Golub, V. Ksenofontov, I. O. Fritsky and W. Tremel, *New J. Chem.*, 2016, **40**, 9012–9016.
36 M.-L. Tong, W. Liu, Y.-Y. Peng, S.-G. Wu, Y.-C. Chen, N. Hoque, Z.-P. Ni and X.-M. Chen, *Angew. Chem., Int. Ed.*, 2017, **129**, 15178–15182.
37 L. Piñeiro-López, F. J. Valverde-Muñoz, M. Seredyuk, M. C. Muñoz, M. Haukka and J. A. Real, *Inorg. Chem.*, 2017, **56**, 7038–7047.
38 L. Piñeiro-López, F. J. Valverde-Muñoz, M. Seredyuk, C. Bartual-Murgui, M. C. Muñoz and J. A. Real, *Eur. J. Inorg. Chem.*, 2018, 289–296.
39 F. J. Valverde-Muñoz, C. Bartual-Murgui, L. Piñeiro-López, M. C. Muñoz and J. A. Real, *Inorg. Chem.*, 2019, **58**(15), 10038–10046.
40 G. Agustí, M. C. Muñoz, A. B. Gaspar and J. A. Real, *Inorg. Chem.*, 2008, **47**, 2552–2561.
41 Y. Ueki, J. Okabayashi and T. Kitazawa, *Chem. Lett.*, 2017, **46**, 747–749.
42 T. Kosone, T. Kawasaki, I. Tomori and J. Okabayashi, *Inorganics*, 2017, 1–10.
43 K. Yoshida, T. Kosone, C. Kanadani, T. Saito and T. Kitazawa, *Polyhedron*, 2011, **30**, 3062–3066.
44 S. Ueno, T. Kawasaki, J. Okabayashi and T. Kitazawa, *Bull. Chem. Soc. Jpn.*, 2015, **88**, 551–553.
45 A. Sugaya, S. Ueno, J. Okabayashi and T. Kitazawa, *New J. Chem.*, 2014, **38**, 1955–1958.
46 S. Ueno, T. Kawasaki, J. Okabayashi and T. Kitazawa, *Bull. Chem. Soc. Jpn.*, 2016, **89**, 581–583.
47 Y. Meng, Q. Q. Sheng, M. N. Hoque, Y. C. Chen, S. G. Wu, J. Tucek, R. Zboril, T. Liu, Z. P. Ni and M. L. Tong, *Chem. – Eur. J.*, 2017, **23**, 10034–10037.
48 J. Okabayashi, S. Ueno, T. Kawasaki and T. Kitazawa, *Inorg. Chim. Acta*, 2016, **445**, 17–21.
49 T. Kosone, I. Tomori, C. Kanadani, T. Saito, T. Mochida and T. Kitazawa, *Dalton Trans.*, 2010, **39**, 1719–1721.
50 G. Agustí, A. B. Gaspar, M. C. Muñoz, P. G. Lacroix, J. A. Real, G. Agustí, A. B. Gaspar, M. C. Muñoz, P. G. Lacroix and J. A. Real, *Aust. J. Chem.*, 2009, **62**, 1155–1165.
51 T. Kosone, C. Kachi-Terajima, C. Kanadani, T. Saito and T. Kitazawa, *Chem. Lett.*, 2008, **37**, 422–423.
52 A. Galet, M. C. Muñoz, V. Martínez and J. A. Real, *Chem. Commun.*, 2004, 2268–2269.
53 B. Benaicha, K. Van Do, A. Yangui, N. Pittala, A. Lusson, M. Sy, G. Bouchez, H. Fourati, C. J. Gómez-García, S. Triki and K. Boukheddaden, *Chem. Sci.*, 2019, **10**, 6791–6798.
54 J. Yuan, S.-Q. Wu, M.-J. Liu, O. Sato and H.-Z. Kou, *J. Am. Chem. Soc.*, 2018, **140**, 9426–9433.
55 J.-L. Wang, Q. Liu, Y.-S. Meng, X. Liu, H. Zheng, Q. Shi, C.-Y. Duan and T. Liu, *Chem. Sci.*, 2018, **9**, 2892–2897.
56 C. Lochenie, K. Schötz, F. Panzer, H. Kurz, B. Maier, F. Puchtler, S. Agarwal, A. Kö and B. Weber, *J. Am. Chem. So.*, 2018, 140, 700–709.
57 B. Schäfer, T. Bauer, I. Faus, J. A. Wolny, F. Dahms, O. Fuhr, S. Lebedkin, H.-C. Wille, K. Schlage, K. Chevalier, F. Rupp, R. Diller, V. Schünemann, M. M. Kappes and M. Ruben, *Dalton Trans.*, 2017, **46**, 2289–2302.
58 H. J. Shepherd, C. M. Quintero, G. Molnar, L. Salmon and A. Bousseksou, in *Spin-Crossover Materials Properties and Applications*, ed. M. Halcrow, 2013, pp. 347–373.
59 M. K. Javed, A. Sulaiman, M. Yamashita and Z.-Y. Li, *Coord. Chem. Rev.*, 2022, **467**, 214625.
60 M. Meneses-Sánchez, L. Piñeiro-López, T. Delgado, C. Bartual-Murgui, M. C. Muñoz, P. Chakraborty and J. A. Real, *J. Mater. Chem. C*, 2020, **8**, 1623–1633.
61 T. Delgado, M. Meneses-Sánchez, L. Piñeiro-López, C. Bartual-Murgui, M. C. Muñoz and J. A. Real, *Chem. Sci.*, 2018, **9**, 8446–8452.

Published on 04 July 2022. Downloaded by Universitat de València on 2/3/2023 8:59:09 AM.

62 J. Ge, Z. Chen, L. Zhang, X. Liang, J. Su, M. Kurmoo and J. Zuo, *Angew. Chem., Int. Ed.*, 2019, **131**, 8881–8885.
63 S. Ghosh, S. Kamilya, T. Pramanik, M. Rouzières, R. Herchel, S. Mehta and A. Mondal, *Inorg. Chem.*, 2020, **59**, 13009–13013.
64 Y. R. Qiu, L. Cui, J. Y. Ge, M. Kurmoo, G. Ma and J. Su, *Front. Chem.*, 2021, **9**, 611.
65 C. F. Wang, J. C. Wu and Q. Li, *Inorg. Chem. Front.*, 2022, 3251–3258.
66 S. Decurtins, P. Gütlich, C. P. Köhler, H. Spiering and A. Hauser, *Chem. Phys. Lett.*, 1984, **105**, 1–4.
67 J.-F. Létard, P. Guionneau, L. Rabardel, J. A. K. Howard, A. E. Goeta, D. Chasseau and O. Kahn, *Inorg. Chem.*, 1998, **37**(17), 4432–4441.
68 A. Hauser, *Coord. Chem. Rev.*, 1991, **111**, 275–290.
69 A. Hauser, A. Vef and P. Adler, *J. Chem. Phys.*, 1991, **91**, 8710–8717.
70 A. Hauser, C. Enachescu, M. L. Daku, A. Vargas and N. Amstutz, *Coord. Chem. Rev.*, 2006, **250**, 1642–1652.
71 T. Delgado, A. Tissot, C. Besnard, L. Guénée, P. Pattison and A. Hauser, *Chem. – Eur. J.*, 2015, **21**, 3664–3670.
72 I. B. Berlman, *Handbook of fluorescence spectra of aromatic Molecules*, 1971, p. 473.
73 Values of V and were calculated with the software UCSF Chimera see E. F. Pettersen, T. D. Goddard, C. C. Huang, G. S. Couch, D. M. Greenblatt, E. C. Meng and T. E. Ferrin, UCSF Chimera-a visualization system for exploratory research and analysis, *J. Comput. Chem.*, 2004, **25**(13), 1605–1612.
74 L. P. Hammett, *J. Am. Chem. Soc.*, 1937, **59**, 96–103.
75 C. Hansch, A. Leo and R. W. Taft, *Chem. Rev.*, 1991, **91**, 165–195.
76 P. Pyykkö and P. Pyykkö, *Annu. Rev. Phys. Chem.*, 2012, **63**, 45–64.
77 P. Samanta, S. Dutta and S. K. Ghosh, Metal–organic frameworks for detection and desensitization of environmentally hazardous nitro-explosives and related high energy materials, *Met. Org. Frameworks (MOFs) Environ. Appl.*, 2019, 231–283.

 This journal is © The Royal Society of Chemistry 2022